Life Cycle Air Quality and Climate Impacts of Conventional and Alternative Light-Duty Transportation in the United States

A DISSERTATION

SUBMITTED TO THE FACULTY OF THE GRADUATE SCHOOL

OF THE UNIVERSITY OF MINNESOTA

BY

Christopher Tessum

IN PARTIAL FULFILLMENT OF THE REQUIREMENTS

FOR THE DEGREE OF

DOCTOR OF PHILOSOPHY

Julian D. Marshall

December, 2014

Acknowledgements

This dissertation would not have been possible without the contributions and support of many. I would like to thank my dissertation committee, Professors Julian Marshall, Jason Hill, Dylan Millet, and Matt Simcik. All four have proven valuable teachers and mentors and have offered insightful feedback throughout my graduate career. I am especially grateful to Julian and Jason for countless hours of explanation, discussion, and feedback, which have greatly changed the way I look at and think about the world.

I would like to thank Matt, Lara, Steve, and all of the students in the Marshall Research Group for help and suggestions with research and with life as a graduate student, and for making the office a place that is not only tornado- and sunlight-proof but also an enjoyable environment.

I am grateful to my wife and family for their support and encouragement during the past six years of graduate school, and during the 24 years before that.

I would also like to acknowledge the University of Minnesota Institute on the Environment Initiative for Renewable Energy and the Environment Grants No. Rl-0026-09 and RO-0002-11, the U.S. Department of Energy Award No. DE-EE0004397, and the U.S. Department of Agriculture NIFA/AFRI Grant No. 2011-68005-30411 for funding; the Minnesota Supercomputing Institute and the Department of Energy National Center for Computational Sciences Award No. DD-ATM007 for computational resources; John Michalakes, Steven Roste, Reuben Verdoljak, and Tom Nickerson for assistance with computer coding and optimization, literature review, and data acquisition; and Stephen Polasky, Jeremy J. Michalek, Andrew Goodkind,

Josh Apte, Dev Millstein, and Kimberly Mullins for review of or discussion about individual chapters of my dissertation.

Dedication

To Mei, my greatest advocate.

Abstract

This dissertation explores air quality, climate, and environmental injustice aspects of potential strategies for reducing the environmental impacts of the light-duty vehicles in the United States. These strategies include the use of alternative fuels—liquid biofuels, electricity from a range of sources, or compressed natural gas (CNG)—to power vehicles, as well as methods for improving vehicle fuel-economy.

Because the magnitude of the air-quality-related health impacts are strongly dependent on the place and time of emission, spatial and temporal information is critical to an accurate understanding of the life cycle impacts of vehicle use. I add process-specific spatial and temporal information to an existing attributional life cycle inventory (LCI) model so as to reveal patterns in the geographic distribution and intra-annual timing of emissions of transportation fuel production and use. I combine this spatially- and temporally-explicit life cycle assessment with comprehensive chemical transport modeling for ozone (O_3) and fine particulate matter ($PM_{2.5}$) to estimate the human health impacts of a range of strategies for reducing light-duty vehicle gasoline use.

I investigate scenarios where 10% of U.S. projected vehicle miles traveled in year-2020 are driven in one of eleven types of passenger cars: 1) conventional gasoline powered vehicles; 2) grid-independent hybrid electric vehicles; 3) diesel powered cars; 4) internal-combustion compressed natural gas vehicles; 5) vehicles powered by ethanol from corn grain through natural-gas powered dry milling; 6) vehicles powered by cellulosic ethanol from corn stover; and battery electric vehicles (EVs) powered by electricity from: 7) the projected year-2020 U.S. average electric generation mix; 8) coal; 9) natural gas; 10) the combustion of corn stover; and 11) wind turbines, dynamic water power, or solar power. I find that powering vehicles with corn ethanol or with coal-based or "grid average" electricity increases monetized environmental health impacts by 80% or more relative to using conventional gasoline. Conversely, EVs powered by low-emitting electricity from natural gas, wind, water, or solar-power reduce

impacts by 50% or more. I also consider the potential climate change impacts of each scenario, which further reinforces the environmental preferability of low-emitting electric vehicles relative to gasoline vehicles.

I expand the above results with two supporting analyses. In the first analysis, I investigate how spatial patterns in the release of climate-forcing emissions in fuel production are linked to spatial patterns in the consumption activities they support. This investigation considers vehicles powered by gasoline, ethanol from corn grain, ethanol from corn stover, and electric fuels. For the gasoline life cycle, I find that emissions of climate-forcers (i.e., GHGs plus radiatively active aerosols) are primarily colocated with vehicle use. For corn ethanol and electric vehicles, however, there is a disconnect between the areas that produce the most fuel (the Midwest "Corn Belt" for ethanol; the Tennessee River Valley and Texas for electrical vehicles) and the areas that consume the most fuel (California, Texas, Florida and New York). Information on where changes to climate-forcing emissions would occur is important in part because of differences between regulatory jurisdictions and the scope of current accounting frameworks for climate-forcers. Many U.S. states have established emission reduction targets; my research shows how a biofuel policy designed to help one state could hinder another.

In the second analysis, I develop and apply a new air quality model, the Intervention Model for Air Pollution (InMAP), which provides estimates of air pollution health impacts resulting from marginal changes in pollutant emissions. By making simplifying assumptions regarding atmospheric chemistry undergoing marginal changes in pollutant emissions, and by focusing on predicting annual average changes in pollutant concentrations—which are the largest predictor of environmental health impacts—InMAP is able to perform simulations that are much less computationally intensive than comprehensive air quality model simulations, but that are more detailed than simulations from other reduced complexity models. I use InMAP to explore the same transportation scenarios described above, but in this case investigating how the scenarios affect disparities in environmental health risks among race, ethnicity, and income groups. InMAP is well-suited to investigate these environmental injustice issues because it can be used with high enough spatial resolution to resolve intra-urban differences in

pollution concentration and to track the long-range transport of pollution at the same time. I find that non-White people and people in poverty generally tend to be disproportionately exposed to air pollution impacts from the various transportation scenarios—what is considered to be an environmentally unjust situation. The scenarios that cause the greatest improvements in overall air quality-related health impacts compared to the business-as-usual gasoline scenario—electric vehicles powered by natural gas or wind, water, or solar power—also yield substantial improvements in environmental justice.

Contents

List of Tables

List of Figures

Chapter 1

Introduction

As the beginning of the 20th century approached, cities in the United States had a problem: horse manure. In the 1890s, horses were producing 150,000 tons of manure annually in New York city alone (*1*). Manure, in addition to being unsightly and unpleasant, was a favorite breeding ground for disease-transmitting horse flies (*2*), and was therefore considered a threat to public health.

A number of revolutionary new technologies appeared in the late 19th century, including bicycles, electric trams, and passenger vehicles powered by electricity or gasoline (*3*). After its development in the 1880s, the electric tram was the early favorite for replacing horse traffic (*2*, *3*), but with developments in automotive technology and production methods in the early 1900s, the gasoline-powered automobile began to increase in popularity (*3*). Feeling that the solution to the unsanitary conditions in cities at the time was to decrease population density by encouraging people to move out of city centers, public policy makers in effect chose to tax the tram operators by limiting fare prices, while subsidizing automobiles through publicly funded road improvement projects (*3*). Excluding the World War II years, tram ridership in the U.S. decreased every year between 1925 and 1970 (*4*) and gasoline-powered vehicles went on to become the dominant mode of passenger transport.

Although gasoline-powered vehicles solved some of the environmental problems of the

late 19th century, they introduced problems of their own. Dominant among these problems are emissions of air pollutants, which lead to chronic health problems (*5*, *6*), and emissions of greenhouse gases (GHGs), which contribute to global climate change (*5–8*). It is difficult to say whether the environmental problems caused by modern automobiles are better or worse than those caused by late 19th century horses, or whether government policy that was more favorable to electric trams would have fixed anything. However, we do know that because the eventual problems that would be caused by gasoline-powered automobiles were not widely foreseen, these downsides were not weighed against the benefits of automobile use when deciding transportation policy during this period.

Today, we are again in an era where the dominant mode of transportation—gasoline-powered vehicles—is the cause of environmental problems and various alternative technologies are emerging to fix these problems. These include technologies to more efficiently use gasoline, such as grid-independent hybrid gasoline-electric vehicles (commonly known as hybrids); internal combustion engines that use gasoline-alternative fuels such as diesel, compressed natural gas, or ethanol; and the reemergence of vehicles powered by electricity. Scientists are now in a position to examine the relative environmental costs and benefits of each of these options, hopefully to identify potential issues with these alternative technologies before they become widely adopted. In this dissertation I hope to contribute to this effort. Specifically, I will examine air quality-related public health impacts and impacts to global-climate-forcing emissions of future scenarios where these alternative technologies have replaced a portion of gasoline vehicles in the United States as compared to a scenario where they haven't.

According to a recent study by Lim et al. (*9*), non-greenhouse gas ambient air pollution is the cause of over 3 million deaths per year. Globally, it is the ninth largest environmental cause of mortalities; in high-income North America it is the 14th largest cause. Approximately 95% of ambient air pollution-related mortalities are caused by fine particulate matter ($PM_{2.5}$), and the remaining 5% are caused by ground-level ozone (O_3). (This study did not find sufficient evidence for mortalities caused by other pollutants.) Tailpipe emissions from on-road transportation account for approximately 8% of the deaths caused by air pollution in the U.S.

(*10*). Upstream processes involved in fuel production also contribute to additional air quality impacts, so changes in emissions of $PM_{2.5}$ and of O_3 and $PM_{2.5}$ and precursors from on-road transportation can substantially impact pollutant concentrations and overall public health.

Society is in the midst of a great effort to understand and mitigate anthropogenic greenhouse gas (GHG) emissions and their effects on the global climate (e.g., *8*, *11–13*). Tailpipe emissions from on-road transportation account for and 22% of GHG (*14*) emissions in the U.S., with additional emissions caused by upstream fuel production processes. The U.S. contributes 19% of global GHG emissions (*15*), so changes in GHG emissions from on-road transportation can substantially impact future global climate change.

In the transportation sector, when different types of environmental impacts are compared to each other, non-GHG air pollution damages, especially those related to public health, generally exceed those from climate change (*7*, *16*, *17*). Therefore, in this dissertation I mainly focus on air quality-related public health impacts, with a secondary focus on emissions of GHGs and other climate forcers.

Some recent publications have also compared the air quality and climate impact performance of conventional vs. alternative vehicles and fuels (*16–27*). However, my analyses include a focus on when and where emissions of pollutants and their resulting impacts occur, combined with a focus on impacts caused along the supply chain or "life cycle" of each fuel or technology option, in an integrated way that previous studies have not.

The following chapters are organized as follows. Chapter 2, which has been published elsewhere (*28*), describes a new modeling framework that tracks the specific locations of pollutant emissions caused by processes throughout the life cycle of each fuel or technology. Chapter 3, also published elsewhere (*29*), describes the application and performance of a comprehensive meteorology and chemical transport model to track these pollutants as they move across the United States, react with other chemicals, and eventually leave the United States or are removed from the atmosphere. In Chapter 4, I use the models from Chapters 2 and 3 to estimate the air quality and climate impacts of traveling 10% of year-2020 vehicle miles traveled (VMT), in either business-as-usual gasoline vehicles, or in one of ten alternative vehicle or

fuel technology options. Chapter 5 provides more detail on the spatial locations of emissions of climate-forcing pollutants, and how these locations may affect the effectiveness of policies aimed at mitigating global climate change. Chapter 6 describes a new model to predict the transport of pollution at higher spatial resolution than previous models. Chapter 7 describes the application of this model to estimate how the use of different fuel and vehicle technologies may differentially impact specific groups of people, such as low-income and racial minority individuals. Finally, Chapter 8 discusses the broad implications of this dissertation and opportunities for future research.

Chapter 2

A spatially and temporally explicit life cycle inventory of air pollutants from gasoline and ethanol in the United States

2.1 Summary

The environmental health impacts of transportation depend in part on where and when emissions occur during fuel production and combustion. Here I describe spatially and temporally explicit life cycle inventories (LCI) of air pollutants from gasoline, ethanol derived from corn grain, and ethanol from corn stover. Previous modeling for the U.S. by Argonne National Laboratory (GREET: Greenhouse Gases, Regulated Emissions, and Energy Use in Transportation) suggested that life cycle emissions are generally higher for ethanol from corn grain or corn stover than for gasoline. My results show that for ethanol, emissions are concentrated in the Midwestern "Corn Belt". I find that life cycle emissions from ethanol exhibit different

temporal patterns than from gasoline, reflecting seasonal aspects of farming activities. Enhanced chemical speciation beyond current GREET model capabilities is also described. Life cycle fine particulate matter emissions are higher for ethanol from corn grain than for ethanol from corn stover; for black carbon, the reverse holds. Overall, my results add to existing state-of-the-science transportation fuel LCI by providing spatial and temporal disaggregation and enhanced chemical speciation, thereby offering greater understanding of the impacts of transportation fuels on human health and opening the door to advanced air dispersion modeling of fuel life cycles.

2.2 Introduction

On-road transportation accounts for approximately 20% of United States energy consumption (*21*). Associated tailpipe emissions alone account for 40–60% of ground-level ozone (O_3) precursors, 6% of fine particulate matter emissions ($PM_{2.5}$) (*30*), and 22% of greenhouse gas (GHGs) (*14*) emissions. Upstream processes involved in fuel production also contribute to overall environmental impacts. Life cycle assessment (LCA) has been used extensively to quantify the combined effects of fuel production and use (*31–40*), but descriptions of where and when emissions occur are typically not reported in life cycle inventories (LCI). Such information is generally not relevant for long-lived GHGs or for fossil fuel depletion, which together have received overwhelming attention among extant LCAs of transportation fuels. For many non-GHG pollutants, knowledge of spatial and temporal aspects of emissions is critical for understanding life cycle impacts; such information has been identified as a priority for inclusion in future analyses (*41–43*).

A wide range of LCA studies incorporate spatial and temporal data to some degree, including those that include spatially explicit treatment of a single process within the life cycle (*31*, *36*, *37*, *44–48*), those that use or create country, region, or state-specific impact factors (*49–59*), those that disaggregate emissions by urban versus rural locations (*60*), those that include county-specific information for the whole life cycle (*16*, *21*), and those that include

both spatial and temporal information for aggregated groups of processes (*23*, *39*). Here I add process-specific spatial and temporal information to an existing attributional life cycle inventory (LCI) model so as to reveal patterns in the geographic distribution and intra-annual timing of emissions of important transportation fuels in the United States. To set the stage for the air quality the advanced life cycle impact assessments (LCIA) for the ten fuel scenarios described in Chapters 4 and 7, I present life cycle inventory results for three of the fuel pathways in this Chapter: gasoline, ethanol from corn grain ("corn ethanol"), and cellulosic ethanol from corn stover ("stover ethanol").

2.3 Methods

The approach presented here builds on the Greenhouse Gases, Regulated Emissions, and Energy Use in Transportation (GREET) model, version 1.8d1, from Argonne National Laboratory (*61*), which is widely used for research (i.e. *32*) and regulatory (*62*) purposes. GREET models the energy use and air emissions of pollutants from activities that occur in fuel production and use. GREET, as configured for this analysis, is an attributional life cycle model, meaning that it models emissions in fuel supply chains, but not those caused indirectly by market-mediated effects. Performing a consequential LCA could add additional realism to the analysis (*63*), but performing an LCA that is both consequential and spatially- and temporally-explicit is beyond the scope of this dissertation. Additional information about GREET is available elsewhere (*61*).

GREET models five groups of air pollutant emissions: oxides of nitrogen (NO_x), non-methane volatile organic chemicals (VOCs), primary particulate matter less than 2.5 μm and 10 μm in diameter ($PM_{2.5}$ and PM_{10}, respectively), and sulfur oxides (SO_x). Following prior work (*16*, *64*), I also include a sixth pollutant, ammonia (NH_3). $PM_{2.5}$ and PM_{10} inhalation can cause human mortality (*5*, *65–67*) and can decrease visibility. Particulate matter can be directly emitted ("primary $PM_{2.5}$") or can form in the atmosphere ("secondary $PM_{2.5}$"). VOCs can directly cause respiratory symptoms (*68–70*), and NO_x can directly increase mortality risk (*69*, *71*). VOCs and NO_x are the precursors for ground-level ozone formation, which has also

been linked to human mortality (*6*, *69*, *72*). VOCs, ammonia, SO_x, and NO_x can each contribute to secondary $PM_{2.5}$. SO_x can cause acid rain.

While the number of fuels and fuel-processes one could study is large, in this chapter I focus on a small number of fuels that are societally relevant, widely studied in previous research, and representative of a range of fuel types. I will apply the process described here to a larger number of fuel scenarios in Chapters 4 and 7. Specifically, I present emission estimates for the production and use of (1) gasoline, (2) ethanol from corn grain through dry milling ("corn ethanol"), and (3) ethanol from corn stover through cellulosic fermentation ("stover ethanol"). Stover ethanol is not currently produced on a large scale; I assume processes for the farming and refining of stover ethanol to be co-located with the corresponding processes for corn grain ethanol. I present results using a functional unit of grams pollutant emitted per vehicle-mile traveled.

I focus on adding to an existing life cycle inventory rather than refining its existing data. Accordingly, I use default GREET settings with the following exceptions: I assume that 1) corn ethanol plants use 100% natural gas process heat; 2) the ethanol produced is 100% ethanol without denaturant; however, because tailpipe emissions depend on blend level, I use tailpipe emission factors for E10 (i.e., a mixture of 90% gasoline, 10% ethanol) for the ethanol fuels (results for E85 [85% ethanol, 15% gasoline] can be found in Appendix B.1); 3) gasoline production is 100% conventional (i.e., not reformulated) gasoline; and 4) crude oil production is 100% conventional crude (most oil sands production occurs outside of my spatial modeling domain and is therefore excluded from my spatial analyses). Vehicle energy-efficiency and emissions are the same for all fuels, except SO_x emissions, which are lower for ethanol vehicles. Efficiencies and emissions factors reported here are for year-2010.

Transportation fuels used in the U.S. are delivered by a global supply chain and their associated pollution likewise occurs worldwide. GREET includes hundreds of unit processes involved in fuel production and use and reports life cycle emissions as global totals. Here, I focus on the fraction of life cycle emissions that occurs in the continental U.S. and its neighboring waters. To estimate GREET emissions inside that boundary, I multiply individual GREET unit

process emissions by the ratio of domestic production of their products ((*73–75*), excluding Alaska and Hawaii) to total consumption. I use the same factor to adjust upstream emissions for each process. For ocean tanker emissions, I consider emissions within the continental United States' Exclusive Economic Zone (within 200 nautical miles from shore) to be within the spatial modeling domain. I assume that ocean tankers acquire 50% of their fuel outside of the spatial modeling domain. Figure 2.1 shows emissions allocated within and outside of the spatial modeling domain. Table 2.1 provides the fractions of each process occurring within the spatial modeling domain; in all cases, most emissions are domestic. In this table, processes that are not listed are assumed to occur 100% within the spatial modeling domain. Emissions occurring outside of the modeling domain are excluded from the analysis by multiplying emissions from the processes below, as well as the emissions upstream of the process, by the corresponding fraction. Figure 2.2 shows domestic emissions for select processes; further details are in Appendix B.1.

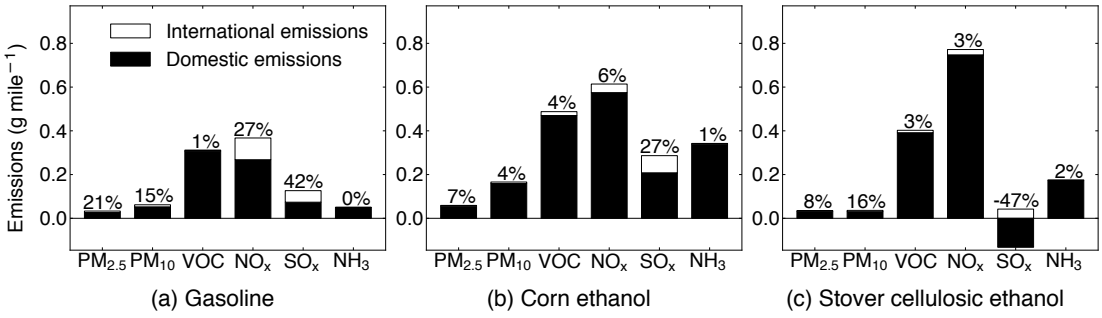

Figure 2.1: Amounts of emissions inside (domestic) and outside (international) the spatial modeling domain in units of grams emitted per vehicle mile traveled. Numeric labels indicate percent of life cycle emissions that are international. My results are for domestic emissions only.

2.3.1 Spatial disaggregation

In this attributional approach, emissions are assumed to come from existing infrastructure. The fraction of emissions allocated to each facility is assumed to be equal to the fraction of total U.S. production at that facility. For example, a refinery that currently produces 5% of

Table 2.1: Fractions of processes occurring within the spatial modeling domain

Process	Domestic fraction	Data source
Natural Gas	77.9%	EIA – Excluding Alaska production (*75*)
Sulfuric Acid	72.0%	USGS: Sulfuric acid (*74*)
Nitrogen–all	56.5%	USGS: Nitrogen (ammonia) (*74*)
Phosphoric Rock and acid	85.0%	USGS: Phosphate Rock (*74*)
Potash	17.0%	USGS: Potash (*74*)
CaCO3	98.0%	USGS: Lime (*74*)
Pesticides–all	90.2%	EPA Market Estimate, Year 2001 (*73*)
Coal	100.0%	EIA (*75*)
Crude Extraction	43.6%	EIA – Excluding Alaska production (*75*)
Gasoline Refining	100.0%	EIA (*75*)
Diesel Refining	100.0%	EIA (*75*)
Residual Oil Refining	100.0%	EIA (*75*)

the gasoline in the U.S. would have 5% of gasoline production emissions allocated to it. This assumption is necessary because GREET provides information about average emission factors only, not how those emissions vary among industrial facilities of a given type. I obtain information on the locations and average U.S. production of coal mines (*76*), crude oil and natural gas extraction (*77*), natural gas processing (*78*), petroleum and natural gas pipelines (*30*), fertilizer production (*79*), sulfuric acid production (*80*), pesticide production (*30*), biorefineries (*81*), petroleum refineries (*82*), corn and soy farm locations (*83*), and vehicle use (*84*, *85*), and use it to spatially distribute the emissions by life cycle stage to a user-defined grid or within geographical polygons (e.g. states, counties, regions, etc.) (*86*). I model year-2010 industry using available data from between 2002 and 2011 (see Table 2.2 for more detail). To accomplish this spatial (and later temporal) assignment of emissions, GREET data and equations are rewritten as a program in the Python language to allow process-specific emissions tracking for at least 97% of emissions for each fuel. I present results for a 12 km grid resolution, with comparisons to 4 and 36 km resolutions in Section 2.4.1. References for the spatial data used for each process, and the year each dataset was collected, are in Table 2.2. The "Map name" column refers to the column of the same name in Appendix B.1, which cross-references each unit process in

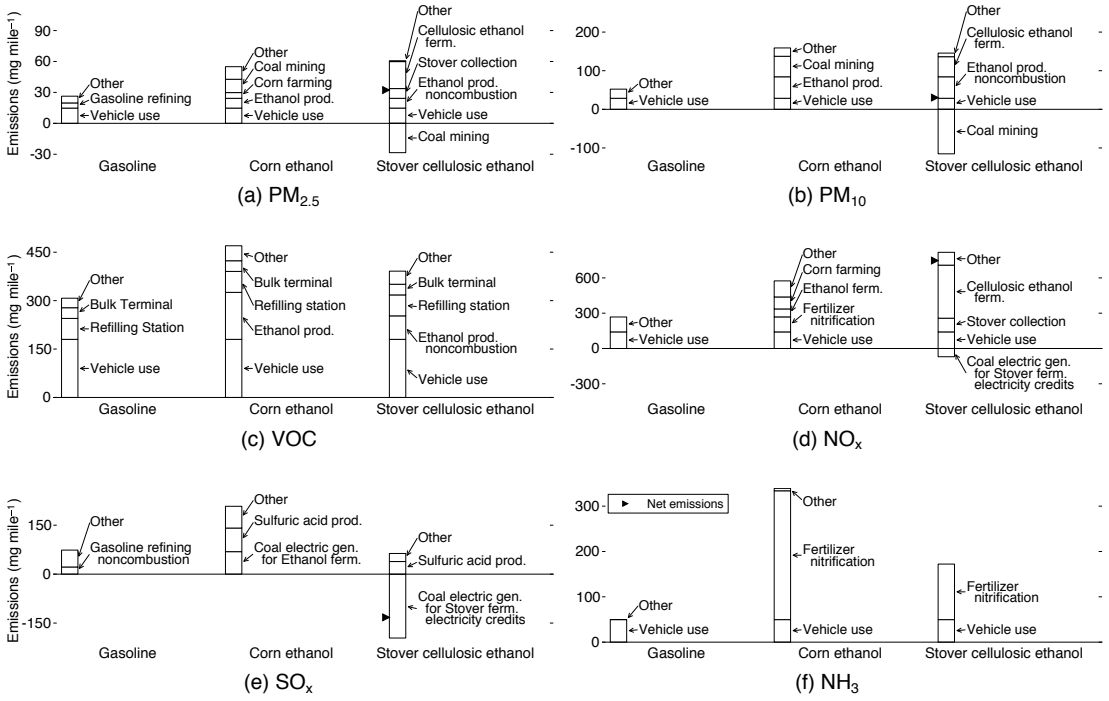

Figure 2.2: Fuel life cycle emissions, disaggregated by process. Plots exclude international emissions. For visual clarity, processes with emissions too small to display individually are lumped into an "Other" category; details regarding "Other" emissions can be found in the Appendix B.1. When a co-product of a fuel production process displaces a competing product, the emissions from the life cycle of the displaced product are treated as negative emissions. For life cycles with negative emissions (e.g. stover cellulosic ethanol in plot (a)), net emissions are indicated by a triangle to the left of that bar. Abbreviations: trans.=transportation, ferm.=fermentation, gen.=generation, prod.=production.

the life cycle to one of the spatial data sources described below. For processes that use electricity, I allocate the electrical generation emissions to generators from the U.S. EPA's eGRID database (*87*) located in the same North American Reliability Corporation (NERC) region as the end-use process. Pipeline and ocean tanker emissions are allocated to existing emission locations (*30*). Co-products, such as distiller's grain with solubles (DGS) production for corn ethanol and excess electricity production for stover ethanol, are treated in GREET using a system expansion approach and are assumed to displace emissions from competing products

(i.e., soy production or electricity generation). I allocate negative emissions resulting from displacement using the same methodology as for positive emissions. Processes are additionally classified as ground-level or elevated releases of pollutants; elevated releases are given a stack height of 23 m, a stack diameter of 3 m, a stack temperature of 465 K, and a stack velocity of 1.8 m s^{-1}. These are the average parameters for U.S. electrical generating units (*30*). Refer to Appendix B.1 for the height classification of each process. Process-specific spatial and temporal information is summarized in Figure 2.3 for six of the more than 400 processes; additional details are in Appendix B.2.

Method for spatial allocation of electricity generation

For processes that use electricity, I assume that the electricity used by the process is generated in the same NERC region as the end-use process. However, because the GREET model only allows users to specify two electricity generation fuel mixes—one for stationary use and one for electric vehicles—for the life cycle processes I model the electricity generation mix in every NERC region as being the same as the national average mix. (For grid-average electricity used to power electric vehicles, see below.) As an illustrative example, I use a projected year-2020 U.S. average electricity mix: approximately 20% natural gas, 45% coal, 20% nuclear, and 15% other fuels. In my model, a refinery (or any other electricity-using process) located in California draws 20% of its power from natural gas electricity generating units in the WECC NERC region (proportional to the fraction of current generation at those units), 45% from coal electric generators in the WECC region, and so on, even though in reality the mix of electrical generation fuels in the WECC region is different from the national average.

I make an exception to this rule for the locations of the electric generators that directly power EVs in the grid-average EV scenario. In this case, instead of allocating electricity generation to NERC regions based on the fraction of vehicle miles traveled in each region, as I do in all other cases, I allocate emissions to generators across the entire U.S. So, in the grid-average EV scenario, for EV use anywhere in the United States, 20% of the electricity directly powering the EV comes from natural gas generators, allocated proportionally to the fraction of current

natural gas electric generation in all natural gas electric generators across the U.S. This allows me to capture regional differences in electricity generation mix. I do this for the direct electricity consumption of grid-average EVs, but not for any other end-use process, because the spatial distribution of electricity consumption is similar to the spatial distribution of vehicle miles traveled, but it is not similar to the spatial distribution of other processes (refinery locations or coal mining, for example).

Table 2.2: Sources of spatial data and the year the data was collected

Map name	Data year	Source
Ammonia, AmmoniumNitrate, K2O, NitricAcid, PhosphoricAcid, PhosphateRock, Urea	2011	(*79*)
CoalMining	2007	(*76*)
CurrentBiorefineries	2010	(*81*)
ElectricGeneration (all types)	2007	(*88*)
FarmAreaCornTotal, FarmProductionCornTotal	2010	(*83*, *89*)
GasPipelines, LNG, OceanTankers, OilPipelines, Pesticides	2005	(*30*)
NaturalGasExtraction, OilExtraction	2009	(*77*)
NGProcessing	2004	(*78*)
OilRefineries	2009	(*82*)
SulfuricAcid	2005	(*80*)
VMT	2002	(*84*)

Transportation emissions allocation

I allocate emissions from transportation via truck, rail, and barge using a combination of geographic network analysis (*86*) and linear optimization (*90*) techniques. To allocate emissions from transportation, I first calculate the shortest routes along major road, rail, and waterway networks (*91*) between all combinations of source and destination locations for each product transported, only considering source and destination combinations that have a viable route between them over the network. For computational expediency, in some cases I only calculate routes between source and receptor pairs with substantial contributions to total production. I then optimize the amount of product transported along each route (*90*) to minimize total

product-distance traveled. Finally, I weigh the fraction of product transported along each route by the route distance to determine the fraction of emissions allocated to each route.

2.3.2 Temporal disaggregation

The time at which air pollutant emissions occur can be an important determinant of their ultimate impacts. For instance, conversion rates of VOCs and NO_x into ground-level ozone are greater during hot summer days than at other times. In contrast, emissions of $PM_{2.5}$ and its precursors may result in higher concentrations during winter than during other times because dilution rates tend to be lower in winter (*92*, *93*). I link each of the processes shown in Appendix B.1 with process-specific temporal profiles (*30*, *94*) to allocate emissions by month, day-of-week, and hour-of-day, with different allocations for weekdays and weekends. Figure 2.3 shows temporal profiles for several processes.

2.3.3 Chemical disaggregation

The species categories that GREET outputs (VOCs, NO_x, SO_x, $PM_{2.5}$, and PM_{10}) are aggregates of many individual chemicals or pollutant types. Such broad categories can limit the accuracy of an impact analysis. For instance, the combustion of gasoline and ethanol both produce VOCs, but they produce different types of VOCs, with varying toxicity, reactivity, and ozone-production potential. The combustion of gasoline and ethanol both produce $PM_{2.5}$ and its precursors, but certain types of $PM_{2.5}$ cause atmospheric cooling (e.g., sulfate aerosols) while others cause atmospheric warming (e.g., black carbon aerosols) (*95*). To develop the inventory presented here, I link each of the processes shown in Appendix B.1 with chemical speciation profiles (*96*) to disaggregate the emissions into 34 chemical species groups according to the Carbon Bond 2005 (CB05, (*97*)) chemical mechanism. CB05 speciates emissions into the following groups:

- **VOCs:** acetaldehyde, higher aldehydes, benzene, methane, ethene, ethane, ethanol, formaldehyde, internal olefins, isoprene, methanol, olefins, paraffins, sesquiterpenes,

terpenes, toluene, xylene, non reactive VOCs, nonvolatile VOCs, and unknown/other VOCs

- **$PM_{2.5}$**: black carbon, nitrate particulates, organic particulates, sulfate particulates, and unclassified $PM_{2.5}$
- **NO_x**: NO and NO_2
- **SO_x**: SO_2 and $SO_{4,g}$.

PM_{10} and NH_3 are not speciated further.

2.4 Results

Figure 2.1 shows fractions of emissions occurring outside of the spatial modeling domain for each fuel (N. B.: These and all other results show emissions of air pollutants, which may or may not be directly correlated with changes in ambient pollution levels. The relationship between emissions and concentrations will be discussed in Chapters 3, 4, 6, and 7). As mentioned above, emissions that would occur outside of the spatial modeling domain (contiguous United States and surrounding waters), are excluded from results below. Excluding international emissions has the largest effect on the gasoline life cycle. This result is because I model 96% of emissions from transportation of crude oil by ocean tanker as occurring outside the spatial modeling domain. International tanker emissions account for 34% of SO_x, 16% of NO_x, 14% of $PM_{2.5}$, and 8% of PM_{10} gasoline life cycle emissions. However, these ocean tanker emissions generally occur over the open ocean where human exposure is very low (*58*), so the exclusion of these emissions will likely not noticeably affect estimates of total human exposure. Other notable spatial modeling domain exclusions include 28% of sulfuric acid production for fertilizer (*98*), accounting for 12% of corn ethanol and 20% of stover ethanol SO_x life cycle emissions, and 56% of crude oil extraction (*99*), accounting for 6% of NO_x emissions from the gasoline life cycle. All other processes either occur completely within the modeling domain or do not comprise an appreciable fraction of the life cycle total emissions.

Figure 2.4 shows 12 km resolution gridded emissions for the gasoline, corn ethanol, and stover cellulosic ethanol fuels. In general, gasoline emissions tend to be correlated with vehicle use and so are distributed in or near urban centers. Ethanol emissions tend to be also correlated with ethanol production and so are concentrated in the Midwest "Corn Belt". The area along the Kentucky/Virginia border extending into West Virginia experiences a reduction in $PM_{2.5}$ emissions (shown in blue in Figure 2.4) owing to reduced coal mining activity caused by excess electricity generation in biorefineries. Excess electricity is sold back to the electrical grid and assumed to offset electricity produced elsewhere.

Figure 2.5 shows emissions contributions by region of the U.S. For all three fuels, the largest portion of emissions occurs in the Northeast () for VOCs (but not other pollutants), owing to the large portion of total vehicle miles traveled per land area occurring there. See Table 2.3 for the fraction of vehicle miles traveled in each region. The Midwest () receives a large amount of emissions for both ethanol fuels, owing to ethanol fermentation plants and ammonia emissions from fertilizer nitrification. For the Midwest, emissions are lower for gasoline than for ethanol, with the exception that SO_x emissions are negative (i.e., reduced) for stover ethanol owing to excess electricity generation at fermentation plants. The large amount of SO_x emissions in the Southeast () for corn ethanol is attributable to Florida-based sulfuric acid production for phosphate fertilizer. The Southwest () and West () regions generally do not receive large proportions of pollutant emissions for any of the three fuels (exception: SO_x emissions for gasoline).

Table 2.3: Fractions of vehicle miles traveled occuring in each region

Region	% VMT	% Land area
	18%	31%
	12%	19%
	23%	26%
	28%	18%
	19%	6%

Emissions are spatially disaggregated by allocating them to cells in a raster grid. As has

been previously noted (*47*), I observe that the resolution of the grid used can influence the apparent locations of emission. Figures 2.8 and 2.9 show the dependence of emissions allocated to urban areas on the spatial scale of the grid used for allocation and compares the results to the urban emissions given by GREET (*60*). Overall, increasing grid resolution leads to an increased allocation of emissions to urban areas, suggesting that a coarse grid tends to artificially dilute urban emissions to the surrounding rural areas. See Section 2.4.1 for further discussion.

Figure 2.7 shows temporal profiles for the fuels and pollutants discussed here. Pollutant emissions from the gasoline life cycle do not vary much by month. For the corn ethanol life cycle, however, there is a spike in NH_3 and NO_x emissions in the spring corresponding to fertilizer application. This is also true to a lesser extent for stover cellulosic ethanol. All fuels show a slight decrease in emissions on weekends. Weekday emissions commonly show a bimodal distribution around the morning and evening rush hours owing to increased vehicle tailpipe emissions at those times. For fuels and pollutants where farming activities are a major contributor, however, the weekday and weekend emissions are unimodally distributed around the daylight farming hours.

My chemical speciation reveals the following. Although stover ethanol emits the lowest total amount of $PM_{2.5}$ of all three fuels, it emits more black carbon (15 mg mi^{-1}), a species of fine particulate matter which contributes to atmospheric warming, than either of the other two fuels (gasoline: 4.5, corn ethanol: 10 mg mi^{-1}). Stover ethanol also emits the lowest amount of sulfate aerosols (-1.3 mg mi^{-1}; gasoline: 1.9, corn ethanol: 3.8), which cause atmospheric cooling. Emissions of ethanol are 30,000–40,000 times higher for the ethanol fuels than for gasoline; ethanol in the atmosphere may be oxidized to form acetaldehyde (a carcinogen). However, emissions of benzene (another carcinogen (*100*)) are higher for gasoline than for the ethanol fuels (the relative amounts by fuel depend on the ethanol feedstock and the blend level of the final fuel). Full results for chemical speciation, including for 85% ethanol blends (E85), are in Appendix B.1.

2.4.1 Urban vs. rural emissions

Because emissions are spatially disaggregated by allocating them to cells in a raster grid, the grid resolution can influence the fraction of emissions in urban areas. Figures 2.8 and 2.9 show emissions allocated to urbanized areas as defined by the 2000 U.S. Census (*101*) using three different grid resolutions for the GREET output pollutants plus ammonia, and compare them to the urban emissions output by the GREET spreadsheet (*60*). This dependence of results on spatial scale has also been noted elsewhere (*47*). In general, gasoline emissions are more concentrated in urban areas. Most (80%) petroleum refinery production, but only 10% of current biorefinery production, is located in urban areas. Overall, increasing grid resolution leads to an increased allocation of emissions to urban areas, suggesting that a coarse grid tends to artificially dilute urban emissions to the surrounding rural areas.

The urban emissions fractions for the 4 km grid generally agree with those reported by Huo et al. (*60*) (as incorporated in GREET spreadsheet) with the exception of SO_x emissions from the two ethanol fuels. A large portion of the SO_x emissions from these fuels come from sulfuric acid production for phosphate fertilizer. Huo et al. assume 0% of sulfuric acid production occurs in urban areas, whereas the data I use allocates 52% of sulfuric acid production to urban areas (*80*), specifically the Tampa, Florida metropolitan area, which is near the United States' largest phosphoric rock mine.

2.5 Discussion

I have presented a spatially and temporally explicit life cycle inventory for transportation fuels. Prior life cycle inventories were typically presented at global, national, or regional levels, which is sufficient for understanding global processes, such as climate change and fossil fuel depletion, but is insufficient for the analysis of local processes such as air pollution. The spatially and temporally explicit life cycle assessment presented here not only provides the level of detail necessary to perform detailed LCIA of air pollutant emissions, it also gives information on spatial and temporal trends that can be useful in policy making and regulation. For

instance, in the United States, air quality regulations, and the plans to meet them, are at least partially determined by individual states. Spatial LCA can help state-level policy makers identify potential sources of air pollutant emissions within their jurisdiction and create appropriate regulations. That type of information is not delivered by conventional LCA approaches.

The framework presented here outputs gridded, time resolved emissions files, which are an important step towards photochemical dispersion modeling. For example, U.S. production and consumption of stover ethanol would increase emissions of NO_x, NH_3, and $PM_{2.5}$ in the Midwest, but would decrease SO_x emissions in the same region. All four of these species influence ambient concentrations of $PM_{2.5}$, so a priori it is unclear whether the net change in $PM_{2.5}$ concentrations will be positive or negative in this region. Photochemical dispersion modeling can help answer this question.

My choice of spatial modeling domain (continental United States) by definition restricts this study. However, I do not see this as a major limitation because most emissions occur within this boundary, and because most of the excluded emissions occur over the open ocean, for which human exposures are much lower than for emissions on land (*58*). This same domain has been used in a previous analysis (*25*). At present, lack of computational power and accurate input data make it impractical to extend the system boundaries to the entire globe. For future work, a nested approach (detailed spatial treatment of emissions within the modeling domain; coarser resolution outside of the domain) could prove useful.

My analyses consider supply chain emissions of existing production. GREET, and by extension the framework presented here, performs an exclusively attributional (static) LCA for non-GHG air pollutants. I do not include indirect (market-mediated) effects. An example of an indirect effect would be if increased corn ethanol production in the United States were to increase global grain prices, resulting in (emissions from) tropical rainforest being burned to grow new crops. A consequential (dynamic) LCA, which I do not do, would aim to capture indirect effects. I assume here that all processes would occur at existing production locations; in reality, new production may cause new facilities to open, or existing facilities to close or change locations. I assume that cellulosic biorefineries for stover ethanol would be co-located

with existing corn ethanol biorefineries; in reality, the difficulty of transporting corn stover may cause biorefineries to be smaller and closer to cornfields. A further limitation to this study is that owing to limited data availability, the spatial data used here represent a range of years (2002–2011; see Table 2.2 for details). Finally, uncertainty and variability in the spatial, temporal, and chemical speciation data used here contribute to the overall uncertainty in the life cycle inventory, but this information is generally unknown or unreported.

I have focused here on the air pollutant implications of the choice between ethanol and gasoline as a transportation fuel. In general, methods presented here can provide insight into any spatially or temporally inhomogeneous environmental impact categories, such as water quality and availability, soil properties, or native habitats. They can also be expanded to study specific processes that affect those impact categories, such as agriculture and food production, building construction, or electricity generation; the possible applications are only limited by the availability of data.

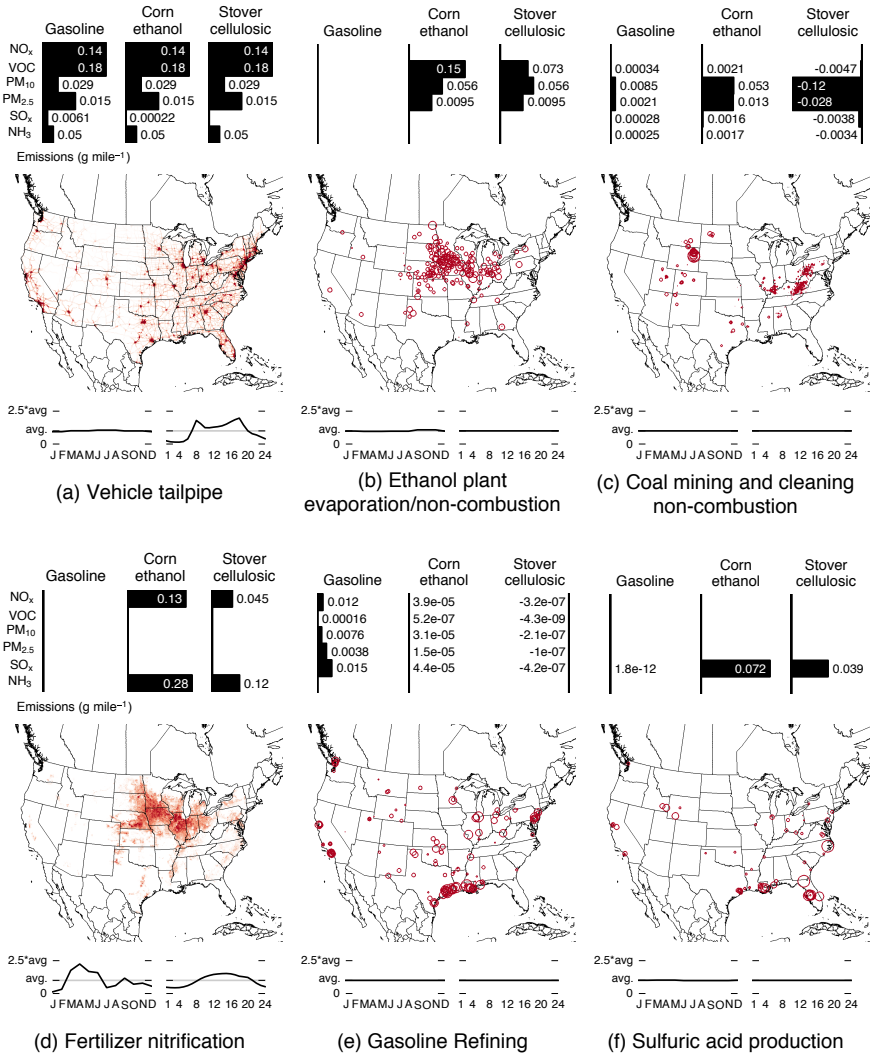

Figure 2.3: An overview of the spatial and temporal disaggregation for six of the highest emitting processes in the life cycles of the fuels discussed here. (Over 400 processes are described for each life cycle; see Appendices B.1 and B.2 for processes not shown here.) The bar charts show emissions by pollutant in grams per vehicle mile traveled; each pollutant has its own bar length scale, and scales are consistent among panels. The maps show the points or areas where the process occurs, with either the grid cell color intensity or the area of the circle proportional to the fraction of total activity occurring at each location. Line plots indicate the relative amount of emissions by month of the year and hour of the weekday. For fertilizer nitrification, temporal profiles vary by location; the average values are plotted for each month.

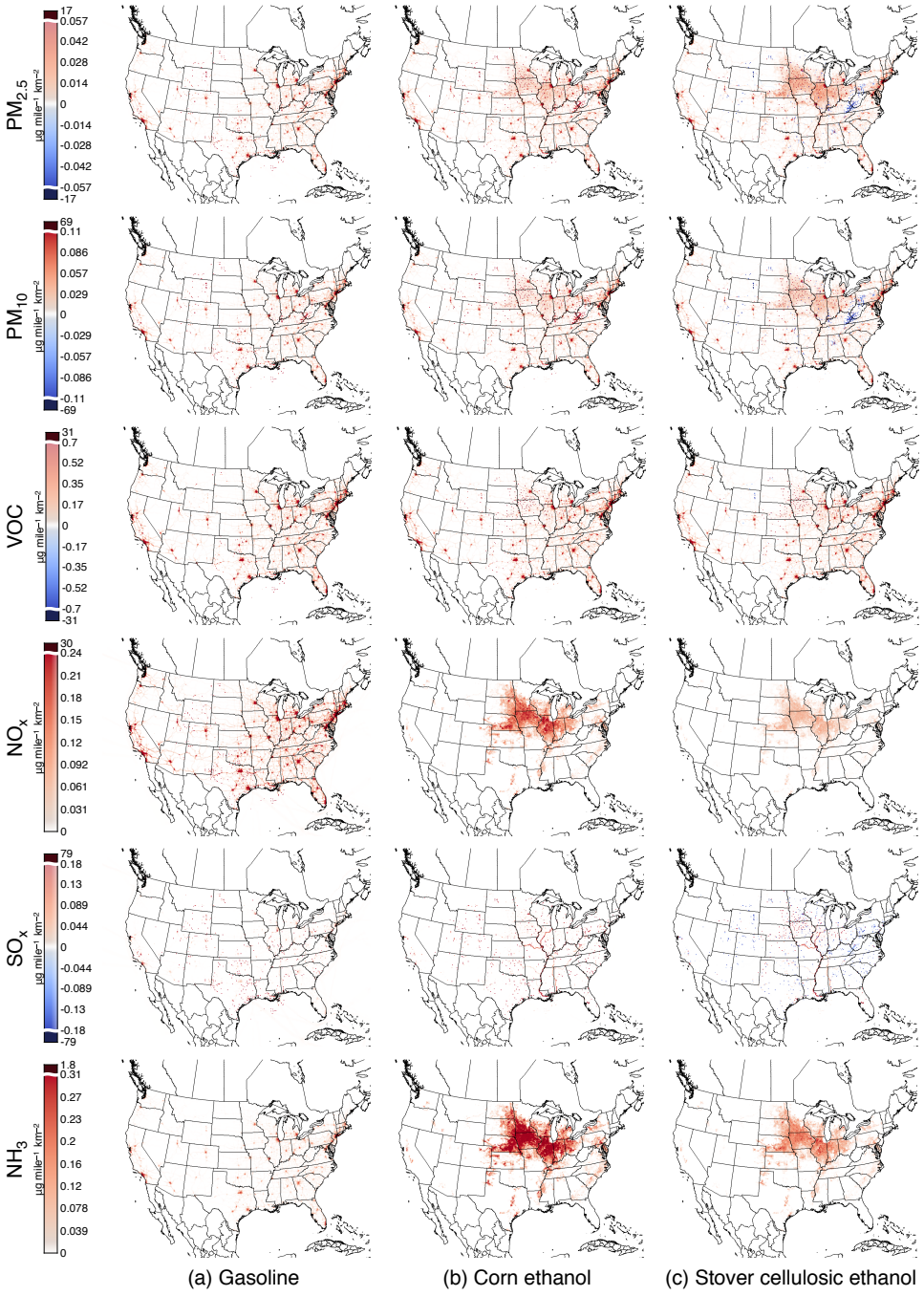

Figure 2.4: Annual total life cycle emissions for three fuels. For ease of viewing, the linear color scale contains a discontinuity at the 99th percentile of emissions.

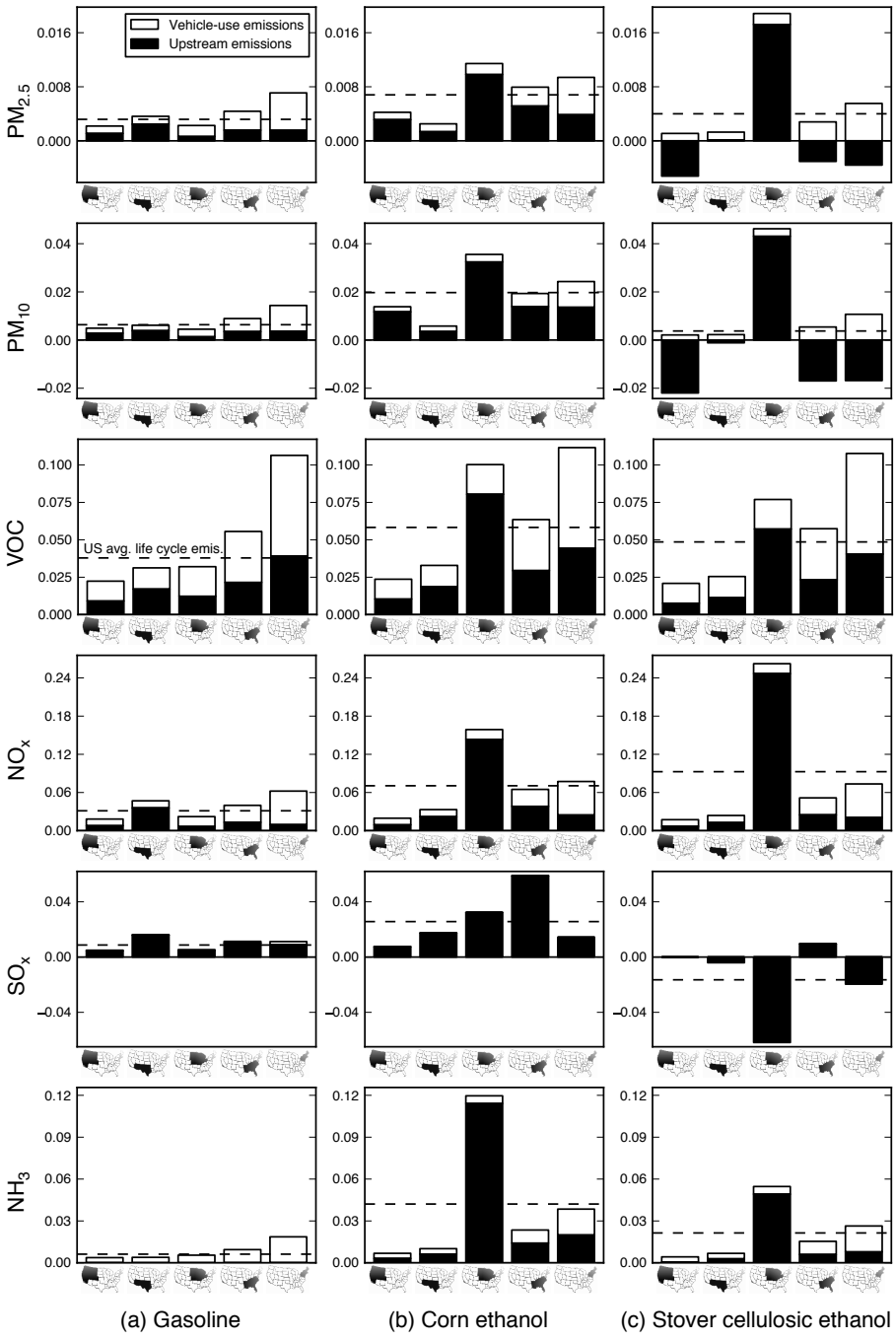

Figure 2.5: Contributions of U.S. regions to total life cycle emissions for three fuels (micrograms emitted per vehicle-mile traveled per square kilometer land area). Dashed lines show U.S. average emissions. Refer to Figure 2.6 for a version of this figure with units of g mi^{-1}.

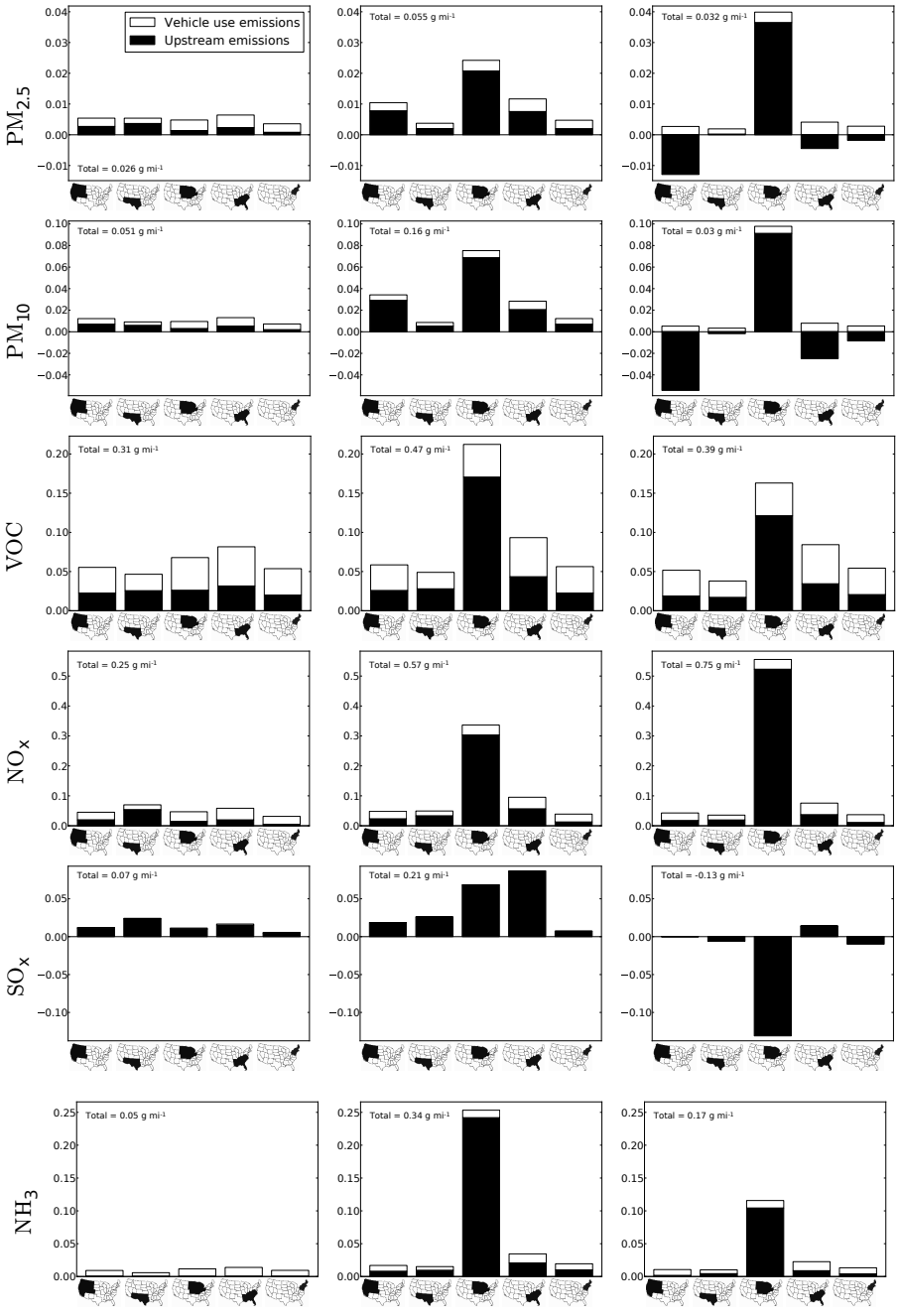

(a) Gasoline (b) Corn ethanol (c) Stover cellulosic ethanol

Figure 2.6: Contributions of U.S. regions to total life cycle emissions (grams emitted per vehicle mile traveled). Emissions occurring outside of all regions (e.g., offshore emissions and international emissions outside of the modeling domain) are not included.

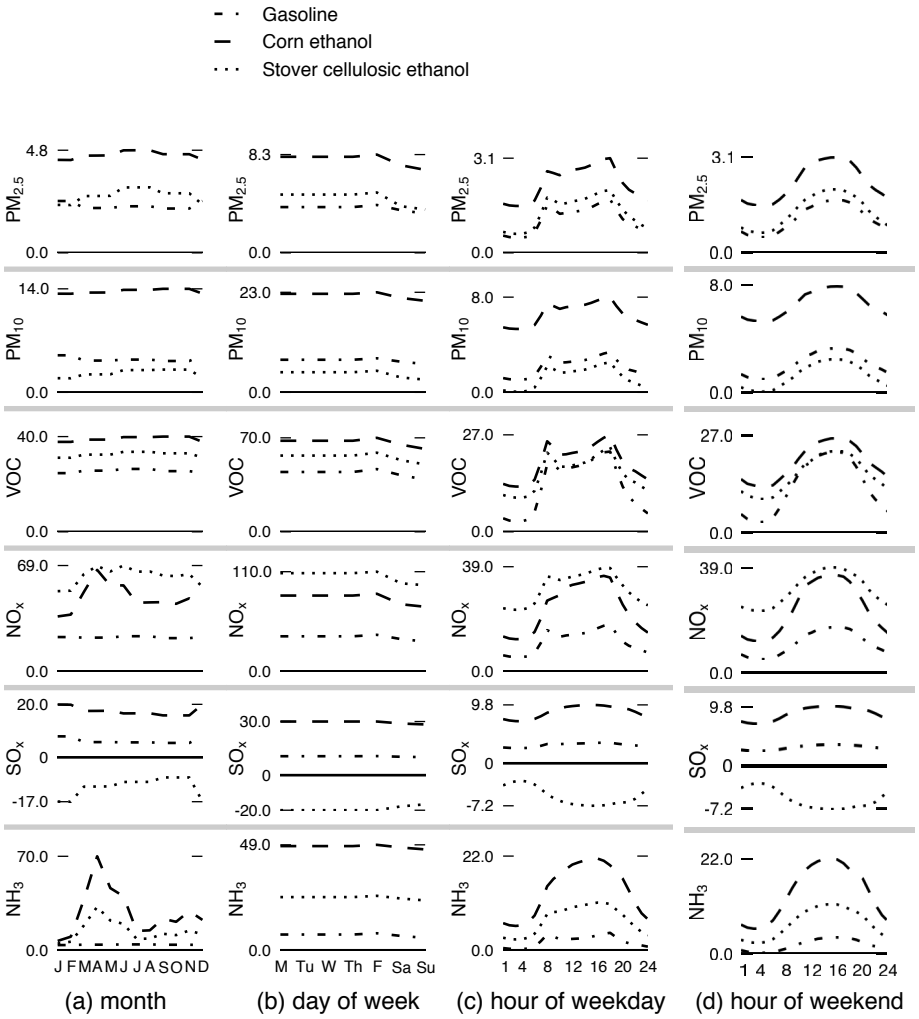

Figure 2.7: Temporal profiles of life cycle emissions (mg emitted per vehicle mile traveled) by month of year, day of week, and hour of day (weekday and weekend)

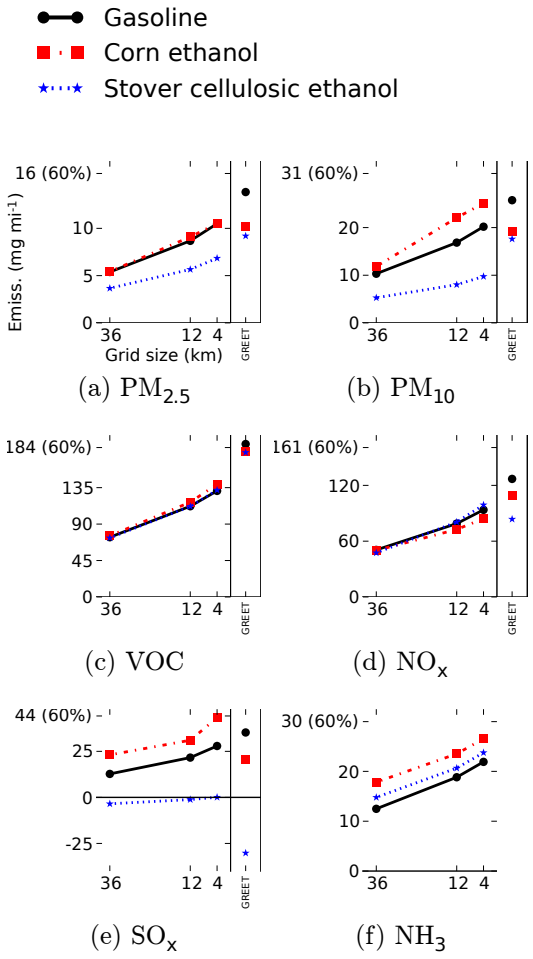

Figure 2.8: Life cycle emissions allocated to urbanized areas as calculated using three different grid resolutions (left section of each plot) and urban emissions calculated using the default GREET spreadsheet (right section of each plot). To allow comparison among pollutants, all plots are scaled to 60% of the gasoline total emissions. In general, more precise estimates (smaller grid sizes) suggest a greater proportion of emissions are urban. For gridded calculations (left sections), emissions occurring outside the spatial system boundary are excluded. Calculations using the GREET spreadsheet (right sections) include all emissions. The GREET model does not calculate ammonia emissions. International emissions are excluded. See Figure 2.9 for a version of this figure calculated without first excluding international emissions.

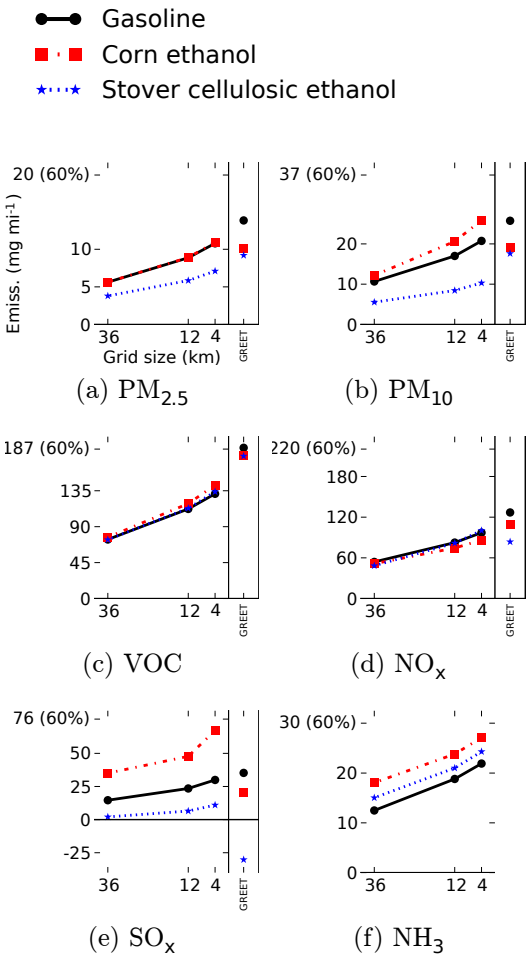

Figure 2.9: Life cycle emissions allocated to urbanized areas as calculated using three different grid resolutions (left section of each plot) and urban emissions calculated using default GREET spreadsheet (right section of each plot). To allow comparison between pollutants, all plots are scaled to 60% of the gasoline total emissions. Calculations include international emissions fractions. The GREET model does not calculate ammonia emissions.

Chapter 3

Twelve-month, 12-km resolution North American WRF-Chem v3.4 air quality simulation: Performance evaluation

3.1 Summary

I present results from and evaluate the performance of a 12-month, 12-km horizontal resolution air pollution simulation for the contiguous United States using the WRF-Chem (Weather Research and Forecasting with Chemistry) meteorology and chemical transport model (CTM). I employ the 2005 U.S. National Emissions Inventory, the Regional Atmospheric Chemistry Mechanism (RACM), and the Modal Aerosol Dynamics Model for Europe (MADE) with a Volatility Basis Set (VBS) secondary aerosol module. Overall, model performance is comparable to contemporary models used for regulatory and health-effects analysis, with an annual average daytime ozone (O_3) mean fractional bias (*MFB*) of 12% and an annual average fine particulate matter ($PM_{2.5}$) *MFB* of -1%. WRF-Chem, as configured here, tends to overpredict total $PM_{2.5}$ at some high concentration locations, and generally overpredicts average 24-hour O_3 concentrations, with better performance at predicting average daytime and daily peak O_3

concentrations. Predictive performance for $PM_{2.5}$ subspecies is mixed: the model overpredicts particulate sulfate (*MFB*=65%), underpredicts particulate nitrate (*MFB*=-110%) and organic carbon (*MFB*=-65%), and relatively accurately predicts particulate ammonium (*MFB*=3%) and elemental carbon (*MFB*=3%), so that the accuracy in total $PM_{2.5}$ predictions is to some extent a function of offsetting over- and underpredictions of $PM_{2.5}$ subspecies. Model predictive performance for $PM_{2.5}$ and its subspecies is in general worse in winter and in the western U.S. than in other seasons and regions, suggesting spatial and temporal opportunities for future WRF-Chem model development and evaluation.

3.2 Introduction

After developing a new model for life cycle air pollutant emissions in Chapter 2, in this chapter I set up and evaluate a model for determining the impacts of those emissions on ambient air quality. Epidemiological studies have established the importance of health effects from acute and chronic exposure to fine particulate matter ($PM_{2.5}$) and ground-level ozone (O_3) (*5*, *6*, *65*). The accuracy of health-impact predictions for future air pollutant emissions depends in part on the performance of air quality models over long time scales and in all seasons. Accurate health-impact predictions often depend on model simulations that cover large geographic areas (such as the continental U.S.), so as to capture the full impacts of the long-range transport of pollutants (*102*). Whereas chemical transport model (CTM) simulations for a full year for the continental U.S. often use 36 km horizontal grids (e.g., *103*, *104*), increasing horizontal grid resolution to 12 km can result in the more accurate prediction of pollutant concentrations (*105*) and population exposure. However, increasing horizontal resolution from 36 km to 12 km in a CTM typically results in a $\sim 27\times$ increase in computational intensity (number of grid cells increases nine-fold; number of time steps increases three-fold). Although recent CTM evaluation efforts have focused on 12-month and contiguous U.S. model evaluations (*106*), CTM model performance for fine-scale horizontal grid size (12 km or better) for an entire year for the entire contiguous U.S. is largely unexplored in the peer-reviewed literature. I know of only

one such study: Appel et al. (*107*) evaluated the performance of the Community Multiscale Air Quality (CMAQ) model (*108*) in reproducing year-2006 concentrations of $PM_{2.5}$ and O_3 for the continental U.S. In a second study (not peer reviewed), the U.S. EPA (*109*) describes model evaluation for $PM_{2.5}$ concentrations for year-2007, also for the continental U.S. and using CMAQ. This chapter contributes to this literature by evaluating a different model with different parameterizations over a different time period. I also provide greater investigation regarding how model performance varies in space, in time, and by chemical species. I employ and evaluate the performance of WRF-Chem (the Weather Research and Forecasting model with Chemistry) (*110*) for year-2005 for a North American domain. WRF-Chem is functionally similar to CMAQ, but differs from the version used by Appel et al. (*107*) in that WRF-Chem predicts meteorological quantities and air pollution concentrations simultaneously, allowing meteorology quantities to be updated more frequently as the model is running and allowing representation of interactions between meteorology and air pollution. WRF-Chem users can follow a simplified modeling workflow that does not require running a separate meteorological model. (This aspect can be beneficial for the modeler, not necessarily for the model's computation demands. For the domain and settings used here, meteorological modeling accounts for only $\sim$10% of the total computational expense.) Table 3.1 summarizes spatial and temporal aspects of recent chemical transport model evaluation efforts, with a focus on WRF-Chem evaluations in the U.S. WRF-Chem performance in predicting air quality observations has been extensively quantified for simulations of individual regions of the U.S., with simulation periods of several weeks or months (*110–117*). One study evaluated WRF-Chem performance for a full year for the contiguous U.S. with a 36 km grid (*104*). I present here WRF-Chem results from a full year, 12-km resolution simulation for the contiguous U.S., evaluate the performance of the model compared to ambient measurements, and compare WRF-Chem performance to published goals and criteria (*118*) and to recent CMAQ results for a similar simulation (*107*).

3.3 Methods

3.3.1 Model setup

I run the WRF-Chem model version 3.4 using a 12-km resolution grid with 444 rows, 336 columns, and 28 vertical layers. The modeling domain (see Figure 3.2) covers the continental U.S., southern Canada, and northern Mexico. Within WRF-Chem, I use the Regional Atmospheric Chemistry Mechanism (RACM) (*119*) for gas-phase reactions and the Modal Aerosol Dynamics for Europe (MADE) (*120*) module for aerosol chemistry and physics. RACM and MADE were selected because of their relatively modest computational expense; at the time of this study, alternatives to RACM/MADE are impractical for large-scale simulations such as this. I use the Volatility Basis Set (VBS) (*111*) to simulate formation and evaporation of secondary organic aerosol (SOA). The VBS approach differs from other SOA parameterizations in that it assumes that primary organic aerosol (POA) is semi-volatile. Meteorology options are set as recommended by the WRF user manual (*121*) and the WRF-Chem user manual (*122*) for situations similar to those studied here. Table 3.2 summarizes the model options and inputs used. See Appendix C for additional details.

I use results from the MOZART global chemical transport model (*123*) as processed by the MOZBC file format converter (available: `http://web3.acd.ucar.edu/wrf-chem`) to provide initial and boundary conditions for chemical species. Because the MOZBC boundary conditions for miscellaneous $PM_{2.5}$ are unrealistic for the southeastern edges of the modeling domain (their use results in substantial $PM_{2.5}$ overpredictions in the southeastern U.S.), I set all initial and boundary concentrations to zero for miscellaneous $PM_{2.5}$. As in Ahmadov et al. (*111*), owing to uncertainty in secondary organic aerosol (SOA) concentrations over the open ocean, I assume that initial and boundary concentrations of SOA are zero. Data from the National Centers for Environmental Prediction (NCEP) Eta model (*124*) provide meteorological inputs; boundary conditions; and, for the Four Dimensional Data Assimilation (FDDA) employed here, observational "nudging" values. I use the 2005 National Emissions Inventory (NEI) (*30*) to estimate pollutant emissions. The NEI includes emissions from area, point, and mobile sources

for year 2005 in the U.S., year 2006 in Canada, and year 1999 in Mexico. I use the model evaluation version of the NEI, which also includes hourly Continuous Emission Monitoring System (CEMS) data for electricity generating units, hourly wildfire data, and biogenic emissions from the BEIS model (*125*), version 3.14. I prepare pollutant emissions at 12-km spatial resolution using the Sparse Matrix Operating Kernel Emissions (SMOKE) program (*126*), version 2.6, as bundled with the NEI data (available from `http://www.epa.gov/ttn/chief/emch/index.html`), then I convert the emissions files output by SMOKE to WRF-Chem format and apply a plume rise algorithm ((*127*), as cited in (*128*)) to estimate the mixing height of elevated emissions sources and wildfires. Source code for the file format conversion and for the plume-rise program is available at `https://bitbucket.org/ctessum/emcnv`. I simulate atmospheric pollutant concentrations for the period from January 1st through December 31st, 2005. I choose the year 2005 because at the time this study was performed it was the most recent year for which emissions data were available. For logistical expediency, I separate the year into eight independent model runs, each approximately 1.5 months in length plus a discarded 5-day model spin-up period. I run the simulations on a high-performance computing system consisting of 2.8 GHz Intel Xeon X5560 "Nehalem EP" processors with a 40-gigabit QDR InfiniBand (IB) interconnect and a Lustre parallel file system. Using 768 processors, each 1.5-month model run takes $\sim$19 hours to complete ($\sim$13 processor-years for each annual model run).

3.3.2 Comparison with observations

I compare WRF-Chem wind speed, air temperature, relative humidity, and precipitation predictions to data from the U.S. Environmental Protection Agency (EPA) Clean Air Status and Trends Network (CASTNET) observations. I compare modeled ground-level concentrations of total $PM_{2.5}$ to EPA Air Quality System (AQS) observations (*97*) using 24-hour average data (EPA parameter code 88101) and using the less extensive hourly measurement network (EPA parameter code 88502), which allows me to compare modeled vs. measured diurnal profiles. I compare WRF-Chem predictions of O_3 to measurements from the AQS (EPA parameter code

44201) and CASTNET networks. I compare the predictions of $PM_{2.5}$ subspecies to observation data from the EPA's Chemical Speciation Network (CSN) (*97*) (formally called Speciation Trends Network [STN]) for organic carbon (OC, parameter code 88305), elemental carbon (EC, code 88307), particulate sulfate (SO_4, code 88403), particulate nitrate (NO_3, code 88306), and particulate ammonium (NH_4, code 88301). I additionally compare predictions to data from the Interagency Monitoring of Protected Visual Environments (IMPROVE) network (*129*) for particulate OC (code 88320), EC (code 88321), SO_4 (code 88169), and NO_3 (code 88306); and to CASTNET observations for particulate SO_4, NH_4, and NO_3. WRF-Chem outputs organic aerosol (OA) concentrations, but methods for measuring organic aerosol only quantify organic carbon (OC). OC comprises a variable fraction of OA, but it is common to assume an OA:OC ratio of 1.4 (*130*). Therefore, I divide WRF-Chem OA predictions by a factor of 1.4 for comparison with OC measurements. Finally, I compare WRF-Chem predictions of gas-phase sulfur dioxide (SO_2) and nitrogen dioxide (NO_2) to AQS observations. I remove from consideration those stations with ≥25% missing data relative to the number of scheduled measurements during the simulation period. The fractions of excluded data for each type of comparison are in Appendix C. WRF-Chem, as configured here, outputs instantaneous concentrations at the start of each hour, whereas the observation data are reported as hourly or daily averages. WRF-Chem calculates grid-cell-average concentrations, whereas observations generally represent concentrations at specific locations. I compare measured and modeled values pair-wise at each time of measurement in the grid cell containing each measurement station. Twenty-four hour average measurements are compared to the average of the modeled (hourly instantaneous) values within the same period. Comparisons are only made with observations that occur within the first (nearest to ground) model layer (average model layer heights are shown in Table 3.3). Source code for the program used to extract and pair model and measurement data is available at `https://bitbucket.org/ctessum/aqmcompare`.

3.3.3 Aggregation of results

In addition to reporting annual average model performance for the entire model domain, I also disaggregate results spatially and temporally. I evaluate performance using two spatial approaches. First, I use four regional subdomains: Midwest, Northeast, South, and West (basis: U.S. Census regions (*131*); see Figure 3.1). Second, I evaluate urban versus rural (i.e., not urban) locations, also as defined by the U.S. Census (*132*). CSN monitors tend to be placed in urban areas (85% of 186 monitors are urban), whereas IMPROVE monitors tend to be placed in protected rural areas (10% of 122 monitors are urban). All 67 monitors in the CASTNET network are in rural locations. I also split the analysis into four seasons: winter (January through March), spring (April through June), summer (July through September), and fall (October through December). Employing these time-periods allows me to compare against previously published results (*107*).

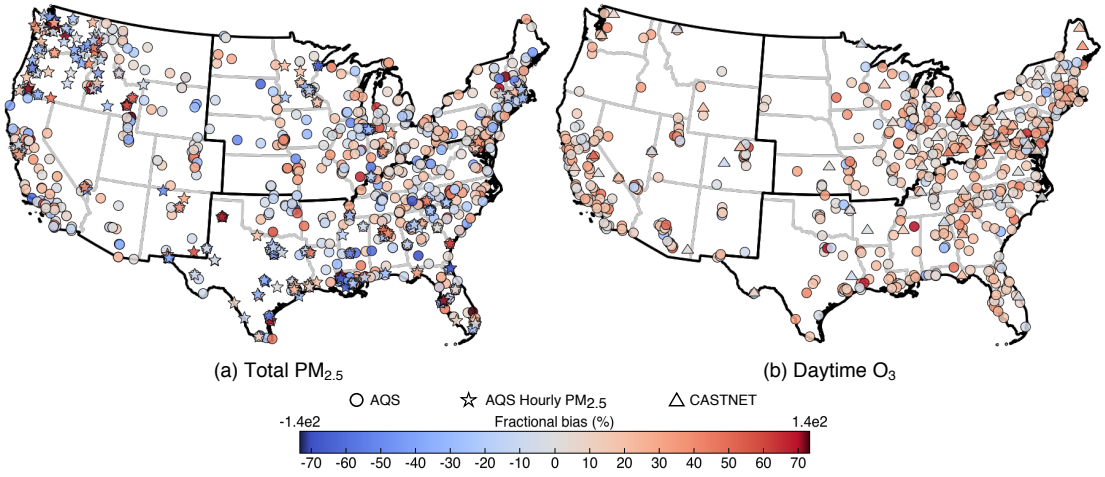

Figure 3.1: AQS, AQS hourly, and CASTNET monitor locations and annual average fractional bias for total $PM_{2.5}$ (panel a) and daytime average O_3 concentrations (panel b). Corresponding information for other pollutants and variables is in Figure 3.7.

3.3.4 Performance metrics

After matching all measured values with their corresponding modeled values, and averaging modeled and measured values across the appropriate time period, I calculate metrics shown in Equations 3.1–3.8:

$$MB = \frac{1}{n}\sum_{i=1}^{n}(M_i - O_i) \tag{3.1}$$

$$ME = \frac{1}{n}\sum_{i=1}^{n}|M_i - O_i| \tag{3.2}$$

$$NMB = \frac{\sum_{i=1}^{n}(M_i - O_i)}{\sum_{i=1}^{n} O_i} \times 100\% \tag{3.3}$$

$$NME = \frac{\sum_{i=1}^{n}|M_i - O_i|}{\sum_{i=1}^{n} O_i} \times 100\% \tag{3.4}$$

$$MFB = \frac{1}{n}\sum_{i=1}^{n}\frac{2(M_i - O_i)}{(M_i + O_i)} \times 100\% \tag{3.5}$$

$$MFE = \frac{1}{n}\sum_{i=1}^{n}\frac{2|M_i - O_i|}{(M_i + O_i)} \times 100\% \tag{3.6}$$

$$MR = \frac{1}{n}\sum_{i=1}^{n}\frac{M_i}{O_i} \tag{3.7}$$

$$RMSE = \sqrt{\frac{\sum_{i=1}^{n}(M_i - O_i)^2}{n}} \tag{3.8}$$

where i corresponds to one of n measurement locations, M and O are time-averaged modeled and observed values, respectively, *MB* is mean bias, *ME* is mean error, *NMB* is normalized mean bias, *NME* is normalized mean error, *MFB* is mean fractional bias, *MFE* is mean fractional error, *MR* is model ratio, and *RMSE* is root-mean-square error. I additionally calculate the slope (S), intercept (I), and squared Pearson correlation coefficient (R^2) of a linear regression between modeled and measured values. Each metric provides a useful and distinct evaluation of model performance. In general, metrics with "bias" in the name evaluate the accuracy of the model, whereas metrics with "error" in the name incorporate both precision and accuracy. Metrics that are in normalized or fractional form tend to emphasize errors where measured and

observed values are relatively small, whereas non-normalized metrics tend to emphasize errors where measured and observed values are relatively large. I mainly focus here on *MFB* and R^2 to evaluate performance as they facilitate direct comparisons among pollutants. Results for all combinations of time periods, measurement networks, spatial subdomains, and metrics are in the Appendix C. For O_3, I calculate model performance via three model-measurement comparisons: 1) annual averages, 2) daytime-only (8am to 8pm) annual averages, as in Appel et al. (*107*), and 3) annual-averages of daily peak concentrations, to match the epidemiological findings in Jerrett et al., (*6*). Model performance goals and criteria have been published for $PM_{2.5}$ (*118*). Goals reflect performance that models should strive to achieve; criteria reflect performance that models should achieve to be used for regulatory purposes. The goals and criteria suggested by Boylan and Russell (*118*) vary with concentration: they are *MFB* less than ±30% and ±60% and *MFE* less than 50% and 75%, respectively, for most concentrations, but increase exponentially as concentration decreases below $\sim$3 μg m^{-3}. To incorporate this aspect of performance evaluation, I calculate the fraction of observation stations for which my $PM_{2.5}$ model results meet both the *MFB* and *MFE* performance goals (fG) and criteria (fC).

3.4 Results

Figure 3.2 shows modeled annual average concentrations of $PM_{2.5}$ and O_3, where the edges of the maps represent the edges of the modeling domain. An animated version of Figure 3.2 showing pollutant concentration as a function of time is available in Appendix C. Maps of additional pollutants, as well as monthly, weekly, and diurnal maps and profiles of population-weighted average concentrations, are also available in Appendix C. Modeled O_3 concentrations over water in the Gulf of Mexico and along the Atlantic coast tend to be higher than concentrations over the adjacent land areas. As only areas over water appear to be affected (as Figure 3.1a shows, O_3 overpredictions along the Gulf of Mexico and Atlantic coasts are not greater than overpredictions further inland), this over-water anomaly in the Gulf of Mexico should not adversely impact estimates of population-weighted concentrations.

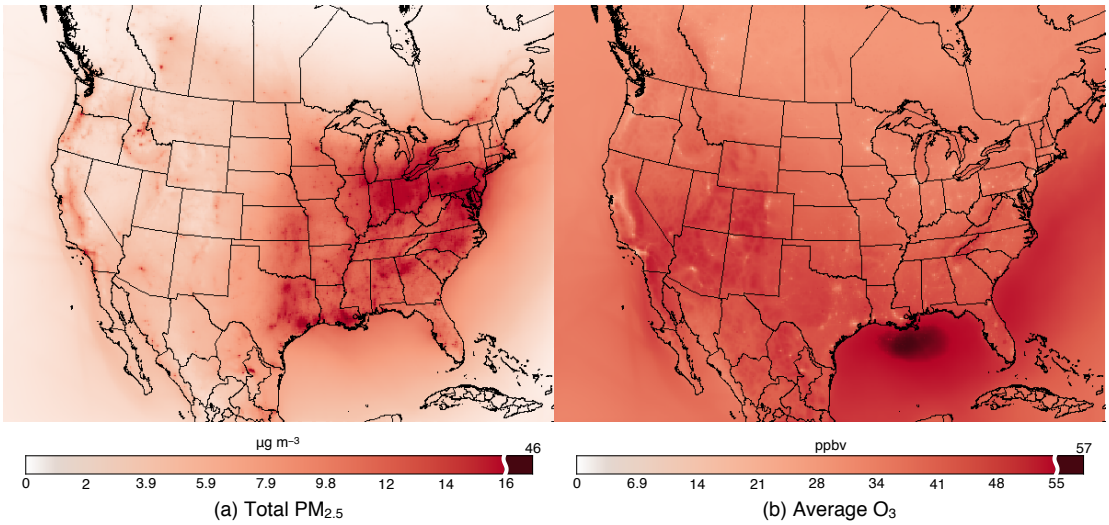

Figure 3.2: Modeled annual average ground level concentrations of (a) $PM_{2.5}$ and (b) O_3. For ease of viewing, the color scales contain a break at the 99^{th} percentile of concentrations.Versions of this figure showing differences by month-of-year, day-of-week, and hour-of-day are in Appendix C.

Figure 3.1 shows monitor locations for total $PM_{2.5}$ and for O_3, as well annual average fractional bias (*MFB*) values at each monitor. Results in Figure 3.1a ($PM_{2.5}$) display high spatial variability, with no obvious spatial patterns in model performance; large overpredictions are sometimes adjacent to large underpredictions (e.g., in southern Louisiana and Florida). WRF-Chem generally overpredicts daytime O_3 concentrations relative to observations (Figure 3.1b). Monitor locations for meteorological variables, $PM_{2.5}$ subspecies, and other gas phase species are in Figure 3.7.

3.4.1 Meteorological Performance

Figure 3.3 contains scatterplots comparing annual average observed and predicted values for meteorological variables and pollutant concentrations. The model tends to overpredict near-ground wind speed (Figure 3.3a) and precipitation (Figure 3.3d) relative to observations, whereas temperature (Figure 3.3b) and relative humidity (Figure 3.3c) predictions agree well

with observations. Figures 3.8-3.11 disaggregate model performance for meteorological variables by region (region boundaries are shown in Figure 3.1) and by season; meteorological performance is relatively consistent among seasons and regions. Model-measurement comparisons provide important evidence on model performance but might overestimate model robustness for meteorological parameters because FDDA "nudges" model meteorological estimates toward observed values.

3.4.2 $PM_{2.5}$ and O_3 Performance

Annual average model-measurement agreement is good for total $PM_{2.5}$ concentration (Figure 3.3e, 94% of measurements meet performance criteria), although the model tends to overpredict $PM_{2.5}$ concentration at relatively high-concentration monitors (Figure 3.3e). The model tends to generally overpredict O_3 concentrations, with worse overpredictions for 24-hour average concentrations (Figure 3.3f) than for daily peak (Figure 3.3g) and daytime average (Figure 3.3h) concentrations. Figure 3.4 shows the median and interquartile range for modeled and measured $PM_{2.5}$ and O_3 concentrations by hour of day (measurements of $PM_{2.5}$ subspecies are only available as 24 hour averages). For $PM_{2.5}$, the model generally agrees with measurements, although on average it underpredicts concentrations at night and overpredicts during the day (Figure 3.4a). For O_3, on average the model overpredicts for all times-of-day, but with a much lower fractional error during the day than during the night. For both pollutants, the model accurately captures the timing of diurnal trends, including the afternoon peak for O_3 and the morning and evening peaks for $PM_{2.5}$. As a result, when comparing the three averaging-time metrics for O_3, I observe better model performance for the annual-average of daily peak concentration (*MFB*=11%) and of average daytime concentration (*MFB*=12%) than for overall annual average (*MFB*=23%). For O_3, the first two metrics may offer greater relevance than the third; for example, the annual average of daily peak concentrations is more strongly correlated with health effects than are annual average concentrations (*6*); and, for comparisons to the 8-hour peak concentration standard (established for the National Ambient Air Quality Standard [NAAQS]), model performance is more important during day than at night. Figures 3.5 and 3.6

disaggregate results by season and by location for total $PM_{2.5}$ and daytime O_3, respectively; analogous results for other pollutants, for other O_3 temporal summaries, and for meteorological variables are in Figures 3.12–3.20. Daytime and peak O_3 predictive performance does not exhibit obvious patterns among seasons or regions; *MFB* values range from -7% to 48% (daytime; Figure 3.6) and -12% to 29% (peak; Figure 3.13). The overprediction of $PM_{2.5}$ concentrations at high-concentration monitors is more prevalent in the South and in urban areas, and is less prevalent in summer than in other seasons (Figure 3.5). Model-measurement correlation for total $PM_{2.5}$ is higher in summer (AQS R^2=0.64) than in fall and winter (AQS R^2=0.20 and 0.24, respectively), but overall $PM_{2.5}$ concentrations are not higher in summer. Previous research has suggested that poor PM predictive performance in winter is common among CTMs and may be attributable to difficulty in reproducing the strongly stable meteorological conditions that are responsible for high winter PM concentrations (*133*). Annual average $PM_{2.5}$ predictive performance in the West (AQS R^2: 0.45 [summer], 0.13 [winter]) is worse than performance in the Northeast (AQS R^2: 0.70 [summer], 0.37 [winter]). In the Northeast, performance is better in the summer (R^2=0.69) than in other seasons (R^2=0.30–0.40). Taken together, these findings suggest that there is an opportunity for future model development for $PM_{2.5}$ to focus on winter or full-year simulations rather than summer-only simulations, and on the western U.S. or the full Continental U.S. rather than just the Northeast.

3.4.3 $PM_{2.5}$ Subspecies Performance

Figure 3.3i-m illustrates model performance for annual average concentrations of $PM_{2.5}$ component species. In all cases, >65% of locations meet performance criteria for at least one of the three observation networks. The model overpredicts particulate SO_4 (CSN *MFB*=34%, IMPROVE *MFB*=126%, CASTNET *MFB*=36%) (Figure 3.3i) and SO_2 (*MFB*=51%) (Figure 3.3n). This finding (overprediction of total sulfur) agrees with prior research for multiple CTMs (*114*). Performance as compared to the IMPROVE network is worse than performance as compared to the CSN and CASTNET networks, perhaps owing to differences in measurement methods. Particulate SO_4 prediction performance does not vary much by region; as with total $PM_{2.5}$,

performance is worse in winter (CSN *MFB*=59%) than summer (CSN *MFB*=10.%) (Figure 3.14). WRF-Chem as configured here performs well in predicting observed particulate NH_4 concentrations, with 99% of locations meeting performance criteria (Figure 3.3k). Similar to total $PM_{2.5}$, performance for particulate NH_4 is worst in the urban areas in the West region (Figure 3.15), where a number of monitors report relatively high measured concentrations but modeled concentrations are relatively low. Particulate NO_3 concentrations are consistently underpredicted (*MFB*=-110%) (Figure 3.3l). Figure 3.16 shows that these underpredictions are more severe in some seasons and regions than in others. The best predictive performance is for the Midwest in summer (*MFB*=-39%) followed by the Northeast in summer (*MFB*=-47%). NO_3 predictions in the West region are poor for all seasons (*MFB*=-148%), as are wintertime predictions for the whole U.S. (*MFB*=-120%). As with other $PM_{2.5}$ species, there is an opportunity for future development and evaluation of models for particulate NO_3 prediction to focus on seasons and regions other than summer in the Northeast. Predictions of gas-phase NO_2 (Figure 3.3o) agree relatively well with observations (*MFB*=4%), but, as with other species, the model tends to overpredict NO_2 concentrations in areas where measured concentrations are relatively high. This effect is especially prominent in the West and in urban areas (Figure 3.20). Model-measurement agreement for EC concentrations is relatively good (Figure 3.3l), with 96% of monitor locations meeting performance criteria. As with other comparisons, for EC the model tends to overpredict concentrations for monitors with relatively high concentrations, especially in urban areas (Figure 3.17). Model predictions of OC concentrations (Figure 3.3m) are biased low compared to CSN (*MFB*=-113%) but agree relatively well with IMPROVE (*MFB*=15%). Mean bias values given here are within the range of values reported by a previous publication using the VBS SOA formation mechanism (*111*). As shown in Figure 3.18, the differences between networks do not appear to be dependent on urban vs. rural monitor location; instead, they may reflect between-network differences in sampling or analysis.

3.4.4 Comparison with other studies

Table 3.4 compares performance of WRF-Chem as configured here to that of the CMAQ model in a similar modeling effort by Appel et al. (*107*). In this table, CMAQ as configured by Appel et al. (*107*) in most cases predicts O_3 observations with greater accuracy and precision than does WRF-Chem as configured here, while WRF-Chem in most cases does a better job predicting $PM_{2.5}$. However, given the many differences in physical and chemical parameterizations and input data (including a difference in simulation year), the observed differences may or may not be generalizable. Instead, my conclusion from Table 3.4 is that the models are generally comparable in performance.

Table 3.5 compares WRF-Chem results from this study to results from Yahya et al. (*104*) for a 12-month, contiguous U.S. WRF-Chem simulation with a 36-km horizontal resolution spatial grid. *NME* results from the simulation performed here are lower than those reported by Yahya et al. for most pollutants and measurement networks, but *NMB* results are more mixed. As horizontal grid resolution, input data, and model parameters all differ between the two studies, I am not able to determine the cause of the differences in results.

3.5 Discussion

I simulated and evaluated $PM_{2.5}$ and O_3 based on 12-month (year-2005) WRF-Chem modeling for the United States. The spatial and temporal extent investigated, and the horizontal spatial resolution (12 km) employed, are nearly unprecedented; to my knowledge, only one prior peer-reviewed article has investigated CTMs using the same extent and resolution (*107*). I find that WRF-Chem performance as configured here is generally comparable to other models used in regulatory and health impact assessment situations in that model performance is similar to that reported by Appel et al. (*107*) and in most cases meets criteria suggested by (*118*). There is potential for further improvement in model accuracy, especially for these cases: $PM_{2.5}$ concentrations in winter and in the western U.S., ground-level O_3 at night and in the summer, and particulate nitrate and organic carbon. The good agreement in total $PM_{2.5}$ predictions

and observations in some cases reflects offsetting over- and underpredictions, including by species (Figures 3.14–3.18) and time-of-day (Figure 3.4a). Performance in predicting concentrations of $PM_{2.5}$ and its subspecies tends to be the worst in winter and in the western U.S. Overall, WRF-Chem as configured here meets the performance criteria described above for total $PM_{2.5}$ concentrations at 94% of monitor locations. The WRF-Chem meteorological and chemical settings employed here are reasonable and justified, but different settings may also be reasonable. Improved understanding of how alternative parameterizations might impact model performance in large-scale applications such as ours is an area for continued research. Another area for future research is identifying opportunities to evaluate model performance in terms of how *changes* in emissions cause changes in outdoor concentrations.

Table 3.1: Temporal and spatial aspects of recent model evaluations, focusing on WRF-Chem and North America

Author and year	Model used	Time period	Spatial extent	Horizontal spatial resolution
Ahmadov et al., 2012 (*111*)	WRF-Chem	August-September, 2006	Contiguous U.S. (evaluation performed for eastern U.S.)	60 and 20 km
Appel et al., 2012 (*107*)	CMAQ	Full year, 2006	Contiguous U.S. and Europe	12 km
Chuang et al., 2011 (*112*)	WRF-Chem	May-September, 2009	Southeastern U.S.	12 km
Fast et al., 2006 (*113*)	WRF-Chem	Late August, 2000	City of Houston	1.3 km
Grell et al., 2005 (*110*)	WRF-Chem	July-August, 2002	Eastern U.S.	27 km
McKeen et al., 2007 (*114*)	WRF-Chem, CHRONOS, AURAMS, STEM, CMAQ/ETA	July-August, 2004	Northeastern U.S.	12, 21, 27, and 42 km
Misenis and Zhang, 2010 (*115*)	WRF-Chem	Late August, 2000	Eastern Texas	4 and 12 km
Tesche et al., 2006 (*103*)	CMAQ, CAMx	Full year, 2002	Contiguous U.S.	12 km Eastern U.S., 36 km Continental U.S.
Yahya et al., 2014 (*104*)	WRF-Chem	Full year, 2006	Contiguous U.S.	36 km
Zhang et al., 2010 (*116*)	WRF-Chem	Late August, 2010	Eastern Texas	12 km
Zhang et al., 2012 (*117*)	WRF-Chem	July, 2001	Contiguous U.S.	36 km

Table 3.2: Selected WRF-Chem v3.4 Settings and Parameters Employed in This Study

Category	Option used
Microphysics	WSM 3-class simple ice scheme
Shortwave and longwave radiation	CAM scheme
Land surface	Unified Noah land surface model
Boundary layer physics	YSU scheme
Cumulus physics	New Grell scheme (G3)
FDDA meteorology nudging	Yes (grid-based)
Gas-phase chemistry	NOAA/ESRL RACM
Aerosol chemistry/physics	MADE/VBS
Aerosol feedback	No
Photolysis	Fast-J
Anthropogenic emissions	2005 NEI
Biogenic emissions	BEIS v3.14
Horizontal grid resolution	12 km
Number of vertical layers	28

Table 3.3: Average Model Layer Heights and Thicknesses

Layer	Height (m)	Δ Height (m)
1	5.7×10^{1}	5.7×10^{1}
2	1.4×10^{2}	8.1×10^{1}
3	2.4×10^{2}	1.1×10^{2}
4	3.8×10^{2}	1.3×10^{2}
5	5.5×10^{2}	1.7×10^{2}
6	7.6×10^{2}	2.2×10^{2}
7	1.0×10^{3}	2.6×10^{2}
8	1.5×10^{3}	4.6×10^{2}
9	2.0×10^{3}	4.8×10^{2}
10	2.5×10^{3}	5.1×10^{2}
11	3.0×10^{3}	5.3×10^{2}
12	4.0×10^{3}	9.9×10^{2}
13	5.0×10^{3}	9.9×10^{2}
14	6.0×10^{3}	9.9×10^{2}
15	7.0×10^{3}	9.9×10^{2}
16	8.0×10^{3}	9.9×10^{2}
17	9.0×10^{3}	9.9×10^{2}
18	9.9×10^{3}	9.9×10^{2}
19	1.1×10^{4}	1.0×10^{3}
20	1.2×10^{4}	1.0×10^{3}
21	1.3×10^{4}	1.0×10^{3}
22	1.4×10^{4}	1.1×10^{3}
23	1.5×10^{4}	1.1×10^{3}
24	1.6×10^{4}	1.2×10^{3}
25	1.8×10^{4}	1.2×10^{3}
26	1.9×10^{4}	1.3×10^{3}
27	2.0×10^{4}	1.4×10^{3}

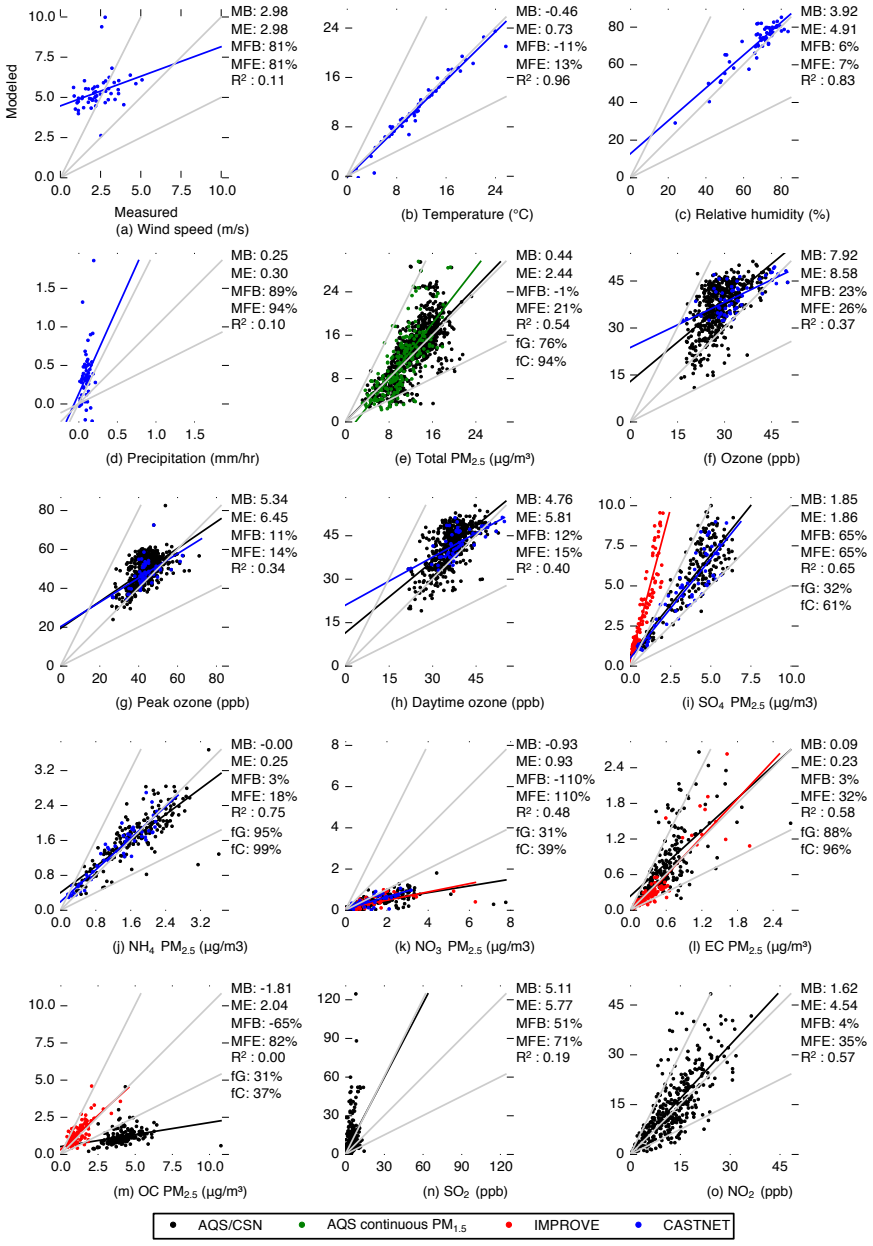

Figure 3.3: Annual average modeled and measured ground-level meteorological variables (panels a-d) and pollutant concentrations (panels e-o). Colored lines show linear least-squares fits of the data for the measurement networks with corresponding colors. Grey lines show model to measurement ratios of 2:1, 1:1, and 1:2. Annual average performance statistics are listed to the right of each plot; acronyms are defined in the methods section.

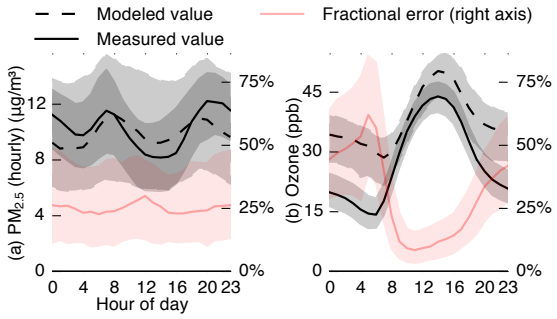

Figure 3.4: Median values (lines) and interquartile ranges (shaded areas) of annual average modeled values, observed values, and fractional error by hour of day for $PM_{2.5}$ (panel a) and O_3 (panel b).

Table 3.4: WRF-Chem and CMAQ[a] Seasonal O_3 and $PM_{2.5}$ Prediction Performance

	Daytime[b] Average O_3 (ppb)		$PM_{2.5}$ (µg m^{-3})	
	WRF-Chem	CMAQ	WRF-Chem	CMAQ
Winter MB	3.5	-3.5	0.8	3.4
Spring MB	1.5	-1.8	2.0	2.0
Summer MB	9.2	4.4	0.0	-0.6
Fall MB	5.2	2.6	-0.9	4.0
Winter ME	5.5	9.0	3.1	6.0
Spring ME	4.6	9.3	3.3	4.5
Summer ME	10.1	11.0	2.6	4.4
Fall ME	6.2	8.8	2.7	5.6
Winter NMB	12%	-13%	6%	30%
Spring NMB	3%	-4%	17%	19%
Summer NMB	21%	10.%	0%	-5%
Fall NMB	19%	8%	-7%	36%
Winter NME	19%	35%	25%	53%
Spring NME	10%	29%	28%	42%
Summer NME	23%	24%	18%	31%
Fall NME	23%	28%	23%	52%

[a]CMAQ results adapted from Appel et al. (2012) Tables 1 and 2.
[b]Daytime is defined as 8am to 8pm local time.

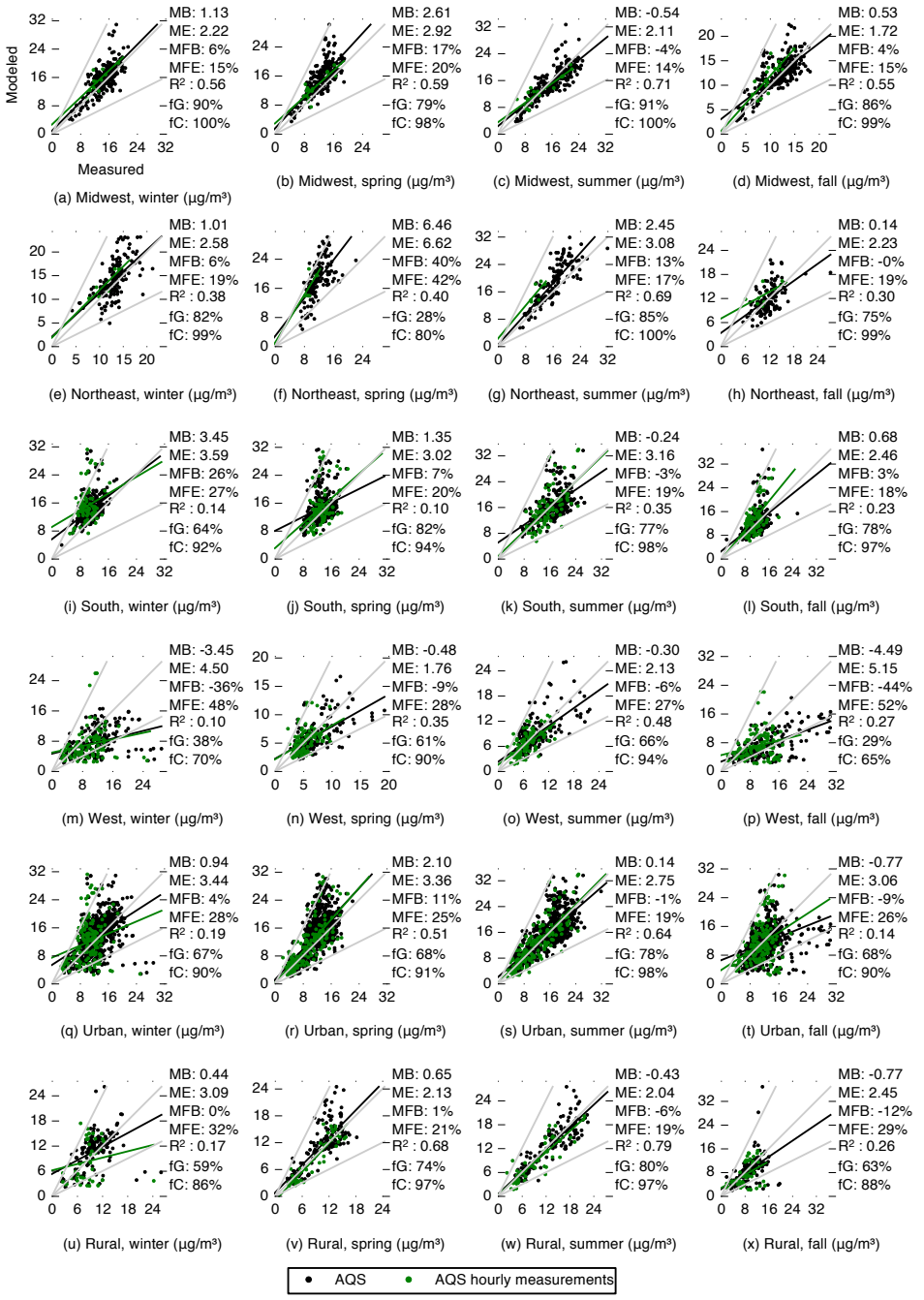

Figure 3.5: Comparison of measured and modeled $PM_{2.5}$ concentration disaggregated by season and region. Region boundaries are shown in Figure 3.1.

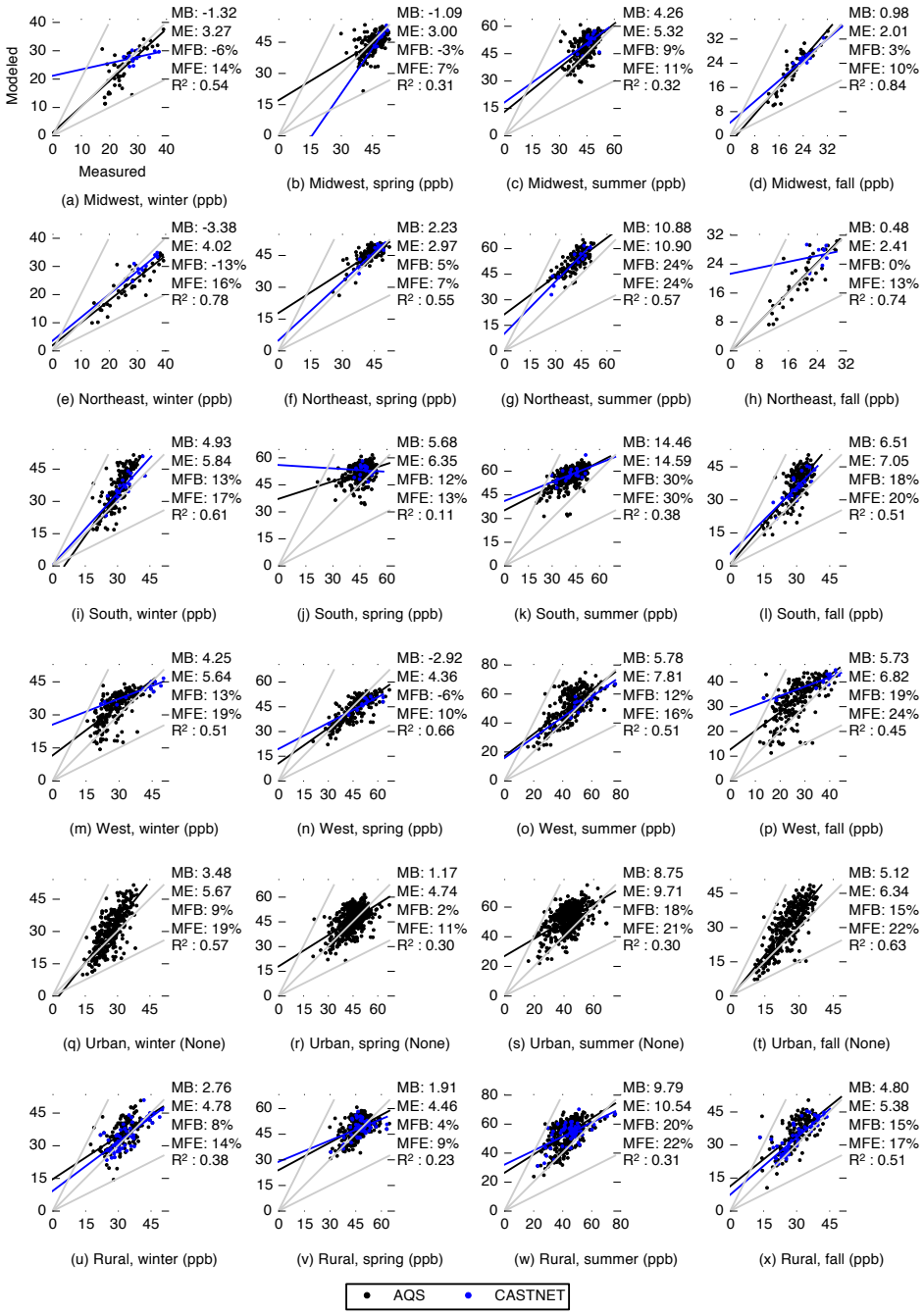

Figure 3.6: Comparison of measured and modeled annual average of daytime O_3 concentration disaggregated by season and region.

Table 3.5: WRF-Chem Predictive Performance by Pollutant in Yahya et al. (*104*) and in the Current Study

		MB		NMB		NME	
Variable	Network	Yahya	Current	Yahya	Current	Yahya	Current
Daily Peak	CASTNET	-8.6	3.9	-18%	9%	24%	12%
O_3 (ppb)	AQS	-0.3	5.5	-5%	13%	9%	15%
Daytime Average	CASTNET	-5.6	3.5	-13%	9%	22%	11%
O_3 (ppb)	AQS	-1.7	4.9	-4%	13%	24%	16%
SO_2 (ppb)	AQS	-0.6	5.1	-18%	130%	87%	150%
NO_2 (ppb)	AQS	1.7	1.6	17%	12%	73%	34%
Total $PM_{2.5}$ ($\mu g\ m^{-3}$)	CSN	0.0	0.4	0%	3%	45%	18%
SO4 $PM_{2.5}$ ($\mu g\ m^{-3}$)	IMPROVE	0.5	2.4	35%	320%	66%	320%
	CSN	0.9	1.6	32%	41%	59%	42%
	CASTNET	0.9	1.3	34%	38%	55%	38%
NH_4 $PM_{2.5}$ ($\mu g\ m^{-3}$)	CSN	0.1	0.0	10.%	-2%	53%	16%
	CASTNET	0.3	0.1	30.%	7%	50.%	16%
NO_3 $PM_{2.5}$ ($\mu g\ m^{-3}$)	IMPROVE	-0.1	-0.5	-14%	-69%	85%	69%
	CSN	-0.6	-1.3	-38%	-72%	75%	72%
	CASTNET	-0.1	-0.7	-15%	-65%	83%	65%
EC $PM_{2.5}$ ($\mu g\ m^{-3}$)	IMPROVE	0.0	0.0	15%	-9%	67%	31%
	CSN	0.4	0.2	54%	25%	90.%	43%
OC $PM_{2.5}$ ($\mu g\ m^{-3}$)	IMPROVE	0.0	0.2	1%	17%	59%	33%

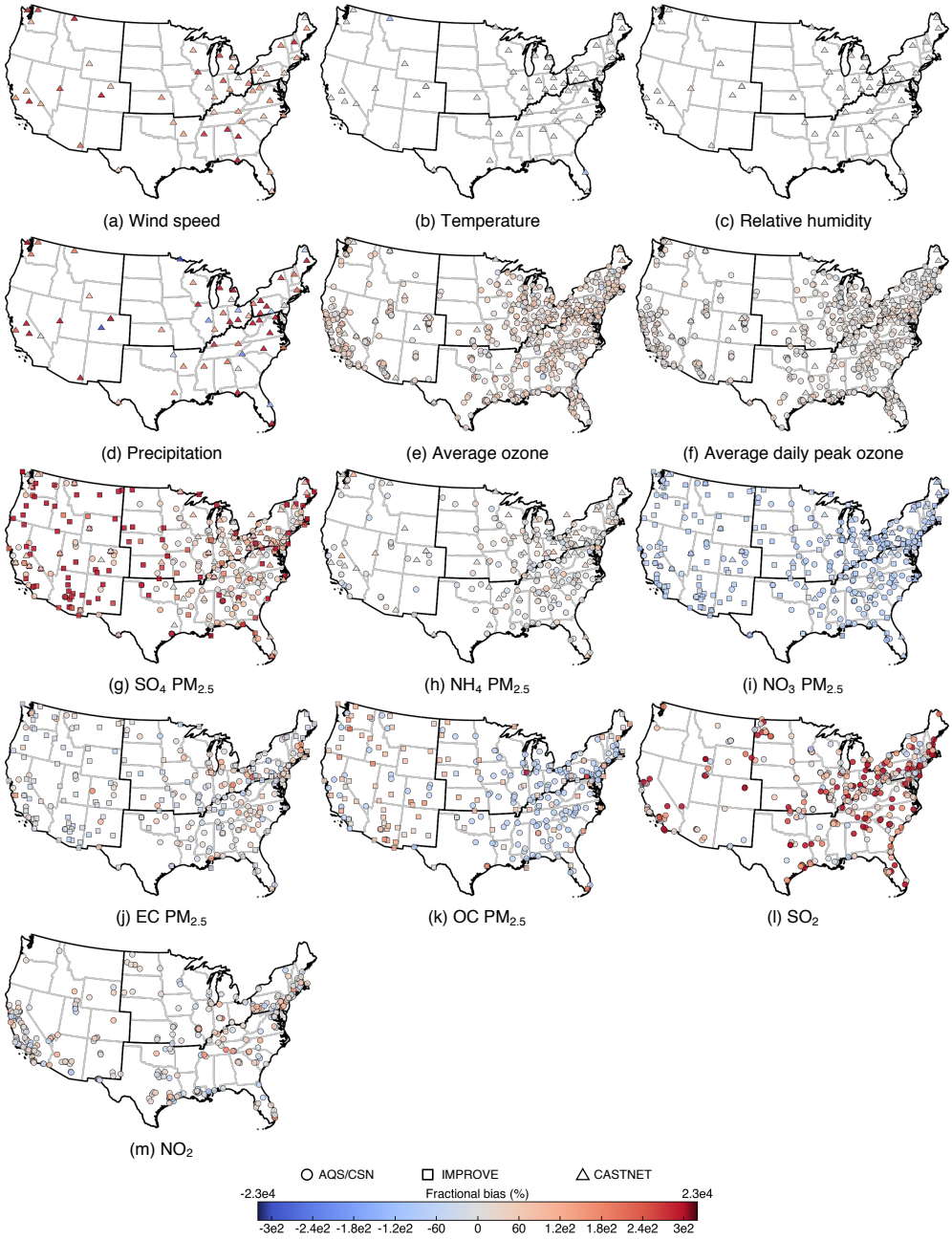

Figure 3.7: AQS, CSN, IMPROVE AQS and CASTNET monitor locations and annual average fractional bias for total meteorological variables (panels a-d) and pollutant concentrations (panels e-m).

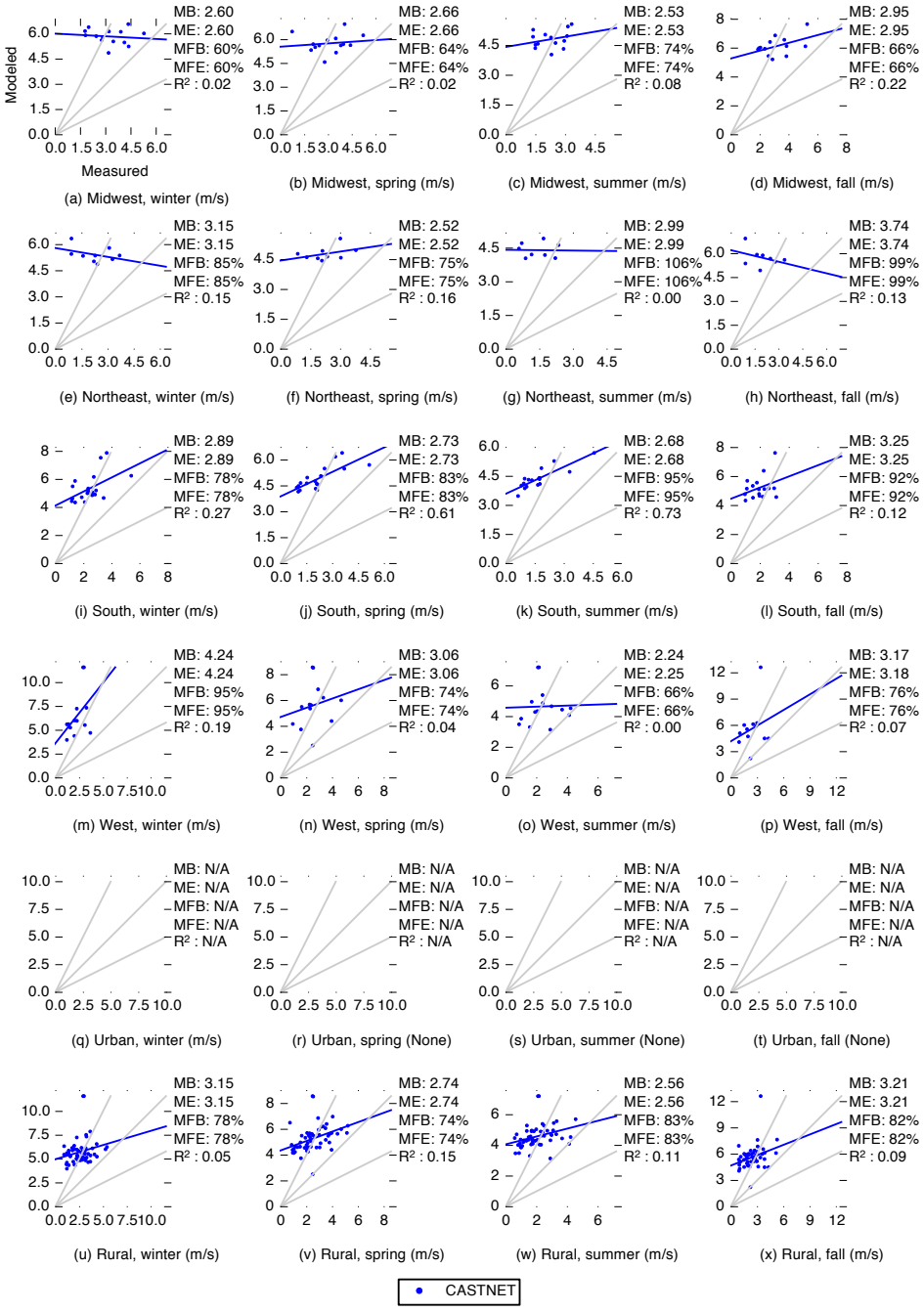

Figure 3.8: Comparison of modeled and measured **wind speed**, disaggregated by region and season.

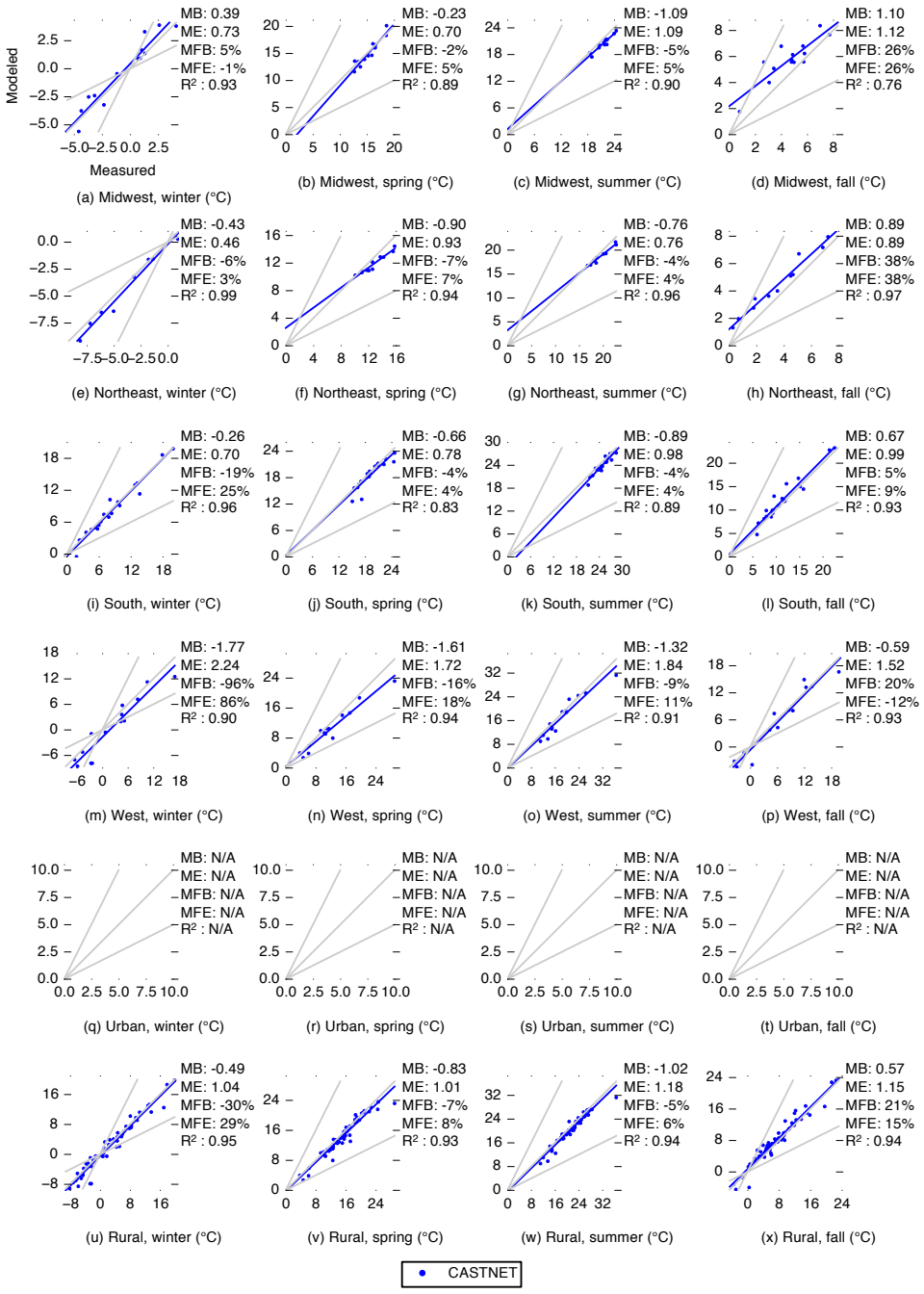

Figure 3.9: Comparison of modeled and measured **temperature**, disaggregated by region and season.

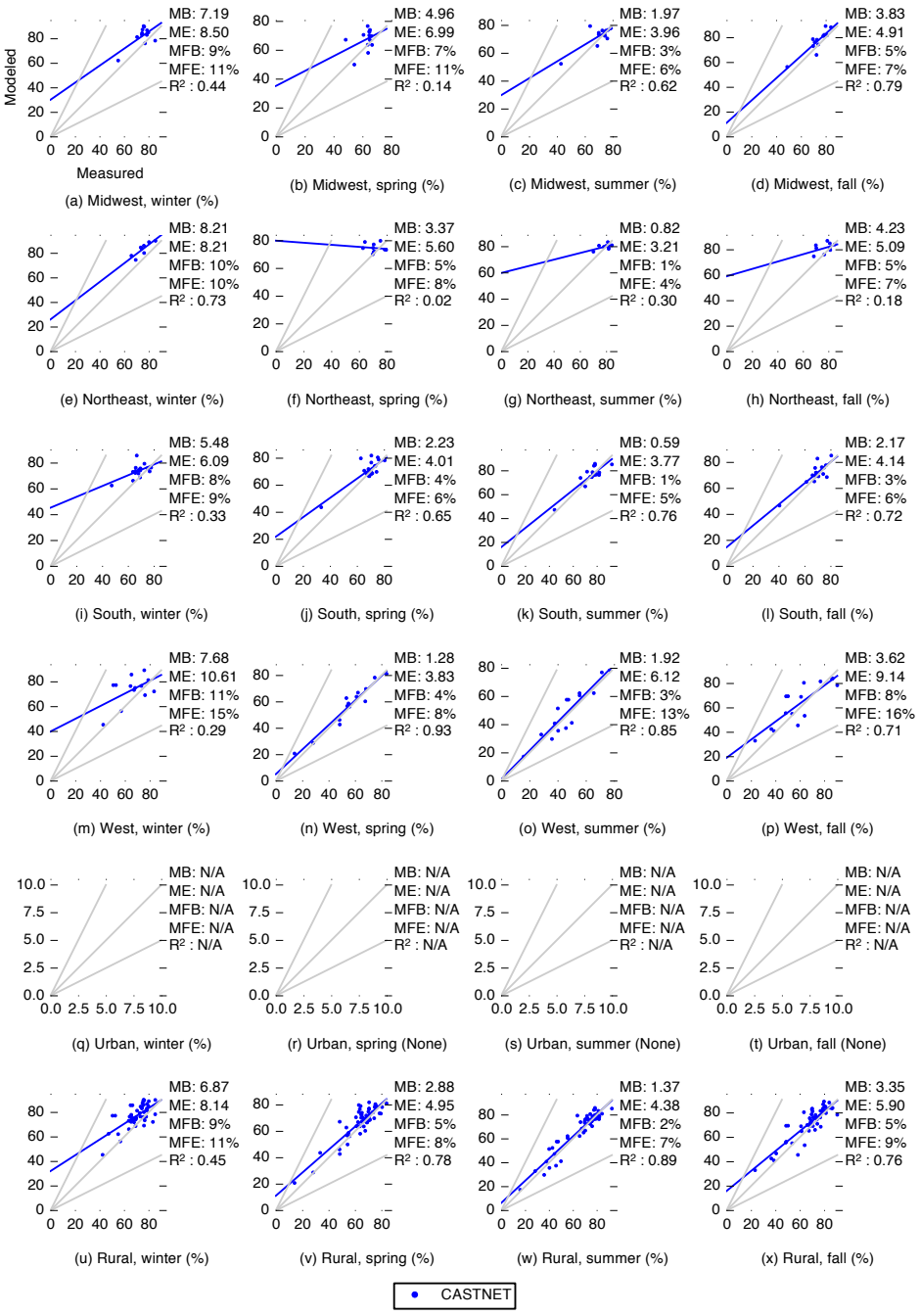

Figure 3.10: Comparison of modeled and measured **relative humidity**, disaggregated by region and season.

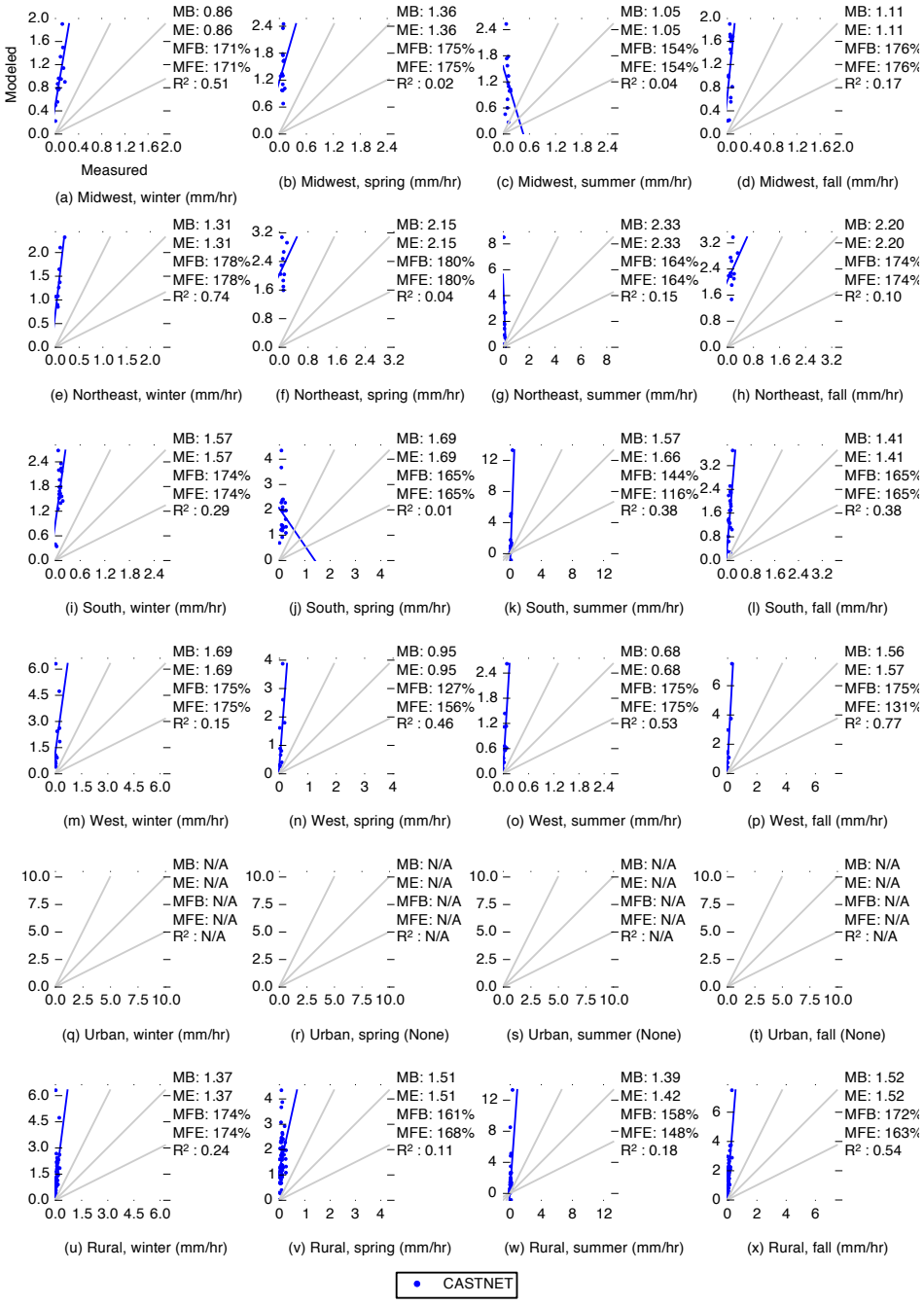

Figure 3.11: Comparison of modeled and measured **precipitation**, disaggregated by region and season.

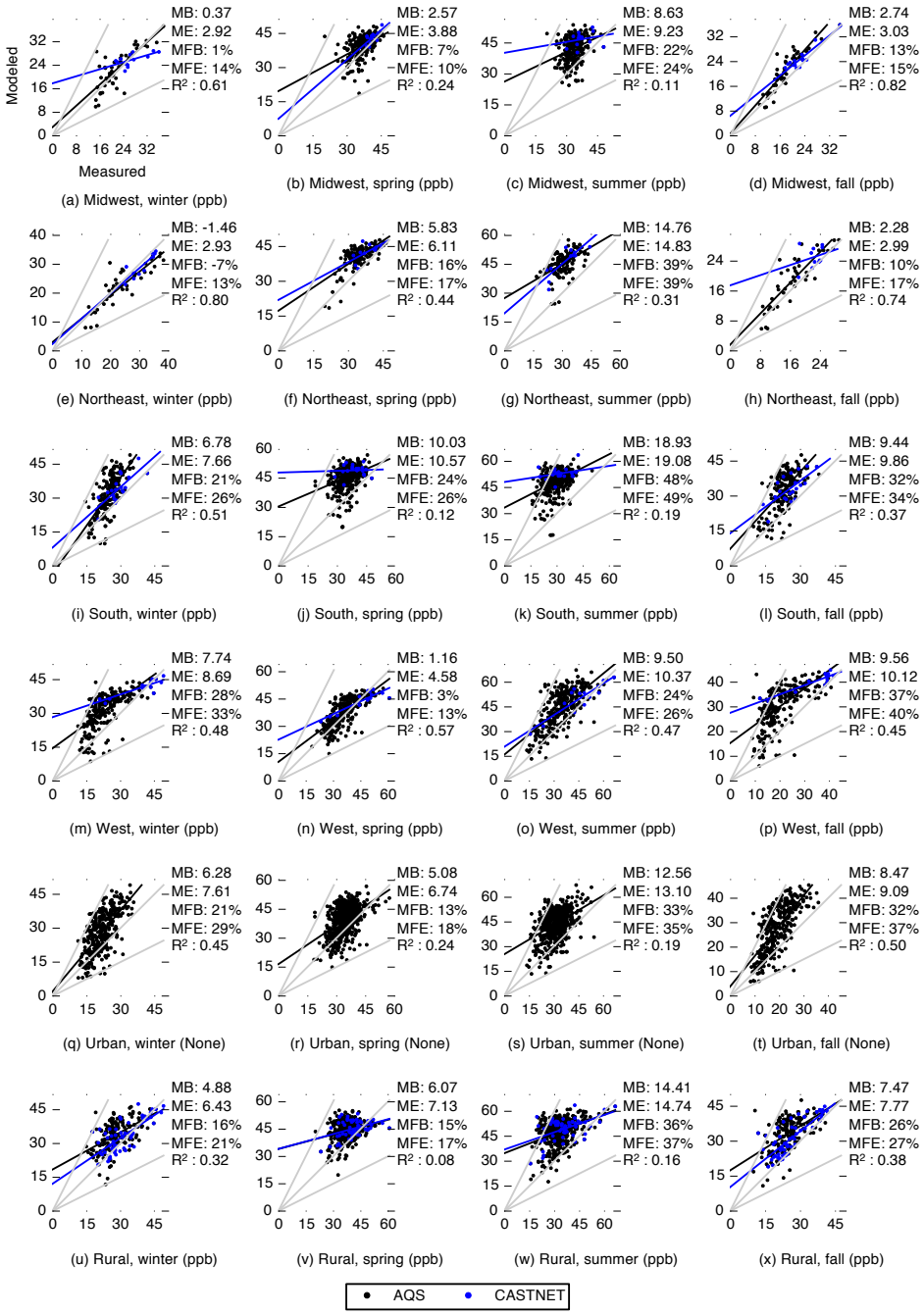

Figure 3.12: Comparison of modeled and measured **annual-average O_3 concentration**, disaggregated by region and season.

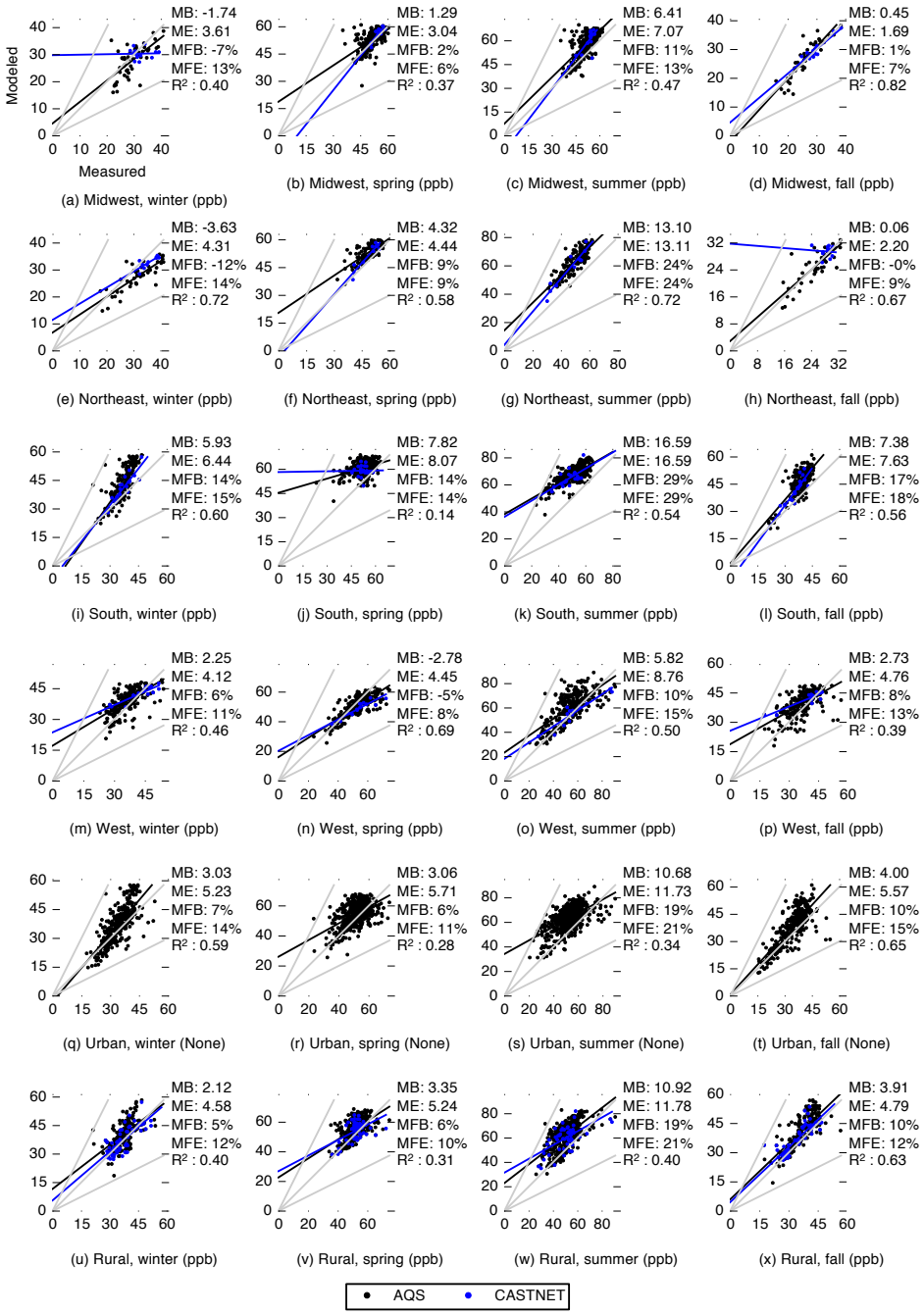

Figure 3.13: Comparison of modeled and measured average **daily peak O_3 concentration**, disaggregated by region and season.

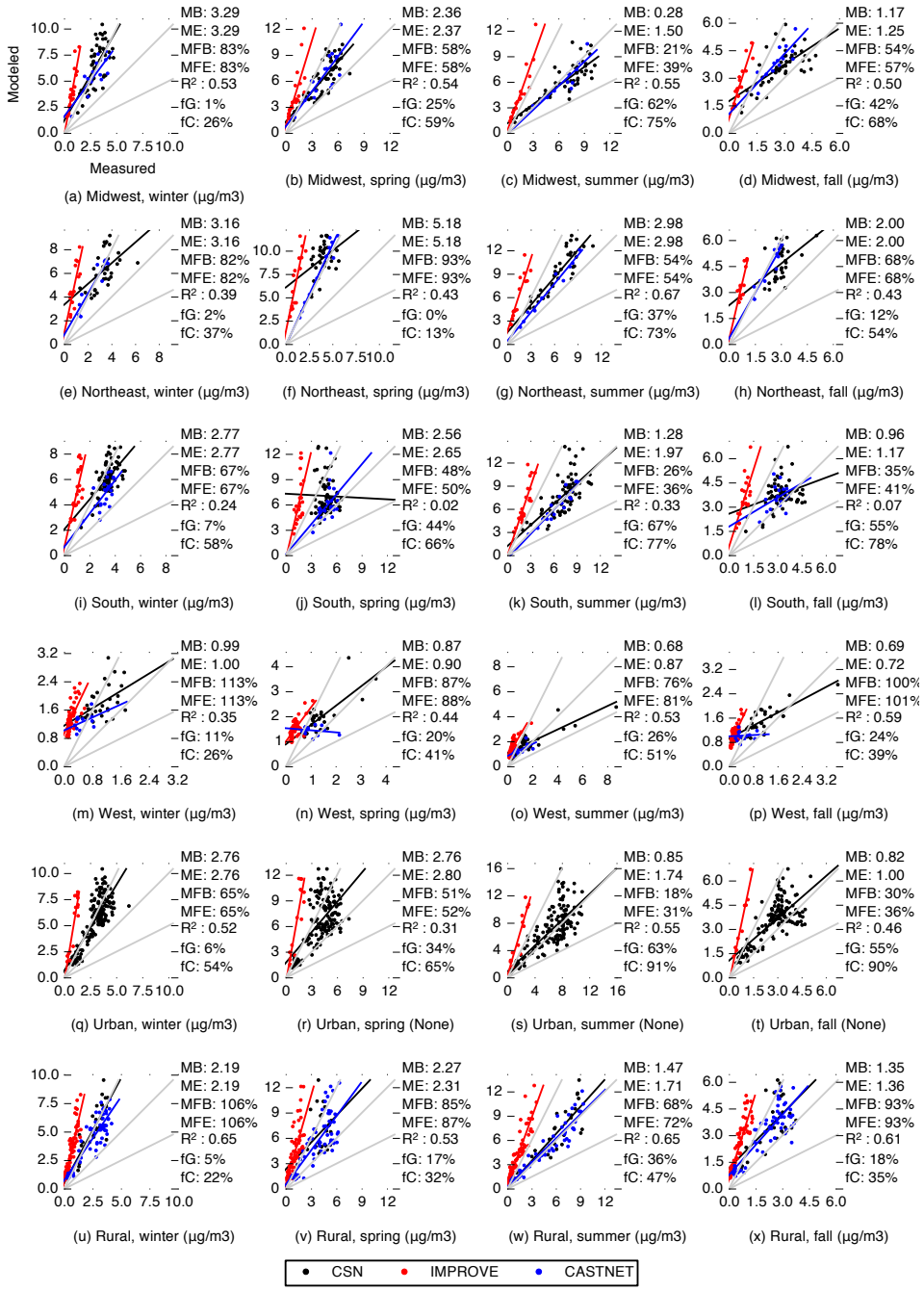

Figure 3.14: Comparison of modeled and measured **particulate SO_4 concentration**, disaggregated by region and season.

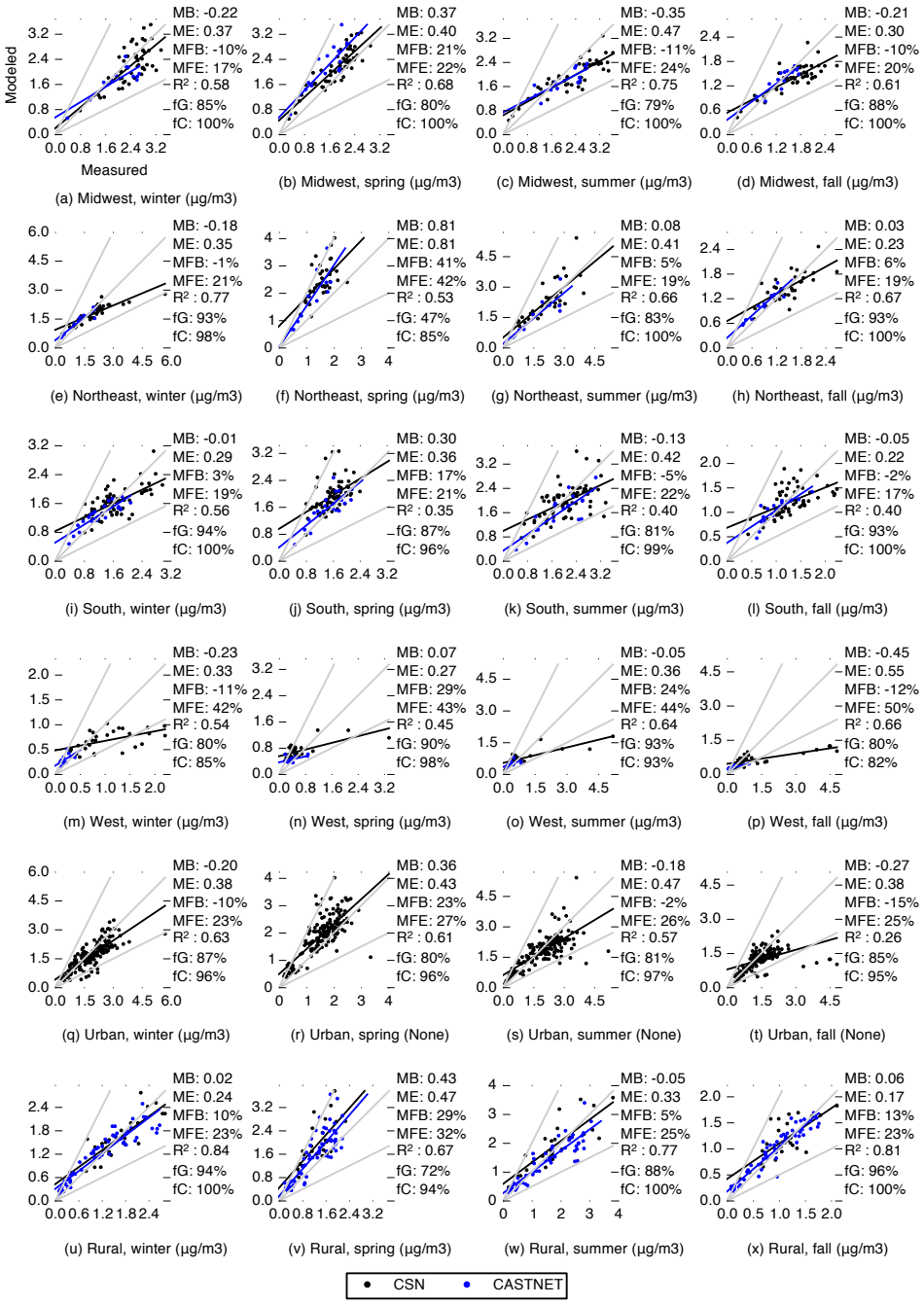

Figure 3.15: Comparison of modeled and measured **particulate NH_4 concentration**, disaggregated by region and season.

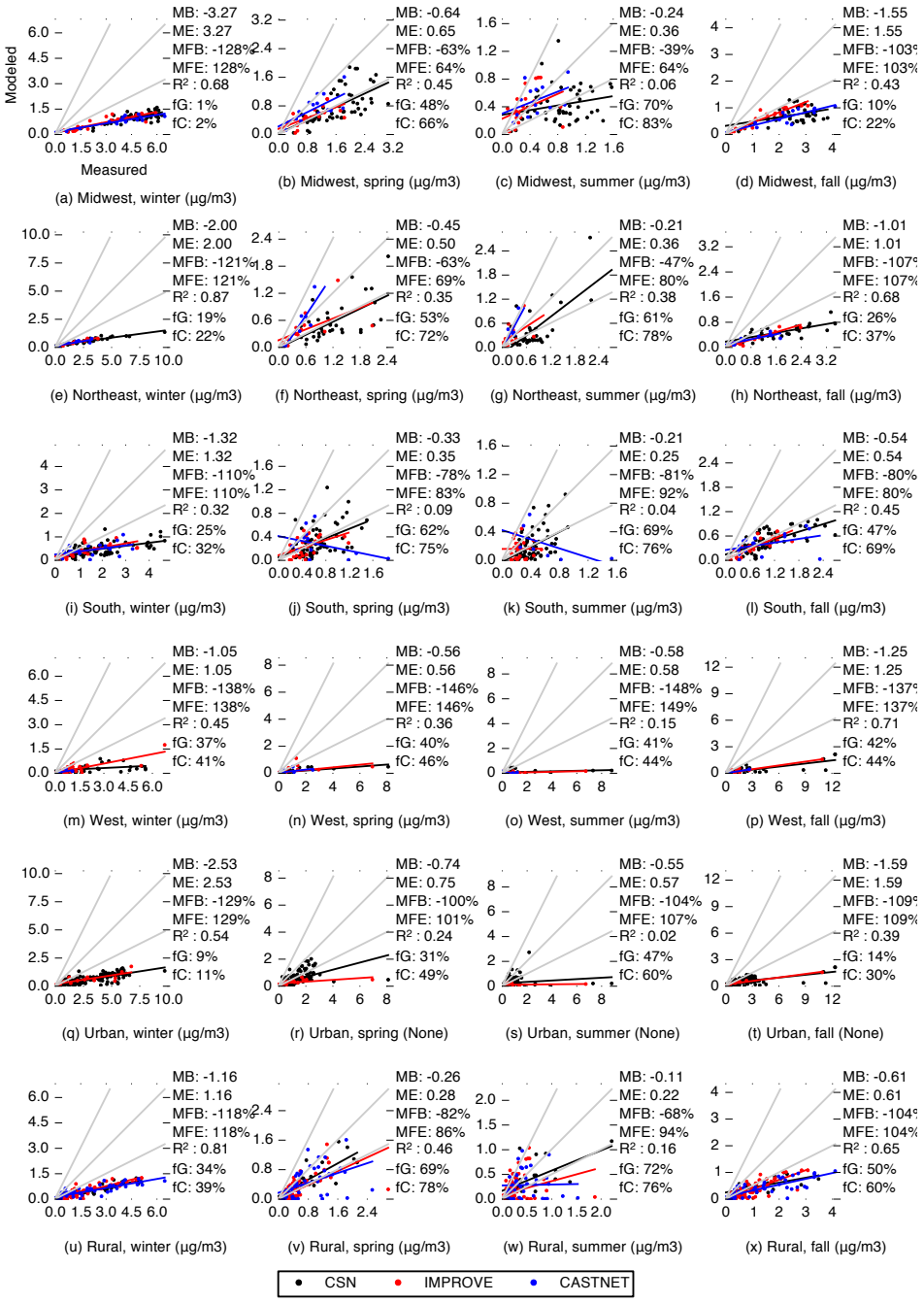

Figure 3.16: Comparison of modeled and measured **particulate NO_3 concentration**, disaggregated by region and season.

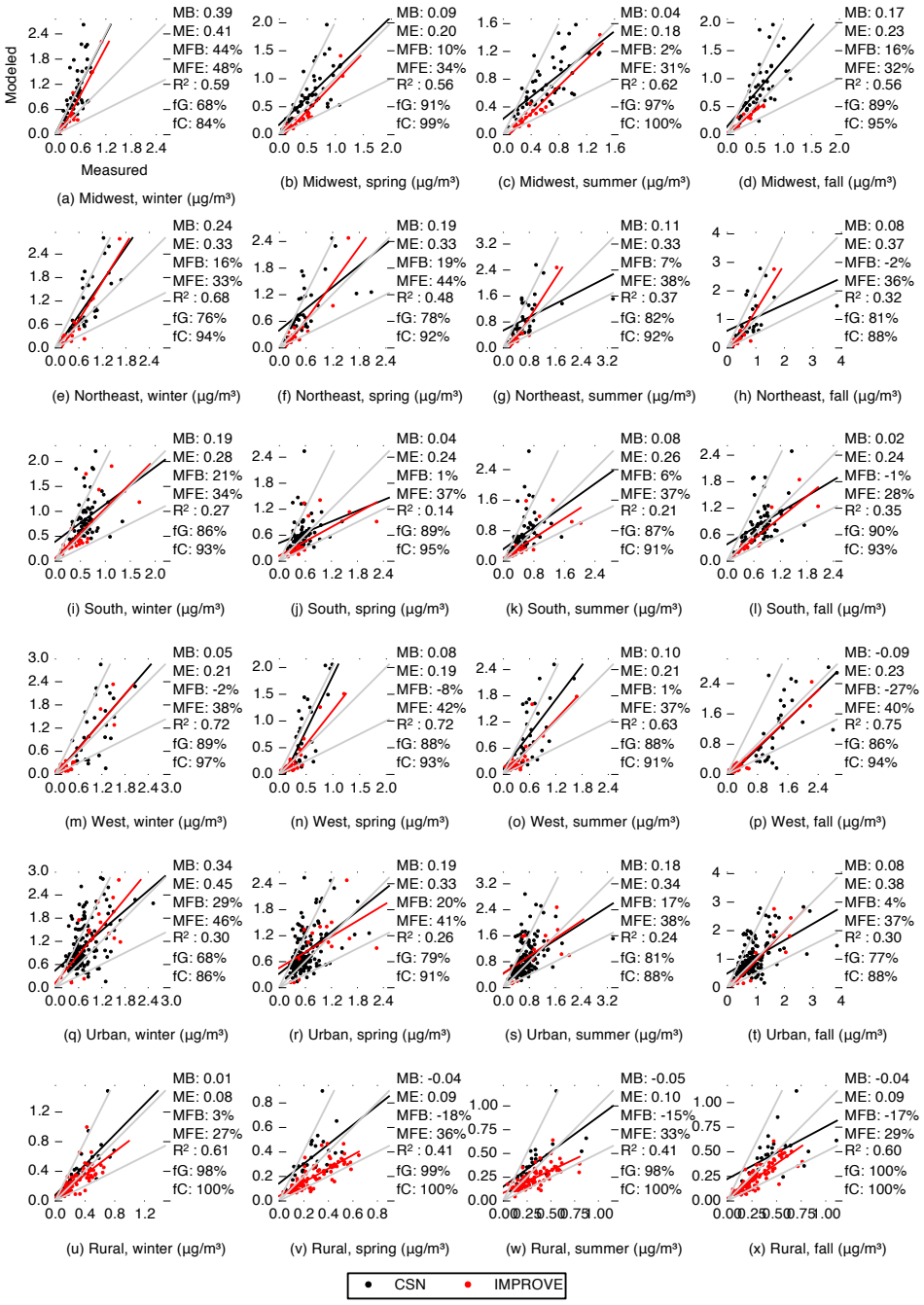

Figure 3.17: Comparison of modeled and measured **particulate EC concentration**, disaggregated by region and season.

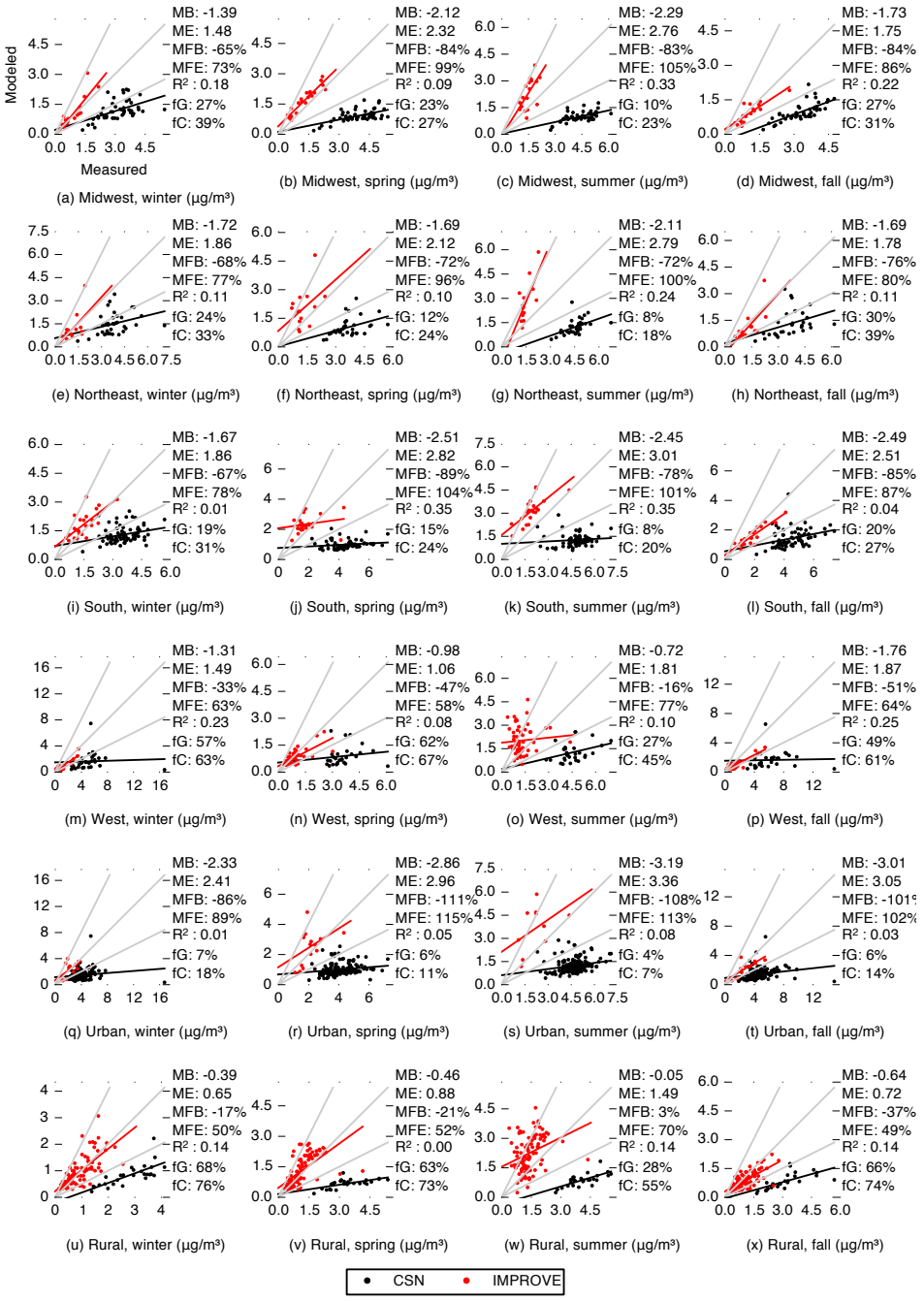

Figure 3.18: Comparison of modeled and measured **particulate OC concentration**, disaggregated by region and season.

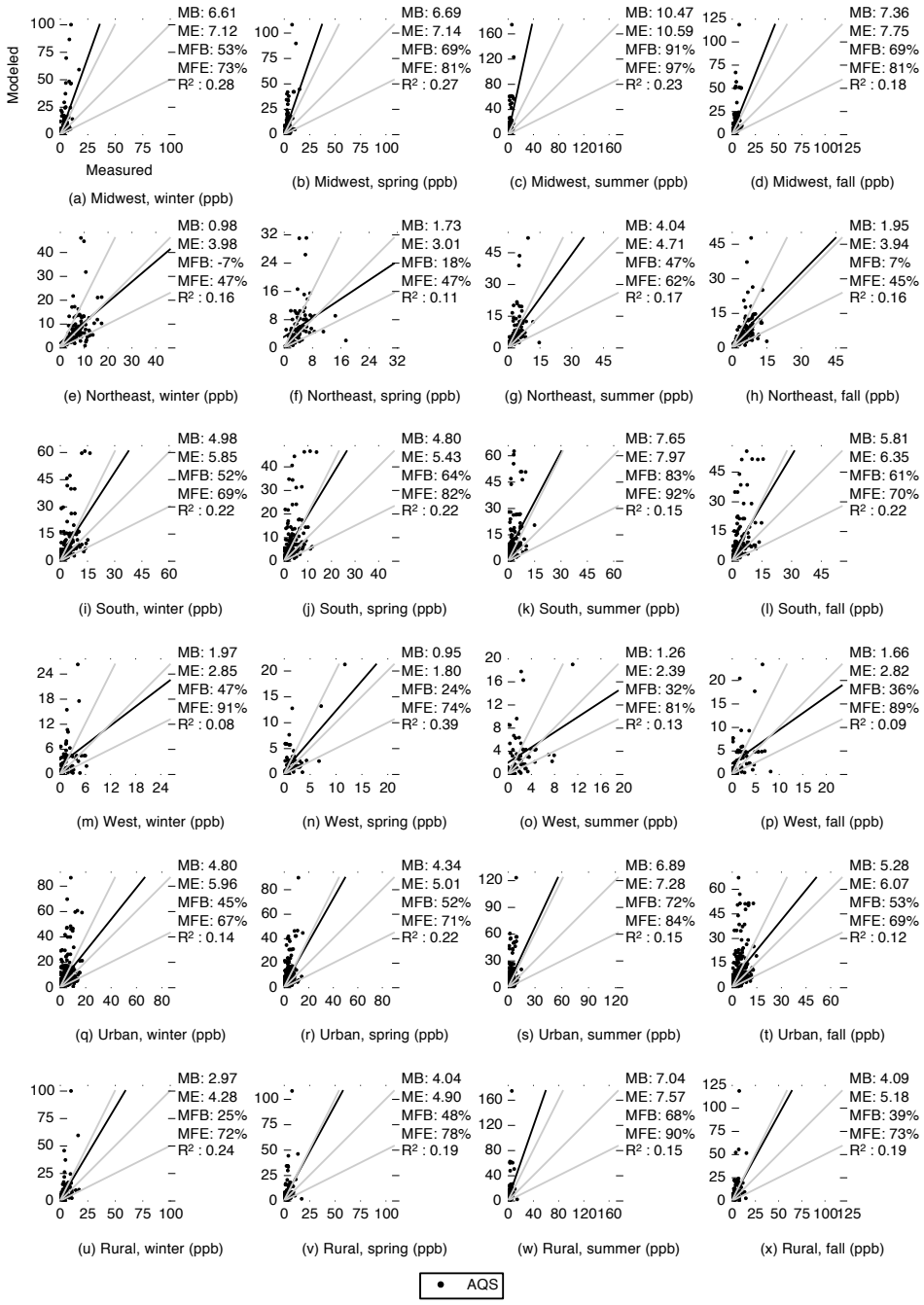

Figure 3.19: Comparison of modeled and measured SO_2 **concentration**, disaggregated by region and season.

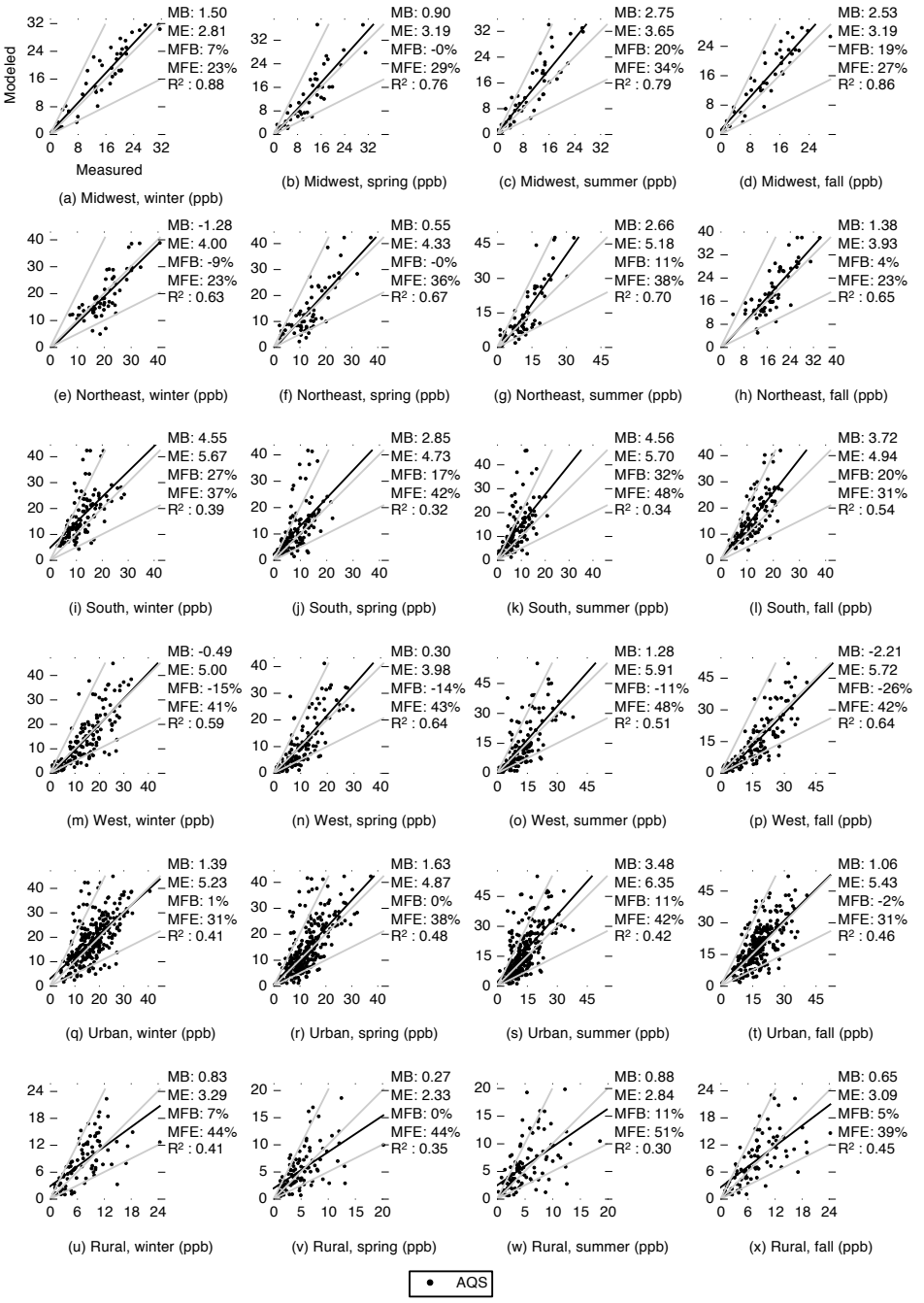

Figure 3.20: Comparison of modeled and measured **NO_2 concentration**, disaggregated by region and season.

Chapter 4

Life Cycle Air Quality Impacts of Conventional and Alternative Light-Duty Transportation in the United States

4.1 Summary

Commonly considered strategies for reducing the environmental impact of light-duty transportation include using alternative fuels and improving vehicle fuel economy. Here I evaluate the air quality-related human health impacts of ten such options, including the use of liquid biofuels, diesel, compressed natural gas (CNG), electricity from a range of conventional and renewable sources, and hybrid electric vehicle technology. My approach combines spatially-, temporally-, and chemically-detailed life cycle emission inventories; comprehensive, fine-scale state-of-the-science chemical transport modeling; and exposure, concentration-response, and economic health-impact modeling for ozone (O_3) and fine particulate matter ($PM_{2.5}$). I find that powering vehicles with corn ethanol or with coal-based or "grid average" electricity increases

monetized environmental health impacts by 80% or more relative to using conventional gasoline. Conversely, electric vehicles (EVs) powered by low-emitting electricity from natural gas, wind, water, or solar-power reduce impacts by 50% or more. Consideration of potential climate change impacts alongside the human health outcomes described here further reinforces the environmental preferability of low-emitting electric vehicles relative to gasoline vehicles.

4.2 Introduction

Society is in the midst of a great effort to understand and mitigate anthropogenic greenhouse gas (GHG) emissions and their effects on the global climate (e.g., (*8*, *11–13*, *134*)). However, GHG damages are not the only environmental impact of human activities, and are often not even the largest. In transportation, for example, non-GHG air pollution damage externalities generally exceed those from climate change (*7*, *16*, *17*). In this chapter, I use the tools described in Chapters 2 and 3 to explore the air quality impacts of the proposed transportation fuel interventions I outline in the abstract: liquid biofuels (*135*), electric vehicles powered by conventional and alternative energy sources (*12*), biomass feedstocks to power electric vehicles (*136*, *137*), the use of compressed natural gas (CNG) powered vehicles (*134*), and improved vehicle fuel-economy.

The air quality impacts of biofuels, transportation electrification, CNG vehicles, and improved fuel economy have been studied (*16–27*); results are summarized in Table 4.1. The work described in this chapter advances prior research by including combined estimates of life cycle emissions (i.e., emissions from production [“upstream”] and consumption [“tailpipe”] of the fuel) with an advanced air quality impact assessment. In addition, I incorporate greater spatial, temporal, and chemical detail than have prior research efforts. I also report non-GHG air quality life cycle impacts of biomass-powered electric vehicles, which to my knowledge have not yet been described.

Table 4.1: Results of Previous Studies of Air Quality Impacts from Alternative Transportation Fuels and Technologies

Article	Result	Notes	Peer reviewed journal?
Alhajeri et al., 2011 (*26*)	17% plug-in hybrid electric vehicle (PHEV) adoption leads to greater decreases in O_3 than 100% biofuel (E85) adoption.	Use detailed photochemical model, but only consider vehicle tailpipe and EGU emissions, and only estimate impacts in Austin, TX.	Yes
Boureima et al., 2009 (*20*)	Battery electric vehicles greatly decrease air quality impacts compared to gasoline or hybrid vehicles.	Full life cycle analysis including battery production, but does not include any spatial information and uses generalized emissions impact functions. Electric generation mix is Belgium average.	Yes
Brinkman et al., 2010 (*24*)	PHEVs decrease O_3 concentrations compared to gasoline vehicles.	Use detailed photochemical model, but only consider vehicle tailpipe and EGU emissions, and only estimate impacts in Denver, CO.	Yes
Cook et al., 2011 (*23*)	Increased ethanol use in the U.S. will increase O_3 concentrations in most areas, but decrease concentrations in some highly-populated areas with poor air quality	Full life cycle analysis with spatially explicit emissions, but the degree of spatial disaggregation is not clear. Impacts on $PM_{2.5}$ concentrations are not reported. Air quality model uses two separate 12km resolution domains, each covering half of the U. S.	Yes

Continued on next page

Article	Result	Notes	Peer reviewed journal?
EPA, 2010 (*14*)	Standard mandating biofuel (both corn grain-based and cellulosic) production and consumption will cause 35-85 cases of adult $PM_{2.5}$ mortality and 36-160 cases of adult O_3 mortality compared to business as usual.	Use detailed air quality model for contiguous U.S. with full life cycle inventory, spatial data is included in the life cycle inventory. Impacts of corn grain and cellulosic ethanol are not reported separately.	No
EPRI, 2007 (*18*)	PHEV adoption decreases O_3 and $PM_{2.5}$ levels compared to business-as-usual in almost all urban areas.	Use detailed photochemical model for contiguous U.S., but only consider tailpipe, EGU, and petroleum supply chain emissions. Assume no marginal SOx or NOx emissions from EGUs. Air quality model uses 36km spatial resolution.	No
Hill et al., 2009 (*16*)	$PM_{2.5}$ impacts from corn ethanol are ∼60% greater than from gasoline, impacts from cellulosic ethanol are slightly better than from gasoline, $PM_{2.5}$ impacts are larger than GHG impacts.	Full life cycle analysis at county-level spatial resolution for contiguous U.S., with reduced-form air quality model	Yes

Continued on next page

Article	Result	Notes	Peer reviewed journal?
Jacobson, 2007 (*19*)	Ethanol vehicles cause increased O_3-related mortalities compared to business-as-usual.	Use detailed photochemical model for contiguous U.S., but only consider tailpipe emissions. Air quality model uses 0.5 by 0.75 degree (approximately 50km by 75km) spatial resolution.	Yes
Michalek et al., 2011 (*17*)	Using "base case" assumptions, electric vehicles do not improve $PM_{2.5}$ and O_3 air quality impacts compared to gasoline, owing largely to emissions from battery production.	Use reduced-form air quality model with full life cycle emissions inventory. Emissions inventory and air quality model have county-level spatial resolution.	Yes
NRC, 2009 (*21*)	For year-2030, corn ethanol causes similar air quality impacts to gasoline; cellulosic ethanol, diesel vehicles, and compressed natural gas vehicles cause decreased impacts; electric vehicles cause increased impacts.	Use reduced-form air quality model with full life cycle emissions inventory. Emissions inventory and air quality model have county-level spatial resolution.	No

Continued on next page

Article	Result	Notes	Peer reviewed journal?
Thompson et al., 2009 (*22*)	PHEVs decrease O_3 concentrations compared to gasoline vehicles.	Use detailed photochemical model, but only consider vehicle tailpipe and EGU emissions, and only estimate impacts in Pennsylvania, New Jersey, and Maryland.	Yes
Thompson et al., 2011 (*27*)	PHEVs decrease O_3 concentrations compared to gasoline vehicles	Use detailed photochemical model, but only consider vehicle tailpipe and EGU emissions, and only estimate impacts in Texas.	Yes

I use the spatially and temporally explicit life cycle inventory model described in Chapter 2 to estimate total fuel supply chain air pollutant emissions for scenarios where 10% of U.S. projected vehicle miles traveled in year-2020 are driven in one of eleven types of passenger cars: 1) conventional gasoline powered vehicles (abbreviation: "gasoline"); 2) grid-independent hybrid electric vehicles ("gasoline hybrid"); 3) diesel powered cars ("diesel"); 4) internal-combustion compressed natural gas vehicles ("CNG"); 5) vehicles powered by ethanol from corn grain through natural-gas powered dry milling ("corn ethanol"); 6) vehicles powered by cellulosic ethanol from corn stover ("stover ethanol"); and battery electric vehicles ("EV") powered by electricity from: 7) the projected year-2020 U.S. average electric generation mix ("EV grid average"); 8) coal ("EV coal"); 9) natural gas ("EV natural gas"); 10) the combustion of corn stover ("EV corn stover"); and 11) wind turbines, dynamic water power, or solar power ("EV WWS"). Because year-2020 electric generation infrastructure is not predetermined, I explore a range of electricity technologies rather than attempting to predict future electrical generation and dispatch deterministically; my approach can inform transportation and electricity-generation policies in tandem. Based on prior research, I assume that the difference among scenarios in emissions from manufacturing and disposal of vehicles and from upstream infrastructure is small relative to differences in vehicle operation emissions (*138*, *139*) with the exception of lithium-ion EV battery production. To highlight battery-related impacts, I analyze them separately from fuel-related impacts.

4.3 Materials and methods

I estimate the changes attributable to each scenario in annual average concentrations of the regulated pollutants fine particulate matter ($PM_{2.5}$) and ground-level ozone (O_3) from spatially- and temporally-explicit simulations using the state-of-the-science mechanistic meteorology and chemical transport model described in Chapter 3. I use spatially explicit population data (*140*), and the results of major epidemiological studies (*5*, *6*) to estimate increases in mortalities attributable to each scenario. I convert mortalities to monetary externalities using a Value of

Statistical Life (VSL) metric.

4.3.1 Scenario selection

I use a functional unit of 10% of year-2020 projected U.S. vehicle miles traveled (VMT), or 388 billion miles per year (*141*). VMT is projected to increase by 25% between 2010 and 2020, so 10% percent of year-2020 VMT is equivalent to approximately 50% of the increase in VMT between year-2010 and year-2020. For the ethanol scenarios, this value corresponds to blending an average of 10% ethanol with gasoline (on an energy equivalent basis). For EV scenarios, it corresponds to an aggressive but plausible adoption of electric vehicles, according to a report prepared for the U.S. Department of Energy by P. Balducci (*142*), which estimated between 10 and 27% market penetration for plug-in electric vehicles (PHEVs) by year-2023.

I do not consider constraints on the availability or cost of resources (e.g., the viability of increased ethanol production; availability of wind, water, or solar electricity). However, as shown in Chapter 6, where a model that assumes a linear relationship between changes in emissions and changes in concentration agrees well with WRF-Chem results, I have found that the modeled air quality impacts I consider scale approximately linearly with changes in the size of the functional unit, so as a first approximation air quality impacts from different amounts of miles traveled or fuel produced could be interpolated from my results.

4.3.2 Life cycle inventory

I create a chemically, spatially, and temporally detailed life cycle inventory for each scenario using the GREET-cst (GREET-chemical, spatial, and temporal) model described in Chapter 2, which is based on the Greenhouse Gases, Regulated Emissions, and Energy Use in Transportation (GREET) model version 1.8d1 from Argonne National Laboratory (*61*). It is worth noting that subsequent versions of GREET have been released since version 1.8d1. I investigate the sensitivity of my results to some of the changes in subsequent GREET versions, as well as to other important factors; investigating the effect of GREET version on the estimated air quality impacts is an area for future research. GREET-cst outputs emissions that are spatially allocated

to a 12 km grid covering the Continental U.S. and surrounding waters, chemically speciated according to the CB05 chemical mechanism (*143*), and temporally disaggregated in one-hour time increments. The GREET model can be obtained at `https://greet.es.anl.gov/`.

For assumptions specific to GREET-cst, including spatial modeling domain, spatial locations of emissions, chemical speciation, and temporal profiles, I configure the model as described in Chapter 2. Briefly, I use the continental U.S. and its surrounding waters as a spatial model domain and exclude from the analysis all emissions occurring outside of the domain. I assume all emissions from individual processes, including vehicle end-use, occur at existing production or activity locations. For material transport emissions, I use network analysis and linear optimization to simulate transport behavior along roadways, rails, and navigable water routes between source and destination locations. I apply temporal and chemical speciation profiles from the 2005 National Emissions Inventory (NEI, (*30*)) to the emissions from each process. I use the results of Bashash et al. (*144*) for electric vehicle battery charging temporal profiles, which assume batteries would be charged to optimize for long battery life and low electricity costs. I use these charging profiles only to determine the timing for emissions release from power plants; for the mix of electrical generation sources I use the hypothetical scenarios discussed in Section 4.2.

For most processes that use electricity, such as electricity generation for use in EVs in the EV coal and EV natural gas scenarios, I assume that electricity generation comes from the same North American Electrical Reliability Corporation (NERC) electrical grid region as the end-use process as in Chapter 2 and that the mix of generation fuels and technologies in each NERC region is the same as the national average. This assumption is a potential limitation of this study. For instance, the GREET 1.8d1 default year-2020 projection for U.S. average electricity is 48% coal, but the GREET year-2020 projection for electricity generation in California is 10%. For electricity generation in the EV corn stover scenario, however, because of the logistical difficulty in transporting corn stover, I assume that electricity generation for EVs occurs in the same electrical grid region as the corn stover production instead of vehicle end-use. For the EV grid average scenario, I assume that electricity generation for EV use is distributed according

to total generation amounts in the year 2007 (*88*) so as to preserve current differences for fuel mixes in electric generation across NERC regions. Further details are in Chapter 2.

In GREET, I model year-2020 passenger cars using default settings with the following exceptions:

- The gasoline used is 100% conventional (0% reformulated gasoline) so as to disentangle the effect of ethanol blends.
- Because almost all oil extraction from oil sands occurs outside of my geographic modeling domain, I assume all oil is extracted conventionally (0% oil sands oil). The sensitivity of my results to this assumption is explored in 4.4.1.
- For gasoline hybrid vehicles, GREET assumes that the tailpipe emission factors for VOCs, CO, PM_{10}, $PM_{2.5}$, and N_2O are the same as for conventional gasoline vehicles on a per mile basis. I therefore adjust gasoline hybrid tailpipe emissions to be 71% (the ratio of hybrid to conventional fuel efficiency) of the conventional vehicle emissions factors.
- I do not include land-use change emissions for the ethanol or bioelectricity scenarios.
- I assume all corn ethanol plants use dry milling and 100% natural gas for process heat.
- I assume that ethanol is produced as 100% ethanol with no denaturant, but I use tailpipe emissions factors for a 10% blend of ethanol with gasoline (E10).
- I update the GREET default year-2020 projection for electricity generation mix to a more recent Energy Information Administration (EIA) projection (*145*).
- I add a corn stover bioelectricity pathway to the GREET 1.8d1 spreadsheet based on parameters from the other bioelectricity pathways and the corn stover ethanol pathway.

I do not assume that marginal emissions from electrical generation or other sources are subject to cap-and-trade or other regulation (e.g., as in (*18, 146*)). I use the GREET default assumption that electricity from biomass (corn stover) is generated using a dedicated biomass boiler. Co-firing biomass with coal may yield different emissions.

I assume that impacts related to the manufacture and disposal of equipment used to supply fuel (e.g., electrical generating units, oil wells, manufacturing plants), as well as those from the manufacture and disposal of vehicles, do not differ among the scenarios investigated here (*17*, *139*), and therefore I exclude them from this analysis. Although these emissions do not differ much among scenarios, their impact on the overall air-quality-related damages from transportation is likely substantial (8, 23) and is an area for future research. I do include, however, production of EV batteries, which I model as a separate scenario to show explicitly the contribution of EV battery manufacturing to total impacts. I model the emissions from the production of enough lithium-ion batteries to power my functional unit of 10% of the projected year-2020 U.S. vehicle miles traveled by expanding GREET-cst to include the GREET2 vehicle cycle model, version 2012 (22). I do this step using the methods in Chapter 2 and including additional spatial data on the locations of aluminum manufacturing (*147*), copper manufacturing (*148*), plastics manufacturing (*30*), steel manufacturing (*30*), and battery assembly (*30*). Table 4.2 shows, for each process, the fractions of emissions from battery production processes that are excluded from the analysis because they occur outside my spatial modeling domain. Information on international fractions for other processes is in Chapter 2. Figure 4.5 shows amounts of domestic (included) and international (excluded) emissions from battery production. Full GREET-cst results for battery production are included in Appendix D. I use the GREET2 default EV battery life assumption of 160,000 miles.

Emissions of greenhouse gases and radiatively active aerosols are calculated using the same assumptions as above (i.e., the exclusion of indirect, market-mediated effects and the exclusion of emissions occurring outside the United States), and reported as CO_2 equivalent emissions using global warming potential (GWP) conversions reported by Bond et al. (*150*). I use GREET default values for all emissions factors and process relationships not otherwise mentioned here.

Table 4.2: Fractions of Processes Related to Battery Production which Occur Outside of the Spatial Modeling Domain[a,b,c]

Process	Percent excluded	Data source
Steel Production	9%	(*149*)
$LiMn_2O_4$	100%	(*138*)
Graphite Production	100%	(*149*)
Copper Production	35%	(*149*)
Aluminum Production	13%	(*149*)
$LiPF_6$	100%	(*138*)

[a]The spatial modeling domain includes the continental U.S. and surrounding waters
[b]Processes not included in this table are assumed occur 100% inside the spatial modeling domain.
[c]Refer to the additional supplemental information for total emissions for each of these processes after the excluded fractions have been removed.

4.3.3 Chemical transport modeling

To estimate changes in $PM_{2.5}$ and O_3 concentrations attributable to each scenario, I run the WRF-Chem (Weather Research and Forecasting with Chemistry) Eulerian meteorology and chemical transport model version 3.4 (*110*) using a 12-km resolution grid with 444 rows, 336 columns, and 28 vertical layers. The modeling domain (5,328km × 4,032km) covers the continental U.S., southern Canada, and northern Mexico as described in Chapter 3.

Setup of WRF-Chem as used here is detailed in Chapter 3. I use the Regional Atmospheric Chemistry Mechanism (RACM) (*119*) for gas-phase reactions, and the Modal Aerosol Dynamics for Europe (MADE) (*120*) module for aerosol chemistry and physics. I use the Volatility Basis Set (VBS) (*111*) to simulate formation and evaporation of secondary organic aerosols.

I compare the change in emissions attributable to each scenario to a baseline or reference case. For the baseline emissions I use the 2005 National Emissions Inventory (NEI) (*30*), which includes area, point, and mobile emissions from year-2005 for the U.S., year-2006 for Canada, and year-1999 for Mexico. The performance of WRF-Chem as used here in reproducing observed $PM_{2.5}$ and O_3 concentrations is described in detail in Chapter 3; the annual mean fractional bias (MFB) and error (MFE), respectively, are 1% and 21% for $PM_{2.5}$, and 11% and

14% for daily peak O_3.

I use year-2005 baseline emissions and meteorology inputs. The NEI has been projected to future years, but I am only able to compare my model predictions to observed pollutant levels for years for which there is an available emissions inventory, pollution monitoring data, and meteorological observations. At the time the simulations described here were run, 2005 was the only year for which an emissions inventory was readily available.

To predict changes in pollutant concentrations attributable to each scenario, I combine the emissions from each scenario with the baseline NEI, re-run WRF-Chem with the resulting emissions, and then subtract the baseline NEI-derived concentrations from the concentrations calculated using the combined emissions. Because some scenarios involve credits for displaced coproducts which I model as negative emissions, and because negative emissions cannot be represented in WRF-Chem, I deal with any grid cell with net negative emissions (where the baseline NEI value plus the scenario value is negative) by subtracting emissions from nearby cells, thereby zeroing out the negative cells while achieving the targeted local total mass of emissions.

4.3.4 Health impact assessment

I use as health endpoints respiratory mortalities attributable to ambient O_3 concentrations and mortalities from all causes attributable to ambient $PM_{2.5}$ concentrations. I use concentration-response (C-R) values as reported by Jerrett et al. for O_3 (*6*) and Krewski et al. for $PM_{2.5}$ (*5*). Jerrett et al. reported that, after accounting for covariation with $PM_{2.5}$ concentrations, a 10 ppb increase in April-September average daily peak-hour O_3 concentration causes a 4% increase in respiratory mortalities. Krewski et al. reported that a 10 μg m^{-3} increase in annual average $PM_{2.5}$ concentration causes a 7.8% increase in all-cause mortalities; the Krewski et al. model does not account for covariance with O_3 concentrations. Both results are based on the Cox proportional hazards model, which assumes that the risk ratio (*RR*) varies exponentially with change in pollutant concentration (C) as in Equation 4.1, where the β coefficients for O_3 (0.00392 ppb^{-1}) and $PM_{2.5}$ (0.00751 (μg $m^{-3})^{-1}$) are calculated from the results of Jerrett

et al. and Krewski et al., respectively. WRF-Chem is configured to output instantaneous concentrations at the beginning of each hour, rather than hourly average concentrations; when calculating C for each scenario I use the instantaneous concentrations output by WRF-Chem as a surrogate for hourly average concentrations. I use equation 4.2 to calculate total annual mortalities (D) attributable to each scenario where n is the total number of ground-level grid cells, P is the population in each cell based on year-2000 U.S. Census block group-level data (*140*), and M is the county-specific population average baseline all-cause (for $PM_{2.5}$) or respiratory (for O_3) mortality rate (*151*).

$$RR = \exp\left(\beta \Delta C\right) \tag{4.1}$$

$$D = \sum_{i=1}^{n} \left(\exp\left[\beta \Delta C\right] - 1\right) P_i M_i \tag{4.2}$$

4.3.5 Economic valuation

I estimate economic damages from the deaths attributable to air pollution impacts of each scenario using a value of statistical life (VSL) of $10.1 million (2012$) using U.S. EPA methodology for income year-2020 (*152*). I assume no lag-time between pollutant emissions and the resulting health effects. I estimate the economic damages from emissions of GHGs and radiatively-active aerosols using a social cost of carbon of $180 MgC^{-1} ($49 $MgCO_2{}^{-1}$) (*153*) (mean value, 1% discount rate, adjusted to 2012$) in the main analyses and $23 MgC^{-1} ($6.19 $MgCO_2{}^{-1}$) (2012$) in a sensitivity analysis.

4.4 Results

Figure 4.1 shows the spatial distributions of the background $PM_{2.5}$ concentrations (Figure 4.1A) and of the changes in $PM_{2.5}$ concentrations for each scenario (Figure 4.1B–L). (Spatial distributions of concentrations of O_3 are in Figure 4.2 and spatial distributions of emissions and of concentrations of other species are in Appendix D.) As all scenarios represent increases in

vehicle miles traveled, concentrations increase in almost all cases in Figure 4.1. Changes in concentrations caused by alternative scenarios (Figure 4.1C–L) may be larger or smaller than the changes caused by the business-as-usual gasoline scenario (Figure 4.1B).

For the petroleum scenarios (gasoline, gasoline hybrid, and diesel; Figure 4.1B-D), vehicle tailpipe emissions are the largest source of impacts. Impacts from vehicle tailpipe emissions for the CNG (Figure 4.1E) and ethanol (Figure 4.1F-G) scenarios are similar to those from the petroleum scenarios, but upstream processes, such as natural gas processing and compression (mainly in Texas) for the CNG scenario and agriculture (mainly in the upper Midwest) for the ethanol scenarios cause additional substantial impacts. Industrial electricity use in the corn ethanol and CNG scenarios creates additional impacts in Wyoming and in the Appalachian Mountains owing to emissions from coal mining; emission credits from excess electricity generation in the stover ethanol scenario cause decreases in concentrations in the same geographic areas.

Impacts are lower for the EV natural gas scenario (Figure 4.1J) than for the CNG scenario (Figure 4.1E) for several reasons: emissions per vehicle-km are lower for natural gas combustion in electricity generators than for CNG combustion in vehicles; natural gas must be compressed for use in CNG vehicles but not in electricity generation; and combustion emissions generally occur further from population centers for electricity generation than for vehicle tailpipe emissions.

The EV corn stover scenario (Figure 4.1K) causes farming-related impacts in the Midwest. Coal mining and combustion in the EV coal (Figure 4.1I) and EV grid average (Figure 4.1H) scenarios cause large impacts in Wyoming and the Appalachian Mountains, and long range transport of sulfur dioxide (SO_2) emitted during coal combustion causes impacts distributed over wide areas in those scenarios. Non-battery-production impacts from wind, water, and solar (WWS) EVs (Figure 4.1L) are much lower than from the other scenarios because WWS electrical generators do not produce any emission while in use.

Emissions from battery production for the EV scenarios are tracked separately. The main emission sources for EV battery production (Figure 4.1M) are coal mining in Wyoming and the

Appalachian Mountains and the extraction and refinement of raw material inputs, including copper in Arizona and Utah and aluminum in Washington State and the Appalachian Mountains.

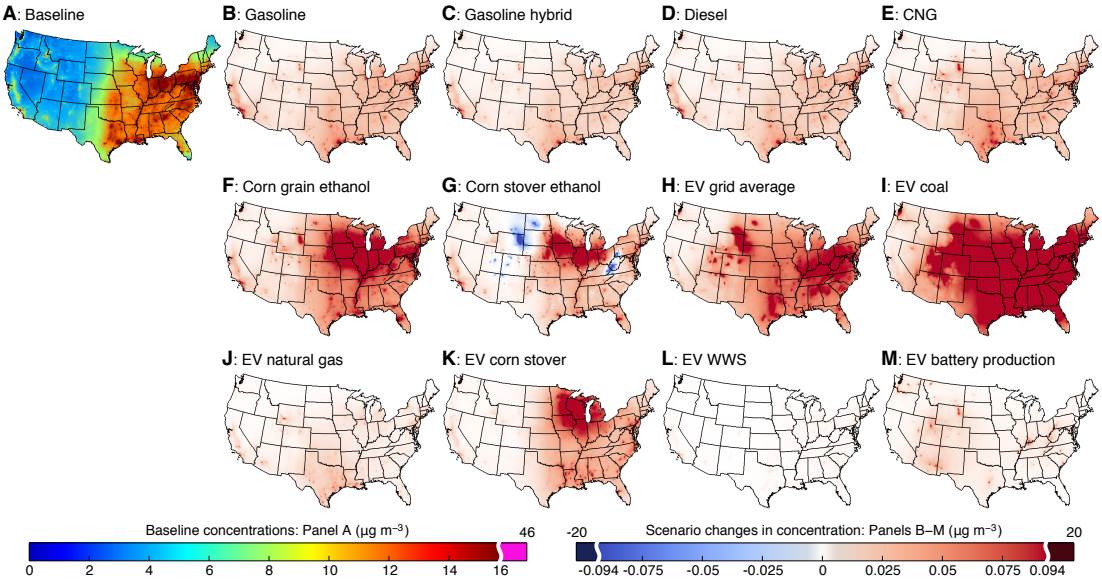

Figure 4.1: Annual average $PM_{2.5}$ concentrations. **A**: Year-2005 baseline modeled concentrations. **B-L**: Increase in concentration above the baseline attributable to replacement of 10% of year-2020 vehicle use with the given technology. **M**: Increase in concentration attributable to EV battery manufacturing. Color scales contain a discontinuity at the 99^{th} percentile of emissions. Abbreviations: EV=electric vehicle; CNG=compressed natural gas vehicle; WWS=wind, water, or solar.

Animated versions of Figure 4.1 showing temporally explicit concentrations for $PM_{2.5}$ and O_3 are available in Appendix D. Notable temporal trends include spikes in $PM_{2.5}$ for the corn ethanol, corn stover ethanol, and EV corn stover scenarios caused by fertilizer application and nitrification emissions during the spring planting season. For these same scenarios, owing to complexities in the chemistry of O_3 formation and removal, O_3 concentrations in the Midwest "corn belt" tend to be increased relative to the baseline in the summer months, but decreased in the winter months.

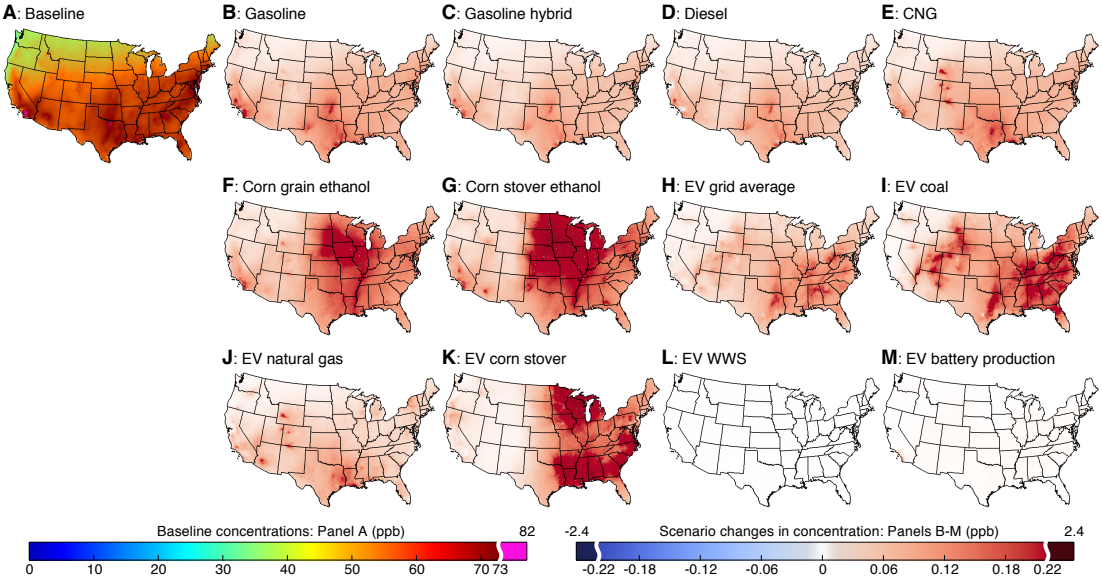

Figure 4.2: Annual average O_3 concentrations. **A**: Year-2005 baseline modeled concentrations. **B-L**: Increase in concentration above the baseline attributable to replacement of 10% of year-2020 vehicle use with the given technology. **M**: Increase in concentration attributable to EV battery manufacturing. Color scales contain a discontinuity at the 99th percentile of emissions. Abbreviations: EV=electric vehicle; CNG=compressed natural gas vehicle; WWS=wind, water, or solar.

Air pollution-related human health impacts for each scenario ($PM_{2.5}$- and O_3-related mortalities, and the corresponding monetized damages) are shown in Figure 4.3. Total impacts range from 230 mortalities per year ($0.14 per gallon gasoline-equivalent) for the WWS EV scenario to 3,200 deaths per year ($1.94 per gallon gasoline-equivalent) for the coal EV scenario. Estimated mortality impacts from $PM_{2.5}$ are approximately an order of magnitude greater than those from O_3. Damages from the production of EV batteries are shown separately in Figure 4.3. Scenarios with substantially decreased air quality-related health impacts compared to gasoline include gasoline hybrid vehicles (30% decrease) and EVs powered by natural gas or by WWS (50% and 70% decrease, respectively); scenarios with substantially higher damages than gaoline include corn ethanol (80% increase) and EVs powered by grid average or coal electricity (200% and 350% increase, respectively).

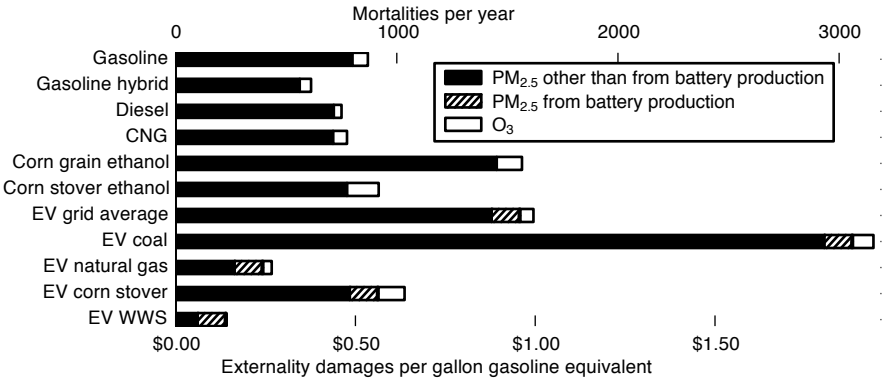

Figure 4.3: Air quality health impacts in the U.S. for each scenario: attributable increases in annual mortality (upper scale) and the resulting monetized health impacts (lower scale).

Changes in combined air pollution and climate damages attributable to each alternative scenario, relative to gasoline, are shown in Figure 4.4. For most scenarios, air pollution impacts are comparable to or larger than climate change impacts. Although corn ethanol as modeled here emits marginally less GHGs than does gasoline, the combined climate and air quality impacts are greater than those from gasoline vehicles. (My corn ethanol GHG results exclude impacts of indirect land-use change, and so likely are lower-bound GHG emission estimates.) Electric vehicles powered by grid-average electricity also have greater impacts than those powered by gasoline. Previous studies (*12*, *134*) have argued that to meet stated goals for GHG emission reductions, it is necessary to both electrify vehicles and decarbonize electricity generation, for example through wind, water, and solar electric generation. My results suggest that such a strategy would have the strong co-benefit of substantially reducing air quality-related mortalities (by $\sim$70%).

4.4.1 Sensitivity analyses

Given the considerable computational demands of my mechanistic meteorology and chemical transport modeling, full quantification of all uncertainty within my analysis is impractical. Rather, I explore uncertainty via sensitivity analyses for several factors that are important

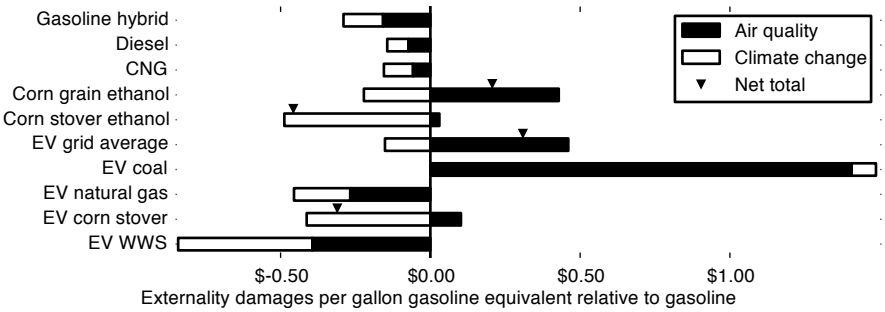

Figure 4.4: Combined air quality plus climate change externalities attributable to each scenario relative to the gasoline scenario. (The gasoline scenario impacts [Air quality=$0.53/gallon; Climate change=$0.46/gallon] would equal zero on this plot.) EV scenarios include battery production. Air quality impacts include $PM_{2.5}$ and O_3. For bars with both positive and negative values, the triangle above each bar shows the net total impact. See Figure 4.8 for the effect of land use change on corn grain ethanol impacts.

in my analyses and that could impact the relative rankings of scenarios. The results of the sensitivity analyses are shown in Figures 4.7–4.9 and described below.

Figure 4.5 shows average percent differences in number of $PM_{2.5}$-related deaths among all scenarios when only considering air quality modeling results from one month as compared to all 12 months. Results from the month of September are close to the annual average results: differences between September-average and annual-average range between -6% and +8% among the different scenarios, with an average absolute bias of 6%. Therefore, for computational expediency, all air quality-related sensitivity analyses are performed for $PM_{2.5}$-related health impacts for the month of September only. The one exception is the grid resolution sensitivity analysis (shown in Figure 4.9) which was performed for the month of July to capture summer peak O_3 conditions.

International emissions

As shown in Figure 4.6, not all emissions from the fuel life cycles occur within my spatial modeling domain, and therefore some emissions are excluded from my analysis. Refer to Chapter

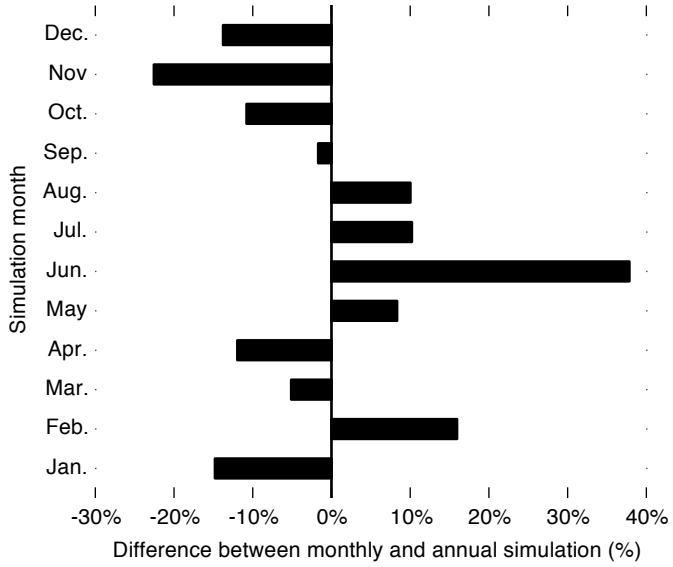

Figure 4.5: Average percent differences in number of deaths among all scenarios when only considering air quality modeling results from one month as compared to all 12 months.

2 for more information. The EV battery production scenario has the most substantial fraction of emissions assumed to occur outside of the U.S., with around 30–40% of emissions of most pollutants from battery production being excluded from the analysis (Figure 4.6). I explore the sensitivity of my results to this assumption by doubling health impacts from battery production (Figure 4.7). I find that this increases damage costs for EVs by $0.08 per gasoline gallon-equivalent, which is between a 4% increase for the coal EV scenario and a 57% increase for the WWS EV scenario, but does not change the rank order of air quality impacts among scenarios.

For scenarios other than battery production, in most cases more than 90% of emissions occur inside the spatial modeling domain (Figure 4.6). A fraction (30–45%) of SO_x and NO_x emissions from the petroleum scenarios (gasoline, gasoline hybrid, and diesel) are also excluded from the analysis but because the excluded emissions are mainly from the extraction of crude oil (as shown in Chapter 2) which largely occurs over the open ocean or far from

population centers, their exclusion is not likely to impact my overall conclusions. These international upstream emissions are also excluded from fossil fuel use in the corn grain and stover ethanol scenarios.

	CH_4	CO	CO_2	N_2O	NH_3	NO_x	PM_{10}	$PM_{2.5}$	SO_x	VOC
Gasoline	96%	100%	97%	99%	100%	68%	86%	81%	55%	99%
Gasoline hybrid	96%	100%	97%	99%	100%	69%	87%	82%	55%	99%
Diesel	96%	98%	98%	99%	100%	71%	87%	83%	54%	97%
CNG	99%	100%	97%	99%	100%	89%	88%	92%	89%	99%
Corn grain ethanol	97%	100%	94%	96%	99%	93%	96%	94%	71%	97%
Corn stover ethanol	123%	100%	115%	95%	98%	97%	86%	91%	190%	97%
EV grid average	100%	98%	100%	100%	100%	98%	100%	100%	100%	99%
EV coal	100%	100%	100%	100%	100%	100%	100%	100%	100%	100%
EV natural gas	99%	96%	99%	99%	80%	93%	98%	98%	98%	98%
EV corn stover	86%	99%	76%	97%	97%	98%	97%	97%	90%	87%
EV WWS	X	X	X	X	X	X	100%	100%	X	X
EV battery production	53%	59%	64%	70%	80%	52%	75%	68%	63%	43%

Figure 4.6: Fractions of emissions from each scenario that occur within the spatial modeling domain. Boxes marked with "X" indicate that total emissions are zero. Emissions outside of spatial modeling domain are not included in the above analyses.

Coal mining emissions

As emissions from coal mining and cleaning cause a substantial fraction of the total health impacts for some scenarios, and recent estimates of emissions factors for coal mining and cleaning for surface mining (*154*) and for underground mining (*155*) exist, I explore updating the GREET model with the new emission factors and re-running all analyses for the month of September. I find that the change in coal mining and cleaning emissions factors does not affect the rank order of scenario impacts (Figure 4.7), although it decreases overall impacts from EVs

powered by coal or grid average electricity by 37% and 33%, respectively.

Life cycle emissions importance

To test the importance of incorporating full life cycle supply chain information when performing air quality impact assessment, I perform a sensitivity analysis that considers only emissions from the single phase of each life cycle most frequently associated with its environmental impacts (for internal combustion vehicles: on-road emissions; for EVs: emissions from electricity generation). This change causes corn ethanol to appear substantially less damaging because emissions during production and transport are overlooked (Figure 4.7).

Climate assumptions

I also investigate the sensitivity of my results to a range of assumptions related to climate change (Figure 4.8). I investigate the use of a lower carbon price, the inclusion of international emissions of climate forcers, the inclusion of indirect land use change, the recently reported possibility of additional gas leakage during natural gas extraction, and sourcing crude oil from oil sands rather than from conventional sources. Details are below; the conclusions of this study are generally robust to these perturbations.

1. Figure 4.4 excludes emissions occurring outside the U.S. for pollutants affecting both air quality and climate change. I investigate the effects of including these international emissions (exclusive of indirect land-use change) on climate change impacts. I find that including international climate-related emissions does not change overall damage costs by more than $0.02 per gallon gasoline equivalent for any scenario.

2. I investigate the impact of including indirect land use change (iLUC) emissions as calculated by Plevin et al. (*156*) (using a value of 80 g CO_2e MJ^{-1}, which is near the middle of the range of estimates in that paper) for the corn ethanol scenario. This substantially increases the overall externality damages from that scenario and reinforces the overall conclusion that corn ethanol is not an attractive alternative fuel in terms of air pollution

or climate change impacts.

3. I investigate the sensitivity of my results to carbon pricing using market-based carbon price of \$6.19 Mg^{-1} CO_2 (from `http://www.pointcarbon.com/productsandservices/carbon/` as of 9 March 2013, adjusted to 2012\$) as opposed to the \$33 Mg^{-1} CO_2e price used in Figure 4.4. I find that this changes the sign of the net externality damages of the EV corn stover scenario from negative to positive, but does not impact the overall conclusions presented in this paper. The value of a statistical life metric that I use for valuing air quality-related health damages is also uncertain: a review by Viscusi and Aldi (*157*) estimated for U.S. workers it is between 4.0 and 25.5 million 2012\$. Here I use the value adopted by the U.S. EPA (10.1 million 2012\$). Using a lower or higher value would affect the air quality-health related damages calculated here proportionally.

4. Recent analysis by Brandt et al. (*158*) suggests that CH_4 emissions may be systematically underestimated in emissions inventories, especially for natural gas extraction. I update the GREET model with the middle value for CH_4 leakage during natural gas extraction from Brandt et al. (*158*), resulting in 1.2% leakage on average instead of the GREET 1.8d1 default of 0.35%. Figure 4.4 shows that the climate impacts of these leakage emissions find does not affect the overall conclusions presented here. (I assume that air-quality-related health impacts [through changes in O_3 concentration] caused by methane emissions are insignificant relative to climate impacts of the same emissions.) Although increased CH_4 emissions may also impact O_3 concentrations, I assume the effect on my overall conclusions to be negligible because O_3 health impacts are small relative to $PM_{2.5}$ health impacts.

5. Because almost all oil extraction from oil sands occurs outside of my geographic modeling domain (*159*), my baseline analysis assumes all oil is extracted conventionally (0% oil sands oil). This sensitivity analysis estimates the climate impacts of using the GREET 1.8d1 year-2020 default value of 21% of crude oil comes from oil sands. I find that this does not affect the overall conclusions presented here. The use of oil sands oil instead

of conventionally extracted crude may also affect air pollution concentrations, but the difference in health impacts is likely small because both the Canadian oil sands and conventional extraction locations are typically located far from population centers.

Air quality model grid resolution

Finally, I investigate the impact of model spatial resolution on estimated health impacts (Figure 4.9). Owing to the computational intensity required for higher resolution simulations, I only analyze two scenarios during the month of July at higher than 12-km resolution. In these simulations, higher resolution analyses tend to produce larger estimates for health impacts. For $PM_{2.5}$, total estimated impacts increase $\sim$10–15% when going from 36 km to 12 km resolution, and another 5% when going from 12-km to 4-km resolution. (O_3 impacts are not highly dependent of grid resolution owing to the comparatively smaller spatial gradients in O_3 concentrations.) My contiguous U.S., 12-km resolution analysis is an improvement over previous studies which used 36-km or county-level resolution or considered only part of the U.S. (see Table 4.1); still, my approach is potentially susceptible to underestimation of near-source exposures. This dependence of impacts on model spatial resolution is likely caused by numerical dispersion and is likely most pronounced in scenarios where the most emissions occur in urban areas (i.e., the gasoline, diesel, and gasoline hybrid scenarios). It currently is not computationally practical to perform the full methodology reported here at 4-km or finer resolution; current models capable of higher resolution analyses (e.g., Gaussian plume models) do so at the expense of the chemical and physical representation of processes that my findings suggest are important (e.g., formation of secondary $PM_{2.5}$). Chapter 6 presents a new reduced complexity air quality model that overcomes some of these limitations.

4.4.2 Comparison to Michalek et al. (2011)

An analysis by Michalek et al. (*17*) finds that in terms of air quality-related health impacts, electric vehicles do not compare favorably to conventional gasoline vehicles: when only emissions from battery production and from brake and tire wear during vehicle use are considered (which is equivalent to the WWS EV scenario presented here), they find that the EVs cause air quality-related damages 150% greater than do conventional gasoline vehicles. (Michalek et al. Table S25, adjusted to make equivalent for comparison by excluding: 1. vehicle and battery production for gasoline vehicles; 2. vehicle and electricity production for EVs; and 3. GHG, CO, and oil premium impacts for both vehicles.) My analysis, however, finds that WWS EVs *reduce* impacts by 70% compared to conventional gasoline vehicles. In both studies, the main source of WWS EV impacts is battery production. I am aware of two major reasons for the difference between my and Michalek et al.'s results: 1) differences in the estimates of amounts of emissions, and 2) differences in the modeled locations of battery manufacturing processes.

1. Michalek et al. use a customized version of GREET 2.7 to calculate emissions from battery production, whereas I use the default settings in the more recently released GREET2_2012. (Note: GREET 2 is not an updated version of GREET 1. GREET 1.x models fuel pathways, and GREET 2.x models vehicle production pathways.) Comparing my emissions results (available in Appendix D) to those of Michalek et al. (Table S3 in their study), my emissions estimates are substantially lower than theirs—87% lower for SO_2 emissions (80% lower if international emissions are included). The battery size used in both studies is similar (66.1 kWh in Michalek et al., 63 kWh in my study). The differences in emissions instead appear to be caused by differences between GREET versions—among other differences, GREET2_2012 uses $LiMn_2O_4$ batteries in place of the $LiCoO_2$ batteries used in GREET 2.7 (*160*)—and my use of year-2020 grid-average electric generation mix for electricity used in battery production, which is cleaner than the year-2010 mix used by Michalek et al.

2. Michalek et al. assume processes upstream from EV battery manufacturing are colocated

with automobile manufacturing facilities, whereas my more detailed analysis shows that, for example, copper ore smelting, which causes the majority of battery production SO_2 emissions, mainly occurs in the sparsely populated southwestern U.S. (*148*). Because the production of copper and other raw materials for batteries occurs far from people, even if impacts from battery production as calculated here are doubled (e.g., to adjust for emissions that occur outside of my spatial modelling domain), impacts from WWS EVs would still be 57% lower than conventional gasoline vehicle impacts. I test this hypothesis by using the ratio of population-weighted average ground level concentrations to area-weighted average ground level concentrations as an (imperfect) surrogate for the proximity of emissions sources to people. The ratio for my results for EV battery production is 1.9, lower than any of the other scenarios. The ratios for the other scenarios range between 3 and 9. If emissions from battery production were located so as to give a population-weighted average to domain average ratio of 9 instead of 1.9, impacts from WWS EVs would be approximately 30% greater than impacts from conventional gasoline vehicles, which is closer to the 70% result reported by Michalek et al. GREET assumes zero transportation emissions between mining operations and smelting facilities. This implies that smelting occurs at the mining site; to maintain consistency with GREET, I have maintained that assumption in my analyses. Given the potentially large importance of those emissions in estimating the impacts of battery electric vehicles, further investigation of this topic is warranted.

4.4.3 Sensitivity of results to EV battery life

In these analyses, I use the GREET default assumption that EV battery life is 160,000 miles: the same as the life of the rest of the vehicle. To explore a hypothetical scenario where battery life is only 100,000 miles, I multiply my results for air quality impacts from battery production by a factor of 1.6. This gives results similar to the sensitivity analysis in Figure 4.7 where I double battery impacts: the air quality impacts of the EV scenario increase (WWS EVs=34% increase, natural gas EVs=18%, corn stover EVs=7%, grid average EVs=5%, coal EVs=2%), but the rank

order of scenarios does not change.

4.5 Discussion

Results provided here combine spatially- and temporally-explicit life cycle assessment with state-of-the-science air quality modeling for a range of potential transportation technology interventions. The updated emissions estimates, better spatial resolution and coverage, better disaggregation of process locations, and more detailed air quality impact analysis incorporated here yield different overall conclusions from a similar recent study by Michalek et al. (*17*). For instance, when only air quality impacets are considered, Michalek et al. found that WWS EVs *increase* impacts by 160% compared to gasoline, whereas I find that WWS EVs *reduce* air quality impacts by 70% compared to gasoline. As discussed in Section 4.4.2, two major factors contributing to this difference are my use of a more recent version of the GREET mdoel and their assumption that all emissions from EV battery manufacturing are colocated with automobile manufacturing facilities; my more detailed analysis places many of the most polluting processes in the battery production life cycle in remote areas.

I have considered here ten alternative transportation fuel and technology options that have been put forward as potentially environmentally preferable to conventional gasoline powered vehicles based largely on reductions in fossil fuel use and GHG emissions. I find that in some cases, such as for EVs powered by natural gas or WWS, considering air quality impacts alongside climate impacts increases the apparent environmental benefit of the alternative fuel relative to gasoline; in both cases (EVs from natural gas; EVs from WWS) the air pollution benefits relative to gasoline are larger than the climate-related benefits. Other fuels, such as corn ethanol (the climate impact of which is unclear (*43*), are more damaging than conventional vehicles when climate and air pollution impacts are considered together. The difference between the least- and most-polluting electricity generation options for electric vehicles increases almost six-fold when air pollution damages are considered alongside climate impacts, instead of when climate impacts are considered alone. My findings thus reinforce the benefit

of pairing electric vehicles with clean electricity (*12*, *134*).

My work supports the inclusion of air pollution health impacts when assessing the environmental impact of transportation; Figure 4.4 shows that in monetized terms, the health impacts can be as great, or greater than, effects on climate change. I also demonstrate the importance of spatial, temporal, and chemical detail and precision in life cycle air quality impact assessment. Although climate change and air quality are often considered the two main transportation-related environmental externalities (*7*), inclusion of other life cycle impact categories not considered here, such as environmental justice, water quality and availability (*161*, *162*, e.g.), biodiversity, or vehicle safety, could add additional insight.

Results given here should not be taken as a final statement that environmental improvements are best achieved by replacing existing private vehicles with less-polluting private vehicles, nor that electric vehicles are the best technology for every transportation need. Instead, these results can be seen as an indication of one direction in which light-duty transportation technologies can shift to reduce pollution, and as an encouragement into the research of less polluting, more sustainable transportation options for the future.

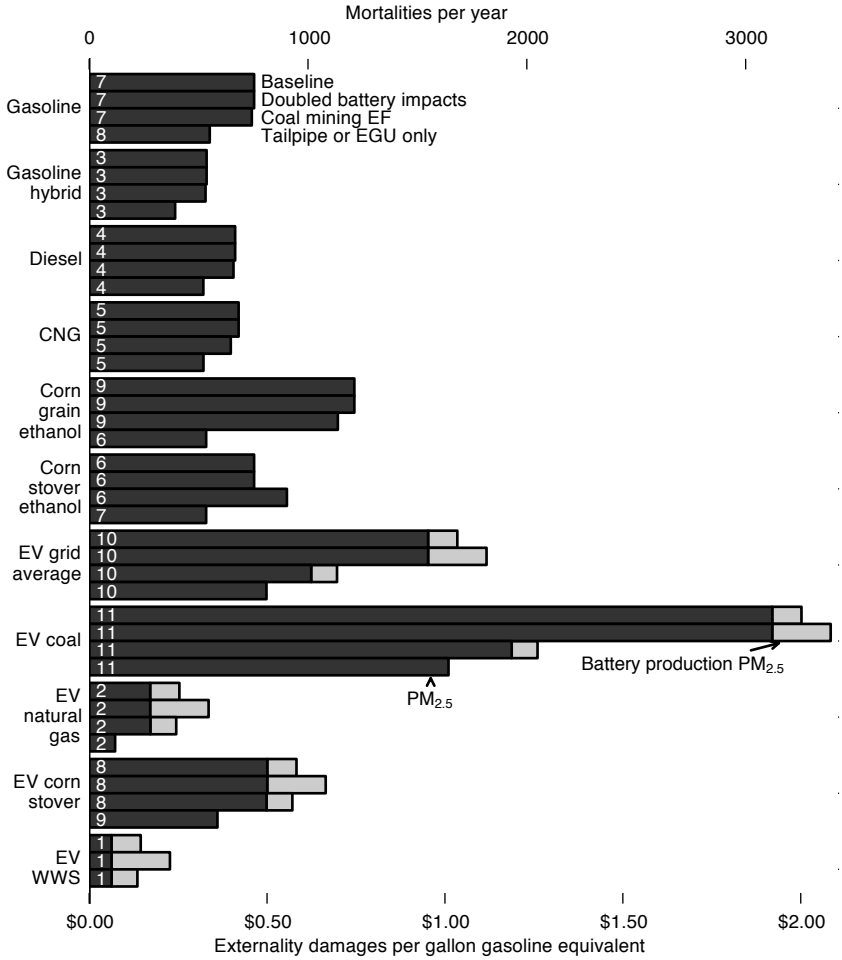

Figure 4.7: Air pollution damages based on air quality modeling for the month of September for the baseline scenarios and sensitivity analyses where battery production impacts are doubled ("Doubled battery impacts"), where coal mining and cleaning emissions factors were updated to a recently published value ("Coal mining EF"), and where only emissions from vehicle tailpipes or electrical generation units are considered ("Tailpipe or EGU only"). The numbers to the right of each bar are rank orders where number 1 has the lowest impacts and number 11 has the highest impacts of all the scenarios. Climate change and air pollution impacts of battery production are added to the EV scenarios assuming effects are additive. Abbreviations: CNG=compressed natural gas vehicle; WWS=wind, water, or solar.

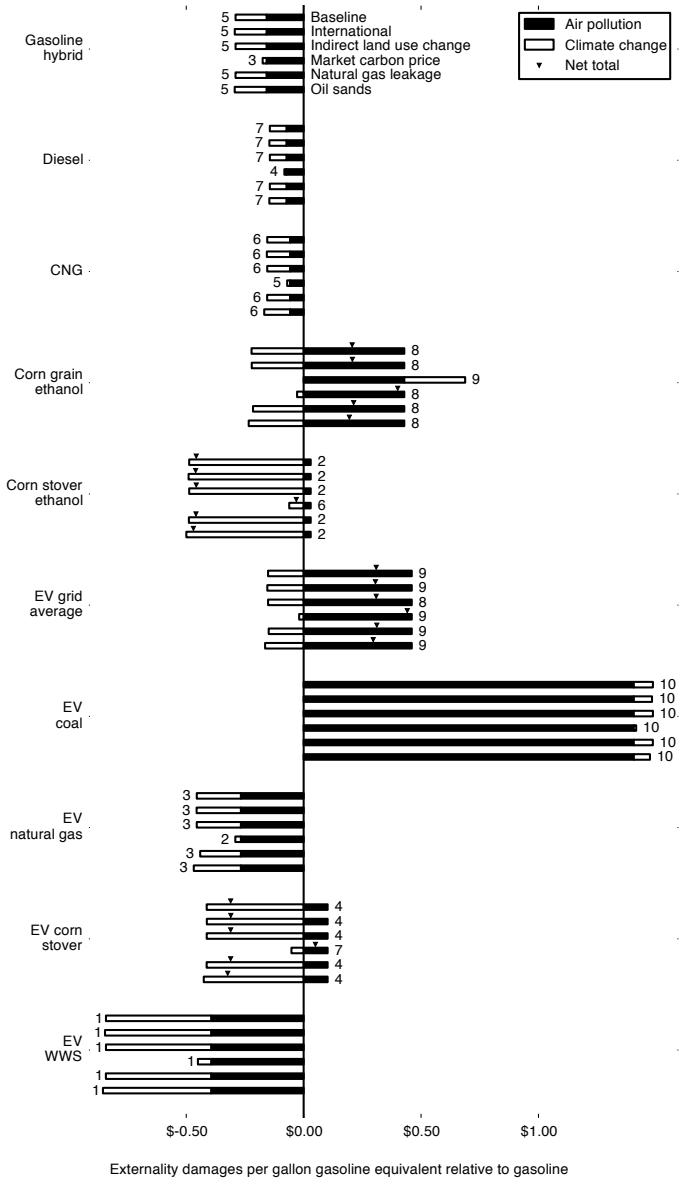

Figure 4.8: Annual air pollution and climate change externalities attributable to each scenario relative to the gasoline scenario ("Baseline") and analyses of sensitivity to important climate change-related assumptions. The numbers at the end of each bar are rank orders where number 1 has the lowest impacts and number 10 has the highest impacts of all the scenarios. Impacts from the gasoline scenario equal zero on this plot. Climate change and air pollution impacts of battery production are added to the EV scenarios assuming effects are additive. Abbreviations: CNG=compressed natural gas vehicle; WWS=wind, water, or solar.

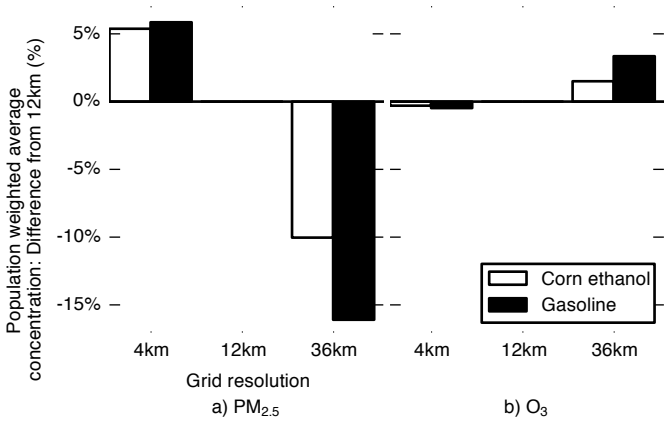

Figure 4.9: Impact of grid resolution on apparent health impacts for two scenarios.

Chapter 5

Spatially resolved life cycle assessment for production- and consumption-based accounting of climate forcing agent emissions from gasoline, ethanol, and electric motor vehicles in the United States

5.1 Summary

Process-based life cycle assessment (LCA) is commonly used for estimating emissions of greenhouse gases (GHGs) and radiatively active aerosols in the production and consumption of transportation fuels. Here, I investigate how spatial patterns in the release of those emissions in fuel production are linked to spatial patterns in the consumption activities they support.

My analysis compares four options for transportation energy for U.S. motor vehicles: gasoline, ethanol from corn grain, ethanol from corn stover, and electric fuels. I use global warming potential (GWP) to aggregate among climate-forcing species. For the gasoline life cycle, I find that emissions of climate-forcers (i.e., GHGs plus radiatively active aerosols) are primarily colocated with vehicle use. For corn ethanol and electric vehicles, however, there is a disconnect between the areas that produce the most fuel (the Midwest "Corn Belt" for ethanol; the Tennessee River Valley and Texas for electrical vehicles) and the areas that consume the most fuel (California, Texas, Florida and New York). The information on the spatial patterns in changes to climate-forcers provided here is important in part because of differences between regulatory jurisdictions and the scope of current accounting frameworks for climate-forcers. Many U.S. states have established emission reduction targets, and my work shows how a biofuel policy designed to help one state could hinder another.

5.2 Introduction

Chapters 2–4 have mainly aimed at estimating air quality-related public health impacts of a range of transportation scenarios. This chapter will focus on climate-related impacts of transportation interventions, with a focus on spatial locations of emissions. There is strong scientific consensus that global climate change is caused by, and is a danger to, human activities (*8*), but consensus has yet to be achieved on how policies should best be designed to address it. Attention has been directed at international (*13*), national (*163*, *164*), and intranational levels. In the United States (U.S.), for example, 23 out of 50 states have set targets for the reduction of greenhouse gas (GHG) emissions (*165*, *166*). In the absence of a unified, universally enforced international climate change policy, national- and intranational-level policymakers must determine which emissions are within their regulatory jurisdictions and how to account for them.

There are two main frameworks for GHG and radiatively active aerosol emissions accounting. *Production-based accounting*, which is more widely implemented in regulatory settings, tracks emissions at the location where they are physically produced. There exist many production-based emissions inventories of climate forcing emissions (*167–171*), some of which are spatially detailed enough to allocate emissions by city block. These production-based inventories can give detailed information on the locations of emissions sources, but do not link the production of emissions to the consumption activities it supports. Since policies that are based on production-based inventories track emissions, but do not link emissions to the consumption activities they support, if such policies are not implemented uniformly in all locations they can result in the shifting of emissions to unregulated areas (*172–175*) instead of achieving the hoped-for overall reduction in emissions. This phenomenon is referred to as "emissions leakage".

Alternatively, *consumption-based accounting*, which usually involves life cycle assessment (LCA), tracks emissions by end-use and reports "embodied" emissions of products or activities (*175–177*). LCA of emissions of climate-forcing species is commonly known as greenhouse gas or carbon accounting. Policies based on consumption-based inventories (e.g., *62*) attempt to avoid emissions leakage by directly connecting the consumption of a product or process with all of the emissions attributable it, but can cause another phenomenon called "emissions shuffling" (also sometimes called "leakage"; I use "shuffling" here to differentiate from leakage as defined above), where products with low embodied emissions are consumed in regulated areas and equivalent products with high embodied emissions amounts are consumed in unregulated areas (*178*, *179*). This shuffling can also yield policies that fail to achieve hoped-for reductions, or potentially can even yield increased emissions from added product transport (*180*).

Because of the problems mentioned above (emission leakage for production-based accounting; emission shuffling for consumption-based accounting), a framework that tracks locations of both production and consumption may be better than either one individually. Previous studies that have linked the locations of emissions production and consumption have used

economic input-output (EIO) LCA (*172–174*), which is based on trade relationships among sectors or political entities. EIO LCA does not track emissions directly, but instead uses economic data as a surrogate for physical process activity and relies on an estimate of emissions per unit of economic activity to determine environmental impacts. As such, EIO LCA is useful for investigating sectors of the economy but is less useful for detailed analyses of specific products or processes.

Process-based LCA, a second type of life cycle assessment, tracks emissions from the physical processes that make up the life cycle (i.e., the supply chain, use, and disposal) of a product or process. Process-based LCA has been used extensively to compare climate-relevant emissions among gasoline, corn ethanol, cellulosic ethanol, and electric vehicles (*17*, *25*, *32*, *35*, *40*, *134*, *181–184*). Previous process-based LCA analyses of climate-relevant pollutants have not included information on the location of emissions production other than the GREET model's labeling emissions as "urban" versus "rural" (*60*). Researchers have previously included GHG emissions in a spatially explicit analysis of air pollutants (*16*, *17*), but their analyses of the GHG LCA emissions have not been spatially explicit. Chapter 2 reports spatially explicit estimates of non-GHG air pollutant emissions. I present here, for the first time, modeled life cycle spatial patterns of climate forcers (GHGs plus aerosols).

The case study in this chapter compares climate impacts from U.S. light duty vehicles using gasoline, ethanol from corn grain, cellulosic ethanol from corn stover, and electricity for electric vehicles. My emissions accounting framework tracks emissions production and consumption simultaneously using a spatially resolved, process-specific life cycle inventory (LCI).

5.3 Methods

I use the approach for calculating life cycle emission amounts and locations is described in detail in Chapter 2. Briefly, I create an extension to the Greenhouse Gases, Regulated Emissions, and Energy Use in Transportation (GREET) model from Argonne National Laboratory (*61*) that adds chemical, spatial, and temporal profiles to all life cycle unit processes. I first

recompile the GREET equations and model framework to obtain process-specific emissions totals, and then allocate the emissions from each process to the spatial locations where the process occurs. The resulting model can output emissions resolved to any user-specified grid or set of geographic boundaries. When a co-product of a fuel production process displaces a competing product, the life cycle emissions of the displaced product are treated as negative emissions (I also include a sensitivity analysis employing no displaced product credits). Processes that remove CO_2 from the atmosphere, such as photosynthesis, are also counted as negative emissions and are balanced out by positive emissions at the process that re-emits the CO_2 (vehicle use or ethanol fermentation). GREET, as configured for this analysis, is strictly an attributional (static) life cycle model; indirect (market-mediated) effects are not included.

I model emissions from four transportation fuel life cycles: internal combustion vehicles powered by gasoline, ethanol from corn grain through dry milling ("corn ethanol"), ethanol from corn stover through cellulosic fermentation ("stover ethanol"), and battery electric vehicles powered by the year-2010 U.S. average electricity generation mix ("electric"). Consistent with Chapter 2, I use default GREET settings with these exceptions: I assume that 1) corn ethanol plants use 100% natural gas process heat; 2) the ethanol produced is 100% ethanol without denaturant, but because vehicle tailpipe emissions depend on blend level, I use tailpipe emission factors for E10 (i.e., a mixture of 90% gasoline, 10% ethanol) for the ethanol fuels; 3) gasoline production is 100% conventional (i.e., not reformulated) gasoline; and 4) crude oil production is 100% conventional crude (most oil sands production occurs outside of my spatial modeling domain and would be therefore excluded from my spatial analyses). Vehicle energy-efficiency and emissions per mile are assumed equal for all liquid fuels. I assume that production and disposal emissions for the vehicle itself are generally similar for all life cycles (*138*) and therefore exclude them from the analysis; one exception is battery production for electric vehicles, which I include using the GREET vehicle cycle model (*138*) and additional spatial information for locations of the production of aluminum (*147*), copper (*148*), steel (*30*), and plastic (*30*), and the assembly of batteries (*30*) in the U.S. I use the GREET default assumption that vehicles and EV batteries have a 160,000 mile lifetime. Since there is currently no

commercial production of lignocellulosic ethanol from corn stover, I assume such biorefineries to be in the same locations as current corn ethanol biorefineries. I use the GREET-default 2010 U.S. average electricity generation mix for electric vehicles (47% coal, 21% nuclear, 20% natural gas, 12% other), and I assume that electricity generation for electric vehicles occurs at existing facility locations proportionally to the existing generation at those facilities (*87*). Efficiencies and emissions factors reported here are for year-2010. Because the main focus of my modeling is to determine the spatial locations of emissions, I do not validate emissions factor, process relationship, energy intensity, or other assumptions in the GREET model.

My analysis focuses on primary emissions of chemicals that affect climate change. GREET tracks the emissions of these greenhouse gases (GHGs): carbon dioxide (CO_2), nitrous oxide (N_2O), methane (CH_4), carbon monoxide (CO), non-methane volatile organic chemicals (VOC), tetrafluoromethane (CF_4), and hexafluoroethane (C_2F_6). GREET also estimates emissions of particulate matter with diameter less than 10μm and 2.5μm (PM_{10} and $PM_{2.5}$, respectively), which can also impact climate. The magnitude and sign of aerosol radiative forcing depends on particle properties (*95*), so knowledge of total mass of PM_{10} and $PM_{2.5}$ emissions does not provide sufficient information to estimate climate impacts. For example, black carbon aerosols generally absorb radiation, causing warming, whereas organic carbon aerosols can scatter radiation, causing cooling (*95*). To overcome this limitation, I chemically speciate $PM_{2.5}$ into particulates made up of elemental (black) carbon and organic carbon, among others (as described in Chapter 2).

I employ global warming potential (GWP; units: CO_2-equivalents, or "CO_2e") to sum impacts across climate-forcers. GWP is widely used but has drawbacks, especially for aerosols. Because different pollutants have different atmospheric residence times, the time horizon over which impacts are considered affects the apparent relative importance of different pollutants (*185*). Additionally, impacts of short-lived pollutants, especially aerosols, are spatially and temporally variable (*95*, *186*, *187*), so any global metric for their impacts will be limited in accuracy. Finally, GWP metrics omit impacts of secondary aerosols, such as sulfate aerosols formed from emissions of SO_2, and indirect impacts of all aerosols (for example, effects on

cloud albedo and lifetime). Globally, each of these effects causes radiative cooling with a magnitude equal to or greater than the direct radiative effect of primary emissions (*95*).

Despite those limitations, robust alternatives are unavailable. I use GWP values compiled by Bond et al. (*150*); 20- and 100-year GWPs are presented here, 500-year GWPs are in Appendix E. Spatially and temporally explicit estimates of the *impacts* of climate-forcers are not included here.

Transportation fuels used in the U.S. are supported by global supply chains; the associated emissions may occur worldwide. Figure 5.1 divides GREET-calculated global emissions into emissions that occur (1) within the U.S., (2) immediately offshore (within the U.S. Exclusive Economic Zone, which extends 200 nautical miles from shore), and (3) internationally or over the open ocean. Because the vast majority of emissions occur in the U.S. or immediately offshore, analyses here consider only those two types of emissions. (See Appendix E for additional information.)

5.4 Results

Figure 5.2 shows, for the four energy sources evaluated, contributions to climate forcing for 20-year (left panels) and 100-year (right panels) GWP. The top panels disaggregate contributions by species; the bottom panels disaggregate by production process. (Plots for individual pollutants and 500-year GWP are in Appendix E.)

With 20-year GWPs, CO_2 has the largest impact; CO, N_2O, CH_4, and black carbon also contribute substantially, VOCs and organic carbon make only minor contributions. With 100-year GWPs, CO_2 and N_2O dominate total impacts.

For gasoline, vehicle tailpipe emissions are the main driver of climate impacts for 20- and 100-year GWPs. For ethanol, energy consumption for ethanol fermentation is also a major source of emissions, while carbon uptake by corn plants is a major source of negative emissions. For stover cellulosic ethanol, credits for excess electricity generation are an additional emissions sink, offsetting $\sim$25% of vehicle use emissions. The major source of emissions from

electric vehicles is electricity generation from coal. Overall, the relative ranking of the four fuels' total climate-forcing emissions, and the relative importance of specific unit processes contributing to the impacts of each fuel, are generally similar among the 20-, 100-, and 500-year GWPs.

Figure 5.3 shows production-based locations of life cycle emissions, for cases where biogenic uptake and subsequent release through combustion of atmospheric CO_2 is not (Figure 5.3a) or is (Figure 5.3b) tracked. Consumption-based emissions are colocated with vehicle use; see Appendix E for maps of vehicle use locations. For gasoline, production-based emissions are correlated with vehicle use and therefore are concentrated in urban areas. For the ethanol fuels, additional emissions occur mainly in the Midwest at biorefinery locations. In the case where biogenic CO_2 is tracked (Figure 5.3 right panel), the ethanol fuels create negative emissions in corn farming areas (shown as blue patches in Figure 5.3b.ii and iii) which are counterbalanced by increased positive emissions at vehicle use and biorefinery locations. When biogenic CO_2 is not tracked (Figure 5.3 left panel) there are no negative emissions at corn farming areas but there are still negative emissions from coproduct credits. Emissions from electric vehicles largely occur at coal electricity generating units (CO_2e emissions from natural gas electric generation are comparatively small). Appendix E provides additional results that include the uptake of carbon by plants and its subsequent emission from vehicles and biorefineries as well as maps of individual pollutants, individual unit processes, and 20- and 500-year GWPs. Figure 5.2 shows the net total of all emissions in Figure 5.3.

Figure 5.4 shows how the choice of consumption- or production-based accounting affects apparent emissions location by U.S. state. For vehicle use, consumption-based emissions (x-axis) are proportional to vehicle miles traveled (VMT), so for all fuels the states with the most VMT—California, Texas, and Florida—have the highest consumption-based emissions. Production-based emissions (y-axis) are correlated with vehicle use but additionally are influenced by the locations of other processes in the fuel life cycle. For the gasoline life cycle, the main difference between production- and consumption-based emissions accounting is in Texas

and to a lesser extent Louisiana owing to the role of those states in petroleum extraction, refining, and transport. For corn ethanol, under the assumption that ethanol use is proportional to vehicle use and is not affected by state-level policies or transport distances, production-based emissions are relatively low compared to consumption-based emissions in states with the most vehicle use, and relatively high in states where corn is grown. For stover ethanol, production- and consumption-based emissions are relatively low overall, with negative production emissions in Wisconsin, Minnesota, and North Dakota owing to substitution of electric generation in those areas with excess electricity generated at biorefineries. For electric vehicles, production-based emissions are relatively high in areas that export electricity—especially electricity from coal—and produce its feedstocks, such as the Tennessee River Valley and Texas. Correspondingly, production-based emissions for electric vehicles are relatively low in states that import electricity, such as California, Florida, and New York. Figure 5.4 does not include offshore emissions. State-specific maps of CO_2e emissions for 20-, 100-, and 500-year GWP horizons and maps showing the locations of individual processes in each life cycle are in Appendix E.

I also perform two sensitivity analyses: 1) where emissions credits from coproduct displacement are not included (shown in Figure 5.5), and 2) where CO_2 uptake from corn production and its subsequent emission at biorefineries and vehicle tailpipes is explicitly tracked (shown in Figure 5.6). The first sensitivity analysis shows that excluding coproduct displacement credits from the analysis increases emissions in some states in the ethanol life cycles, but does not change core conclusions above. The second sensitivity analysis (which also corresponds to Figure 5.3b) shows that if an emissions accounting framework accounts for net CO_2 fluxes into and out of the atmosphere (i.e., fossil carbon plus modern carbon instead of just fossil carbon), many of the corn farming states in the ethanol life cycles appear as net sinks of, rather than net sources of, CO_2e emissions.

5.5 Discussion

I have presented a spatial life cycle inventory for four U.S. transportation fuels and have shown how the choice of transportation fuel can dramatically affect the resulting spatial patterns of CO_2e emissions. I find that the choice of time horizon over which the GWP metric is assessed generally does not affect the relative climate impacts of the four fuels or the relative impacts of the individual unit process in their life cycles, but the choice of accounting method (production- versus consumption-based) can affect the apparent spatial locations of emissions. These findings have direct relevance to how biofuel and low-carbon fuel policies are established and managed.

Production- and consumption-based emissions accounting frameworks both have strengths and weaknesses. The approach I develop here implements and connects both approaches simultaneously. My approach also shows how regulations based on either method can interact. For example, the California Low Carbon Fuel Standard (*62*) mandates decreased (consumption-based) CO_2e emissions for transportation, partially through consumption of corn ethanol. Conversely, Minnesota has mandated a decrease in production-based CO_2 emissions (*166*). My modeling results show that because of the production-based emissions in Minnesota as a part of the corn ethanol life cycle, the existence of the California consumption-based standard could make Minnesota's production-based standard more difficult for Minnesota to attain.

Limitations of my approach include the following. The attributional LCA employed here ignores indirect, market-mediated effects of fuel choice. For example, corn prices in the U.S. could increase because of ethanol production, which could impact global food production and its resulting GHG emissions. Also, I assume that unit processes in the life cycle are colocated with existing production and that stover cellulosic ethanol production is colocated with corn ethanol production. In reality, facilities could open or close as fuel production increases. Consequential LCA, which I do not perform here, would aim to capture these effects.

A further limitation of my study is the use of GWP values to quantify climate impacts of short-lived pollutants. Because those impacts, especially for aerosols, are dependent on

the time and location of emission, spatiotemporal modeling of the interaction between these emissions and the atmosphere would provide a more accurate measure of their impacts (*95*). That type of analysis is an opportunity for further research.

The approach described here is general; with additional data it could be applied to compare production- and consumption-based emissions accounting for the life cycle of any product or process.

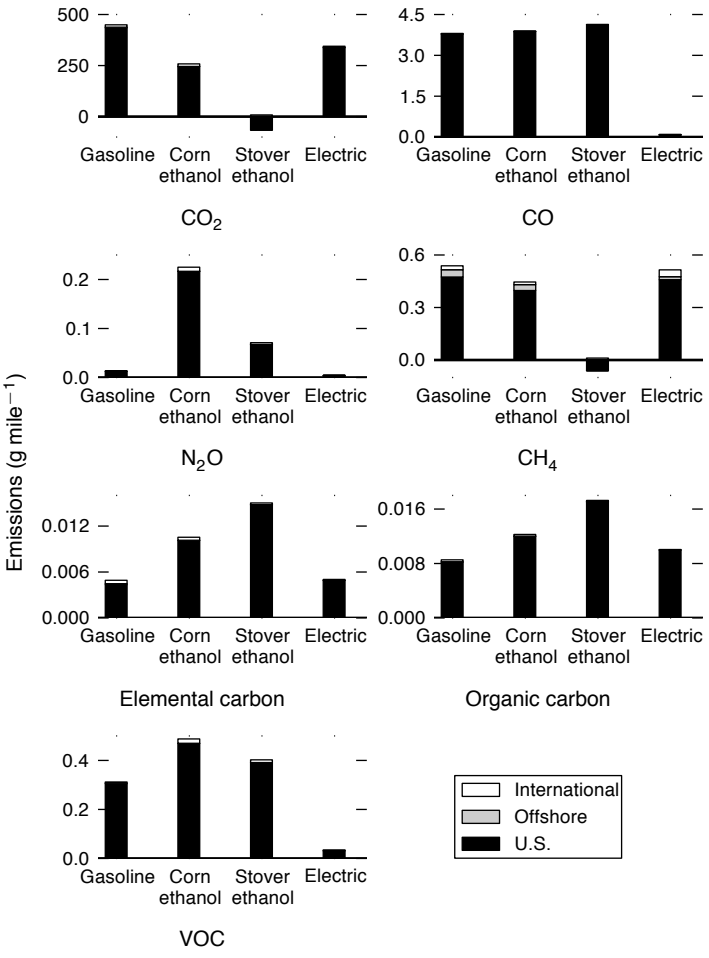

Figure 5.1: Life cycle total emissions disaggregated by emission location: within the U.S., immediately offshore (i.e., within the U.S. Exclusive Economic Zone), and internationally or over the open ocean (International). This paper focuses on the U.S. and offshore emissions, which account for the majority of total emissions.

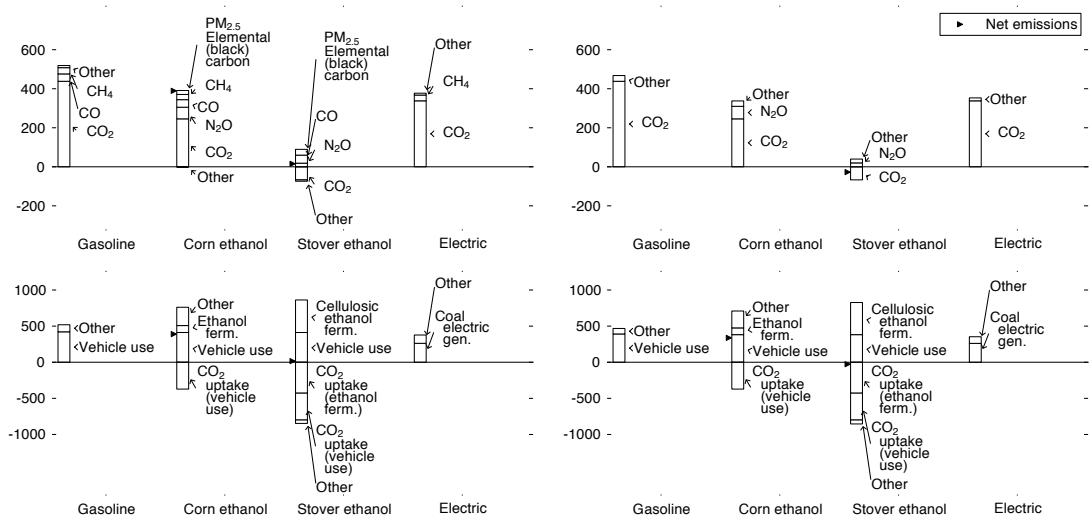

(a) 20 year GWP

(b) 100 year GWP

Figure 5.2: Fuel life cycle emissions of climate forcers (grams CO_2-equivalents per vehicle mile traveled) disaggregated by pollutant (top) and life cycle process (bottom) for 20- and 100-year GWP horizons. For visual clarity, pollutants with emissions too small to display individually are combined into "Other" (see Appendix E for details). For life cycles that include negative emissions, net emissions are indicated by a triangle to the left of that bar. Abbreviations: ferm.=fermentation; gen.=generation. Values reflect U.S. averages.

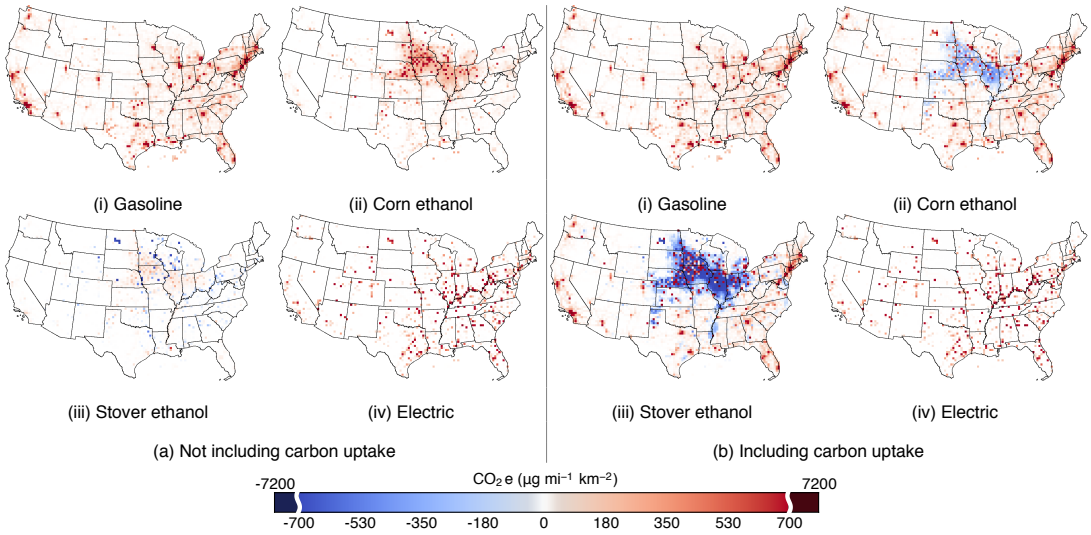

Figure 5.3: Location of annual total life cycle CO_2 equivalent emissions production (100-year GWPs; see Figure 5.2) allocated to a 36 km grid. Units are micrograms per vehicle mile traveled per square kilometer land area. Results are present for simulations that do not (left panel) and do (right panel) track the biogenic uptake and subsequent release through combustion of atmospheric CO_2. For ease of viewing, the linear color scale contains a discontinuity at the 99^{th} percentile of emissions. Blue areas reflect displacement of electricity production (panels a:iii and b:iii) or uptake of atmospheric CO_2 (panels b:ii and b:iii).

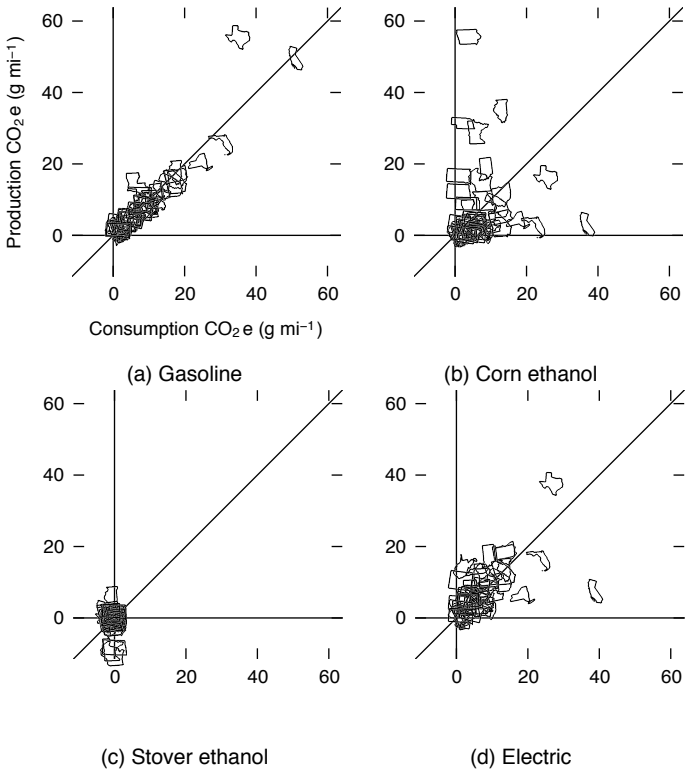

Figure 5.4: State-specific CO_2e emissions (100-year GWP) allocated according to production location (y-axis) and consumption location (x-axis). For example, for corn ethanol and for electricity, California's transportation emissions are much lower for production-based accounting than for consumption-based accounting. For Minnesota, Nebraska, and Illinois, the reverse holds for corn ethanol. States on the 1:1 line have equal emissions for production- and consumption-based accounting.

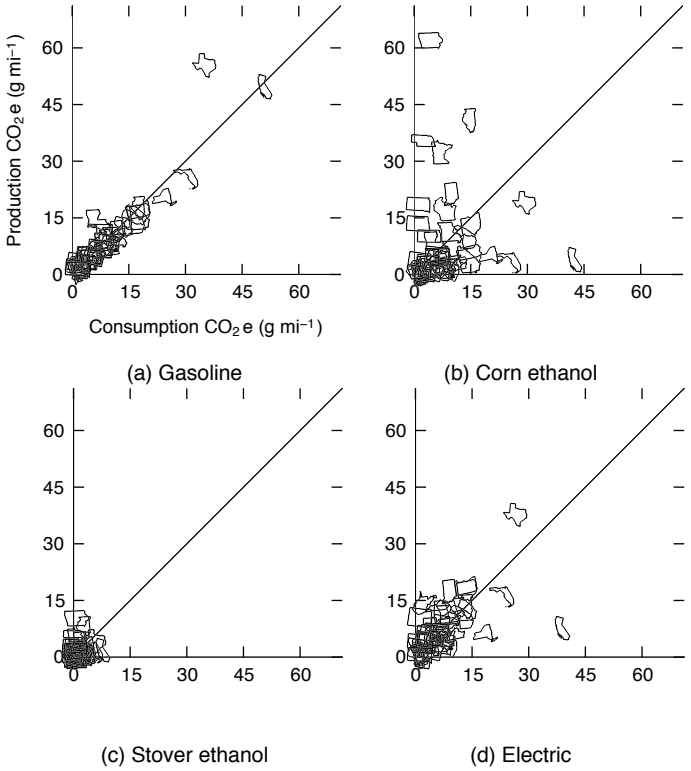

Figure 5.5: State-specific CO_2e emissions (100-year GWP) allocated according to production location (y-axis) and consumption location (x-axis), where coproduct displacement credits are ignored. States falling on the 1:1 line produce and consume the same amount of emissions. Offshore emissions are not included in this figure.

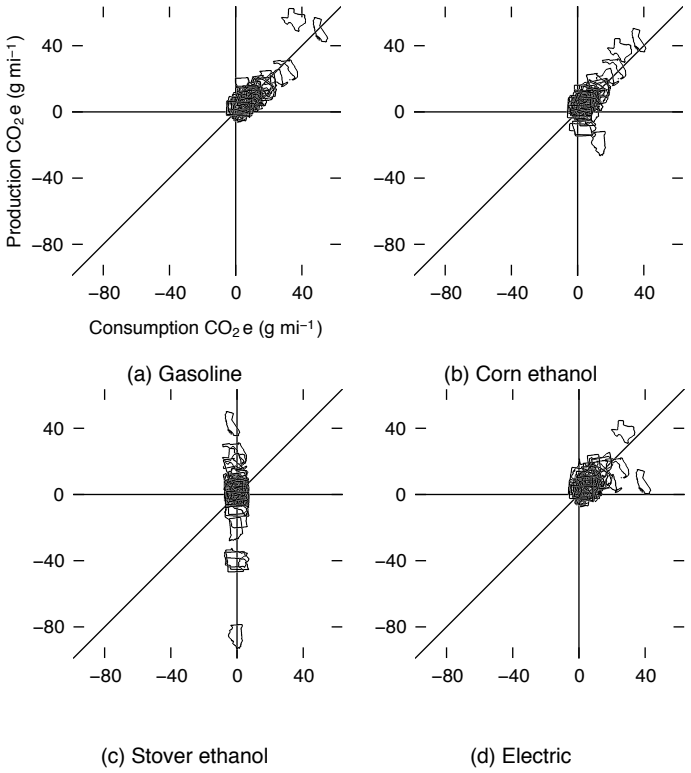

Figure 5.6: State-specific CO_2e emissions (100-year GWP) allocated according to production location (y-axis) and consumption location (x-axis), where CO_2 uptake by plants at farming locations and its subsequent release by vehicle combustion and ethanol fermentation is explicitly tracked. States falling on the 1:1 line produce and consume the same amount of emissions. Offshore emissions are not included in this figure.

Chapter 6

InMAP: A New Model for Air Pollution Interventions

6.1 Summary

Mechanistic air quality models are essential tools for air quality management. However, existing mechanistic air quality models are either too computationally intensive to simulate concentrations at high spatial resolution over a continental spatial extent, not designed to track pollution transport over long distances, or only able to track a single emissions source at a time. I have developed an Intervention Model for Air Pollution (InMAP) to provide estimates of air pollution health impacts resulting from marginal changes in pollutant emissions, such as those caused by the implementation of new regulations. By making simplifying assumptions regarding atmospheric chemistry undergoing marginal changes in pollutant emissions, and by focusing on predicting annual average changes in pollutant concentrations—which are the largest predictor of environmental health impacts—InMAP is able to perform simulations that are much less computationally intensive than comprehensive air quality model simulations, but more detailed than simulations from other reduced complexity models.

6.2 Introduction

Of the three million deaths per year attributed to ambient air pollution by Lim et al. (*9*), approximately 95% are caused by fine particulate matter ($PM_{2.5}$). The most important predictor for these mortalities is chronic $PM_{2.5}$ exposure over periods of a year or more (*65*). $PM_{2.5}$ can be directly emitted from pollution sources (called primary $PM_{2.5}$) or formed in the atmosphere from gas-phase chemicals (called secondary $PM_{2.5}$). Both primary and secondary $PM_{2.5}$ contribute significantly to total $PM_{2.5}$ concentrations (*102*). However, the chemical and physical relationships between emissions of $PM_{2.5}$ and its precursors and the resulting ambient concentrations are complex and nonlinear (*128*), so it is often not immediately clear which reductions in emissions would be most effective in reducing pollutant concentrations and the associated health effects. Furthermore, poor air quality is only detrimental to human health when the pollution is inhaled by humans, so the spatial relationships between the locations of humans and pollutant emissions must be accounted for.

Reducing emissions of air pollutants is a common strategy to reduce the associated health impacts; it is often useful to use a computer model to estimate the effects of a plan for emissions reduction before such a plan is put into effect. With respect to the nature of air pollution health impacts as described above, desirable characteristics for models that estimate the health impacts of changes in pollutant emissions include:

1. The ability to accurately predict pollutant concentrations both near to and far from emissions sources, as both near-source and far-from-source exposures may be important determinants of public health impacts (*102*). This requires the model domain to include a high spatial resolution and also a large spatial extent.

2. The ability to accurately predict concentrations of primary and secondary air pollution, specifically fine particulate matter ($PM_{2.5}$).

3. The ability to predict the impacts of changes in emissions from many sources of pollution at once as policies to control pollution often affect many sources simultaneously.

4. The ability to show the differences between many possible scenarios, and to quantify uncertainty in results or the sensitivity to uncertain factors. This requires that running the model be relatively computationally inexpensive.

Existing models can be split into several groups. One group of models (including CAMx (*188*), CMAQ, (*189*), WRF-Chem (*110*), and GATOR-GCMOM (*190*)), generally referred to as chemical transport models (CTMs), are designed to be able to predict concentrations of pollutants at discrete locations in space and in time from many simultaneous sources. As CTMs attempt to account for everything that happens in the atmosphere over a relatively large spatial domain, they are the most accurate option for predictions of both combined effects of primary and secondary $PM_{2.5}$ concentrations, but they are computationally intensive to operate. Limitations in available computing resources can restrict the spatial and temporal extents of simulations as well as the spatial resolution of the results. For example, a single simulation for chronic pollutant exposure in the contiguous United States with a 12 km spatial resolution can take a week to run on a high performance computing system, as shown in Chapter 3. Pollution concentration and population density is variable at spatial scales of less than 12 km; simulations with increased spatial resolution can provide improved predictions, as shown in Chapter 6. Increased horizontal resolution only yields improved predictions up to a certain point, however. The most accurate resolution in current models appears to be approximately 1 km; beyond this point increased horizontal resolution may not lead to increased accuracy (*191*). This phenomenon occurs because the simplified fluid dynamic equations at the core of CTMs assume that turbulent eddies in the boundary layer are not resolved by the spatial grid, and therefore they use boundary layer parameterizations to account for these effects. However, as the horizontal grid resolution approaches the size of large boundary layer eddies—several hundreds of meters—this assumption is no longer valid (*192*).

A second group of models (such as AERMOD (*193*)), generally referred to as Gaussian plume models, is designed to simulate pollutant concentrations caused by a single source or small group or emissions sources. Although running these models is less computationally intensive compared to the previous group, they are not designed to predict the behaviour of

pollution from many simultaneous sources, and they are not recommended for predictions of pollution transport over distances of more than 20-50 km (*194*). Additionally, these models are usually not able to predict concentrations of secondary $PM_{2.5}$, especially for cases where the formation chemistry is nonlinear or otherwise complex.

A third group of models (including CALPUFF (*195*) and HYSPLIT (*196*)), called "Puff" models, predicts the long range transport of pollution from a single emissions source by tracking a packet of air as it interacts with its surroundings. These models, however, are also not able to predict pollution concentrations caused by many simultaneous emissions sources.

A fourth group of models, such as the Response Surface Model (*197*) and a model developed by Buonocore et al. (*198*), use statistical analyses of CTM runs to calculate spatially-explicit relationships between emissions and health impacts. The models include impacts of both primary and secondary $PM_{2.5}$ and are very computationally inexpensive to run after they have been created. However, they must be created based on a specific set of CTM runs. For instance, Buonocore et al.'s model is for impacts of emissions from electrical generating units, so if a user desired to study impacts from a different source type, a new statistical model would need to be created.

A final group of models (including COBRA (*199*), APEEP (*200*), and the model developed by Lobscheid et al. (*201*)), called source-receptor (SR) models, are essentially transfer matrices describing linear relationships between pollutant emissions at source locations and changes in concentrations at receptor locations. Because existing SR models are created using results from gaussian plume models, which are not recommended for use for predicting the long-range transport of pollution or the formation of secondary $PM_{2.5}$ (*128*), some of the predictions that these SR models make do not have a strong theoretical basis. Additionally, existing SR models can either predict long range transport at and secondary $PM_{2.5}$ formation at low (county-level) spatial resolution (e.g., COBRA, APEEP) or only short range transport of primary $PM_{2.5}$ at high spatial resolution (e.g., (*201*)).

None of the these groups of existing models embody all of the desirable characteristics

listed above. CTMs are accurate, but too computationally intensive for many questions requiring high resolution analyses of large spatial and temporal domains, for many types of uncertainty quantification, or for the analysis of a large number of scenarios. Other models do not capture important aspects of $PM_{2.5}$ generation, transport, and fate as they relate to human exposure. Here I present a novel model, the Intervention Model for Air Pollution (InMAP). InMAP is designed to provide estimates of air pollution health impacts resulting from marginal changes in pollutant emissions, such as those caused by the implementation of new regulations. By making simplifying assumptions regarding atmospheric chemistry undergoing marginal changes in pollutant emissions, and by focusing on predicting annual average changes in $PM_{2.5}$ concentrations—which, as mentioned above, are the largest predictor of environmental health impacts—InMAP is able to perform simulations that are much less computationally intensive than CTM simulations, but more detailed than simulations from other types of models.

6.3 Methods

6.3.1 Model formulation

There are two main frameworks for quantitative models of the atmosphere: (1) With an Eulerian framework, the frame of reference is fixed relative to the surface of the Earth, and the wind moves through the reference frame. (2) With a Lagrangian framework, the frame of reference is fixed relative to a packet of air; the model tracks how that packet of air moves through and interacts with its surroundings. Like the state-of-the-science CTMs described above, InMAP is an Eulerian model.

Once a frame of reference is chosen, there are also two ways to solve the differential equations that govern our understanding of the fate and transport of atmospheric pollution. The first option is to solve the equations analytically, manipulating them in a way that allows the direct calculation of pollutant concentration at any place and time. (The Gaussian plume model is an example of applying that approach.) The equations involved, however, are too complex

to be solved without making many simplifying assumptions. These assumptions reduce the ability of the model to represent complex chemical and physical processes, especially when considering the transport of pollution over long distances or time scales. InMAP uses a second option, which is to use numerical integration to solve the equations. Numerical integration of the equations, which is also used in CTMs, is more computationally intensive than analytically solving them, but it allows a more realistic representation of the atmosphere.

Spatial discretization

To use numerical integration to solve the chemical and physical equations that describe the processes relevant to air pollution, a model must break up the spatial and temporal domains of interest into finite elements. InMAP spatially discretizes the model domain using a variable resolution rectangular grid, where individual grid cells can nest and telescope between lower and higher resolution based on human population density or other attributes. Grid cell resolution is determined by the following algorithm. Given a list of possible grid cell sizes, the model domain is first filled with the lowest resolution grid cells (48 km). Then, the program iterates through the grid cells, determining if the population in each grid cell is above a certain threshold level. If the population in the grid cell is above the threshold level, the grid cell is split into grid cells of the next smallest size. The algorithm recurses through this process until either all of the cells are below the population threshold or the smallest specified grid cell size has been reached. The algorithm also has a second constraint, where any of the smallest-size grid cells have an average population density greater than a certain threshold level are kept at the highest resolution. Because variability in pollutant concentrations decreases with increased height above the ground, all grid cells above a given height cutoff are kept at the lowest model resolution. As shown in Figure 6.1, I use here a spatial domain which covers the contiguous U.S., southern Canada, and northern Mexico, with grid cell edge lengths of 48, 24, 12 4, 2, and 1 km, a population threshold of 40,000 people per grid cell, a population density threshold of 3,000 people km^{-1}, and a height cutoff of the eighth model layer (approximately

1,500 m). These settings are chosen to achieve a balance between the coverage of high resolution grid cells and model runtime. Other spatial domains are possible: the spatial extent of the modeling domain is only limited by the availability of meteorological and chemical input data. Meteorological and chemical properties in InMAP cells that do not exactly coincide with grid cells in the input data set are taken as the average of all input grid cells that they overlap with.

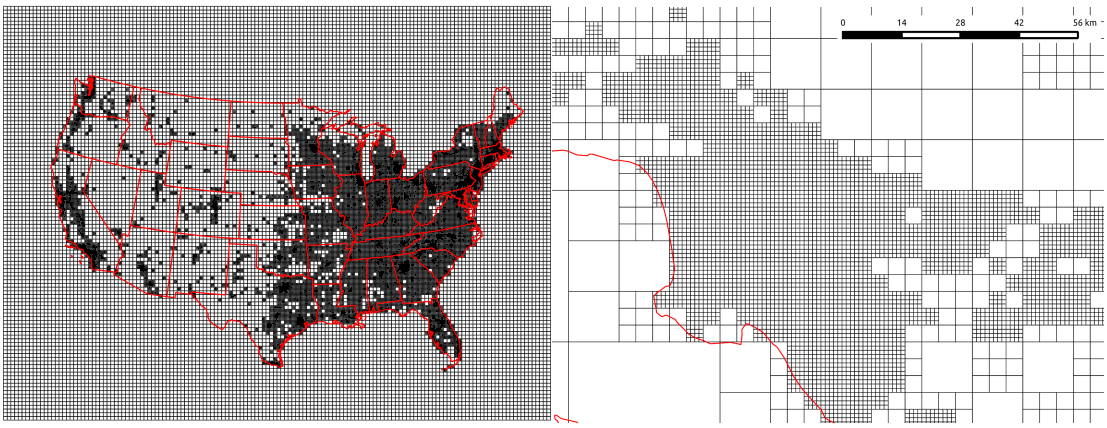

Figure 6.1: Spatial discretization of the model domain into variable resolution grid cells. Left panel: full domain; right panel: a small section of the domain centered around the city of Los Angeles.

Input data

To reduce model complexity and runtime, there are many atmospheric phenomena that InMAP does not explicitly model. Instead, an InMAP preprocessor uses the output of a more comprehensive model—here, I use output from the WRF-Chem model as configured and run in Chapter 3—to extract emergent atmospheric properties. Information collected or inferred from the comprehensive model output includes spatially explicit annual averages of wind speed and direction, eddy diffusivity and convective transport coefficients, dry and wet deposition rates of various pollutants, chemical reaction rates, partitioning coefficients between chemical and gaseous phases of various compounds, air temperature and density, and stability parameters

for the calculation of emissions plume rise.

Temporal discretization

Most air pollution models that use numerical integration do so to solve for the state of the atmosphere at specific and consecutive points in time. To calculate an annual average (the time period most strongly correlated with the largest health effects from $PM_{2.5}$) pollutant concentration, a temporally explicit model calculates the changes in concentrations at every point in time during the year and then averages them. In contrast, InMAP is designed as a steady-state model that directly calculates annual averages. To do this, instead of using temporally-explicit input information and iterating through an entire year, it uses annual average input information and iterates to a steady-state annual average solution.

Many of the chemical and physical processes important to the fate and transport of air pollution vary with the time of day and the season. A steady state, annual average model risks being unable to represent the results of these temporally-explicit phenomena. InMAP mitigates this limitation by using temporally explicit information wherever possible when calculating annual average properties. For instance, the gas-phase oxidation of SO_2 to SO_4^{2-} is represented as the product of the SO_2 concentration and a reaction rate constant, but the reaction rate constant has a non-linear dependence on temperature and on the concentration of hydroxyl radical (HO^*), both of which are temporally variable. To represent the formation of particulate SO_4 (pSO_4), InMAP needs an annual average rate constant, however. To capture some of the effects of this temporal variability, instead of calculating the rate constant using annual average values for temperature and HO^*, I use temporally explicit temperatures and HO^* concentrations to calculate rate constants for every hour during the year, and then take the average of these 8,760 rate-constant values to yield the reaction rate I use in InMAP for a given grid cell.

To reach a steady-state solution, InMAP starts with an initial guess of the changes in concentrations caused by an emissions scenario (the initial guess is that there are no changes in concentrations) and iterates the model forward in time until the concentrations converge to

a steady-state solution (i.e., until the predicted concentrations no longer change as the model continues to run). The integration time step Δt is chosen using the Courant-Friedrichs-Lewy condition (*202*) as in Equation 6.1:

$$\Delta t = \frac{C_{\max}}{\sqrt{3}} \left(\max \left[\frac{U_{i,pos}}{\Delta x_i}, \frac{U_{i,neg}}{\Delta x_i}, \frac{V_{i,pos}}{\Delta y_i}, \frac{V_{i,neg}}{\Delta y_i}, \frac{W_{i,pos}}{\Delta z_i}, \frac{W_{i,neg}}{\Delta z_i} \right]; i = 1...n \right)^{-1} \tag{6.1}$$

where $C_{\max}$ is the maximum allowable Courant number (set to 1.0 for InMAP), the U, V, and W variables are annual average wind speeds in each of n total grid cells as defined below, and Δx, Δy, and Δz are the dimensions of each grid cell. With the model settings described here, $\Delta t \sim 1$ minute, and is limited by the Courant number in the 1-km grid cells near ground level. In contrast, in CTMs with constant-resolution grids, Δt is typically limited by the high wind speeds in grid cells near the top of the model spatial domain, so 1-minute time step typically corresponds to approximately 10-km horizontal resolution grid. Because InMAP uses a variable resolution grid with 48 km grid cells at the top of the model domain, it is able to use higher-resolution grid cells near ground level without decreasing Δt.

During each time step in each grid cell, InMAP first adds in the flux of new emissions, accounting for plume rise from elevated sources (*127*) (as cited in (*128*)) using annual average windspeed and stability parameters, and then calculates how changes in pollutant concentrations are affected by physical and chemical processes including advection, turbulent mixing, atmospheric aerosol chemistry, dry deposition, and wet deposition.

Advection

Advection is the movement of pollutants among grid cells by air movement that is resolved at the spatial and temporal scales of the model. After calculating annual average wind velocity components in the east, west, north, south, above, and below directions from the WRF-Chem output, I use the upwind differences scheme for calculating advection as shown in Equation 6.2:

$$\Delta C = \frac{\sum_{w_i}^{1,n_w} \left(\left[U_{pos} C_{w_i} - C U_{neg} \right] f_{w_i} \right) + \sum_{e_i}^{1,n_e} \left(\left[U_{neg} C_{e_i} - C U_{pos} \right] f_{e_i} \right)}{\Delta x} \times \Delta t \tag{6.2}$$

where ΔC is the change in volume-specific pollutant concentration in a grid cell caused by East-West advection during time step Δt, w_i and e_i are one of n_w and n_e adjacent cells to the West and East, respectively (because grid resolution varies each cell can have more than one adjacent cell in each direction), U_{neg} and U_{pos} are the annual average wind velocity vector components in the Westward and Eastward directions, respectively, C is the concentration in the grid cell at the beginning of the time step, C_{w_i} and C_{e_i} are the changes in concentrations in the adjacent cells, f_{w_i} and f_{e_i} are the fractions of the west and east edges of the grid cell that are touching the neighbor currently being considered, and Δx is the length of the grid cell in the East-West direction. Equation 6.2 is repeated for the North-South and above-below directions to yield the overall change in concentration due to advection in each grid cell during each time step.

Mixing

Some meteorological processes, such as turbulence and boundary layer convection, are of a temporal or spatial scale too small to be resolved by the model. Pollutant transport by these processes is represented by a mixing parameterization that is designed to reproduce the overall effects of these processes without explicitly modeling them. For mixing within the planetary boundary layer, I use a combined local-nonlocal closure scheme (*203*) which represents both turbulent mixing and convective transport from the surface. For mixing above the boundary layer and for horizontal mixing, I only consider turbulent mixing. Mixing is calculated using a version of Pleim's (*203*) Equation 10, adapted in Equation 6.3 below to allow a variable number

of adjacent cells in each direction and to include horizontal as well as vertical mixing.

$$
\begin{aligned}
m_g = &\ \sum_{g_i}^{1,n_g} \left(\mathrm{M2u}_i C_{g_i} f_{g_i}\right) \\
m_a = &\ \sum_{a_i}^{1,n_a} \left(\left[\mathrm{M2d}_{a_i} C_{a_i} \frac{\Delta z_{a_i}}{\Delta z} - \mathrm{M2d}_i C_i + \Delta z^{-1} K_{zz,a_i} \frac{2\left(C_{a_i} - C\right)}{\Delta z + \Delta z_{a_i}} \right] f_{a_i} \right) \\
m_b = &\ \sum_{b_i}^{1,n_b} \left(\Delta z^{-1} K_{zz,b_i} \frac{2\left(C_{b_i} - C_i\right)}{\Delta z + \Delta z_{b_i}} f_{b_i} \right) \\
m_w = &\ \sum_{w_i}^{1,n_w} \left(\Delta x^{-1} K_{xx,w_i} \frac{2\left(C_{w_i} - C_i\right)}{\Delta x + \Delta z_{w_i}} f_{w_i} \right) \\
m_e = &\ \sum_{e_i}^{1,n_e} \left(\Delta x^{-1} K_{xx,e_i} \frac{2\left(C_{e_i} - C_i\right)}{\Delta x + \Delta x_{e_i}} f_{e_i} \right) \\
m_s = &\ \sum_{s_i}^{1,n_s} \left(\Delta y^{-1} K_{yy,n_i} \frac{2\left(C_{s_i} - C_i\right)}{\Delta y + \Delta y_{s_i}} f_{s_i} \right) \\
m_n = &\ \sum_{n_i}^{1,n_n} \left(\Delta y^{-1} K_{yy,n_i} \frac{2\left(C_{n_i} - C_i\right)}{\Delta y + \Delta y_{n_i}} f_{n_i} \right) \\
\Delta C_i = &\ \left(m_g + m_a + m_b + m_w + m_e + m_s + m_n\right) \Delta t
\end{aligned}
\tag{6.3}
$$

In Equation 6.3, C_i refers to the pollutant concentration in a grid cell of interest, g_i refers to one of n_g cells at ground level directly below the cell of interest, and b_i, a_i, w_i, e_i, s_i, and n_i refer to cells directly below, above, west, east, south, and north of the cell of interest, respectively. M2u and M2d are upward and downward convective mixing coefficients (*203*). K_{zz} is the turbulent mixing coefficient in the vertical direction, calculated according to Pleim (*203*) for grid cells within the boundary layer, and according to Wilson (*204*) for grid cells above the boundary layer, and K_{xx} and K_{yy} are horizontal mixing coefficients calculated using the same method. I calculate mixing coefficients (both local and nonlocal) for each time step in the WRF-Chem model output, using the boundary layer height specific to that time step, and then use the average of these values to represent mixing in InMAP.

Chemistry

To model the secondary formation of $PM_{2.5}$, InMAP calculates partitioning between the gas and aerosol phases for sulfur, nitrogen oxide, ammonia, and organic compounds. For sulfur compounds, there are two main pathways from sulfur dioxide (SO_2) gas to sulfate SO_4^{2-} particles: gas phase oxidation by hydroxyl radical (HO^*) and aqueous phase oxidation by hydrogen

peroxide (H_2O_2) (*128*). There are no major pathways for reaction of SO_4^{2-} back to SO_2. After calculating an annual average reaction rate k_S for SO_2 to SO_4^{2-} using WRF-Chem output data and formulas for the gas phase and aqueous pathways from Seinfeld and Pandis (*128*), I calculate the formation of SO_4^{2-} particles from SO_2 gas as in Equation 6.4:

$$\Delta C_{S,g2p} = k_S C_{S,g} \Delta t \tag{6.4}$$

where $\Delta C_{S,g2p}$ is the transformation of sulfur from gas to particle phase during a time step and $C_{S,g}$ is the gas phase concentration of sulfur at the beginning of the timestep.

For nitrogen oxide, ammonia, and organic compounds, the chemical reaction mechanisms governing partitioning between the gas and particle phase are more complex than the reactions driving sulfate formation. They are also reversible: gas-phase compounds can convert to aerosols and then back to gas-phase; the direction of the reactions can vary according to the time of day and according to the season. It is not possible to directly represent these reactions in a steady-state, annual average model such as InMAP, so I instead calculate annual average partitioning coefficient $f_g = \frac{m_g}{m_g + m_p}$ from the WRF-Chem output data, where m_g is mass in the gas phase and m_p is mass in the particle phase. Then, assuming that gas/particle partitioning for marginal changes in concentrations from the WRF-Chem baseline is the same as the baseline partitioning, I use this coefficient to calculate gas/particle partitioning in InMAP as in Equations 6.5 and 6.6:

$$C_{g,f} = (C_{g,i} + C_{p,i})\, f_g \tag{6.5}$$

$$C_{g,f} = (C_{g,i} + C_{p,i})\, (1 - f_g) \tag{6.6}$$

where $C_{g,i}$, $C_{p,i}$, $C_{g,f}$ and $C_{p,f}$ are gas and particle phase concentrations at the beginning and end of the time step, respectively. The concentration at the end of one time step is used as the concentration at the beginning of the next time step. Note that because I assume that the partitioning coefficient is the same as in the baseline, InMAP is only recommended for use in predicting the impacts of marginal changes in emissions from the baseline.

Dry deposition

I assume that dry deposition v_{dd} for gases can be represented as a function of resistances in series as in Equation 6.7 (*128*), where r_a is aerodynamic resistance, r_b is quasi-laminar boundary layer resistance, and r_c is surface resistance. For particles, this equation is slightly altered to account for settling velocity. I calculate an annual average dry deposition velocity for each ground-level grid cell using the output from WRF-Chem and algorithms for r_c for gases from Wesely (*205*, *206*). To calculate r_c for particles and to calculate r_a and r_b I use algorithms from Seinfeld and Pandis (*128*). I then calculate dry deposition within InMAP using Equation 6.8:

$$|v_d d| = (r_a + r_b + r_c)^{-1} \tag{6.7}$$

$$\Delta C = -C v_{dd} \frac{\Delta t}{\Delta z} \tag{6.8}$$

where C is pollutant concentration in a grid cell in the lowest model layer.

Wet deposition

I calculate an annual average wet deposition rate r_{wd} for each grid cell using output from WRF-Chem and a simple algorithm from the EMEP model (*207*) that estimates a rate of wet deposition from in-cloud and below-cloud scavenging rate as a function of cloud fraction, precipitation rate, and air density. The algorithm provides separate rate estimates for particles, SO_2, and other gases. I then calculate wet deposition within InMAP using Equation 6.9:

$$\Delta C = -C r_{wd} \Delta t \tag{6.9}$$

Dry deposition is only assumed to occur in ground-level grid cells, but wet deposition is calculated for every grid cell (with location-specific deposition rates).

6.3.2 Model inputs

My goal is to make InMAP as easy to operate as possible. Toward this goal, the only user-specified input required by InMAP is a shapefile or set of shapefiles (format specification at

`http://www.esri.com/library/whitepapers/pdfs/shapefile.pdf`) containing the spatial locations of changes in annual total emissions of volatile organic compounds (VOCs), sulfur oxides (SO_x), oxides of nitrogen (NO_x), ammonia gas (NH_3), and primary fine particulate matter ($PM_{2.5}$). Locations can be specified as either polygon, line, or point entities, and can include stack attributes for elevated sources. InMAP will allocate the emissions from the shapefiles to the corresponding model cells using area-weighting.

6.3.3 Performance evaluation

The primary purpose of InMAP is to serve as a quick alternative to CTM modeling for marginal changes in emissions, so I aim to evaluate its performance in predicting marginal changes in concentrations rather than total ambient concentrations. Although the strongest evaluation would be to compare InMAP predictions to measured pollutant concentrations, there do not exist any nationwide, long-term measurements of the effects of small changes in emissions on pollutant concentrations. Instead, I compare InMAP predictions to results from the more comprehensive WRF-Chem model for 11 scenarios of changes in pollutant emissions resulting from the adoption of alternative light-duty transportation technologies. These scenarios include emissions from a combination of transportation, electric generation, agriculture, and various industrial sources, resulting in changes in total $PM_{2.5}$ concentration on the order of 1% of the total. The emission scenarios and WRF-Chem results are described in further detail in Chapters 2 and 4, respectively. I also compare the results to predictions from the COBRA source-receptor model (*199*) for the same emissions scenarios.

6.4 Results

Figure 6.2 shows how each of the models in the comparison predict that total $PM_{2.5}$ concentrations would change in an example one of the 11 emissions scenarios tested. In general, InMAP (as compared to WRF-Chem) tends to overpredict concentration changes in areas where changes in emissions are higher (usually in urban areas) and to underpredict concentration

changes in areas where changes in emissions are lower.

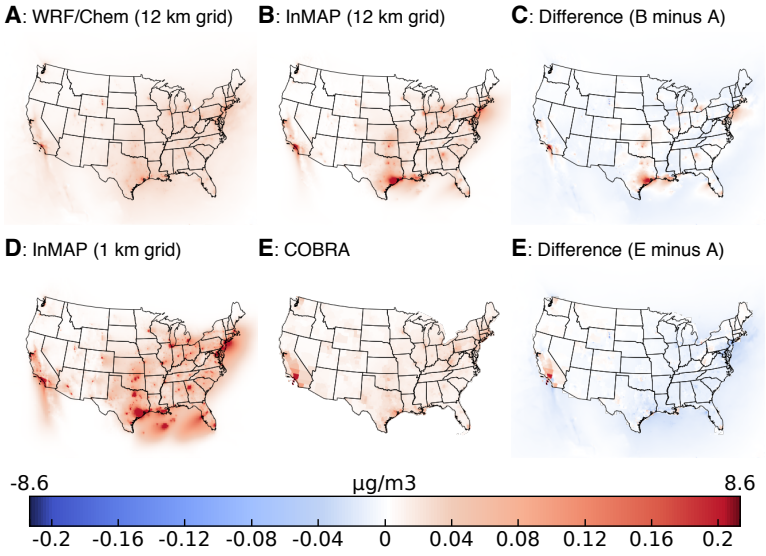

Figure 6.2: Changes in concentrations resulting from one emissions scenario as calculated by A) the WRF-Chem, B) InMAP with a 12 km resolution grid, D) InMAP with a 1 km to 36 km variable resolution grid (i.e., a typical setup for InMAP), and D) COBRA. Panel C shows the difference between panels B and A.

Figure 6.3 compares InMAP predictions for changes in concentrations of total $PM_{2.5}$ (both primary and secondary) from a range of different emissions scenarios to WRF-Chem predictions for the same scenarios. Comparisons are shown for two InMAP configurations: one using the same 12 km spatial grid as does WRF-Chem (referred to as "InMAP 12 km") and one using the variable resolution grid described in Section 6.3.1 ("InMAP 1 km"). For each configuration, two sets of comparisons are performed: a comparison of changes in area-weighted average ground level concentrations, which give a general estimate of how well the model represents mixing and removal processes, and a comparison of changes in population-weighted average concentrations, which are a surrogate for human exposure.

InMAP 12 km reproduces the WRF-Chem predictions relatively well for changes in area-weighted average concentrations (Fig. 6.3a) with an R^2 of 0.98 and a mean fractional bias of

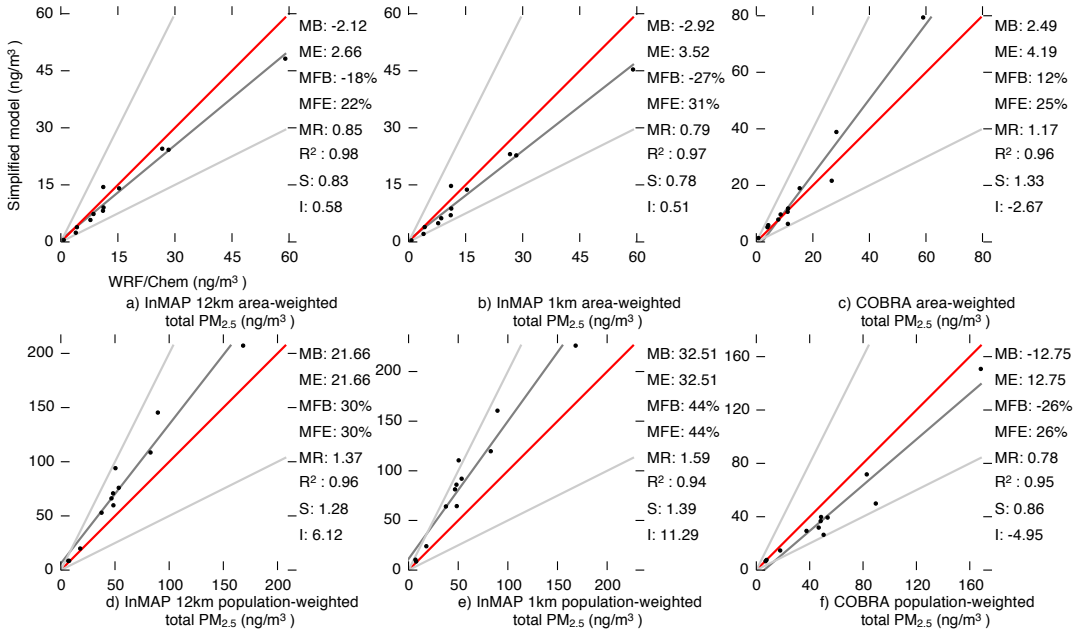

Figure 6.3: Comparison of total (primary plus secondary) $PM_{2.5}$ area-weighted (panels a-c) and population-weighted (panels d-f) annual average predictions between WRF-Chem (x-axis) and reduced-complexity models (RCM; y-axis) for 11 emissions scenarios. The red line represents 1:1 ratio of RCM to WRF-Chem predictions, the light gray lines represent RCM:WRF-Chem ratios of 2:1 and 1:2, and the dark gray line represents a least-squares regression between RCM and WRF-Chem predictions. Abbreviations: MB=mean bias; ME=mean error; MFB=mean fractional bias; MFE=mean fractional error; MR=model ratio; S=slope of regression line; I=intercept of regression line.

-18%. For population-weighted changes in concentrations, the InMAP predictions still correlate well with WRF-Chem (R^2=0.96) but the changes in concentrations are biased high relative to WRF-Chem (mean fractional bias=30%, meaning that InMAP predicts population exposures on average 30% higher than does WRF-Chem). Since changes in emissions in these scenarios are correlated with population density, this finding reflects the same phenomenon seen in Figure 6.2 where changes in concentrations are overpredicted near emissions sources and underpredicted far from emissions sources. This result suggests that at least one of the mechanisms responsible for moving pollution away from emissions sources—advection, vertical mixing, or

horizontal mixing—is underacting in InMAP as compared to WRF-Chem. It is possible that this gap is caused by the inability of the annual average values for advection and mixing I use here to account for temporal correlations in these parameters that may be important for the dispersion of pollution. Some examples of these correlations may be weather fronts that can carry pollution long distances in a relatively short period of time, or the collapsing of the boundary layer at night to allow pollution that was within the boundary layer during the day to be carried away by the relatively high-speed winds of the free atmosphere.

InMAP 1 km predicts greater changes in population-weighted concentrations than does InMAP 12 km. Increases in predicted exposure with increased model resolution have been observed before. As shown in Chapter 4, changes in emissions in these scenarios are correlated with population density. By nature, lower-resolution model analyses predict less variability in pollutant concentration than do higher-resolution analysis (pollutant concentrations are assumed to be perfectly mixed within each grid cell), so pollution concentrations tend to be artificially diluted away from high population areas in lower-resolution analyses.

Figure 6.3 also shows that InMAP performance statistics are similar to those of the existing COBRA model. It should be noted, however, that as described throughout this chapter, InMAP has capabilities that COBRA does not (e.g., the ability to predict how pollutant concentations differ within a county); the two models should not be compared based on their ability to reproduce WRF-Chem predictions alone.

Figure 6.4 compares InMAP 12 km and InMAP 1 km predictions for $PM_{2.5}$ subgroups—primary $PM_{2.5}$, particulate nitrate (pNO_3), particulate ammonium (pNH_4), particulate sulfate (pSO_4), and secondary organic aerosol SOA—with the corresponding WRF-Chem predictions. InMAP primary $PM_{2.5}$ area-weighted averages (Figure 6.4a-d) agree with WRF-Chem very well, with an R^2 value of 0.97 and a mean fractional bias of -4% for InMAP 12 km. The same general patterns hold for primary $PM_{2.5}$ that were described for total $PM_{2.5}$: InMAP tends to overpredict population-weighted averages, and higher population-weighted averages are predicted by InMAP 1 km than by InMAP 12 km.

InMAP reproduces WRF-Chem predictions of changes in pNO_3 concentrations with moderate fidelity (InMAP 12 km area-weighed R^2 = 0.59, population-weighed R^2 = 0.45). This outcome is because the chemistry that drives pNO_3 creation is highly temporally variable across both diurnal and seasonal scales, and therefore is perhaps more challenging to represent in a steady-state, annual average model such as InMAP.

InMAP predictions of pNH_4 are better correlated with WRF-Chem for population-weighted averages (InMAP 12-km R^2 = 0.77) than they are for area-weighted averages (InMAP 12 km R^2 = 0.64). However, InMAP also tends to substantially overpredict population-weighted pNH_4 averages (InMAP 12 km regression line slope = 3.0) even though it does not especially overpredict area-weighted averages relative to WRF-Chem (InMAP 12-km regression line slope = 1.23). This result may be partially caused by my assumption that the partitioning ratio between gaseous NH_3 and particulate NH_4 is the same for marginal changes in concentrations as it is for total ambient concentrations. That assumption may not be realistic in all cases as this partitioning is governed by complex and nonlinear relationships.

For pSO_4, InMAP predictions agree well with WRF-Chem (InMAP 12 km area-weighted R^2 = 0.76, population-weighted R^2 = 0.99). This good agreement is expected because pSO_4 formation is governed by a set of comparatively simple and slow-acting chemical mechanisms as described in Section 6.3.1. However, InMAP somewhat underpredicts changes in area-weighted concentrations and overpredicts changes in population-weighted concentrations. This overprediction is likely caused by the issue with temporal correlation described above.

For secondary organic aerosol (SOA), InMAP tends to substantially underpredict changes in concentrations relative to WRF-Chem (InMAP 12-km area-weighted average model ratio = 0.1). This may be because when calculating partitioning coefficients, InMAP assumes that all volatile organic chemical (VOC) species contribute equally to SOA formation, but in reality (and in WRF-Chem) lower-volatility species form SOA more readily than do higher-volatility species. For the emissions scenarios considered—with emissions from a combination of transportation, electric generation, agricultural and assorted industrial sources—SOA does not make a large contribution to changes in total $PM_{2.5}$ concentrations, so poor performance

in SOA prediction does not substantially affect predictive performance for total $PM_{2.5}$.

Figures 6.6–6.11 show InMAP performance in reproducing WRF-Chem predictions disaggregated by region of U.S. region (region boundaries are shown in Figure 6.5). Figure 6.6 shows InMAP predictive performance for total $PM_{2.5}$. In general performance is worst in the West region; I will offer possible explanations for this in the course discussing predictions of the subspecies that make up total $PM_{2.5}$. Predictive performance is for primary $PM_{2.5}$ (Figure 6.7) is also poorer in the West region than in other regions. This result is possibly because, as changes in emissions per unit land area in these scenarios are typically lower in the West than in other regions, a larger fraction of changes in concentrations in the West are caused by long-range transport than is the case in other regions. Performance for particulate sulfate (Figure 6.9) is similar to that of primary $PM_{2.5}$, with predictive performance in the West region being lower than elsewhere, possibly for the same reason. There are not any clear patterns in performance for particulate nitrate (Figure 6.9), particulate ammonium (Figure 6.9), or secondary organic aerosol (Figure 6.11), with the exception of the relatively high accuracy for particulate nitrate in the Midwest region. Because particulate nitrate formation is strongly temperature dependent (*128*), the relatively colder temperatures in the Midwest region may cause this process to be more reliably represented by the simplified approach used here.

6.5 Discussion

I have presented here a new air quality model for determining the human health impacts of marginal changes in pollutant emissions. It is freely available at `https://github.com/ctessum/inmap`. InMAP is reduced in complexity compared to comprehensive chemical transport models but more theoretically robust than the models typically used by researchers who are not air quality modeling specialists or for studies that do not have the resources to use a CTM to carry out all of the desired simulations. One of these existing models is the COBRA model, which I show performs comparably to the InMAP model presented here in terms of reproducing WRF-Chem changes in population-weighted average concentrations. InMAP, however, has features

and capabilities that make it better suited than COBRA or any other existing model for certain use cases (e.g., for simulations where it is desirable to estimate within-city differences in $PM_{2.5}$ concentrations).

One unique attribute of InMAP is its ability to perform analyses with large spatial domains combined with high spatial resolution in high-population areas. Figure 6.12 shows a small area of the maps in Figure 6.2 centered around the city of Los Angeles. In this figure it can be seen that the COBRA model represents all of Los Angeles county, including Santa Catalina Island, as having the same $PM_{2.5}$ concentration. WRF-Chem, as configured here, is able to resolve differences in pollutant levels at a 12 km scale for the contiguous U.S. (If the size of the total spatial domain were decreased to only include the city of Los Angeles, WRF-Chem could resolve differences at a 1 or 2 km scale.) InMAP is unique among existing models in that it can model changes in pollutant concentrations across an entire continent with 1 km spatial resolution in all high-population areas, all in a single model run.

The ability to perform high-resolution analyses in high-population areas is useful because as shown above and in Chapter 4, higher resolution analyses tend to yield higher, and arguably more accurate, estimates of population exposure to $PM_{2.5}$. Additionally, high resolution modeling is necessarily for certain types of analyses, such as those that seek to determine how pollution exposure differs among demographic groups of people or among different neighborhoods within cities.

InMAP is much less computationally intensive than are comprehensive chemical transport models. For example, 1 km InMAP produces the results for each of the scenarios shown here in approximately 45 minutes on a desktop computer, requiring a factor of $\sim$25,000 less computational power than was required to produce the WRF-Chem results shown here. This computational speed-up makes possible uncertainty, sensitivity, and scenario analyses that could not be attempted with WRF-Chem or other comprehensive chemical transport models.

As discussed above, there are some limitations that should be taken into consideration when using InMAP. Possibly owing to its use of annual average coefficients for turbulent and convective vertical mixing, InMAP tends to overpredict changes in $PM_{2.5}$ concentrations near

emissions sources and underpredict changes in concentrations far from emissions sources as compared to WRF-Chem.

Additionally, InMAP is more skilled at predictions of changes in primary $PM_{2.5}$ and pSO_4 concentrations than it is in predicting changes in pNO_3, pNH_4, and especially SOA concentrations. In the case of the emissions scenarios tested here, changes in SOA concentrations do not make up a large fraction of total $PM_{2.5}$, so overall model performance is not substantially degraded by poor prediction of SOA concentrations; however, further testing is needed before using InMAP for emissions scenarios where SOA does contribute a large fraction of total $PM_{2.5}$, such as, for example, forest fires.

Finally, InMAP does not predict concentrations of ground-level ozone (O_3), which is considered the distant-second largest source of human health burden from air pollution after $PM_{2.5}$ (*9*). A future version of InMAP, which included more comprehensive mechanisms for gas- and aerosol-phase and iterated through diurnal cycles representative of each season of the year instead of using annual average information, could reduce or remove most or all of these limitations. This future version would by necessity be more computationally intensive than the current version and require more user input information, however, so increased predictive power would come at the expense of speed and flexibility.

The analyses I have presented here have been for the contiguous U.S. The main requirement to use InMAP for a different spatial or temporal domain is output from a comprehensive chemical transport model for the new region. By producing an air quality model that is computationally inexpensive to operate, relatively easily adaptable to new geographical regions, and able to be operated with a relatively low level of specialist knowledge, I hope to make air quality modeling more accessible to scientists, policymakers, and concerned citizens worldwide.

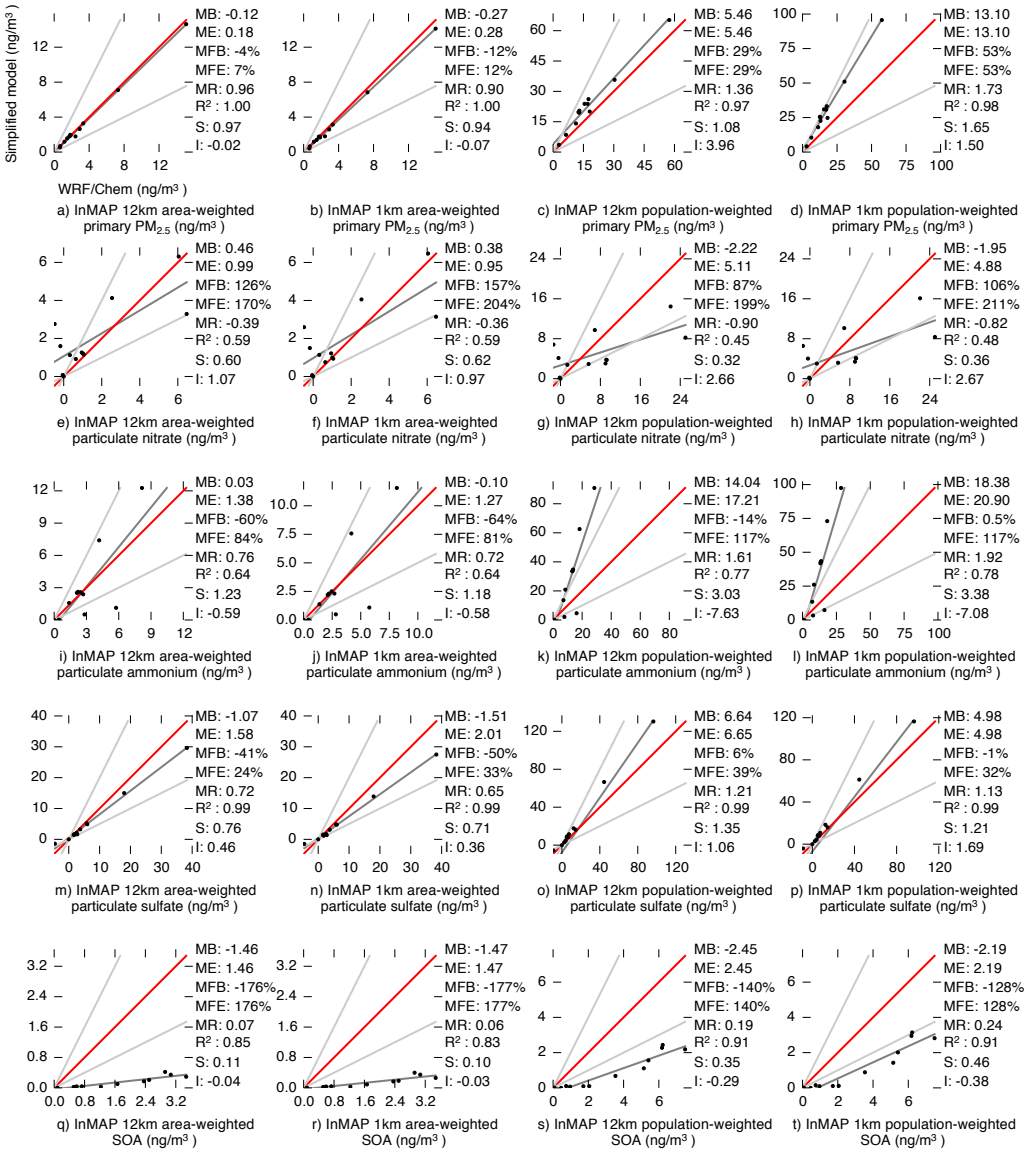

Figure 6.4: Comparison of area-weighted (left two columns) and population-weighted (left two columns) annual average predictions of $PM_{2.5}$ subspecies between WRF-Chem (x-axis) and InMAP (y-axis) for 11 emissions scenarios. The red line represents 1:1 ratio of InMAP:WRF-Chem predictions, the light gray lines represent InMAP:WRF-Chem ratios of 2:1 and 1:2, and the dark gray line represents a least-squares regression between InMAP and WRF-Chem predictions. Abbrevations: MB=mean bias; ME=mean error; MFB=mean fractional bias; MFE=mean fractional error; MR=model ratio; S=slope of regression line; I=intercept of regression line.

Figure 6.5: Boundaries of U.S. regions used here.

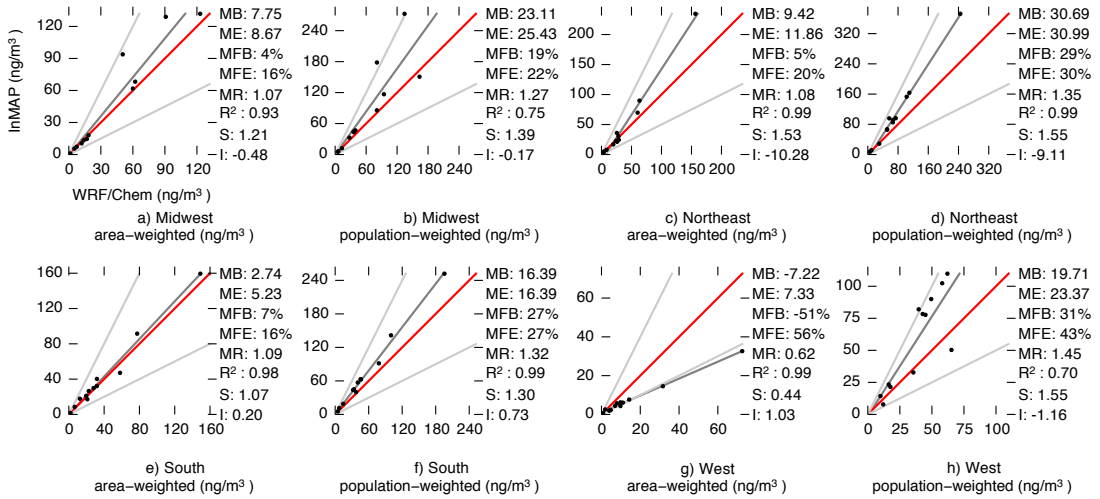

Figure 6.6: Region-specific comparison of area-weighted and population-weighted annual average predictions of **total $PM_{2.5}$** between WRF-Chem (x-axis) and InMAP (y-axis) for 11 emissions scenarios. The red line represents 1:1 ratio of InMAP:WRF-Chem predictions, the light gray lines represent InMAP:WRF-Chem ratios of 2:1 and 1:2, and the dark gray line represents a least-squares regression between InMAP and WRF-Chem predictions. Abbrevations: MB=mean bias; ME=mean error; MFB=mean fractional bias; MFE=mean fractional error; MR=model ratio; S=slope of regression line; I=intercept of regression line.

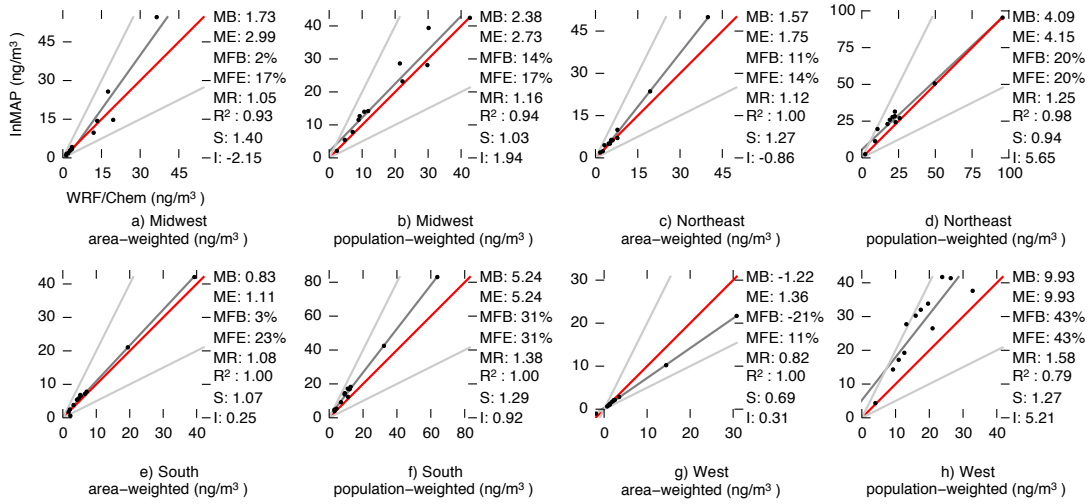

Figure 6.7: Region-specific comparison of area-weighted and population-weighted annual average predictions of **primary $PM_{2.5}$** between WRF-Chem (x-axis) and InMAP (y-axis) for 11 emissions scenarios. The red line represents 1:1 ratio of InMAP:WRF-Chem predictions, the light gray lines represent InMAP:WRF-Chem ratios of 2:1 and 1:2, and the dark gray line represents a least-squares regression between InMAP and WRF-Chem predictions. Abbrevations: MB=mean bias; ME=mean error; MFB=mean fractional bias; MFE=mean fractional error; MR=model ratio; S=slope of regression line; I=intercept of regression line.

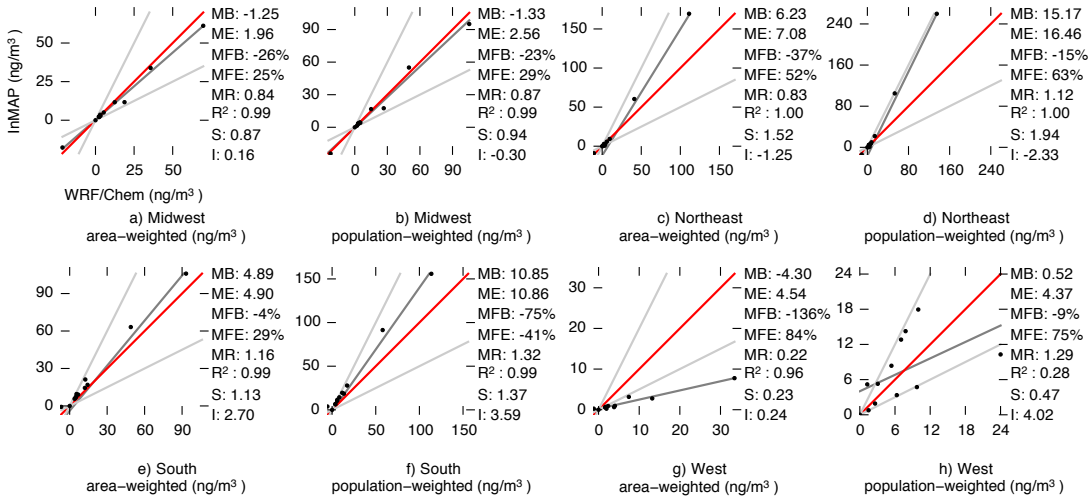

Figure 6.8: Region-specific comparison of area-weighted and population-weighted annual average predictions of **sulfate $PM_{2.5}$** between WRF-Chem (x-axis) and InMAP (y-axis) for 11 emissions scenarios. The red line represents 1:1 ratio of InMAP:WRF-Chem predictions, the light gray lines represent InMAP:WRF-Chem ratios of 2:1 and 1:2, and the dark gray line represents a least-squares regression between InMAP and WRF-Chem predictions. Abbrevations: MB=mean bias; ME=mean error; MFB=mean fractional bias; MFE=mean fractional error; MR=model ratio; S=slope of regression line; I=intercept of regression line.

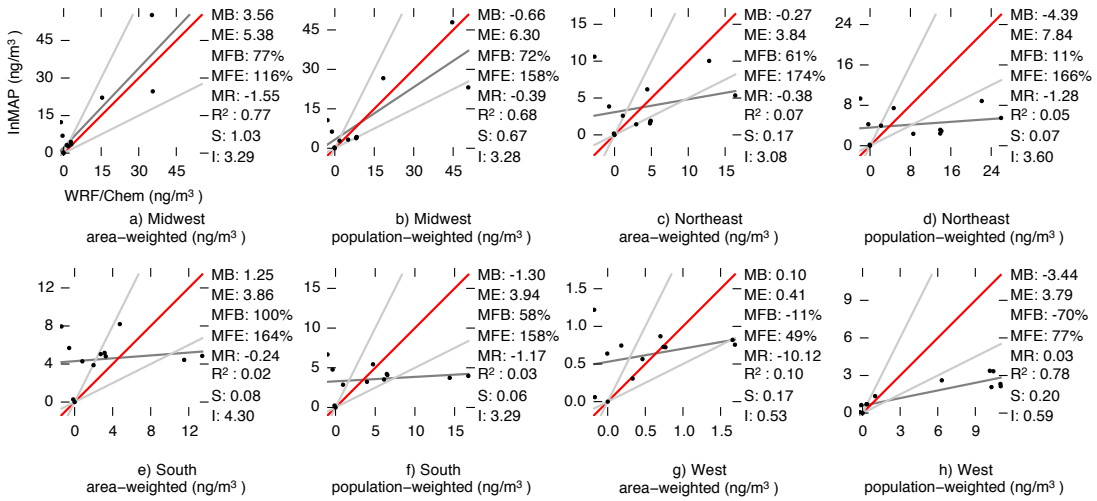

Figure 6.9: Region-specific comparison of area-weighted and population-weighted annual average predictions of **nitrate $PM_{2.5}$** between WRF-Chem (x-axis) and InMAP (y-axis) for 11 emissions scenarios. The red line represents 1:1 ratio of InMAP:WRF-Chem predictions, the light gray lines represent InMAP:WRF-Chem ratios of 2:1 and 1:2, and the dark gray line represents a least-squares regression between InMAP and WRF-Chem predictions. Abbreviations: MB=mean bias; ME=mean error; MFB=mean fractional bias; MFE=mean fractional error; MR=model ratio; S=slope of regression line; I=intercept of regression line.

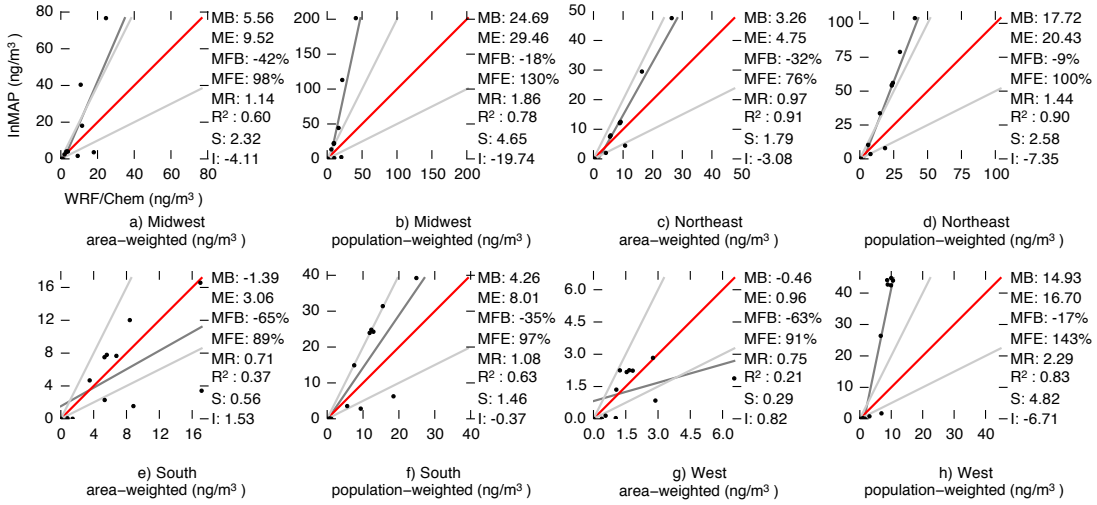

Figure 6.10: Region-specific comparison of area-weighted and population-weighted annual average predictions of **ammonium $PM_{2.5}$** between WRF-Chem (x-axis) and InMAP (y-axis) for 11 emissions scenarios. The red line represents 1:1 ratio of InMAP:WRF-Chem predictions, the light gray lines represent InMAP:WRF-Chem ratios of 2:1 and 1:2, and the dark gray line represents a least-squares regression between InMAP and WRF-Chem predictions. Abbreviations: MB=mean bias; ME=mean error; MFB=mean fractional bias; MFE=mean fractional error; MR=model ratio; S=slope of regression line; I=intercept of regression line.

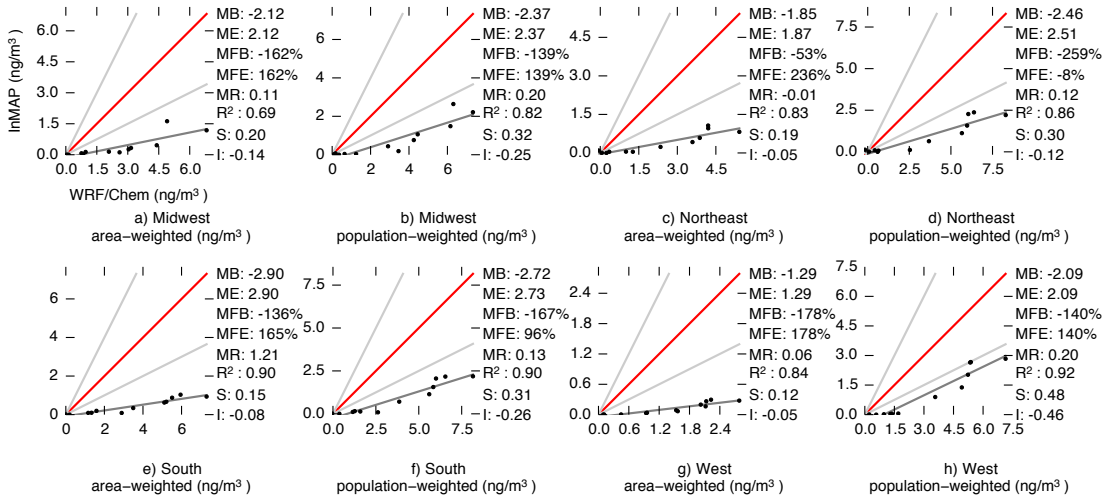

Figure 6.11: Region-specific comparison of area-weighted and population-weighted annual average predictions of **secondary organic $PM_{2.5}$** between WRF-Chem (x-axis) and InMAP (y-axis) for 11 emissions scenarios. The red line represents 1:1 ratio of InMAP:WRF-Chem predictions, the light gray lines represent InMAP:WRF-Chem ratios of 2:1 and 1:2, and the dark gray line represents a least-squares regression between InMAP and WRF-Chem predictions. Abbrevations: MB=mean bias; ME=mean error; MFB=mean fractional bias; MFE=mean fractional error; MR=model ratio; S=slope of regression line; I=intercept of regression line.

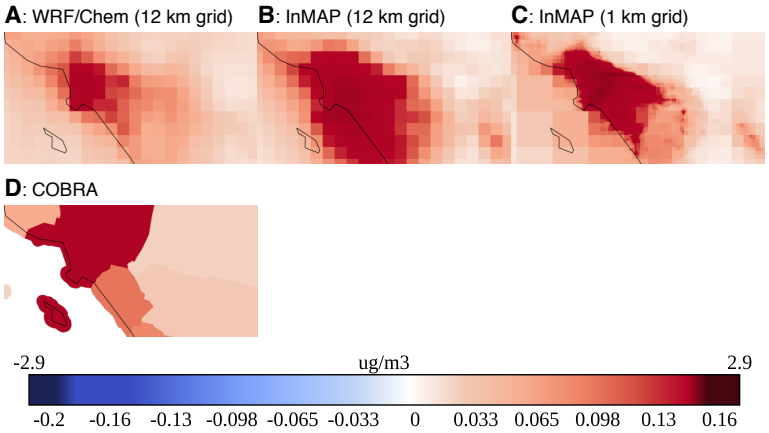

Figure 6.12: A detail view of Figure 6.2 centered on the city of Los Angeles. Changes in concentrations resulting from one of the emissions scenarios as calculated by A) the WRF-Chem, B) InMAP with a 12 km resolution grid, C) InMAP with a 1 km to 36 km variable resolution grid, and D) COBRA.

Chapter 7

Environmental Injustice and Inequality Implications of Conventional and Alternative Light-Duty Transportation in the United States

7.1 Summary

Human exposure to environmental hazards, including air pollution, is often unequally distributed within a population (environmental inequality) and among income, social class, and racial subpopulations (environmental injustice). In this chapter, I investigate how future alternative light-duty transportation fuels and technologies may impact inequality and injustice in air quality-related health burdens. I find that alternative fuel and technology scenarios that decrease the overall air quality-related health impacts from light-duty transportation can also serve to mitigate environmental injustice, but not necessarily environmental inequality,

compared to business-as-usual. Light-duty transportation scenarios that increase environmental injustice tend to do so for Hispanics, Blacks, and Asians, but not for American Indians. Race- and ethnicity-based differences in exposure are larger than are income-based differences, and in many cases race- and ethnicity-based exposure differences increase after adjusting for difference in income. Additionally, for the emissions scenarios investigated here, higher-resolution air quality modeling tends to result in predicted pollutant exposures that are more unjust than those predicted by lower-resolution air quality modeling.

7.2 Introduction

Human exposure to environmental hazards, including air pollution, is often unequally distributed across social class and, especially, racial divisions within a population (*208*, *209*). These systematic differences in exposures are undesirable from the ethical standpoint that groups of people should not be exposed to systematic differences in opportunity, including the opportunity to have good health (*210*). Systematic differences in opportunity are viewed as unjust, so systematic differences across groups of people in exposure to environmental hazards are generally referred to as *environmental injustice*.

In addition to avoiding systematic differences in hazard exposure among subpopulations, it may also be desirable to avoid excessively large variability in exposure within the overall population. The variability in exposure to hazards among individuals is generally called *environmental inequality*. Others have argued that unlike income inequality, which may be desirable in limited amounts, environmental inequality yields no social benefits (*210*).

In general, air quality interventions typically aim to reduce the overall public health burden caused by air pollution (e.g., (*109*)). In the United States, government agencies are also tasked with make achieving environmental justice a part of their mission (*211*). In light of these considerations and the discussion above, the most effective air quality policies would be those that simultaneously minimize overall public health burden, injustice in environmental health burden, and inequality in environmental health burden.

In the U.S., people who are non-White or living in poverty have higher average exposure to NO_2 air pollution than the overall population (*212*). Ideally interventions to improve overall air quality would also decrease these race- and income-based exposure disparities.

This chapter expands on the work described in Chapter 4: that earlier chapter investigated a range of alternative fuel and technology options for reducing the total air pollution-related health impacts from the light duty transportation sector; here, I investigate impacts on environmental injustice for poor and non-white individuals, environmental inequality, and total health impacts of each of these scenarios.

7.3 Methods

7.3.1 Emissions scenarios

Emissions scenarios here are the same as those described in Chapter 4. Briefly, I use a spatially and temporally explicit life cycle inventory model (described in Chapter 2) to estimate total supply chain air pollutant emissions for scenarios where 10% of U.S. projected vehicle miles traveled in year 2020 are undertaken in one of eleven types of passenger cars: 1) conventional gasoline powered vehicles (abbreviation: "gasoline"); 2) grid-independent hybrid electric vehicles ("gasoline hybrid"); 3) diesel powered cars ("diesel"); 4) internal-combustion compressed natural gas vehicles ("CNG"); 5) vehicles powered by ethanol from corn grain through natural-gas powered dry milling ("corn ethanol"); 6) vehicles powered by cellulosic ethanol from corn stover ("stover ethanol"); and battery electric vehicles ("EV") powered by: 7) the projected 2020 U.S. average electric generation mix ("EV grid average"); 8) electricity from coal ("EV coal"); 9) electricity from natural gas ("EV natural gas"); 10) electricity generated by combustion of corn stover ("EV corn stover"); and 11) electricity generated by wind turbines, dynamic water power, or solar power ("EV WWS").

7.3.2 Air quality modeling

To predict how each emissions scenario affects ambient average concentrations of $PM_{2.5}$, I primarily use the InMAP model described in Chapter 6. InMAP is well suited for environmental justice calculations because population demographics (e.g., race and income) can vary substantially between adjacent neighborhoods within an urban area and InMAP is able to perform air quality analyses at a spatial scale fine enough (as configured here: 1 km in high-population areas) to capture intra-urban variability in air pollutant concentrations. The 12-km gridded results from the WRF-Chem analyses in Chapter 4 typically cover entire cities with just a few grid cells (see Figure 6.12). However, because InMAP's representation of the atmosphere is reduced in complexity as compared to WRF-Chem, I also repeat the analyses here using the WRF-Chem simulation results described in Chapter 4.

7.3.3 Health impact assessment

Once I have estimates for the changes in pollutant concentration caused by each scenario, I estimate public health impacts using the methodology described in 4.3.4, with the exception that in addition to calculating the health impacts to the entire U.S population, I calculate separate impacts to specific subgroups. The subgroups employed here, which are from the year-2012 U.S. Census Bureau American Community Survey (*213*, *214*), are shown in Table 7.1. Population and income data employed here are spatially aggregated by block group. As shown in Chapter 6, the modeling domain is the contiguous U.S., which excludes Alaska, Hawaii, and Puerto Rico. The domain contains 220,000 block groups, of which the median block group is 1.3 km^2 (mean=36 km^2) and contains 1,200 people (mean=1,400). In order to preserve block group-level differences in race and income, I allocate the concentration results from the air quality model spatial grid to block groups, using area-weighting for block groups that are not completely covered by a single grid cell.

In addition to investigating how exposures differ among the race, ethnicity, and population groups above, I also estimate how exposures differ among racial groups after accounting for

Table 7.1: Demographic Groups Used for Environmental Justice Calculations

Census category	Population in millions (% of total U.S. population)	Abbreviation used here	Percent urban
Total population	307 (98%[a])	—	56%
Not Hispanic or Latino: White alone	196 (63%)	White	46%
All people not in the "White" category	110 (35%)	Non-White	72%
Hispanic or Latino (all races)	50 (16%)	Hispanic	74%
Not Hispanic or Latino: Black or African American alone	38 (12%)	Black	71%
Not Hispanic or Latino: Asian alone	14 (5%)	Asian	80%
Not Hispanic or Latino: Native Hawaiian and other Pacific Islander alone; Some other race alone; or two or more races	7 (2%)	Other	62%
Not Hispanic or Latino: American Indian and Alaska Native alone	2 (1%)	American Indian	31%
Population for whom poverty status is determined, with income less than the poverty limit	45 (14%)	In-poverty	62%
Population for whom poverty status is determined, with income more than 2 times the poverty limit.	199 (64%)	2× poverty line	54%

[a]The remaining 2% live outside of my contiguous U.S. modeling domain

differences in income. The American Community Survey releases block group-level data on median annual household income (in year-2012 inflation-adjusted dollars), but this data is only disaggregated by the racial group of the householder, rather than the race-ethnicity categories in Table 7.1. Therefore I estimate income-adjusted exposures for the groups in Table 7.2.

7.3.4 Income adjustment

To examine the exposure difference among races independent of differences in income, for a subset of analyses I statistically account for and then remove the impact of income for each

Table 7.2: Demographic Groups Used for Income-Adjusted Environmental Justice Calculations

Census category	Population in millions (% of total U.S. population)	Average income[a]	Abbreviation used here	Percent urban
Not Hispanic or Latino: White alone	196 (63%)	$66,000	White	46%
Hispanic or Latino (all races)	50 (16%)	$49,000	Hispanic	74%
Black or African American alone (both Hispanic and non-Hispanic)	39 (12%)	$43,000	Black	72%
Asian alone (both Hispanic and non-Hispanic)	14 (5%)	$87,000	Asian	80%
American Indian and Alaska Native alone (both Hispanic and non-Hispanic)	2 (1%)	$40,000	American Indian	38%

[a]Average income is the population-weighted mean of median income in each block group

of the demographic groups in Table 7.2. I do this by performing a linear regression using the R statistical software v3.1.1 (*215*). In this regression, the dependent variable is the increase in risk (deaths per 100,000 people) attributable to a scenario in each block group, and the independent variables are: 1) the difference between the median income in the block group and the national year-2012 median income of $51,371 (*216*), and 2) the square of that difference to account for non-linear effects. The regression algorithm returns coefficients for the two independent variables and an intercept; the intercept is the income-adjusted risk.

7.3.5 Environmental injustice and inequality assessment

Once I have estimated the health damages to each demographic group caused by each emissions scenario, I can use metrics to determine the impact of each scenario on environmental injustice and inequality.

To measure environmental injustice, I evaluate whether per-capita health damages to one group are more or less than damages to another group. This difference is the *risk difference*

(RD) as defined in Equation 7.1:

$$RD_s = \frac{\Delta M_{a,s}}{P_a} - \frac{\Delta M_{b,s}}{P_b} \tag{7.1}$$

where ΔM is the number of mortalities in group a or b attributable to emissions scenario s and P is the total population of group a or b. Group a is defined as the more vulnerable group (in-poverty and/or non-White individuals) so that a positive value of RD_s indicates that scenario s yields greater environmental health risks to the more vulnerable population.

There are a number of available metrics of inequality. Here I use the population-weighted Atkinson index with $\epsilon = 0.75$ as well as the population-weighted extended Gini index (*217*), both as implemented in the R statistical software v3.1.1 (*215*) package IC2 (*218*). With both of these indices, a value of zero indicates perfect equality (i.e., all individuals are exposed to the same amount of pollution) and a value of one indicates perfect inequality (i.e. one individual is exposed to all of the pollution and all other individuals are exposed to none). Because inequality indices are designed to measure inequality in benefits, but air pollution-related health impacts are burdens, before inputting the health damages into the inequality formulas, I subtract all values from a constant large enough so that all values are greater than zero. Specifically, the constant I use is 1.001 times the larger of either the maximum risk value or the range between the maximum and minimum risk values. Note that the inequality results reported here can only be compared to other studies if the same subtraction method is used.

In all cases, I am interested in estimating how environmental injustice and inequality will *change* as a result of the proposed transportation scenarios. Therefore, I first calculate the demographic disparity or inequality in risk caused by the baseline $PM_{2.5}$ concentrations discussed in Chapter 3, and then I subtract it from the inequality in baseline risk added to the risk caused by the concentration increases attributable to each scenario.

7.4 Results

7.4.1 Race-ethnicity- and income-based disparities

Figure 7.1 shows risk differences for non-White vs. White individuals and in-poverty vs. 2× poverty line individuals for the air quality-related health damages attributable to each emissions scenario. For the non-White vs. White comparison, all alternative scenarios are more environmentally just than the business-as-usual gasoline scenario.The scenarios with the lowest overall impacts, EVs powered by natural gas, wind, water, or solar electricity, are also among the most environmentally just.

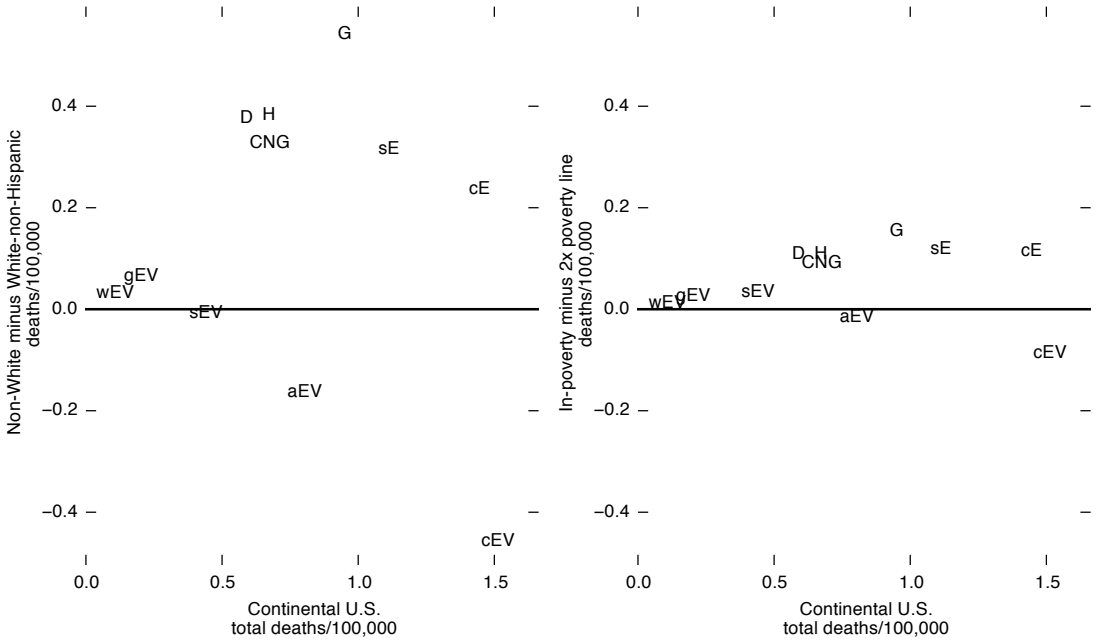

Figure 7.1: Risk difference in air quality-related health burdens in poor non-White vs. White and in-poverty vs. 2× poverty line individuals. Abbreviations: G=gasoline; H=gasoline hybrid; D=diesel; CNG=compressed natural gas; cE=corn ethanol; sE=stover ethanol; aEV=electric vehicle (EV) grid average; cEV=EV coal; gEV=EV natural gas; sEV=EV corn stover; wEV=EV wind, water, and solar.

In all cases except for stover EVs, there is a greater difference between White and non-White damages than there is between in-poverty and 2× poverty line damages. This finding

is broadly consistent with the previous finding that NO_2 exposure disparities are greater for differences by race than for differences income (*212*).

In general, scenarios with internal combustion vehicles tend to cause greater health effects for non-Whites and in-poverty individuals, whereas EV scenarios tend to cause greater health effects for Whites and 2× poverty line individuals. The fact that electrical generating units tend to be located in rural areas, where there is a lower fraction of nonwhites and a lower fractions of households below the poverty line (Table 7.1) underlies both of these trends. The corn ethanol and corn stover ethanol scenarios, which create emissions from a combination of vehicle tailpipe and agricultural sources, tend to be more unjust than the EV scenarios but less unjust than the gasoline and diesel scenarios.

Figures 7.2 and 7.3 are versions of Figure 7.1 where calculations are performed using InMAP with a 12-km grid and WRF-Chem with a 12-km grid, respectively, instead of using InMAP with a 1-km variable resolution grid as in Figure 7.1. Comparing the 1-km InMAP results in Figure 7.1 to the 12-km InMAP results in Figure 7.2 shows that the higher-spatial resolution analysis generally yields results that are more unjust (greater calculated disparities) than does the lower-spatial resolution analysis. At least two factors contribute to this result: (1) the higher-resolution analysis picks up intra-urban differences in exposure among demographic groups that the lower-resolution analysis is unable to resolve. (2) InMAP tends to over-predict concentrations near sources and underpredict concentrations far from sources; therefore, InMAP may be exaggerating differences in exposure, especially near-source exposure.

Ideally, Figures 7.2 and 7.3 would be identical because they are based on the same emissions scenarios and use the same spatial grid. In practice, InMAP is a reduced complexity model and does not exactly reproduce the WRF-Chem results, including for environmental justice. For example, the 12-km InMAP results in Figure 7.2 show that non-Whites are more exposed than Whites to emissions from corn ethanol vehicles, but the WRF-Chem results in Figure 7.3 show the opposite. Nevertheless, general patterns in the results are the same for the two models and the conclusions described above (e.g., internal combustion vehicles cause greater

environmental injustice than do EVs) using the 1-km InMAP results also hold for the 12-km InMAP and the WRF-Chem results.

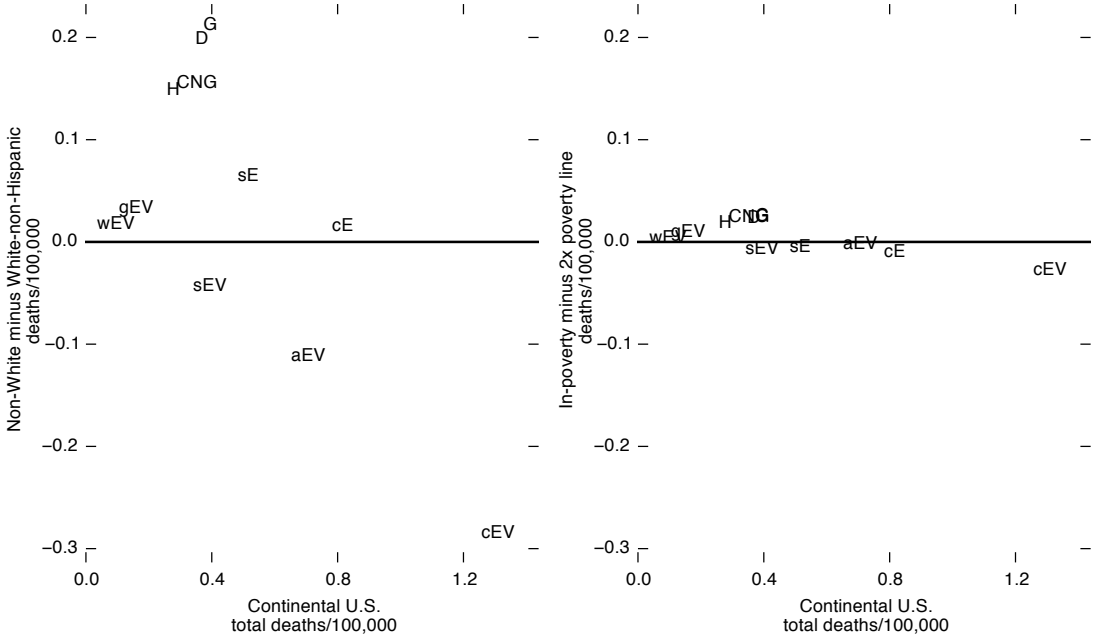

Figure 7.2: Sensitivity analysis of risk difference in non-White vs. White and in-poverty vs. 2× poverty line individuals for each emissions scenario, using 12-km InMAP results instead of 1-km InMAP. Abbreviations: G=gasoline; H=gasoline hybrid; D=diesel; CNG=compressed natural gas; cE=corn ethanol; sE=stover ethanol; aEV=electric vehicle (EV) grid average; cEV=EV coal; gEV=EV natural gas; sEV=EV corn stover; wEV=EV wind, water, and solar.

7.4.2 Detailed race-ethnicity- and income-based disparities by U.S. region

Figure 7.4 shows air quality burdens to non-White individuals relative to White individuals disaggregated by U.S. region (region boundaries are shown in Figure 6.5). Health damages from coal EVs are the largest and the most biased toward Whites in the Northeast region, owing to the concentration of coal-powered electricity generating units in that region, which tend to be in rural areas. Health damages from ethanol are the largest and the most biased toward non-Whites in the Midwest region, owing to the agricultural activities and emissions in that region. Note that this disparity in Midwest ethanol scenario impacts does not appear

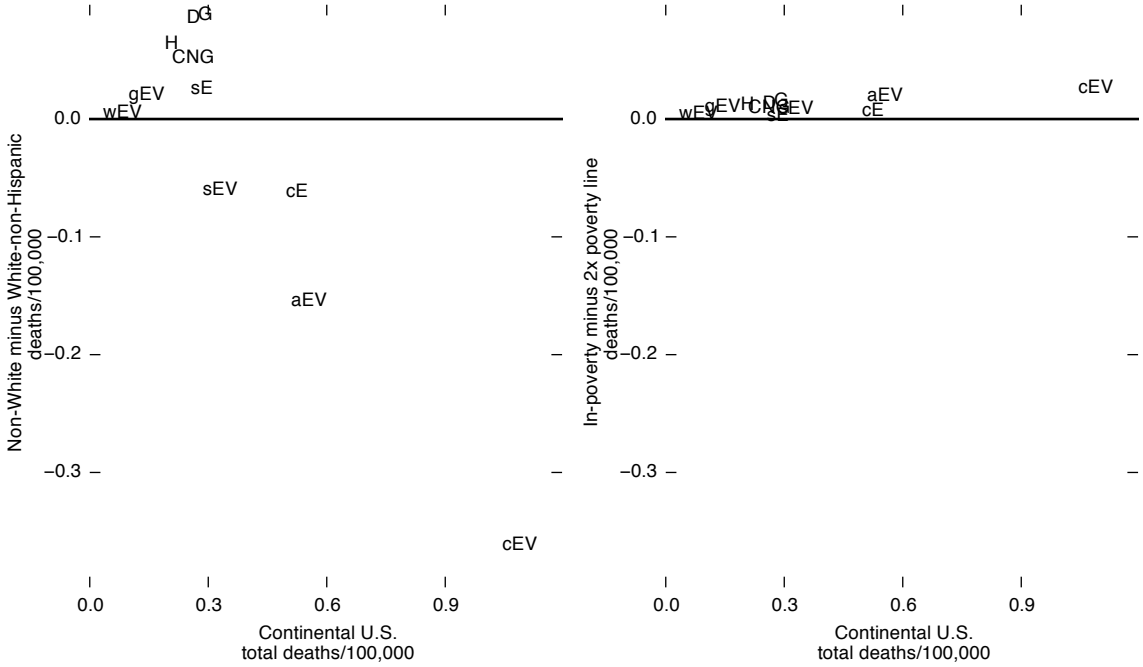

Figure 7.3: Sensitivity analysis of risk difference in air quality-related health burdens in non-White vs. White and in-poverty vs. 2× poverty line individuals. for each emissions scenario, using 12-km WRF-Chem results instead of 1-km InMAP. Abbreviations: G=gasoline; H=gasoline hybrid; D=diesel; CNG=compressed natural gas; cE=corn ethanol; sE=stover ethanol; aEV=electric vehicle (EV) grid average; cEV=EV coal; gEV=EV natural gas; sEV=EV corn stover; wEV=EV wind, water, and solar.

in the WRF-Chem results (Figure 7.7) and may be an artifact of InMAP overpredictions of particulate ammonium concentrations (Figure 6.4). Gasoline scenario impacts are more biased toward non-Whites in the West region than elsewhere in the U.S.

Figure 7.5 shows air quality burdens to non-White, Hispanic, Black, Asian, American Indian and Other individuals relative to White individuals, and burdens to in-poverty relative to 2× poverty-line individuals, disaggregated by U.S. region. In general, injustice to Hispanics and Asians is similar to injustice to the average for non-Whites, but Blacks tend to exposed more than the average for non-Whites. In most scenarios and regions, American Indians' exposure to air pollution is less than average non-Whites' exposure, likely because American Indians tend to live in areas that are more rural than the average for non-Whites (Table 7.1).

Figures 7.6 and 7.7 show sensitivity analyses of these effects using the 12-km InMAP and WRF models, respectively. The results are similar among the three models, again with 1-km InMAP showing the largest health burden and inequality.

7.4.3 Income adjusted race-based disparities

Figure 7.8 shows $PM_{2.5}$-related health burdens to Hispanic, Black, Asian, and American Indian individuals relative to health burdens to Whites after accounting for differences in income. Coefficients for income dependence are in Appendix F. Results are very similar to the non-income-adjusted results in Figure 7.5, suggesting that race is a bigger driver for environmental injustice than is income. In fact, in many cases differences in exposure between Whites and non-Whites are larger after adjusting for income differences. This increase in disparities with income adjustment occurs because in many cases exposure for Whites and American Indians tends to increase with increasing income, whereas exposure for Hispanics, Blacks, and Asians tends to decrease with increasing income. Figure 7.9 shows an example of this effect for the gasoline scenario.

7.4.4 Inequality

Figure 7.10 shows the change in Atkinson and extended Gini indices of inequality in air quality-related human health damages caused by each of the scenarios. Both indices yield similar trends: most scenarios do not cause significant changes in $PM_{2.5}$ exposure inequality from the baseline, with the exception of the EV coal and EV grid average scenarios, which have the effect of decreasing inequality as compared to the baseline. Figures 7.11 and 7.4.4 show sensitivity analyses for environmental inequality impacts using the 12-km InMAP and WRF-Chem models. These lower-resolution models both estimate changes in inequality that are more than an order of magnitude lower than 1-km InMAP estimates, suggesting that the largest inequality is at fine spatial scales that cannot be resolved with a 12-km model grid. These figures differ from the figures above in that values below zero indicate reductions in inequality from the baseline exposure level.

7.5 Discussion

I have shown here that interventions to decrease the overall air quality-related health impacts from light-duty transportation can also serve to mitigate environmental injustice, but not necessarily environmental inequality, compared to business-as-usual. Light-duty transportation scenarios that increase environmental injustice tend to do so for Hispanics, Blacks, and Asians, but not for American Indians. Race- and ethnicity-based differences in exposure are larger than are income-based-differences, and in many cases race- and ethnicity-based exposure differences increase after adjusting for difference in income. Additionally, using InMAP I have shown that, for the emissions scenarios investigated here, higher-resolution air quality modeling tends to result in predicted pollutant exposures that are more unjust than those predicted by lower-resolution air quality modeling.

The analysis here is somewhat limited by its use of census data in determining exposure to air pollution. The U.S. Census reports where people live, but people typically do not spend all of their time at home. Some portion of people's air pollution exposure may occur outside of the home, for instance at work and while commuting. Future analyses could expand on the work here by also including pollution exposures incurred while away from home.

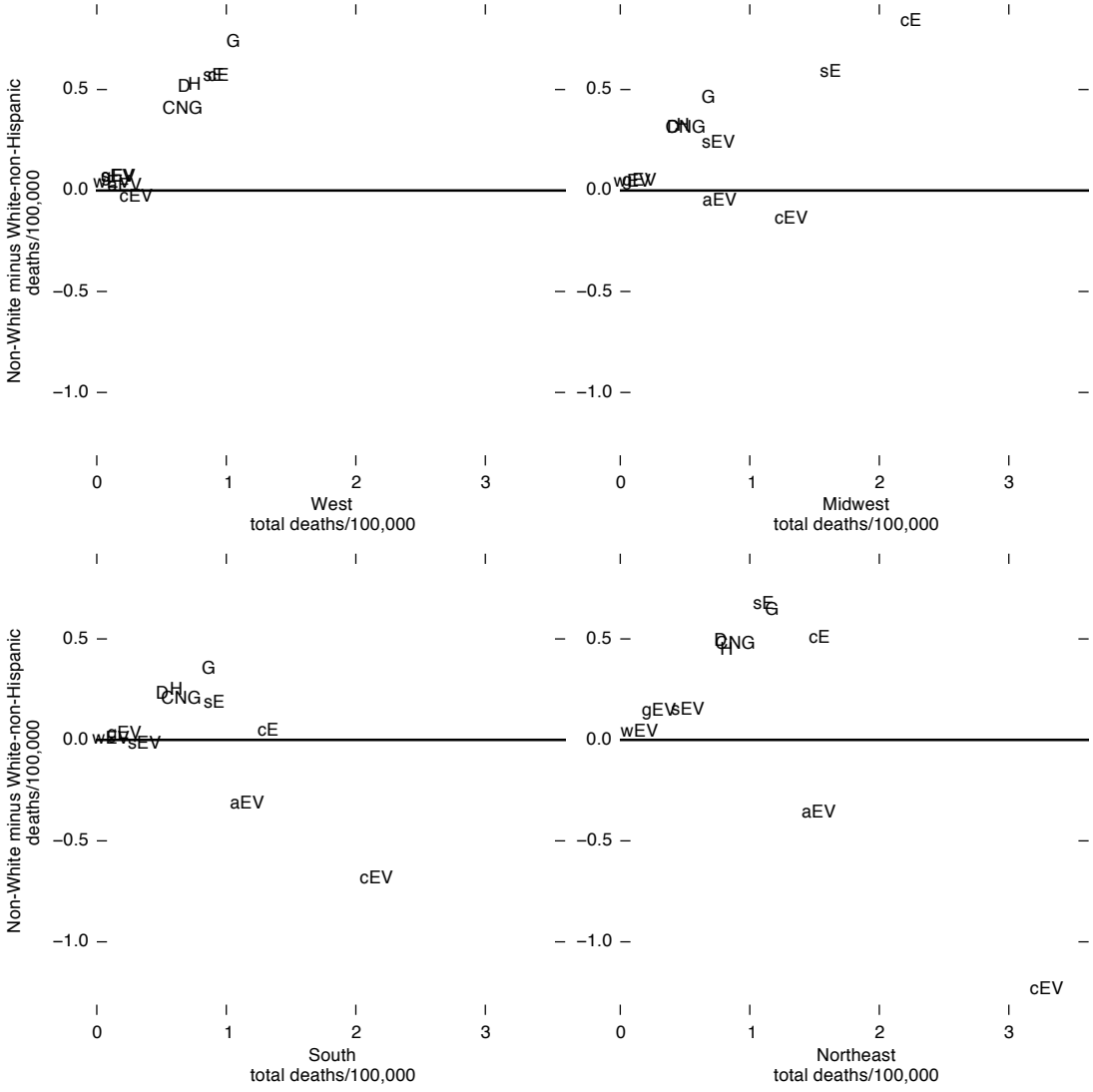

Figure 7.4: Risk difference in air quality-related health burdens in non-White vs. White individuals, disaggregated by U.S. region. Abbreviations: G=gasoline; H=gasoline hybrid; D=diesel; CNG=compressed natural gas; cE=corn ethanol; sE=stover ethanol; aEV=electric vehicle (EV) grid average; cEV=EV coal; gEV=EV natural gas; sEV=EV corn stover; wEV=EV wind, water, and solar.

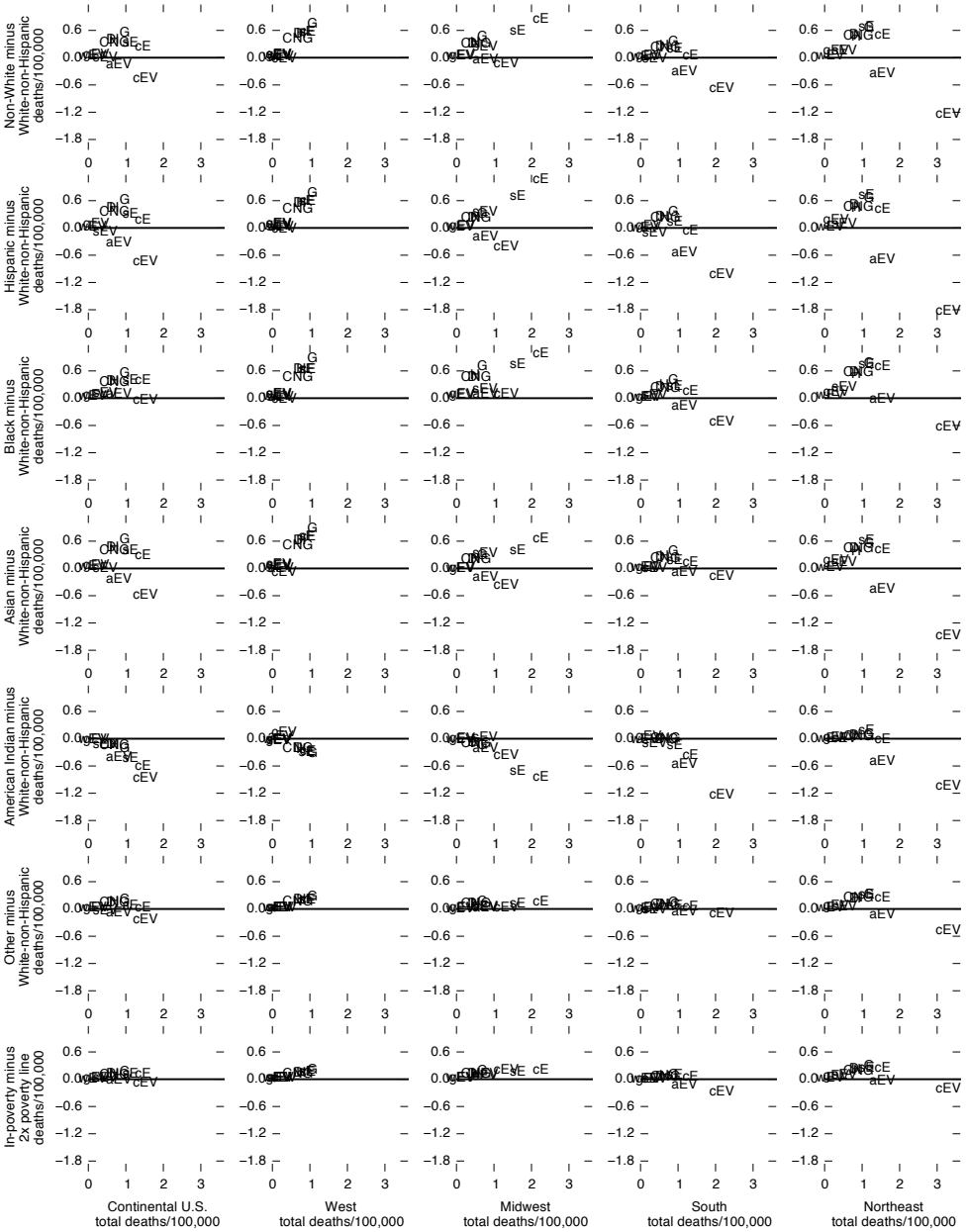

Figure 7.5: Risk difference in air quality-related health burdens in various race and ethnicity groups vs. White individuals and in-poverty vs. 2× poverty line individuals, disaggregated by U.S. region. Abbreviations: G=gasoline; H=gasoline hybrid; D=diesel; CNG=compressed natural gas; cE=corn ethanol; sE=stover ethanol; aEV=electric vehicle (EV) grid average; cEV=EV coal; gEV=EV natural gas; sEV=EV corn stover; wEV=EV wind, water, and solar.

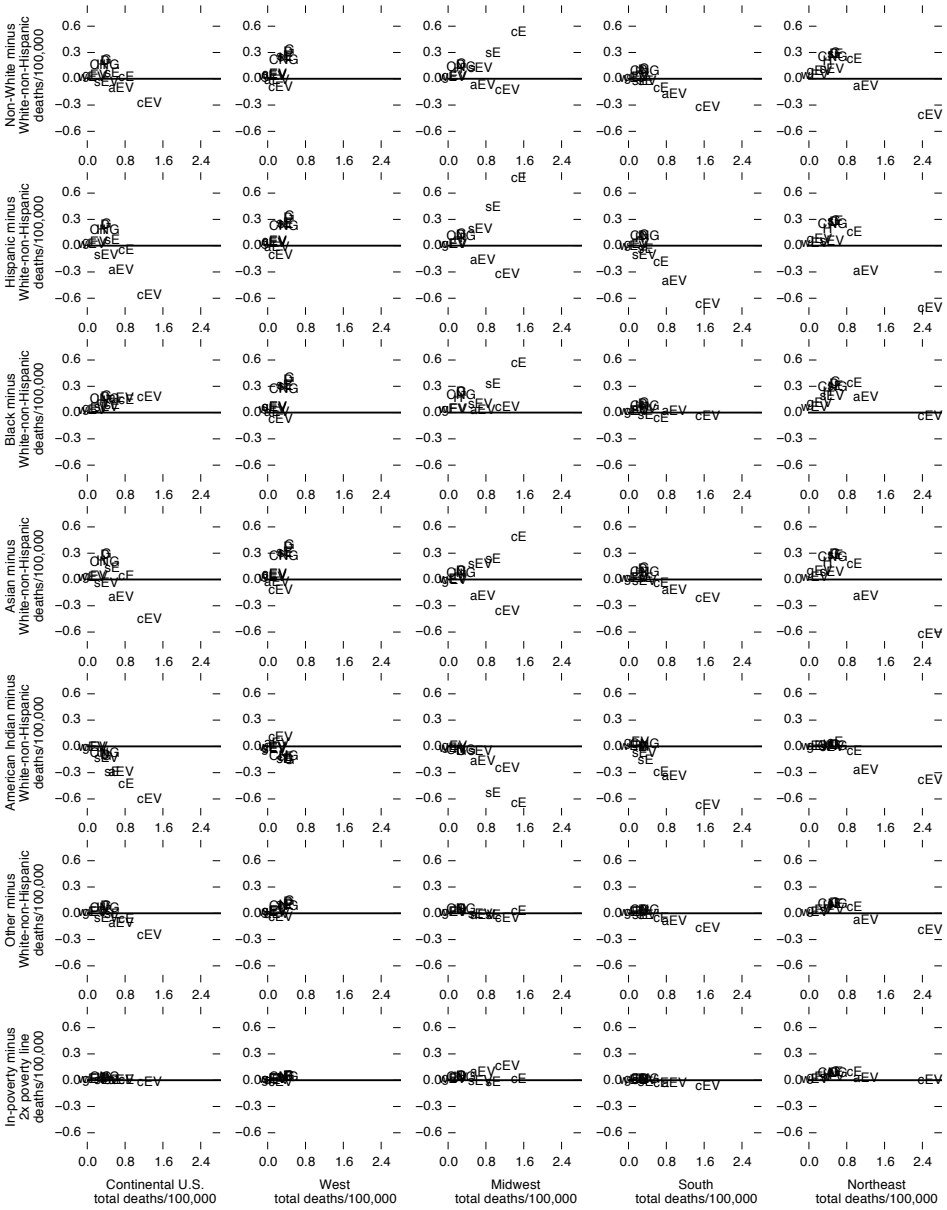

Figure 7.6: Sensitivity analysis using 12-km InMAP for risk difference in air quality-related health burdens in various race and ethnicity groups vs. White individuals and in-poverty vs. 2× poverty line individuals, disaggregated by U.S. region. Abbreviations: G=gasoline; H=gasoline hybrid; D=diesel; CNG=compressed natural gas; cE=corn ethanol; sE=stover ethanol; aEV=electric vehicle (EV) grid average; cEV=EV coal; gEV=EV natural gas; sEV=EV corn stover; wEV=EV wind, water, and solar.

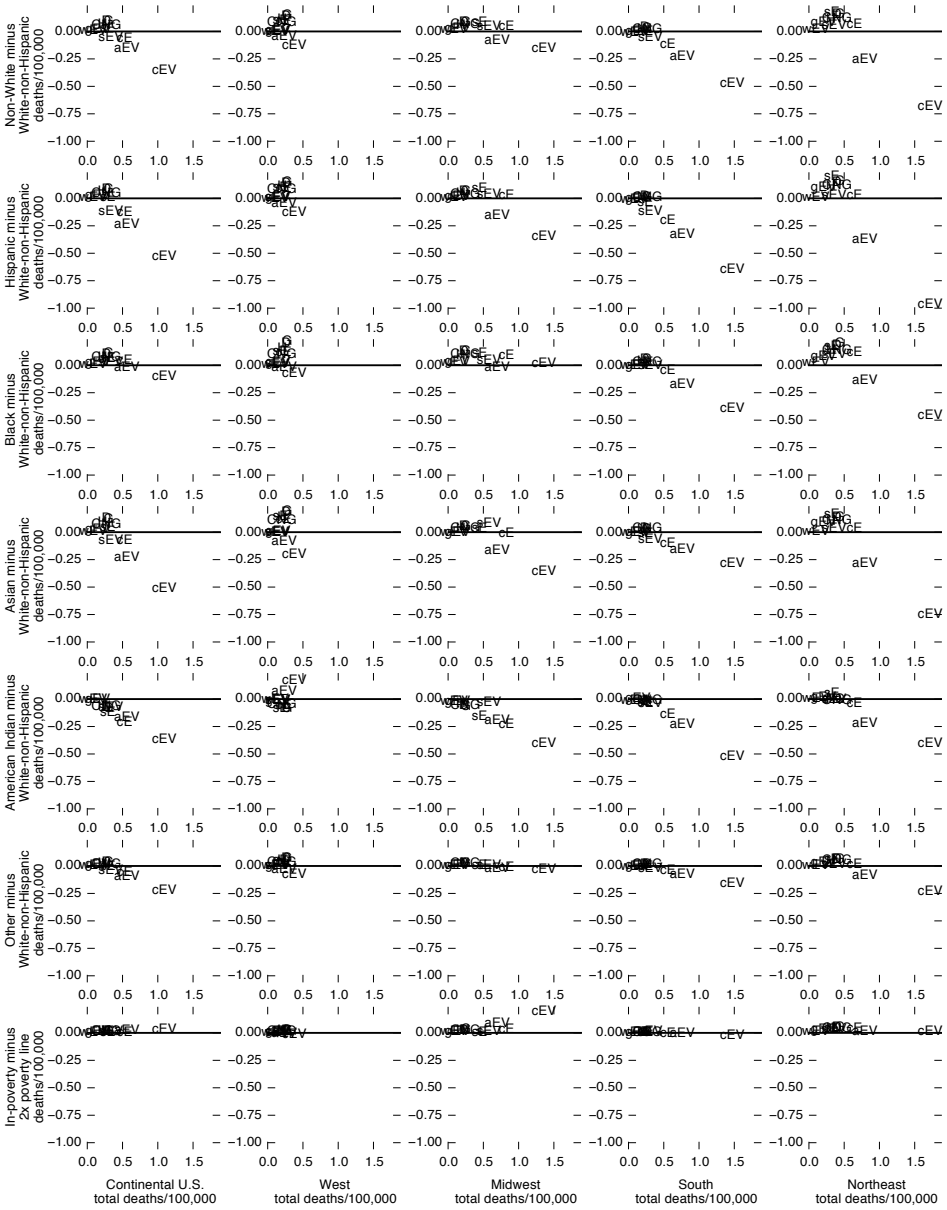

Figure 7.7: Sensitivity analysis using WRF-Chem for risk difference in air quality-related health burdens in various race and ethnicities vs. White individuals and in-poverty vs. 2× poverty-line individuals, disaggregated by U.S. region. Abbreviations: G=gasoline; H=gasoline hybrid; D=diesel; CNG=compressed natural gas; cE=corn ethanol; sE=stover ethanol; aEV=electric vehicle (EV) grid average; cEV=EV coal; gEV=EV natural gas; sEV=EV corn stover; wEV=EV wind, water, and solar.

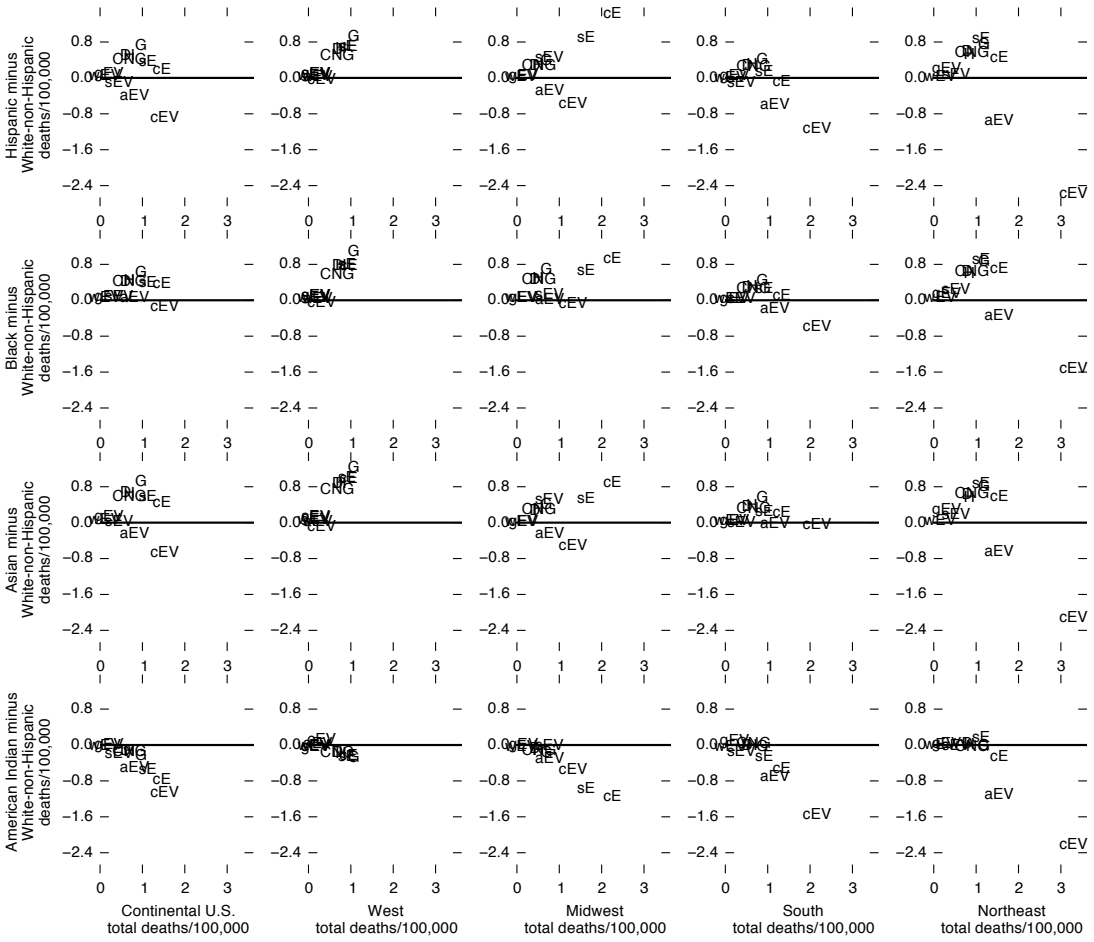

Figure 7.8: Risk difference in air quality-related health burdens in various races vs. White individuals after adjusting for differences in income, disaggregated by U.S. region. Abbreviations: G=gasoline; H=gasoline hybrid; D=diesel; CNG=compressed natural gas; cE=corn ethanol; sE=stover ethanol; aEV=electric vehicle (EV) grid average; cEV=EV coal; gEV=EV natural gas; sEV=EV corn stover; wEV=EV wind, water, and solar.

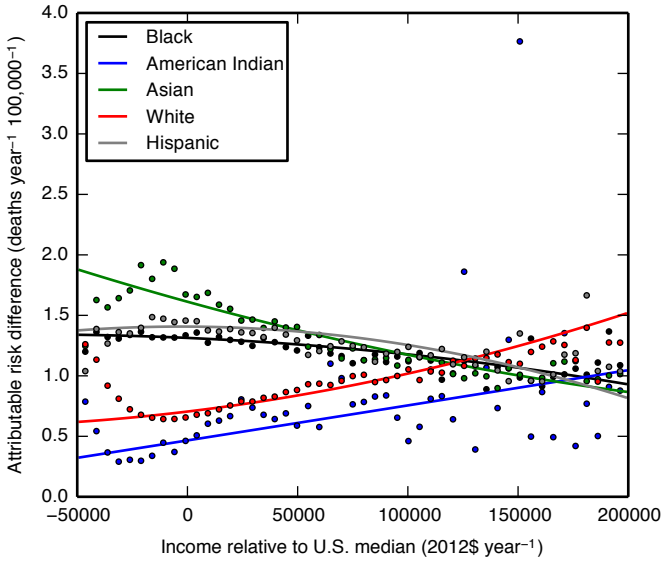

Figure 7.9: Risk attributable to the gasoline scenario vs. income, disaggregated by race. Dots show population-weighted average exposure, binned by income level. Lines show regression results.

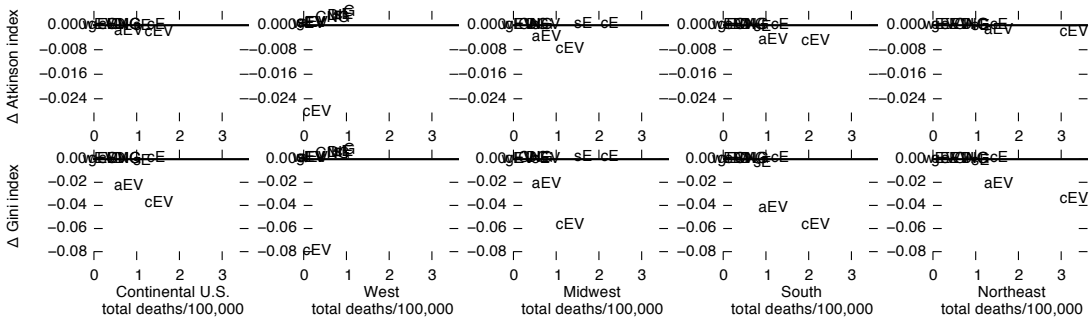

Figure 7.10: Population inequality in air quality-related health impacts using Atkinson ($\epsilon = 0.75$) and extended Gini indices for each emissions scenario. Abbreviations: G=gasoline; H=gasoline hybrid; D=diesel; CNG=compressed natural gas; cE=corn ethanol; sE=stover ethanol; aEV=electric vehicle (EV) grid average; cEV=EV coal; gEV=EV natural gas; sEV=EV corn stover; wEV=EV wind, water, and solar.

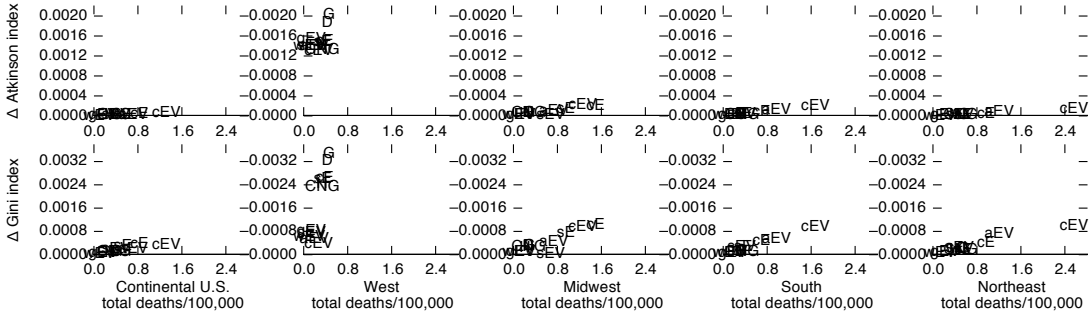

Figure 7.11: Population inequality in air quality-related health impacts using Atkinson ($\epsilon = 0.75$) and extended Gini indices for each emissions scenario. Abbreviations: G=gasoline; H=gasoline hybrid; D=diesel; CNG=compressed natural gas; cE=corn ethanol; sE=stover ethanol; aEV=electric vehicle (EV) grid average; cEV=EV coal; gEV=EV natural gas; sEV=EV corn stover; wEV=EV wind, water, and solar.

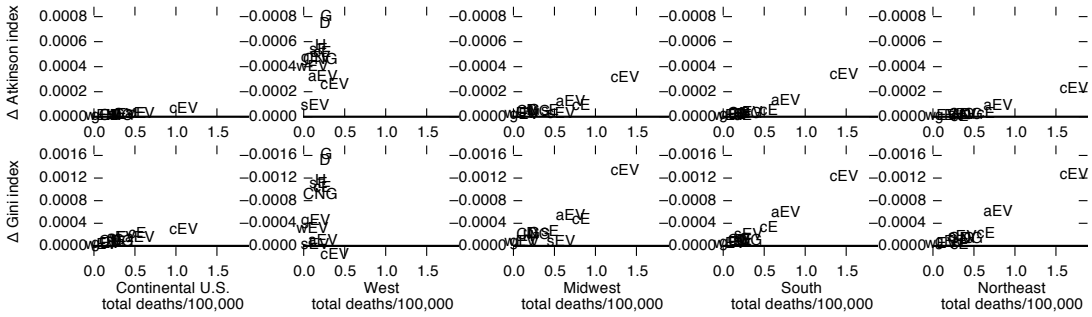

Figure 7.12: Population inequality in air quality-related health impacts using Atkinson ($\epsilon = 0.75$) and extended Gini indices for each emissions scenario. Abbreviations: G=gasoline; H=gasoline hybrid; D=diesel; CNG=compressed natural gas; cE=corn ethanol; sE=stover ethanol; aEV=electric vehicle (EV) grid average; cEV=EV coal; gEV=EV natural gas; sEV=EV corn stover; wEV=EV wind, water, and solar.

Chapter 8

Conclusions and future work

In this dissertation I have shown that it is possible for currently-available alternative vehicle technologies to reduce the climate, public health, and environmental justice impacts of light-duty transportation relative to business-as-usual gasoline vehicles. Of the options I have investigated, electric vehicles powered by low-emitting electricity generation are the only ones to make substantial improvements in all of three categories. Electricity from natural gas, which is currently widely available, may be the most effective near-term option for powering electric vehicles, but in the long term, electric vehicles powered by electricity from wind, water, or solar power will effect the largest reductions in the negative social costs of light-duty transportation.

Opportunities for future research are described in details each chapter, so here I will summarize some common themes. The analyses herein have evaluated emissions and impacts within the United States. The life cycles of conventional and alternative transportation fuels include processes in many countries of the world, however, and future analyses could expand the framework described here for worldwide analysis. Additionally, I have assumed here that relationships between the processes in the fuel life cycles and their emission rates will be the same for future marginal changes in fuel use as they are on average today. In reality, these relationships are dynamic, and future analyses could account for this. I have attempted to

create scenarios that are robust to uncertainties in future human behavior, and I have performed sensitivity analyses to ensure that the conclusions I have presented here are robust to some possible methodological limitations and uncertainty in physical relationships. However, future analysis could more rigorously quantify uncertainty in the results presented here, perhaps using the reduced complexity air quality model described in Chapter 6. Finally, the physical models used here to relate emissions of pollutants to their ultimate impacts to human health are imperfect and could always use improvement.

As a final note, I would like to refer back to the anecdote at the beginning of the Introduction. The United States entered the 20^{th} century with a transportation-related manure problem, and left it with transportation-related air quality and climate problems. This begs the question, what will be the problems of tomorrow caused by our fixes for the problems of today? This study and others have identified some of these potential problems, for example the air quality damages caused by the production of ethanol and by the powering electric vehicles with electricity from coal. I do not claim to have found them all. We must be ever vigilant to foresee the potential problems of the future, so they do not become the unforeseen problems of the present.

Bibliography

1. C. McShane, *Down the Asphalt Path: The Automobile and the American City* (Cambridge University Press, Cambridge, United Kingdom and New York, NY, USA, 1995).

2. J. A. Tarr, Urban pollution—many long years ago, *Am. Herit. Magizine*, `http://www.banhdc.org/archives/ch-hist-19711000.html` (1971).

3. F. W. Geels, The dynamics of transitions in socio-technical systems: A multi-level analysis of the transition pathway from horse-drawn carriages to automobiles (1860–1930), *Technol. Anal. Strateg. Manag.* **17**, 445–476 (2005).

4. G. Yago, *The Decline of Transit: Urban Transportation in German and U.S. Cities 1900-1970* (Cambridge University Press, Cambridge, United Kingdom and New York, NY, USA, 1984).

5. D. Krewski, M. Jerrett, R. T. Burnett, R. Ma, E. Hughes, Y. Shi, M. C. Turner, C. A. Pope III, G. Thurston, E. E. Calle, M. J. Thun, "Extended Follow-Up and Spatial Analysis of the American Cancer Society Study Linking Particulate Air Pollution and Mortality", tech. rep. (Health Affects Institute, 2009), `http://www.ncbi.nlm.nih.gov/pubmed/19627030`.

6. M. Jerrett, R. T. Burnett, C. A. Pope III, K. Ito, G. Thurston, D. Krewski, Y. Shi, E. Calle, M. Thun, Long-term ozone exposure and mortality., *New Engl. J. Med.*. **360**, 1085–1095 (2009).

7. M. A. Delucchi, Environmental externalities of motor-vehicle use in the US, *J. Transp. Econ. Policy* **34**, 135–168 (2000).

8. Intergovernmental Panel on Climate Change, "Climate Change 2007: Synthesis Report", tech. rep. (Intergovernmental Panel on Climate Change, Geneva, Switzerland, 2007), http://www.ipcc.ch/publications%5C_and%5C_data/publications%5C_ipcc%5C_fourth%5C_assessment%5C_report%5C_synthesis%5C_report.htm.

9. S. S. Lim *et al.*, A comparative risk assessment of burden of disease and injury attributable to 67 risk factors and risk factor clusters in 21 regions, 1990-2010: a systematic analysis for the Global Burden of Disease Study 2010., *Lancet* **380**, 2224–60 (2012).

10. N. Fann, C. M. Fulcher, K. Baker, The recent and future health burden of air pollution apportioned across U.S. sectors, *Environ. Sci. Technol.* **47**, 3580–3589 (2013).

11. S. Pacala, R. Socolow, Stabilization wedges: solving the climate problem for the next 50 years with current technologies, *Science* **305**, 968–972 (2004).

12. J. H. Williams, A. DeBenedictis, R. Ghanadan, A. Mahone, J. Moore, W. R. Morrow, S. Price, M. S. Torn, The technology path to deep greenhouse gas emissions cuts by 2050: the pivotal role of electricity., *Science* **335**, 53–9 (2012).

13. United Nations, *Kyoto Protocol to the United Nations Framework Convention on Climate Change*, 1998, http://unfccc.int/kyoto%5C_protocol/items/2830.php/.

14. "Draft Inventory of U.S. Greenhouse Gas Emissions and Sinks: 1990-2009", tech. rep. (US Environmental Protection Agency #EPA-430-R-11-005, 2011), www.epa.gov/climatechange/emissions/usinventoryreport.html.

15. U.S. Environmental Protection Agency, *Global Greenhouse Gas Emissions Data*, 2008, http://www.epa.gov/climatechange/ghgemissions/global.html (visited on 10/07/2014).

16. J. Hill, S. Polasky, E. Nelson, D. Tilman, H. Huo, L. Ludwig, J. Neumann, H. Zheng, D. Bonta, Climate change and health costs of air emissions from biofuels and gasoline., *Proc. Natl. Acad. Sci.* **106**, 2077–82 (Mar. 2009).

17. J. J. Michalek, M. Chester, P. Jaramillo, C. Samaras, C.-S. N. Shiau, L. B. Lave, Valuation of plug-in vehicle life-cycle air emissions and oil displacement benefits., *Proc. Natl. Acad. Sci.* **108**, 16554–8 (2011).

18. Electric Power Research Institute, "Environmental Assessment of Plug-In Hybrid Electric Vehicles, Volume 2: United States Air Quality Analysis Based on AEO-2006 Assumptions for 2030", tech. rep. (Electric Power Research Institute, 2007), `http://www.epri.com/abstracts/Pages/ProductAbstract.aspx?ProductId=000000000001015326`.

19. M. Z. Jacobson, Effects of ethanol (E85) versus gasoline vehicles on cancer and mortality in the United States., *Environ. Sci. Technol.* **41**, 4150–4157 (2007).

20. F. Boureima, M. Messagie, Comparative LCA of electric, hybrid, LPG and gasoline cars in Belgian context, *World Electr. Veh. J.* **3**, 1–8 (2009).

21. J. L. Cohon, M. L. Cropper, M. R. Cullen, E. M. Drake, M. English, C. B. Field, D. S. Greenbaum, J. K. Hammitt, R. F. Henderson, C. L. Kling, A. J. Krupnick, R. Lee, H. S. Matthews, T. E. McKone, G. E. Metcalf, R. G. Newell, R. L. Revesz, I. S. Wing, T. G. Surles, "Hidden Costs of Energy: Unpriced Consequences of Energy Production and Use", tech. rep. (National Research Council, 2009), `http://www.nap.edu/catalog.php?record%5C_id=12794`.

22. T. Thompson, M. Webber, D. T. Allen, Air quality impacts of using overnight electricity generation to charge plug-in hybrid electric vehicles for daytime use, *Environ. Res. Lett.* **4**, 014002 (2009).

23. R. Cook, S. Phillips, M. Houyoux, P. Dolwick, R. Mason, C. Yanca, M. Zawacki, K. Davidson, H. Michaels, C. Harvey, Air quality impacts of increased use of ethanol under the United States' Energy Independence and Security Act, *Atmos. Environ.* **45**, 7714–7724 (2011).

24. G. L. Brinkman, P. Denholm, M. P. Hannigan, J. B. Milford, Effects of plug-in hybrid electric vehicles on ozone concentrations in Colorado, *Environ. Sci. Technol.* **44**, 6256–6262 (2010).

25. "Renewable Fuel Standard Program (RFS2) Regulatory Impact Analysis", tech. rep. (US Environmental Protection Agency #EPA-420-R-10-006, 2010), http://www.epa.gov/otaq/renewablefuels/420r10006.pdf.

26. N. S. Alhajeri, E. C. McDonald-Buller, D. T. Allen, Comparisons of air quality impacts of fleet electrification and increased use of biofuels, *Environ. Res. Lett.* **6**, 024011 (2011).

27. T. M. Thompson, C. W. King, D. T. Allen, M. E. Webber, Air quality impacts of plug-in hybrid electric vehicles in Texas: evaluating three battery charging scenarios, *Environ. Res. Lett.* **6**, 024004 (2011).

28. C. W. Tessum, J. D. Marshall, J. D. Hill, A spatially and temporally explicit life cycle inventory of air pollutants from gasoline and ethanol in the United States, *Environ. Sci. Technol.* **46**, 11408–11417 (2012).

29. C. W. Tessum, J. D. Hill, J. D. Marshall, Twelve-month, 12-km resolution North American WRF-Chem air quality simulation: Performance evaluation, *Geosci. Model Dev. Discuss.* **7**, 8433–8476 (2014).

30. U.S. Environmental Protection Agency, *2005 National Emissions Inventory (NEI)*, 2009, http://www.epa.gov/ttn/chief/emch/index.html (visited on 03/07/2012).

31. J. Fargione, J. Hill, D. Tilman, S. Polasky, P. Hawthorne, Land clearing and the biofuel carbon debt, *Science* **319**, 1235–1238 (2008).

32. A. E. Farrell, R. J. Plevin, B. T. Turner, A. D. Jones, M. O'Hare, D. M. Kammen, Ethanol can contribute to energy and environmental goals, *Science* **311**, 506–8 (2006).

33. J. Hill, E. Nelson, D. Tilman, S. Polasky, D. Tiffany, Environmental, economic, and energetic costs and benefits of biodiesel and ethanol biofuels, *Proc. Natl. Acad. Sci.* **103**, 11206–10 (July 2006).

34. D. D. Hsu, D. Inman, G. A. Heath, E. J. Wolfrum, M. K. Mann, A. Aden, Life cycle environmental impacts of selected U.S. ethanol production and use pathways in 2022., *Environ. Sci. Technol.* **44**, 5289–97 (2010).

35. H. von Blottnitz, M. Curran, A review of assessments conducted on bio-ethanol as a transportation fuel from a net energy, greenhouse gas, and environmental life cycle perspective, *J. Clean. Prod.* **15**, 607–619 (2007).

36. T. W. Hertel, A. A. Golub, A. D. Jones, M. O'Hare, R. J. Plevin, D. M. Kammen, Effects of US maize ethanol on global land use and greenhouse gas emissions: Estimating market-mediated responses, *Bioscience* **60**, 223–231 (2010).

37. T. Searchinger, R. Heimlich, R. Houghton, F. Dong, A. Elobeid, J. Fabiosa, S. Tokgoz, D. Hayes, T.-H. Yu, Use of U.S. croplands for biofuels increases greenhouse gases through emissions from land use change, *Science* **319**, 1238–1240 (2008).

38. X. Yan, A. M. Boies, Quantifying the uncertainties in life cycle greenhouse gas emissions for UK wheat ethanol, *Environ. Res. Lett.* **8**, 015024 (2013).

39. C.-C. Tsao, J. E. Campbell, M. Mena-Carrasco, S. N. Spak, G. R. Carmichael, Y. Chen, Increased estimates of air-pollution emissions from Brazilian sugar-cane ethanol, *Nat. Clim. Chang.* **2**, 53–57 (2011).

40. M. Wang, J. Han, J. B. Dunn, H. Cai, A. Elgowainy, Well-to-wheels energy use and greenhouse gas emissions of ethanol from corn, sugarcane and cellulosic biomass for US use, *Environ. Res. Lett.* **7**, 045905 (2012).

41. J. Reap, F. Roman, S. Duncan, B. Bras, A survey of unresolved problems in life cycle assessment: Part 2: impact assessment and interpretation, *Int. J. Life Cycle Assess.* **13**, 374–388 (2008).

42. T. McKone, W. Nazaroff, P. Berck, M. Auffhammer, T. Lipman, M. Torn, E. Masanet, A. Lobscheid, N. Santero, U. Mishra, A. Barrett, M. Bomberg, K. Fingerman, C. Scown, B. Strogen, A. Horvath, Grand challenges for life-cycle assessment of biofuels., *Environ. Sci. Technol.* **45**, 1751–6 (2011).

43. L. B. Lave, I. C. Burke, W. E. Tyner, V. H. Dale, K. E. Halvorsen, J. D. Hill, S. R. Kaffka, K. C. Klasing, S. J. McGovern, J. A. Miranowski, A. Patrinos, J. L. Schnoor, D. B. Schweikhardt,

T. L. Selfa, B. L. Sohngen, J. A. Soria, "Renewable Fuel Standard: Potential Economic and Environmental Effects of U.S. Biofuel Policy", tech. rep. (National Research Council, 2011), http://www.nap.edu/catalog.php?record%5C_id=13105.

44. K. R. Fingerman, M. S. Torn, M. H. O'Hare, D. M. Kammen, Accounting for the water impacts of ethanol production, *Environ. Res. Lett.* **5**, 014020 (2010).

45. R. Geyer, D. M. Stoms, J. P. Lindner, F. W. Davis, B. Wittstock, Coupling GIS and LCA for biodiversity assessments of land use, *Int. J. Life Cycle Assess.* **15**, 454–467 (2010).

46. X. Zhang, R. Izaurralde, D. Manowitz, T. O. West, W. M. Post, A. M. Thomson, V. P. Bandaru, J. Nichols, J. R. Williams, An integrative modeling framework to evaluate the productivity and sustainability of biofuel crop production systems, *Glob. Chang. Biol. Bioenergy* **2**, 258–277 (2010).

47. C. L. Mutel, S. Pfister, S. Hellweg, GIS-based regionalized life cycle assessment: How big is small enough? Methodology and case study of electricity generation., *Environ. Sci. Technol.* **46**, 1096–1103 (2011).

48. D. B. Millet, E. Apel, D. K. Henze, J. Hill, J. D. Marshall, H. B. Singh, C. W. Tessum, Natural and anthropogenic ethanol sources in North America and potential atmospheric impacts of ethanol fuel use, *Environ. Sci. Technol.* **46**, 8484–92 (2012).

49. M. Posch, J. Seppälä, J.-P. Hettelingh, M. Johansson, M. Margni, O. Jolliet, The role of atmospheric dispersion models and ecosystem sensitivity in the determination of characterisation factors for acidifying and eutrophying emissions in LCIA, *Int. J. Life Cycle Assess.* **13**, 477–486 (2008).

50. D. W. Pennington, M. Margni, C. Ammann, O. Jolliet, Multimedia fate and human intake modeling: Spatial versus nonspatial insights for chemical emissions in Western Europe, *Environ. Sci. Technol.* **39**, 1119–1128 (2005).

51. M. Raugei, S. Ulgiati, A novel approach to the problem of geographic allocation of environmental impact in life cycle assessment and material flow analysis, *Ecol. Indic.* **9**,

1257–1264 (2009).

52. V. P. Shah, R. J. Ries, A characterization model with spatial and temporal resolution for life cycle impact assessment of photochemical precursors in the United States, *Int. J. Life Cycle Assess.* **14**, 313–327 (2009).

53. M. Hauschild, J. Potting, "Spatial Differentiation in Life Cycle Impact Assessment—the EDIP2003 Methodology", tech. rep. (Danish Ministry of the Environment: Environmental Protection Agency, 2005), `www2.mst.dk/udgiv/publications/2005/87-7614-579-4/pdf/87-7614-580-8.pdf`.

54. G. A. Norris, Impact characterization in the tool for the reduction and assessment of chemical and other environmental impacts: Methods for acidification, eutrophication, and ozone formation, *J. Ind. Ecol.* **6**, 79–101 (2002).

55. A. Wegener Sleeswijk, R. Heijungs, GLOBOX: A spatially differentiated global fate, intake and effect model for toxicity assessment in LCA., *Sci. Total Environ.* **408**, 2817–32 (2010).

56. F. Querini, S. Morel, V. Boch, P. Rousseaux, USEtox relevance as an impact indicator for automotive fuels. Application on diesel fuel, gasoline and hard coal electricity, *Int. J. Life Cycle Assess.* **16**, 829–840 (2011).

57. S. M. Lloyd, R. Ries, Spatial and Temporal Life Cycle Assessment: Ozone Formation Potential from Natural Gas Use in a Typical Residential Building in Pittsburgh, USA, in *Dyn. Reg. Networks Ind. Ecosyst.* Ed. by M. Ruth, B. Davidsdottir (The MIT Press, 2009).

58. S. Humbert, J. D. Marshall, S. Shaked, J. V. Spadaro, Y. Nishioka, P. Preiss, T. E. McKone, A. Horvath, O. Jolliet, Intake fraction for particulate matter: Recommendations for life cycle impact assessment., *Environ. Sci. Technol.* **45**, 4808–16 (2011).

59. R. Manneh, M. Margni, L. Deschênes, Spatial variability of intake fractions for Canadian emission scenarios: A comparison between three resolution scales., *Environ. Sci. Technol.* **44**, 4217–24 (2010).

60. H. Huo, Y. Wu, M. Wang, Total versus Urban: Well-to-wheels assessment of criteria pollutant emissions from various vehicle/fuel systems, *Atmos. Environ.* **43**, 1796–1804 (2009).

61. M. Wang, *The Greenhouse Gases, Regulated Emissions, and Energy Use in Transportation Model v1.8d1*, 2010, `http://greet.es.anl.gov/`.

62. California Air Resources Board, *Low Carbon Fuel Standard Program*, 2011, `http://www.arb.ca.gov/fuels/lcfs/lcfs.htm` (visited on 05/11/2013).

63. R. J. Plevin, M. a. Delucchi, F. Creutzig, Using attributional life cycle assessment to estimate climate-change mitigation benefits misleads policy makers, *J. Ind. Ecol.* **18**, 73–83 (2014).

64. M. D. Goebes, R. Strader, C. Davidson, An ammonia emission inventory for fertilizer application in the United States, *Atmos. Environ.* **37**, 2539–2550 (2003).

65. C. Pope III, D. Dockery, Health effects of fine particulate air pollution: Lines that connect, *J. Air Waste Manag. Assoc.* **56**, 709–742 (2006).

66. C. A. Pope III, R. T. Burnett, M. J. Thun, E. E. Calle, D. Krewski, K. Ito, G. D. Thurston, Lung cancer, cardiopulmonary mortality, and long-term exposure to fine particulate air pollution, *J. Amer. Med. Assoc.* **287**, 1132–1141 (2002).

67. D. W. Dockery, C. A. Pope III, X. Xu, J. D. Spengler, J. H. Ware, M. E. Fay, B. G. Ferris, F. E. Speizer, An association between air pollution and mortality in six US cities, *N Engl J Med* **329**, 1753–1759 (1993).

68. K. Andersson, J. V. Bakke, O. Bjorseth, C.-G. Bornehag, G. Clausen, J. K. Hongslo, M. Kjellman, S. Kjaergaard, F. Levy, L. Molhave, S. Skerfving, J. Sundell, TVOC and health in non-industrial indoor environments, *Indoor Air* **7**, 78–91 (1997).

69. L. Curtis, W. Rea, P. Smith-Willis, E. Fenyves, Y. Pan, Adverse health effects of outdoor air pollutants., *Environ. Int.* **32**, 815–30 (2006).

70. J. H. Ware, J. D. Spengler, L. M. Neas, J. M. Samet, G. R. Wagner, D. Coultas, H. Ozkaynak, M. Schwab, Respiratory and irritant health effects of ambient volatile organic compounds: The Kanawha County health study, *Am. J. Epidemiol.* **137**, 1287–1301 (1993).

71. M. Chiusolo, E. Cadum, M. Stafoggia, C. Galassi, G. Berti, A. Faustini, L. Bisanti, M. A. Vigotti, M. P. Dessì, A. Cernigliaro, S. Mallone, B. Pacelli, S. Minerba, L. Simonato, F. Forastiere, Short term effects of nitrogen dioxide on mortality and susceptibility factors in ten Italian cities: The EpiAir study., *Environ. Heal. Perspect.* **119**, 1233–1238 (2011).

72. M. L. Bell, A. McDermott, S. L. Zeger, J. M. Samet, F. Dominici, Ozone and short-term mortality in 95 US urban communities, 1987-2000, *J. Amer. Med. Assoc.* **292**, 2372–2378 (2004).

73. T. Kiely, D. Donaldson, A. Grube, "Pesticides Industry Sales and Usage: 2000 and 2001 Market Estimates", tech. rep. (US Environmental Protection Agency, 2004), http://www.epa.gov/pesticides/pestsales/01pestsales/market%5C_estimates2001.pdf.

74. US Geological Survey, *Mineral Commodity Summaries*, 2010, http://minerals.usgs.gov/minerals/pubs/mcs/ (visited on 03/07/2012).

75. US Energy Information Administration, *Independent Statistics & Analysis*, http://www.eia.gov (visited on 03/07/2012).

76. US Energy Information Administration, *Coal Production by MSHA ID, Mine Operation, Union Status, and Average Number of Employees and Hours*, 2007, http://www.eia.gov/cneaf/coal/page/database.html (visited on 05/10/2010).

77. "Top 100 Oil and Gas fields of 2009", tech. rep. (US Energy Information Administration, 2010), http://www.eia.gov/pub/oil%5C_gas/natural%5C_gas/data%5C_publications/crude%5C_oil%5C_natural%5C_gas%5C_reserves/current/pdf/top100fields.pdf.

78. "Natural Gas Processing: The Crucial Link Between Natural Gas Production and Its Transportation to Market", tech. rep. (US Energy Information Administration, 2006), http://www.arcticgas.gov/sites/default/files/documents/2006-eia-ng-processing.

pdf.

79. International Fertilizer Development Center (IFDC), "North America Fertilizer Capacity", tech. rep., http://www.ifdc.org/getdoc/5fee0591-47b9-4226-9338-cf43a980e15a/Fertilizer%5C_Market-Related%5C_Reports%5C_(1).

80. ICIS Chemical Market Intelligence, Chemical profile: Sulfuric acid, *Chem. Bus.* http://www.icis.com/ (2005).

81. Renewable Fuels Association, *Biorefinery Locations*, 2010, http://www.ethanolrfa.org/bio-refinery-locations/ (visited on 02/08/2010).

82. US Energy Information Administration, *Ranking of U.S. Refineries*, 2009, http://www.eia.gov/neic/rankings/refineries.htm (visited on 03/07/2010).

83. US Department of Agriculture, *National Agricultural Statistics Service*, 2010, http://www.nass.usda.gov/Data%5C_and%5C_Statistics/index.asp (visited on 05/01/2011).

84. "EPA's National Inventory Model (NMIM), A Consolidated Emissions Modeling System for MOBILE6 and NONROAD", tech. rep. (US Environmental Protection Agency, 2005), www.epa.gov/otaq/models/nmim/420r05024.pdf.

85. US Census Bureau, *TIGER/line Shapefiles*, 2003, http://www.census.gov/geo/www/tiger/ (visited on 03/07/2012).

86. GRASS Development Team, *Geographic Resources Analysis Support System (GRASS GIS) Software*, 2012, http://grass.osgeo.org.

87. US Environmental Protection Agency, *2007 eGRID Database*, 2010, http://www.epa.gov/cleanenergy/energy-resources/egrid/index.html (visited on 03/07/2012).

88. US Environmental Protection Agency, *eGRID2007 Version 1.1*, http://www.epa.gov/cleanenergy/energy-resources/egrid/index.html (visited on 12/04/2014).

89. D. M. Johnson, R. Mueller, "The 2009 Cropland Data Layer", tech. rep. (United States Department of Agriculture/National Agricultural Statistics Service, 2010), http://www.nass.usda.gov/research/Cropland/SARS1a.htm.

90. GNU, *GLPK (GNU Linear Programming Kit)*, 2008, http://www.gnu.org/software/glpk/.

91. Research and Innovative Technology Administration/Bureau of Transportation Statistics, *National Transportation Atlas Database (NTAD) 2010*, 2010, http://www.bts.gov/publications/national%5C_transportation%5C_atlas%5C_database/2010/ (visited on 03/07/2012).

92. F. J. Ries, J. D. Marshall, M. Brauer, Intake fraction of urban wood smoke, *Environ. Sci. Technol.* **43**, 4701–4706 (2009).

93. J. Apte, E. Bombrun, J. D. Marshall, W. Nazaroff, Global intraurban intake fractions for primary air pollutants from vehicles and other distributed sources., *Environ. Sci. Technol.* **46**, 3415–3423 (2012).

94. S. Sokhansanj, A. Turhollow, J. Cushman, J. Cundiff, Engineering aspects of collecting corn stover for bioenergy, *Biomass Bioenergy* **23**, 347–355 (2002).

95. P. Forster, V. Ramaswamy, P. Artaxo, T. Berntsen, R. Betts, D. Fahey, J. Haywood, J. Lean, D. Lowe, G. Myhre, J. Nganga, R. Prinn, G. Raga, M. Schulz, R. Van Dorland, Changes in Atmospheric Constituents and in Radiative Forcing, in *Clim. Chang. 2007 Phys. Sci. Basis. Contrib. Work. Gr. I to Fourth Assess. Rep. Intergov. Panel Clim. Chang.* Ed. by S. Solomon, D. Qin, M. Manning, Z. Chen, M. Marquis, K. Averyt, M.Tignor, H. Miller (Cambridge University Press, Cambridge, United Kingdom and New York, NY, USA, 2007).

96. H. Simon, L. Beck, P. V. Bhave, F. Divita, Y. Hsu, D. Luecken, J. D. Mobley, G. A. Pouliot, A. Reff, G. Sarwar, M. Strum, The development and uses of EPA's SPECIATE database, *Atmos. Pollut. Res.* **1**, 196–206 (2010).

97. US Environmental Protection Agency, *Technology Transfer Network (TTN) Air Quality System (AQS) Data Mart*, 2005, http://www.epa.gov/ttn/airs/aqsdatamart/ (visited on 06/02/2012).

98. "Mineral Commodity Summaries: Sulfur", tech. rep. 703 (US Geological Survey, 2010), http://minerals.usgs.gov/minerals/pubs/commodity/sulfur/index.html%5C#mcs.

99. "Petroleum Supply Annual", tech. rep. (US Energy Information Administration, 2010), http://205.254.135.24/petroleum/supply/annual/volume1/.

100. National Institute for Occupational Safety and Health, *Carcinogen List*, 2010, http://www.cdc.gov/niosh/topics/cancer/npotocca.html (visited on 07/11/2011).

101. US Census Bureau, *Census 2000 Urbanized Areas Cartographic Boundary Files*, 2001, http://www.census.gov/geo/www/cob/ua2000.html (visited on 05/01/2011).

102. J. I. Levy, A. M. Wilson, J. S. Evans, J. D. Spengler, Estimation of primary and secondary particulate matter intake fractions for power plants in Georgia., *Environ. Sci. Technol.* **37**, 5528–5536 (Dec. 2003).

103. T. Tesche, R. Morris, G. Tonnesen, D. McNally, J. Boylan, P. Brewer, CMAQ/CAMx annual 2002 performance evaluation over the eastern US, *Atmos. Environ.* **40**, 4906–4919 (2006).

104. K. Yahya, K. Wang, M. Gudoshava, T. Glotfelty, Y. Zhang, Application of WRF/Chem over North America under the AQMEII Phase 2: Part I. Comprehensive evaluation of 2006 simulation, *Atmos. Environ.* DOI: 10.1016/j.atmosenv.2014.08.063, http://linkinghub.elsevier.com/retrieve/pii/S1352231014006657 (2014).

105. C. Fountoukis, D. Koraj, H. Denier van der Gon, P. Charalampidis, C. Pilinis, S. Pandis, Impact of grid resolution on the predicted fine PM by a regional 3-D chemical transport model, *Atmos. Environ.* **68**, 24–32 (2013).

106. S. Galmarini, S. Rao, D. Steyn, AQMEII: An international initiative for the evaluation of regional-scale air quality models - Phase 1 preface, *Atmos. Environ.* **53**, 1–3 (2012).

107. K. W. Appel, C. Chemel, S. J. Roselle, X. V. Francis, R.-M. Hu, R. S. Sokhi, S. Rao, S. Galmarini, Examination of the Community Multiscale Air Quality (CMAQ) model performance over the North American and European domains, *Atmos. Environ.* **53**, 142–155 (2012).

108. K. M. Foley, S. J. Roselle, K. W. Appel, P. V. Bhave, J. E. Pleim, T. L. Otte, R. Mathur, G. Sarwar, J. O. Young, R. C. Gilliam, C. G. Nolte, J. T. Kelly, a. B. Gilliland, J. O. Bash, Incremental testing of the Community Multiscale Air Quality (CMAQ) modeling system version 4.7, *Geosci. Model Dev.* **3**, 205–226 (2010).

109. "Regulatory Impact Analysis for the Proposed Revisions to the National Ambient Air Quality Standards for Particulate Matter", tech. rep. (US Environmental Protection Agency #EPA-452/R-12-003, 2012), `http://www.epa.gov/ttnecas1/regdata/RIAs/PMRIACombinedFile%5C_Bookmarked.pdf`.

110. G. A. Grell, S. E. Peckham, R. Schmitz, S. A. McKeen, G. Frost, W. C. Skamarock, B. Eder, Fully coupled "online" chemistry within the WRF model, *Atmos. Environ.* **39**, 6957–6975 (2005).

111. R. Ahmadov, S. a. McKeen, a. L. Robinson, R. Bahreini, a. M. Middlebrook, J. a. de Gouw, J. Meagher, E.-Y. Hsie, E. Edgerton, S. Shaw, M. Trainer, A volatility basis set model for summertime secondary organic aerosols over the eastern United States in 2006, *J. Geophys. Res.* **117**, D06301 (2012).

112. M.-T. Chuang, Y. Zhang, D. Kang, Application of WRF/Chem-MADRID for real-time air quality forecasting over the Southeastern United States, *Atmos. Environ.* **45**, 6241–6250 (2011).

113. J. D. Fast, W. I. Gustafson, R. C. Easter, R. a. Zaveri, J. C. Barnard, E. G. Chapman, G. a. Grell, S. E. Peckham, Evolution of ozone, particulates, and aerosol direct radiative forcing in the vicinity of Houston using a fully coupled meteorology-chemistry-aerosol model, *J. Geophys. Res.* **111**, D21305 (Nov. 2006).

114. S. McKeen, S. Chung, J. Wilczak, G. Grell, I. Djalalova, S. Peckham, W. Gong, V. Bouchet, R. Moffet, Y. Tang, G. Carmichael, R. Mathur, S. Yu, Evaluation of several $PM_{2.5}$ forecast models using data collected during the ICARTT/NEAQS 2004 field study, *J. Geophys. Res* **112**, D10S20 (2007).

115. C. Misenis, Y. Zhang, An examination of sensitivity of WRF/Chem predictions to physical parameterizations, horizontal grid spacing, and nesting options, *Atmos. Res.* **97**, 315–334 (2010).

116. Y. Zhang, Y. Pan, K. Wang, J. D. Fast, G. A. Grell, WRF/Chem-MADRID: Incorporation of an aerosol module into WRF/Chem and its initial application to the TexAQS2000 episode, *J. Geophys. Res.* **115**, DOI: 10.1029/2009JD013443, http://www.agu.org/pubs/crossref/2010/2009JD013443.shtml (2010).

117. Y. Zhang, Y. Chen, G. Sarwar, K. Schere, Impact of gas-phase mechanisms on Weather Research Forecasting Model with Chemistry (WRF/Chem) predictions: Mechanism implementation and comparative evaluation, *J. Geophys. Res.* **117**, D01301 (2012).

118. J. W. Boylan, A. G. Russell, PM and light extinction model performance metrics, goals, and criteria for three-dimensional air quality models, *Atmos. Environ.* **40**, 4946–4959 (2006).

119. W. Stockwell, F. Kirchner, M. Kuhn, S. Seefeld, A new mechanism for regional atmospheric chemistry modeling, *J. Geophys. Res.* **102**, 25, 847–25, 879 (1997).

120. I. J. Ackermann, H. Hass, M. Memmesheimer, A. Ebel, F. S. Binkowski, U. Shankar, Modal Aerosol Dynamics Model for Europe: Development and first applications, *Atmos. Environ.* **32**, 2981–2999 (1998).

121. W. Wang, C. Bruyère, M. Duda, J. Dudhia, D. Gill, M. Kavulich, K. Keene, H.-C. Lin, J. Michalakes, S. Rizvi, X. Zhang, "Weather Research and Forecasting: ARW: Version 3 Modeling System User's Guide", tech. rep., http://www.mmm.ucar.edu/wrf/users/docs/user%5C_guide%5C_V3/contents.html.

122. S. E. Peckham, G. A. Grell, S. A. McKeen, R. Ahmadov, M. Barth, G. Pfister, C. Wiedinmyer, J. D. Fast, W. I. Gustafson, S. J. Ghan, R. Zaveri, R. C. Easter, J. Barnard, E. Chapman, M. Hewson, R. Schmitz, M. Salzmann, V. Beck, S. R. Freitas, "WRF/Chem Version 3.4 User's Guide", tech. rep., http://ruc.noaa.gov/wrf/WG11/.

123. L. K. Emmons, S. Walters, P. G. Hess, J.-F. Lamarque, G. G. Pfister, D. Fillmore, C. Granier, A. Guenther, D. Kinnison, T. Laepple, J. Orlando, X. Tie, G. Tyndall, C. Wiedinmyer, S. L. Baughcum, S. Kloster, Description and evaluation of the Model for Ozone and Related chemical Tracers, version 4 (MOZART-4), *Geosci. Model Dev.* **3**, 43–67 (2010).

124. UCAR, *GCIP NCEP Eta model output*, 2005, `http://rda.ucar.edu/datasets/ds609.2/` (visited on 01/15/2012).

125. D. Schwede, G. Pouliot, T. Pierce, Changes to the biogenic emissions inventory system version 3 (BEIS3), presented at the 4th Annu. C. Model. User's Conf. Vol. 3, `http://cmascenter.org/conference/2005/abstracts/2%5C_7.pdf`, (2005).

126. M. R. Houyoux, J. M. Vukovich, Updates to the Sparse Matrix Operator Kernel Emissions (SMOKE) modeling system and integration with Models-3, presented at the Proc. Emiss. Invent. Reg. Strateg. Futur. (1999).

127. American Society of Mechanical Engineers (ASME), *Recommended Guide for the Prediction of the Dispersion of Airborne Effluents* (ASME, New York, ed. 2, 1973).

128. J. H. Seinfeld, S. N. Pandis, *Atmospheric chemistry and physics from air pollution to climate change* (J. Wiley, Hoboken, N.J., 2nd, 2006).

129. University of California Davis (U. C. Davis), "IMPROVE Data Guide: A Guide to Interpret Data", tech. rep. (Prepared for National Park Service, Air Quality Research Division, Fort Collins, CO, 1995), `http://vista.cira.colostate.edu/improve/publications/OtherDocs/IMPROVEDataGuide/IMPROVEdataguide.htm`.

130. A. C. Aiken, P. F. DeCarlo, J. H. Kroll, D. R. Worsnop, J. A. Huffman, K. S. Docherty, I. M. Ulbrich, C. Mohr, J. R. Kimmel, D. Sueper, Y. Sun, Q. Zhang, A. Trimborn, M. Northway, P. J. Ziemann, M. R. Canagaratna, T. B. Onasch, M. R. Alfarra, A. S. H. Prevot, J. Dommen, J. Duplissy, A. Metzger, U. Baltensperger, J. L. Jimenez, O/C and OM/OC ratios of primary, secondary, and ambient organic aerosols with high-resolution time-of-flight aerosol mass spectrometry, *Environ. Sci. Technol.* **42**, 4478–4485 (2008).

131. U.S. Census Bureau, *Cartographic Boundary Shapefiles - Regions*, 2013, https://www.census.gov/geo/maps-data/data/cbf/cbf%5C_region.html (visited on 10/02/2014).

132. U.S. Census Bureau, *Year-2014 US urban areas and clusters*, 2014, ftp://ftp2.census.gov/geo/tiger/TIGER2014/UAC/ (visited on 10/02/2014).

133. E. Solazzo, R. Bianconi, G. Pirovano, V. Matthias, R. Vautard, M. D. Moran, K. Wyat Appel, B. Bessagnet, J. Brandt, J. H. Christensen, C. Chemel, I. Coll, J. Ferreira, R. Forkel, X. V. Francis, G. Grell, P. Grossi, A. B. Hansen, A. I. Miranda, U. Nopmongcol, M. Prank, K. N. Sartelet, M. Schaap, J. D. Silver, R. S. Sokhi, J. Vira, J. Werhahn, R. Wolke, G. Yarwood, J. Zhang, S. T. Rao, S. Galmarini, Operational model evaluation for particulate matter in Europe and North America in the context of AQMEII, *Atmos. Environ.* **53**, 75–92 (2012).

134. National Research Council, "Transitions to Alternative Vehicles and Fuels", tech. rep., http://www.nap.edu/catalog.php?record%5C_id=18264.

135. US Environmental Protection Agency (EPA), *Regulation of Fuels and Fuel Additives: Changes to Renewable Fuel Standard Program; Final Rule*, 2010, http://www.epa.gov/otaq/fuels/renewablefuels/regulations.htm.

136. J. Campbell, D. Lobell, C. Field, Greater transportation energy and GHG offsets from bioelectricity than ethanol., *Science* **324**, 1055–1057 (2009).

137. J. Ohlrogge, D. Allen, B. Berguson, D. Dellapenna, Y. Shachar-Hill, S. Stymne, Driving on biomass, *Science* **324**, 1019–20 (2009).

138. M. Wang, A. Burnham, Y. Wu, *The Greenhouse Gases, Regulated Emissions, and Energy Use in Transportation Model v2_2012*, 2012, http://greet.es.anl.gov/.

139. H. L. MacLean, L. B. Lave, Life cycle assessment of automobile/fuel options., *Environ. Sci. Technol.* **37**, 5445–52 (2003).

140. US Census Bureau, *Census 2000 Datasets*, 2000, http://www2.census.gov/census%5C_2000/datasets/ (visited on 06/03/2012).

141. "Transportation Vision for 2030", tech. rep. (U.S. Department of Transportation Research and Innovative Technology Administration, 2008), http://www.rita.dot.gov/sites/default/files/rita%5C_archives/rita%5C_publications/transportation%5C_vision%5C_2030/index.html.

142. P. J. Balducci, "Plug-in Hybrid Electric Vehicle Market Penetration Scenarios", tech. rep. (Pacific Northwest National Laboratory, 2008), http://www.pnl.gov/main/publications/external/technical%5C_reports/pnnl-17441.pdf.

143. G. Yarwood, S. Rao, M. Yocke, G. Z. Whitten, "Updates to the Carbon Bond Mechanism: CB05", tech. rep., http://www.camx.com/publ/pdfs/CB05%5C_Final%5C_Report%5C_120805.pdf.

144. S. Bashash, S. J. Moura, H. K. Fathy, On the aggregate grid load imposed by battery health-conscious charging of plug-in hybrid electric vehicles, *J. Power Sources* **196**, 8747–8754 (2011).

145. U.S. Energy Information Administration, "Annual Energy Outlook 2011", tech. rep., DOE/EIA–0383.

146. C. W. Murphy, N. C. Parker, Impact of air pollution control costs on the cost and spatial arrangement of cellulosic biofuel production in the U.S., *Environ. Sci. Technol.* **48**, 2157–2164 (2014).

147. "Mineral Industry Surveys: Primary Aluminum Plants", tech. rep. July (US Geological Survey, 1999), http://minerals.usgs.gov/minerals/pubs/commodity/aluminum/alplants.html.

148. B. D. L. Edelstein, "U.S. Geological Survey 2010 Minerals Yearbook: Copper", tech. rep. (U.S. Geological Survey, 2010), http://minerals.usgs.gov/minerals/pubs/commodity/copper/myb1-2010-coppe.pdf.

149. "Mineral Commodity Summaries 2012", tech. rep. (U.S. Geological Survey, 2012), http://minerals.usgs.gov/minerals/pubs/mcs/.

150. T. Bond, C. Venkataraman, O. Masera, Global atmospheric impacts of residential fuels, *Energy Sustain. Dev.* **8**, 20–32 (2004).

151. US Centers for Disease Control and Prevention, *Compressed Mortality File*, 2000, http://www.cdc.gov/nchs/data%5C_access/cmf.htm (visited on 11/06/2011).

152. "Technical Support Document: Estimating the Benefit per Ton of Reducing $PM_{2.5}$ Precursors from 17 Sectors", tech. rep. January (U.S. Environmental Protection Agency, 2013), http://www.epa.gov/airquality/benmap/models/Source%5C_Apportionment%5C_BPT%5C_TSD%5C_1%5C_31%5C_13.pdf.

153. R. S. J. Tol, The economic effects of climate change, *J. Econ. Perspect.* **23**, 29–51 (2009).

154. U.S. Environmental Protection Agency, *Fugitive Dust from Mining and Quarrying (2325000000)*, 2013, ftp://ftp.epa.gov/EmisInventory (visited on 08/12/2013).

155. Xstrata Coal, "Ravensworth Underground Mine - Coal Mine Particulate Matter Control Best Management Practice Determination", tech. rep., http://www.xstratacoalravensworth.com.au/EN/RavensworthUndergroundMine/Publications/Mt%20plans%20and%20programs/RUM%20Coal%20Mine%20PM%20BMP%20Determination.pdf.

156. R. J. Plevin, M. O'Hare, A. D. Jones, M. S. Torn, H. K. Gibbs, Greenhouse gas emissions from biofuels' indirect land use change are uncertain but may be much greater than previously estimated, *Environ. Sci. Technol.* **44**, 8015–21 (2010).

157. W. K. Viscusi, J. E. Aldy, The value of a statistical life: A critical review of market estimates throughout the world, *J. Risk Uncertain.* **27**, 5–76 (2003).

158. A. Brandt, G. Heath, E. Kort, F. O'Sullivan, Methane leaks from North American natural gas systems, *Science* **343**, 7–9 (2014).

159. M. B. Dusseault, Comparing venezuelan and canadian heavy oil and tar sands, presented at the Proc. Pet. Soc. Can. Int. Conf. (2001).

160. Argonne National Laboratory, "Summary of Expansions and Revisions in GREET2_2012 Version", tech. rep. July, https://greet.es.anl.gov/files/greet2-2012-memo.

161. C. Costello, W. M. Griffin, A. E. Landis, H. S. Matthews, Impact of biofuel crop production on the formation of hypoxia in the Gulf of Mexico., *Environ. Sci. Technol.* **43**, 7985–91 (2009).

162. C. King, M. Webber, Water intensity of transportation, *Environ. Sci. Technol.* **42**, 7866–7872 (2008).

163. D. Burtraw, US climate change policy efforts, *Cent. Eur. Policy Stud. Policy Br.* 1–8 (2011).

164. U.S. Environmental Protection Agency, *Climate Change Regulatory Initiatives*, 2012, http://www.epa.gov/climatechange/EPAactivities/regulatory-initiatives.html (visited on 03/13/2012).

165. N. Lutsey, D. Sperling, America's bottom-up climate change mitigation policy, *Energy Policy* **36**, 673–685 (2008).

166. C2ES: Center for Climate and Energy Solutions, *Greenhouse Gas Emissions Targets*, 2012, http://www.c2es.org/us-states-regions/policy-maps/emissions-targets (visited on 08/07/2012).

167. IPCC, "Guidelines for National Greenhouse Gas Inventories", tech. rep. (IPCC WGI Technical Support Unit, Bracknell, UK, 2006), http://www.ipcc-nggip.iges.or.jp/public/2006gl/index.html.

168. T. Ghosh, C. D. Elvidge, P. C. Sutton, K. E. Baugh, D. Ziskin, B. T. Tuttle, Creating a global grid of distributed fossil fuel CO_2 emissions from nighttime satellite imagery, *Energies* **3**, 1895–1913 (2010).

169. P. J. Rayner, M. R. Raupach, M. Paget, P. Peylin, E. Koffi, A new global gridded data set of CO_2 emissions from fossil fuel combustion: Methodology and evaluation, *J. Geophys. Res.* **115**, D19306 (2010).

170. T. Oda, S. Maksyutov, A very high-resolution (1 km×1 km) global fossil fuel CO_2 emission inventory derived using a point source database and satellite observations of nighttime lights, *Atmos. Chem. Phys.* **11**, 543–556 (2011).

171. K. Gurney, I. Razlivanov, Y. Song, Quantification of fossil fuel CO_2 emissions on the building/street scale for a large US City, *Environ. Sci. Technol.* **46**, 12194–12202 (2012).

172. S. J. Davis, K. Caldeira, Consumption-based accounting of CO_2 emissions., *Proc. Natl. Acad. Sci. U. S. A.* **107**, 5687–92 (2010).

173. S. J. Davis, G. P. Peters, K. Caldeira, The supply chain of CO_2 emissions, *Proc. Natl. Acad. Sci. U.S.A.* **108**, 18554–18559 (2011).

174. K. Steen-Olsen, J. Weinzettel, G. Cranston, A. E. Ercin, E. G. Hertwich, Carbon, land, and water footprint accounts for the european union: consumption, production, and displacements through international trade, *Environ. Sci. Technol.* **46**, 10883–10891 (2012).

175. P. Erickson, D. Allaway, M. Lazarus, E. A. Stanton, A consumption-based GHG inventory for the U.S. state of Oregon, *Environ. Sci. Technol.* **46**, 3679–3686 (2012).

176. A. Ramaswami, T. Hillman, B. Janson, M. Reiner, G. Thomas, A demand-centered, hybrid life-cycle methodology for city-scale greenhouse gas inventories, *Environ. Sci. Technol.* **42**, 6455–6461 (2008).

177. J. Heinonen, S. Junnila, Implications of urban structure on carbon consumption in metropolitan areas, *Environ. Res. Lett.* **6**, 014018 (2011).

178. J. Bushnell, C. Peterman, C. Wolfram, California's Greenhouse Gas Policies: Local Solutions to a Global Problem?, 2007, `www.ucei.berkeley.edu/PDF/csemwp166.pdf`.

179. S. Yeh, D. Sperling, Low carbon fuel standards: Implementation scenarios and challenges, *Energy Policy* **38**, 6955–65 (2010).

180. B. Strogen, A. Horvath, T. E. McKone, Fuel miles and the blend wall: Costs and emissions from ethanol distribution in the United States., *Environ. Sci. Technol.* **46**, 5285–5293 (2012).

181. C. Samaras, K. Meisterling, Life cycle assessment of greenhouse gas emissions from plug-in hybrid vehicles: Implications for policy., *Environ. Sci. Technol.* **42**, 3170–3176 (2008).

182. A. Elgowainy, J. Han, L. Poch, M. Wang, A. Vyas, M. Mahalik, A. Rousseau, "Well-to-Wheels Analysis of Energy Use and Greenhouse Gas Emissions of Plug-in Hybrid Electric Vehicles", tech. rep. (Energy Systems Division, Argonne National Laboratory #ANL/ESK/10-1, 2010), http://www.osti.gov/bridge/purl.cover.jsp?purl=/982352-XonYa7/.

183. S. Spatari, Y. Zhang, H. L. Maclean, Life cycle assessment of switchgrass- and corn stover-derived ethanol-fueled automobiles, *Environ. Sci. Technol.* **39**, 9750–9758 (2010).

184. T. R. Hawkins, B. Singh, G. Majeau-Bettez, A. H. Strømman, Comparative environmental life cycle assessment of conventional and electric vehicles, *J. Ind. Ecol.* **17**, 53–64 (2013).

185. S. C. Jackson, Parallel pursuit of near-term and long-term climate mitigation., *Science* **326**, 526–527 (2009).

186. D. T. Shindell, G. Faluvegi, D. M. Koch, G. A. Schmidt, N. Unger, S. E. Bauer, Improved attribution of climate forcing to emissions., *Science* **326**, 716–718 (2009).

187. J. Tollefson, A break in the clouds, *Nature* **485**, 164–166 (2012).

188. ENVIRON, "User's Guide—Comprehensive Air-Quality Model with Extensions", tech. rep. (ENVIRON International Corporation, Novato, CA, 2004), http://www.camx.com.

189. D. W. Byun, J. K. S. Ching, "Science Algorithms of the EPA Models-3 Community Multiscale Air Quality (CMAQ) Modeling System", tech. rep. (US Envinromental Protection Agency #EPA/600/R-99/030, Washington, D.C., 1999).

190. M. Z. Jacobson, GATOR-GCMM: A global- through urban-scale air pollution and weather forecast model: 1. Model design and treatment of subgrid soil, vegetation, roads, rooftops, water, sea ice, and snow, *J. Geophys. Res.* **106**, 5385 (2001).

191. K. Horvath, D. Koracin, R. Vellore, J. Jiang, R. Belu, Sub-kilometer dynamical downscaling of near-surface winds in complex terrain using WRF and MM5 mesoscale models, *J. Geophys. Res.* **117**, D11111 (2012).

192. J. C. Wyngaard, Toward numerical modeling in the "terra incognita", *J. Atmos. Sci.* **61**, 1816–1826 (2004).

193. A. J. Cimorelli, S. G. Perry, A. Venkatram, J. C. Weil, R. J. Paine, R. B. Wilson, R. F. Lee, W. D. Brode, R. W. Peters, AERMOD: A dispersion model for industrial source applications. Part I: General model formulation and boundary layer characterization, *J. Appl. Meteorol.* **44**, 682–693 (2005).

194. B. Paine, Short-range model distance applicability study, presented at the 10th EPA Model. Conf. http://www.epa.gov/scram001/10thmodconf/presentations/3-10-Steady-State%5C_Model%5C_Distance%5C_Applicability%5C_Study.pdf, (2012).

195. J. S. Scire, D. G. Strimaitis, R. J. Yamartino, "A User's Guide for the CALPUFF Dispersion Model", tech. rep. January (Earth Tech, Inc., Concord, MA, 2000), http://www.src.com/calpuff/download/CALPUFF%5C_UsersGuide.pdf.

196. R. R. Draxler, "Description of the HYSPLIT_4 Modeling System", tech. rep. (NOAA Technical Memorandum #ERL ARL-224, Silver Spring, MD, 2004), http://www.ciecem.uhu.es/hysplitweb08/document/arl-224.pdf.

197. "Technical Support Document for the Proposed PM NAAQS Rule: Response Surface Modeling", tech. rep. February (U.S. Environmental Protection Agency, 2006), http://www.epa.gov/scram001/reports/pmnaaqs%5C_tsd%5C_rsm%5C_all%5C_021606.pdf.

198. J. J. Buonocore, X. Dong, J. D. Spengler, J. S. Fu, J. I. Levy, Using the Community Multiscale Air Quality (CMAQ) model to estimate public health impacts of $PM_{2.5}$ from individual power plants., *Environ. Int.* **68**, 200–8 (2014).

199. "User's Manual for the Co-Benefits Risk Assessment (COBRA) Screening Model", tech. rep. (U.S. Environmental Protection Agency, Washington, D.C., 2013), http://epa.gov/statelocalclimate/documents/pdf/cobra-2.61-user-manual-july-2013.pdf.

200. N. Z. Muller, R. Mendelsohn, "The Air Pollution Emission Experiments and Policy Analysis Model (APEEP): Technical Appendix", tech. rep. 203, https://sites.google.com/

site/nickmullershomepage/home/ap2-apeep-model-2.

201. A. B. Lobscheid, W. W. Nazaroff, M. Spears, A. Horvath, T. E. McKone, Intake fractions of primary conserved air pollutants emitted from on-road vehicles in the United States, *Atmos. Environ.* **63**, 298–305 (2012).

202. R. Courant, K. Friedrichs, H. Lewy, Über die partiellen Differenzengleichungen der mathematischen Physik, *Math. Ann.* **100**, 32–74 (1928).

203. J. E. Pleim, A combined local and nonlocal closure model for the atmospheric boundary layer. Part I: Model description and testing, *J. Appl. Meteorol. Climatol.* **46**, 1383–1395 (2007).

204. R. Wilson, Turbulent diffusivity in the free atmosphere inferred from MST radar measurements: A review, *Ann. Geophys.* **22**, 3869–3887 (2004).

205. M. Wesely, Parameterization of surface resistances to gaseous dry deposition in regional-scale numerical models, *Atmos. Environ.* **23**, 1293–1304 (1989).

206. J. Walmsley, M. Wesely, Modification of coded parametrizations of surface resistances to gaseous dry deposition, *Atmos. Environ.* **30**, 1181–1188 (1996).

207. D. Simpson, H. Fagerli, J. E. Jonson, S. Tsyro, P. Wind, J.-P. Tuovinen, "Transboundary Acidification, Eutrophication and Ground Level Ozone in Europe, Part I: Unified EMEP Model Description", tech. rep. (Norwegian Meteorological Institute, 2003), http://www.emep.int/UniDoc/.

208. P. Brown, Race, class, and environmental health: A review and systemization of the literature, *Environ. Res.* **69**, 15–30 (1995).

209. P. Mohai, D. Pellow, J. T. Roberts, Environmental justice, *Annu. Rev. Environ. Resour.* **34**, 405–430 (2009).

210. S. Anand, The concern for equity in health, *J. Epidemiol. Community Health* **56**, 485–487 (2002).

211. W. J. Clinton, *Federal Actions To Address Environmental Justice in Minority Populations and Low-Income Populations*, 1994, http://www.archives.gov/federal-register/executive-orders/pdf/12898.pdf.

212. L. P. Clark, D. B. Millet, J. D. Marshall, National Patterns in Environmental Injustice and Inequality: Outdoor NO_2 Air Pollution in the United States., *PLoS One* **9**, e94431 (2014).

213. U.S. Census Bureau, *American Community Survey: 2012 Data Release*, 2012, http://www.census.gov/acs/www/data%5C_documentation/2012%5C_release/ (visited on 12/04/2014).

214. Minnesota Population Center, "National Historical Geographic Information System: Version 2.0." Tech. rep. (University of Minnesota, Minneapolis, MN, 2011), http://www.nhgis.org.

215. R Development Core Team, *R: A Language and Environment for Statistical Computing*, http://www.r-project.org/.

216. U.S. Census Bureau, "Household Income: 2012", tech. rep., http://www.census.gov/prod/2013pubs/acsbr12-02.pdf.

217. J. I. Levy, S. M. Chemerynski, J. L. Tuchmann, Incorporating concepts of inequality and inequity into health benefits analysis., *Int. J. Equity Heal.* **5**, DOI: 10.1186/1475-9276-5-2 (2006).

218. D. Plat, *IC2: Inequality and Concentration Indices and Curves*, 2012, http://cran.r-project.org/web/packages/IC2/index.html (visited on 11/20/2014).

Appendix A

Model availability

The GREET model is available at https://greet.es.anl.gov/. GREET-cst is freely available upon request. WRF/Chem is available at http://www2.mmm.ucar.edu/wrf/users/. The SMOKE model is available at https://www.cmascenter.org/smoke/. My program used to convert between SMOKE and GREET-cst output and WRF/Chem input formats is available at https://bitbucket.org/ctessum/emcnv/. InMAP is available at https://github.com/ctessum/inmap.

Appendix B

Supplemental information for Chapter 2

All supplemental data for Chapter 2 is located at http://pubs.acs.org/doi/suppl/10.1021/es3010514.

B.1 Process specific emissions results

In the above website, three Microsoft Excel files contain the percent of total life cycle emissions by process for three fuels ("es3010514_si_001.xls": gasoline, "es3010514_si_002.xls": corn ethanol, "es3010514_si_003.xls": cellulosic corn stover ethanol), with total life cycle emissions in mg/mile at the bottom of each page. Results are presented for chemical groups output by GREET as well as for pollutants groups speciated according to the CB05 chemical mechanism. The CB05 chemical mechanism is described in Table B.1. For ethanol fuels, speciated results are presented for both E10 and E85 fuel blends.

B.2 Process specific emissions maps and temporal profiles

Within the above website directory, the PDF formatted files:

- “es3010514_si_005.pdf”
- “es3010514_si_006.pdf”
- “es3010514_si_007.pdf”

contain maps and plots of temporal profiles for emissions locations and times for all processes and pollutants with emissions of more than 1% of the life cycle total.

Table B.1: Full Names of Chemical Species in CB05 Chemical Mechanism

Abbreviation	Name
ALD2	Acetaldehyde
ALDX	Higher aldehydes
BENZENE	Benzene
CO	Carbon Monoxide
ETH	Ethene
ETHA	Ethane
ETOH	Ethanol
FORM	Formaldehyde
HONO	Nitrous acid
IOLE	Internal olefins
ISOP	Isoprene
MEOH	Methanol
NH3	Ammonia
NO	Nitrogen monoxide
NO2	Nitrogen dioxide
NVOL	Nonvolatile organic chemicals
OLE	Olefins
PAR	Paraffins
PEC	Elemental carbon
PM10	Particulate matter less than 10 micrometers in diameter
PMFINE	Particulate matter less than 2.5 micrometers in diameter; unclassified
PNO3	Nitrate particulates less than 2.5 micrometers in diameter
POC	Organic particulates less than 2.5 micrometers in diameter
PSO4	Sulfate particulates less than 2.5 micrometers in diameter
SO2	Gaseous sulfur dioxide
SULF	Gaseous sulfate
TERP	Terpenes
TOL	Toluene
UNK	Unknown VOCs
UNR	Unreactive VOCs
XYL	Xylene

Appendix C

Supplemental information for Chapter 3

Supporting information available at http://www.geosci-model-dev-discuss.net/7/8433/2014/gmdd-7-8433-2014-supplement.zip includes WRF-Chem configuration settings (ascii format), maps showing spatial patterns in pollutant concentrations by annual average, month of year, day of week, and hour of day (pdf format), model-measurement comparison statistics (xlsx format), and monitor-specific paired model and measurement data (json ascii format). A video showing spatially- and temporally-explicit O_3 and total $PM_{2.5}$ concentrations is at http://youtu.be/4bpQXBAUVwE.

Appendix D

Supplemental information for Chapter 4

Supplemental results and data are available in an external repository at `http://dx.doi.org/10.13020/D6159V`. The contents of the repository are described below:

- **DatasetS1.xls**: A directory of Microsoft Excel files containing emissions amounts disaggregated by life cycle stage for each scenario.
- **DatasetS2.pdf**: Maps of annual average ground level concentrations of $PM_{2.5}$, O_3, PM_{10}, NO_x, HCHO, NH_3, particulate SO_4, particulate NH_4, particulate NO_3, organic aerosol, elemental carbon aerosol, particle number, and CO; maps of annual average daily peak O_3 concentrations; and maps of $PM_{2.5}$ and O_3 concentrations animated by month of year, day of week, and hour of day for the baseline simulation and each scenario. A pdf viewer that allows embedded javascript, such as Adobe Acrobat, is required to view the animations.
- **VideoS1.mp4**: A video showing temporal variation in $PM_{2.5}$ concentrations attributable to each scenario.
- **VideoS2.mp4**: A video showing temporal variation in O_3 concentrations attributable to

each scenario.

Appendix E

Supplemental information for Chapter 5

All supplemental information for Chapter 5 accompanies this dissertation.

The Microsoft Excel (*.xls) files contain the percent of total life cycle emissions by process for four fuel scenarios, with total life cycle emissions in µg/mile at the bottom of each page. Results are presented for chemical groups output by GREET as well as for pollutant groups speciated according to the CB05 chemical mechanism.

The PDF format files named "ProcessMaps_*" contain maps of emissions times, amounts, and locations for individual unit processes in each life cycle.

The file SupplementalFigures.pdf contains contributions of emissions from individual processes for each of the GREET output pollutants as well as or pollutant groups speciated according to the CB05 chemical mechanism. It also includes maps of total emissions of individual pollutants and CO2e emissions for 20, 100, and 500 year GWP horizons.

Abbreviations in file names:

- gasoline = gasoline fuel
- corn = corn ethanol

- cell_stover = cellulosic ethanol from corn stover
- ev = battery electric vehicle

Appendix F

Supplemental information for Chapter 7

A Microsoft Excel file containing risk and inequality results disaggregated by scenario, region, model, and race-ethnicity accompanies this dissertation.